

THESIS TITLE

Clear-Air Radioclimatological Modeling for Terrestrial Line of Sight Links in Southern Africa

SUBMITTED BY

Odedina Peter Kemi

IN FULFILLMENT OF THE DEGREE OF

Doctor of Philosophy in Electronic Engineering at the University of KwaZulu-Natal
(Howard College Campus)

DATE OF SUBMISSION

AUGUST 2010

SUPERVISED BY

Professor T.J. Afullo

As the candidate's supervisor, I have approved this thesis for submission.

Signed: _____

Name: _____ Date: _____

PREFACE

The research work done in this thesis was performed by Odedina Peter Kemi, under the supervision of Professor Thomas J. Afullo, at the School of Electrical, Electronic and Computer Engineering at the University of KwaZulu-Natal's, Durban, South Africa. The work was supported by Telkom and Alcatel South Africa as part of the Center of Excellence Programme.

Part of this thesis has been published in the South African Institute of Electrical Engineer (SAIIEEE) African Research Journal September 2008. The author has presented some part of this thesis during the South Africa Telecommunications Networks and Applications Conference (SATNAC) September 2008 at Wild coast Sun, South Africa, IEEE Regional Conference AFRCON 2007 in Windhoek, Namibia, International Association for Science And Technology Development IASTED, July 2009 Banff, Canada, South Africa Telecommunications Networks and Application Conference (SATNAC) August 2009, in Swaziland, and the Progress In Electromagnetic Research Symposium (PIERS) March 2009, in Beijing, China.

The whole thesis, unless specifically indicated to the contrary in the text, is the author's work, and has not been submitted in part, or in whole to any other University.

ACKNOWLEDGEMENTS

To God is the glory for giving me the strength to complete this work. Also I will like to thank my brothers Mr. Joe Odedina and Mr. Gabriel Odedina for their financial and moral support.

I would like to especially thank my supervisor Prof. T.J. Afullo for painstakingly going through the report several times; his constructive criticism and professional guidance are highly appreciated.

I sincerely appreciate the contribution of Amith S. Dabideen for releasing the Durban data collected from the South Africa Weather Service used in the thesis. Also appreciated is the clear-air measurement data recorded by K. Naicker and Prof. S.H. Mnenney, also used in the multipath modeling section of the report.

My sincere gratitude to the following academic staff in the school of Electrical, Electronic and Computer Engineering, University of KwaZulu – Natal including; Mr. Rathi Sewsunker, Dr. L.L Jarvis, Prof. N. Ijumba and Prof. S.H. Mnenney for creating a friendly and conducive atmosphere to do the research.

Also appreciated is the effort, assistance and the support of the administrative staff, especially Mrs. B. Bennett, Mrs. Y. Veeran, and Ms. B. Hlongwa for their moral support during the research period.

I thank my dear friend, sister, colleague and wife Mrs. Modupe Odedina and my son Mst. Leke Odedina for their support and understanding during the research period. Finally, I appreciate the support of my colleagues and friends such as Mr. O.O. Oyerinde, Dr. L. Khumalo, Dr. O. Akintola, Mrs. F. Ademola-Adeola, Mr. O. Ilesanmi, Mr. G. Aiyetoro and Mr. P.A. Owolawi.

ABSTRACT

This thesis has investigated radioclimatological study in a clear-air environment as applicable to terrestrial line of sight link design problems. Radioclimatological phenomena are adequately reviewed both for the precipitation effect and clear-air effect. The research focuses more on the clear-air effect of radioclimatological studies. Two Southern African countries chosen for case study in the report are Botswana and South Africa. To this end, radiosonde data gathered in Maun, Botswana and Durban, South Africa are used for model formulation and verification. The data used in the thesis ranges from three years to ten years in these two stations. Three to ten years of refractivity data gathered in Botswana and South Africa is used for the model formulation. On the other hand, eight months signal level measurement data recorded from the terrestrial line of sight link set up between Howard College and Westville Campuses of the University of KwaZulu-Natal, Durban South Africa is used for model verification.

Though various radioclimatic parameters could affect radio signal propagation in the clear-air environment, this report focuses on two of these parameters. These two parameters are the geoclimatic factor and effective earth radius factor (k-factor). The first parameter is useful for multipath fading determination while the second parameter is very important for diffraction fading, modeling and characterization. The two countries chosen have different terrain and topographical structures; thus further underlying the choice for these two parameters. While Maun in Botswana is a gentle flat terrain, Durban in South Africa is characterized by hilly and mountainous terrain structure, which thus affects radioclimatological modeling in the two countries.

Two analytical models have been proposed to solve clear-air radioclimatic problems in Southern Africa in the thesis. The first model is the fourth order polynomial analytical expression while the second model is the parabolic equation. The fourth order polynomial model was proposed after an extensive analysis of the eight month signal level measurement data gathered in Durban, South Africa. This model is able to predict the fade exceedance probabilities as a function of fade depth level. The result from the fourth order polynomial model is found to be comparable with other established multipath propagation model reviewed in the thesis. Availability of more measurement data in more location will be necessary in future to further refine this model.

The second model proposed to solve clear-air propagation problem in the thesis is the modified parabolic equation. We chose this technique because of its strength and its simplistic adaptation to terrestrial line of sight link design problem. This adaptation is possible because, the parabolic equation can be modified to incorporate clear-air parameters. Hence this modification of the parabolic equation allows the possibility of

formulating a hybrid technique that incorporates both the statistical and mathematical procedures perfectly into one single process. As a result of this, most of the very important phenomena in clear-air propagation such as duct occurrence probabilities, diffraction fading and multipath fading is captured by this technique.

The standard parabolic equation (SPE) is the unmodified parabolic equation which only accounts for free space propagation, while the modified parabolic equation (MPE) is the modified version of the parabolic equation. The MPE is classified into two in the thesis: the first modified parabolic equation (MPE1) and second modified parabolic equation (MPE2). The MPE1 is designed to incorporate the geoclimatic factor which is intended to study the multipath fading effect in the location of study. On the other hand, MPE2 is the modified parabolic equation designed to incorporate the effective earth radius factor (k-factor) intended to study the diffraction fading in the location of study. The results and analysis of the results after these modifications confirm our expectation. This result shows that signal loss is due primarily to diffraction fading in Durban while in Botswana, signal loss is due primarily to multipath. This confirms our expectation since a flatter terrain attracts signal loss due to multipath while hilly terrain attracts signal loss due to diffraction fading.

TABLE OF CONTENTS

CONTENT	TITLE	PAGE
TITLE PAGE.....		i
PREFACE.....		ii
ACKNOWLEDGEMENTS.....		iii
ABSTRACT.....		iv
TABLE OF CONTENTS.....		vi
LIST OF ACRONYMS.....		xi
LIST OF FIGURES.....		xvi
LIST OF TABLES.....		xvi
CHAPTER ONE.....		1
INTRODUCTION AND BASIC BACKGROUND STUDY OF RADIOCLIMATOLOGICAL MODELING.....		1
1.0 INTRODUCTION.....		1
1.1 Thesis Objective and proposed way to achieve stated objective.....		3
1.2 Thesis Overview.....		4
1.3 Original Contribution.....		8
1.4 Publications.....		9
1.5 Chapter Summary.....		10
CHAPTER TWO.....		11
LITERATURE REVIEW.....		11
2.0 INTRODUCTION.....		11
2.1 Overview of Clear-Air Multipath Modeling.....		11
2.2 Overview of Clear-Air Diffraction Fading Modeling.....		13
2.3 Clear-Air Line of Sight Path Characterization.....		14
2.3.1 Investigation Study Area.....		14
2.3.2 Clear-Air Digital Terrain Characterization.....		18
2.4 Refractivity, Refractivity Gradient and Geoclimatic Factor Determination.....		20
2.4.1 Spatial Interpolation Technique		20
2.4.2 Application of Spatial Interpolation Technique to Clear-air Study.....		21
2.4.3 Application of Simplified Statistical Technique to Clear-Air Study.....		23
2.5 Kernel Estimation Technique.....		29

2.5.1 Results of Kernel Estimates.....	31
2.6 Chapter Summary.....	36
CHAPTER THREE.....	37
BACKGROUND INFORMATION AND REVIEW OF CLAR-AIR RADIOCLIMATIC MODELING BY DIFFERENT AUTHORS.....	37
3.0 INTRODUCTION.....	37
3.1 Atmospheric Effects on Propagation for Line of Sight (LOS) Links.....	37
3.1.1 Precipitation (non clear-air) Effect on Line of Sight (LOS) Links.....	38
3.1.2 Rain.....	38
3.1.3 Clouds and Fog.....	39
3.1.4 Snow.....	39
3.2 Clear-Air Radioclimatic Effect on Line of Sight (LOS) Links.....	39
3.2.1 Primary Clear-Air Radioclimatic Effect.....	39
3.2.2 Secondary Clear-Air Radioclimatic Effect.....	40
3.3 Other Line of Sight Link Design Issues.....	42
3.3.1 Multipath Propagation.....	42
3.3.2 Diffraction Effects.....	44
3.3.3 Fresnel Zone Radius.....	44
3.3.4 Knife – Edge Diffraction Loss.....	46
3.3.5 k-factor Fading.....	48
3.3.6 Link Budget and Link Reliability.....	50
3.4 Free Space Propagation.....	51
3.5 Clear-Air Multipath Propagation Modeling Techniques by Various Authors.....	53
3.5.1 The K. Morita and K. Kakita Model (Japan).....	53
3.5.2 Distance Dependence of Rayleigh Fading Occurrence Probability.....	53
3.5.3 Relation between Path Height and Rayleigh Fading Occurrence Probability.....	54
3.5.4 Relation between Inclination of Propagation Path and Rayleigh Fading Occurrence Probability.....	56
3.5.5 Frequency Dependence of Rayleigh Fading Occurrence Probability.....	56
3.5.6 Empirical Formula of Rayleigh Fading Occurrence Probability.....	57
3.5.7 The M.S. Wheeler Model.....	58
3.5.8 The A. Vigants Model (USA).....	60
3.5.9 The Space –Diversity Effect.....	62

3.5.10	Comparison of Space and Frequency Diversity.....	64
3.5.11	The Crombie Model (USA).....	65
3.5.12	Data Used for Analysis.....	67
3.5.13	Analysis of Data.....	67
3.5.14	Summary of Crombie Model.....	73
3.5.15	The R.L. Olsen and B. Segal Approach (North America and Canada).....	74
3.5.16	Method for Initial Planning and Licensing Purposes.....	74
3.5.17	Method Requiring Path Profile.....	77
3.5.18	Limitation and Accuracy of the First and Second Methods.....	80
3.5.19	Approach of T. Tjelta, T.G. Hayton, B.Segal , E. Salomen, R. Olsen. and L. Martin (Western Europe).....	82
3.5.20	Correlation of Multipath Occurrence Parameters Derived from radiosonde, Surface Stations and Numerical Atmospheric Model.....	82
3.5.21	Systematic Development of New Multivariable Techniques for Predicting the Distribution of Multipath Fading on Terrestrial Microwave Links.....	84
3.5.22	Limitation of the Approach.....	87
3.6	Clear-Air Diffraction Fading Techniques by different Authors.....	88
3.6.1	The M.S. Wheeler Approach.....	88
3.6.2	The D.C. Baker and A.J. Palmer Approach.....	89
3.6.3	The “Dry – Wet” Model.....	89
3.6.4	The T.J. Afullo <u>et al</u> Approach.....	91
3.7	Analytical or Semi-Empirical Approach to Solving Clear-Air Radioclimatic Problems.....	95
3.7.1	Martin’s Analytical / Semi-Empirical Approach (Australia).....	95
3.7.2	The Parabolic Equation Method.....	97
3.7.3	Parabolic Equation Framework.....	97
3.7.4	Numerical Methods of Parabolic Equations.....	99
3.7.5	Parabolic Approximation Method of Parabolic Equation.....	101
3.8	Chapter Summary.....	102
CHAPTER FOUR		105
A PROPOSED MODEL OF CLEAR-AIR RADIOCLIMATIC STUDY.....		105
4.0	INTRODUCTION.....	105
4.1	Basic information on Data used for Analysis and Model Formulation.....	105
4.2	Daily Signal Level Analysis for Percentage of Time that a Particular Fade Depth is Exceeded.....	106

4.2.1	Daily Signal Level Analysis for February.....	106
4.2.2	February 20 2004.....	107
4.2.3	February 28 2004.....	108
4.2.4	Daily Signal Level Analysis for March.....	109
4.2.5	March 6 2004.....	110
4.2.6	March 16 2004.....	111
4.2.7	Daily Signal Level Analysis for April.....	112
4.2.8	April 15 2004.....	113
4.2.10	Daily Signal Level Analysis for May.....	115
4.2.11	May 3 2004.....	116
4.2.12	May 27 2004.....	117
4.2.13	Daily Signal Level Analysis for June.....	119
4.2.14	June 3 2004.....	120
4.2.15	June 20 2004.....	121
4.2.16	Daily Signal Level Analysis for July.....	122
4.2.17	July 4 2004.....	123
4.2.18	July 22 2004.....	123
4.2.19	Daily Signal Level Analysis for August.....	124
4.2.20	August 1 2004.....	125
4.2.21	August 21 2004.....	126
4.2.22	Daily Signal Level Analysis for December.....	127
4.2.23	December 12 2004.....	127
4.3	Monthly Signal Level Analysis for Percentage of Time that a Particular Fade Depth is Exceeded..	130
4.3.1	Monthly Signal Level Analysis for February.....	131
4.3.2	Monthly Signal Level Analysis for March.....	133
4.3.3	Monthly Signal Level Analysis for April.....	136
4.3.4	Monthly Signal Level Analysis for May.....	140
4.3.5	Monthly Signal Level Analysis for June.....	143
4.3.6	Monthly Signal Level Analysis for July.....	146
4.3.7	Monthly Signal Level Analysis for August.....	148
4.3.8	Monthly Signal Level Analysis for December.....	150
4.4	Total Signal Level Analysis for Percentage of Time that a Particular Fade Depth is Exceeded.	153

4.5	Proposed Analytical Model for Clear-Air Radioclimatic Study in Southern Africa.....	155
4.6	Application of Parabolic Equation to Clear-Air Radioclimatological Study.....	160
4.6.1	The Narrow-angle Code.....	161
4.6.2	Path Loss.....	165
4.7	Alternative Formulation for Determination of Geoclimatic Factor.....	168
4.8	First Modified Parabolic Equation (MPE1) (Takes into account the effect of multipath).....	172
4.9	Second Modified Parabolic Equation (MPE2) (Takes into account the effect of diffraction fading)	178
4.10	Chapter Summary.....	182
CHAPTER FIVE.....		184
COMPARISON OF THE RESULTS OBTAINED USING DIFFERENT MODELS AND THE PROPOSED MODEL.....		184
5.0	INTRODUCTION.....	184
5.1	Comparison of Morita and Kakita Models.....	184
5.2	Comparison of Vigants Models.....	186
5.3	Comparison of Crombies' Model.....	195
5.3.1	Comparison of Crombies' Model 4.....	196
5.3.2	Comparison of Crombies' Model 5.....	197
5.4	Comparison of Olsen and Segal Models.....	197
5.4.1	Comparison of Olsen and Segal First Method.....	198
5.4.2	Comparison of Olsen and Segal Second Method.....	199
5.5	Comparison of all Multipath Propagation Models with our Proposed Model.....	202
5.6	Combined Parabolic Equation in Durban and Botswana for Different Season.....	204
5.7	Chapter Summary.....	209
CHAPTER SIX.....		211
SUMMARY, CONCLUSIONS AND RECOMMENDATION FOR FUTURE STUDIES		211
6.0	SUMMARY AND CONCLUSIONS.....	211
6.1	Recommendation for Future Work.....	214
REFERENCES.....		216
APPENDICES.....		231

LIST OF ACRONYMS

LOS	Line-of-Sight
RMS	Root mean square
ITU-R	International Telecommunications Union – Recommendation
CCIR	International Radio Consultative Committee
P_R	Occurrence Probability of Rayleigh fading
F_r	Fading range
K	Geoclimatic factor
k	Effective earth radius factor (k-factor)
P	Percentage of Exceedance probability of fade depth
P_A	Percentage of time that fade depth A is exceeded
ISE	Integral Square Error
P_r	Received Power
P_t	Transmitted Power
FSL	Free Space Loss
DEM	Digital Elevation Model
DTM	Digital Terrain Model
IDW	Inverse Distance Weight
MTD	Mean Temperature Deviation
MPD	Mean Pressure Deviation
MHD	Mean Humidity Deviation
SDTD	Standard Deviation of Temperature Deviation
SDPD	Standard Deviation of Pressure Deviation
SDHD	Standard Deviation of Humidity Deviation
SD	Standard Deviation
SPE	Standard Parabolic Equation
MPE1	First Modified Parabolic Equation
MPE2	Second Modified Parabolic Equation
G_F	Geoclimatic Factor
AFA	Alternative Formulation Approach

LIST OF FIGURES

Figure	Title	Pages
Figure 2.1	Location Map of the Study Area.....	15
Figure 2.2	An Areal Photo Of The Study Area.....	15
Figure 2.3	The Path Profile for 6.73 Km Terrestrial Line-Of-Sight Link from the Howard College Campus to the Westville Campus.....	17
Figure 2.4	A Digital Elevation Model (DEM) of the Study Area	19
Figure 2.5	Contour map of the Study Area	19
Figure 2.6	Cumulative distribution of dN/dh for Durban and Botswana	28
Figure 2.7	Point refractivity gradient for Durban and Botswana	28
Figure 2.8	Geoclimatic factor for different months for Durban and Botswana.....	29
Figure 2.9	Biweight Kernel estimates of the k-factor distribution, Botswana, 0-200 m a.g.l.	33
Figure 2.10	Triangular Kernel estimates of the k-factor distribution, Botswana, 0-200 m a.g.l.	34
Figure 2.11	Gaussian Kernel estimates of the k-factor distribution, Botswana, 0-200 m a.g.l.	34
Figure 2.12	Comparison of Kernel estimates of k-factor distribution, Botswana, 0-200 m a.g.l., $h=0.1$	35
Figure 2.13	Comparison of Kernel estimates of k-factor distribution, Botswana, 0-500 m a.g.l., $h=0.1$	35
Figure 2.14	Comparison of Kernel estimates of k-factor distribution, Botswana, 0-500 m a.g.l., $h=0.25$	36
Figure 3.1	Mechanism of Multipath Fading	43
Figure 3.2	Fresnel Zone Geometry.....	45
Figure 3.3	Definition of v for obstacles above and below Line-of-Sight	47
Figure 3.4	Path Profile for radio link between Sherwood and Umlazi: Antenna Heights For 60% Clearance – Sherwood-60m, Umlazi-88m, $k = 4/3$, $F = 23$ GHz	49
Figure 3.5	Gaborone-Molepolole Path Profile: Antenna Heights for 60% Clearance – Gaborone-56m, Molepolole-30m, $k = 4/3$, $F = 23$ Ghz	50
Figure 3.6	Distance dependence of Rayleigh fading occurrence probability	54
Figure 3.7	Relation between path height and Rayleigh fading occurrence probability over the sea.....	55
Figure 3.8	Relation between path height and Rayleigh fading occurrence probability.....	55
Figure 3.9	Relation between inclination of propagation path and Rayleigh fading occurrence probability	56
Figure 3.10	Cumulative distribution curve of the hourly fading range for six typical propagation paths....	57
Figure 3.11	Path length and average antenna height for which fade statistics have been measured	59
Figure 3.12	Distance at which Rayleigh fade is attained from three sources of data.....	60
Figure 3.13	Definition of L and fade duration (-30 dBm assumed Normal as an example)	61

Figure 3.14	Definition of simultaneous fade	63
Figure 3.15	Nomogram for available improvement I_0	64
Figure 3.16	Comparison of observed and predicted probabilities of multipath fading ≥ 20 dB for all paths	69
Figure 3.17	Comparison of observed and predicted probabilities of multipath fading ≥ 20 dB on paths with adequate fresnel zone clearance	71
Figure 3.18	Comparison of observed and predicted probabilities of multipath fading ≥ 20 dB for paths with known physical clearance.....	73
Figure 3.19	Contour map indicating logarithmic geoclimatic factor G for Canada	75
Figure 3.20	Map of Canada showing different water bodies and provinces	76
Figure 3.21	Minimum effective earth radius k exceeded 99.9 percent of time in continental temperate climate	88
Figure 3.22	Measured and estimate pdf g(k) and f(k) All Year (0-500m a.g.l.) Botswana.....	94
Figure 3.23	Measured and estimate pdf g(k) and f(k) All Year (0-500m a.g.l.) Durban	95
Figure 4.1	Measured and estimated pdf, g(x) and f(x) for Rx signal level measurement, February 2004	107
Figure 4.2	Measured and estimated pdf, g(x) and f(x) for Rx signal level measurement, March 2004...	110
Figure 4.3	Measured and estimated pdf, g(x) and f(x) for Rx signal level measurement, April 2004.....	113
Figure 4.4	Measured and estimated pdf, g(x) and f(x) for Rx signal level measurement, May 2004.....	116
Figure 4.5	Measured and estimated pdf, g(x) and f(x) for Rx signal level measurement, June 2004.....	120
Figure 4.6	Measured and estimated pdf, g(x) and f(x) for Rx signal level measurement, July 2004.....	123
Figure 4.7	Measured and estimated pdf, g(x) and f(x) for Rx signal level measurement, August 2004..	126
Figure 4.8	Measured and estimated pdf, g(x) and f(x) for Rx signal level measurement, December 2004	128
Figure 4.9	Clear-Air signal level variation over 24hrs, February 2004, Durban.....	131
Figure 4.10	Fade depth exceedance probability (%) for February 2004.....	133
Figure 4.11	Clear-Air signal level variation over 24hrs, March 2004, Durban.....	134
Figure 4.12	Fade depth exceedance probability (%) for March 2004	136
Figure 4.13	Clear-Air signal level variation over 24hrs, April 2004, Durban.....	137
Figure 4.14	Fade depth exceedance probability (%) for April 2004	139
Figure 4.15	Clear-Air signal level variation over 24hrs, May 2004, Durban.....	140
Figure 4.16	Fade depth exceedance probability (%) For May 2004	143
Figure 4.17	Clear-Air signal level variation over 24hrs, June 2004, Durban.....	144
Figure 4.18	Fade depth exceedance probability (%) for June 2004	146

Figure 4.19 Clear-Air signal level variation over 24hrs, July 2004, Durban	147
Figure 4.20 Fade depth exceedance probability (%) for July 2004.....	147
Figure 4.21 Clear-Air signal level variation over 24hrs, August 2004, Durban.....	149
Figure 4.22 Fade depth exceedance probability (%) for August 2004.....	149
Figure 4.23 Clear-Air signal level variation over 24hrs, December 2004, Durban.....	151
Figure 4.24 Fade depth exceedance probability (%) for December 2004	153
Figure 4.25 Fade depth exceedance probability (%) for Whole Year	155
Figure 4.26a Percentage of time that fade depth A(dB) is exceeded; A = 2, 5, 10 and 15 dB	157
Figure 4.26b Percentage of time that fade depth A(dB) is exceeded; A = 20, 30 and 40 dB.....	157
Figure 4.27 Analytical Model for exceedance probability plot for May 2004.....	158
Figure 4.28 Analytical Model for exceedance probability plot for June 2004.....	158
Figure 4.29 Analytical Model for exceedance probability plot for Whole Year 2004.....	159
Figure 4.30 Finite difference grid for Crank-Nicolson scheme.....	161
Figure 4.31 Probability distribution of refractive index for different Kernels, Nov'03-Aug'04, Durban..	170
Figure 4.32 Probability distribution of refractive index for different Kernels, Feb-Dec'96, Maun Botswana	170
Figure 4.33 Probability distribution of refractive index for Biweight Kernels, Nov'03-Aug'04, Durban.	171
Figure 4.34 Probability distribution of refractive index for Biweight Kernels, Feb-Dec'96, Maun, Botswana	171
Figure 4.35 (a) Path Loss against Height at 19.5 GHz for MPE1 February 2004 Durban.....	174
Figure 4.35 (b) Path Loss against Height at 19.5 GHz for MPE1 February 1996 Botswana.....	174
Figure 4.36 (a) Path Loss against Height at 19.5GHz for MPE1 August 2004 Durban.....	175
Figure 4.36 (b) Path Loss against Height at 19.5GHz for MPE1 August 1996 Botswana.....	175
Figure 4.37 (a) Path Loss against Range at 19.5GHz for MPE1 February 2004 Durban.....	177
Figure 4.37 (b) Path Loss against Range at 19.5GHz for MPE1 February 1996 Botswana.....	177
Figure 4.38 (a) Path Loss against Range at 19.5GHz for MPE1 August 2004 Durban	177
Figure 4.38 (b) Path Loss against Range at 19.5GHz for MPE1 August 1996 Botswana	177
Figure 4.39 (a) Path Loss against Height at 19.5GHz For MPE2 February 2004 Durban.....	179
Figure 4.39 (b) Path Loss against Height at 19.5GHz for MPE2 February 1996 Botswana.....	179
Figure 4.40 (a) Path Loss against Height at 19.5GHz for MPE2 August 2004 Durban.....	180
Figure 4.40 (b) Path Loss against Height at 19.5GHz for MPE2 August 1996 Botswana.....	180
Figure 4.41 (a) Path Loss against Range at 19.5GHz for MPE2 February 2004 Durban.....	180
Figure 4.41 (b) Path Loss against Range at 19.5GHz for MPE2 February 1996 Botswana.....	180
Figure 4.42 (a) Path Loss against Range At 19.5GHz for MPE2 August 2004 Durban	181

Figure 4.42 (b) Path Loss against Range At 19.5GHz for MPE2 August 1996 Botswana	181
Figure 5.1 Fading exceedance of Vigants Model: Fade depth; A = 2, A = 5, A = 10, And A = 15 dB	193
Figure 5.2 Fading exceedance of Vigants Model: Fade depth; A = 20, A = 30, And A = 40 dB	193
Figure 5.3 Fading exceedance of Measurement: Fade depth; A = 2, A = 5, A = 10 And A = 15 dB	194
Figure 5.4 Fading exceedance of Measurement: Fade Depth; A = 20, A = 30, And A = 40 dB.....	194
Figure 5.5 Fading exceedance of Olsen and Segal Method 1: Fade depth; A = 20, A = 30, And A = 40 dB	199
Figure 5.6 Fading exceedance of Olsen and Segal Method 2: Fade depth; A = 20, A = 30, And A = 40 dB	201
Figure 5.7 Comparison Of Olsen-Segal Methods 1 and 2 at Fade depth of 20 dB	201
Figure 5.8 Comparison Of Olsen-Segal Methods 1 and 2 at Fade depth of 30 dB	202
Figure 5.9 (a) Path Loss against Height for all PE at 19.5GHz, Range 20 km February 2004 Durban	205
Figure 5.9 (b) Path Loss against Height for all PE at 19.5GHz, Range 20 km February 1996 Botswana .	205
Figure 5.10 (a) Path Loss against Height for all PE at 19.5GHz , Range 20 km August 2004 Durban	205
Figure 5.10 (b) Path Loss against Height for all PE At 19.5GHz, Range 20 km August 1996 Botswana...	205
Figure 5.11(a) Path Loss against Range for all PE At 19.5GHz, Height 20 m a.g.l. February 2004 Durban	206
Figure 5.11(b) Path Loss against Range for all PE At 19.5GHz, Height 20 m a.g.l. February 1996 Botswana	206
Figure 5.12 (a) Path Loss against Range for all PE at 19.5GHz, Height 20 m a.g.l. August 2004 Durban	206
Figure 5.12 (b) Path Loss against Range for all PE at 19.5GHz, Height 20 m a.g.l. August 1996 Botswana	206

LIST OF TABLES

Table	Title	Pages
Table 2.1	Terrestrial link parameters for the los shf system	17
Table 2.2 (a)	Data set for month of April 2004 before and after applying Spatial Interpolation Techniques	22
Table 2.2(b)	Data Set for Month of April 2004 before and after applying Spatial Interpolation Techniques	23
Table 2.3	Compensation factor for Temperature and Pressure Jan-Dec (1985-1990)	26
Table 2.4	Compensation factor for Humidity Jan-Dec (1985-1990).....	27
Table 2.5	Typical Kernels and their efficiencies (η)	31
Table 2.6	ISE for some Kernels for best k-factor pdf, Botswana, 200 m a.g.l., 740 samples	32
Table 2.7	Median values of the k-factor for Botswana, 200 m a.g.l., 740 samples.....	32
Table 2.8	Median values of the k-factor and ISE for Botswana, 500 m a.g.l., 1600 samples	32
Table 3.1	Refractivity profile for different atmospheric condition.....	42
Table 3.2	Pathloss exponent and standard deviation measured in different building	44
Table 3.3	k- factor variation with diffraction gain g (sherwood – umlazi) [42].....	49
Table 3.4	Effect of the k-factor variation on diffraction gain G for Gaborone-Molepolole link	50
Table 3.5	Classification of propagation path condition	54
Table 3.6	Crombie regression results – all paths, d, f, (model 1)	68
Table 3.7	Crombie regression results – all paths, d, f, θ (model 2).....	70
Table 3.8	Paths with adequate fresnel zone clearance – all paths, d, f, θ (model 3).....	70
Table 3.9	Paths with known clearance d, f, θ , h (model 4).....	72
Table 3.10	Paths with known clearance d, f, θ (model 5)	72
Table 3.11	Summary of Mean (m), Standard deviation (s), and Maximum (max) of prediction errors* (in dB) for various groupings of links	81
Table 3.12	Values of μ_k , A, and ISE for Botswana	93
Table 3.13	Values of μ_k , A, and ISE for Durban.....	93
Table 4.1	Measurement Information for Model Formulation	105
Table 4.2	Percentage of exceedance probabilities for the days in February 2004 measurement	109
Table 4.3 (a)	Percentage of exceedance probabilities for the days in March 2004 measurement.....	111
Table 4.3 (b)	Percentage of exceedance probabilities for the days in March 2004 measurement.....	112
Table 4.4 (a)	Percentage of exceedance probabilities for the days in April 2004 measurement.....	114
Table 4.4 (b)	Percentage of exceedance probabilities for the days in April 2004 measurement.....	115

Table 4.5 (a)	Percentage of exceedance probabilities for the days in May 2004 measurement.....	118
Table 4.5 (b)	Percentage of Exceedance probabilities for the days in May 2004 measurement.....	119
Table 4.6	Percentage of Exceedance probabilities for the days in June 2004 measurement.....	121
Table 4.7	Percentage of Exceedance probabilities for the days in July 2004 measurement	124
Table 4.8	Percentage of Exceedance probabilities for the days in August 2004 measurement.....	127
Table 4.9 (a)	Percentage of Exceedance probabilities for the days in December 2004 measurement ..	129
Table 4.9 (b)	Percentage of Exceedance probabilities for the days in December 2004 measurement..	130
Table 4.10	Estimates of measurement time at different fade depths in February 2004.....	132
Table 4.11 (a)	Estimates of measurement time at different fade depths in March 2004.....	134
Table 4.11 (b)	Estimates of measurement time at different fade depths in March 2004.....	135
Table 4.12 (a)	Estimates of measurement time at different fade depths in April 2004.....	138
Table 4.12 (b)	Estimates of measurement time at different fade depths in April 2004.....	139
Table 4.13 (a)	Estimates of measurement time at different fade depths in May 2004	141
Table 4.13 (b)	Estimates of measurement time at different fade depths in May 2004.....	142
Table 4.14	Estimates of measurement time at different fade depths in June 2004.....	145
Table 4.15	Estimates of measurement time at different fade depths in July 2004	148
Table 4.16	Estimates of measurement time at different fade depths in August 2004	150
Table 4.17 (a)	Estimates of measurement time at different fade depths in December 2004	151
Table 4.17 (b)	Estimates of measurement time at different fade depths in December 2004.....	152
Table 4.18	Estimates of measurement time at different fade depths for whole Year.....	154
Table 4.19	Percentage of exceedance probabilities at different fade depths for whole Year.....	154
Table 4.20	Analytical expressions of percentage exceedance probabilities for the different months.....	162
Table 4.21	Calculated geoclimatic factor(k) for durban and botswana using itu-r and the new Alternative Formulation Approach (AFA)	172
Table 5.1	Height Profile estimation for los link path.....	190
Table 5.2	Multipath modeling parameters for Olsen and Segal method two.....	200
Table 5.3	Outage probability for the measurement compared with semi-empirical models	206
Table 5.4	Path loss value for different types of parabolic equation at height 10 m a.g.l., range 20 km for both stations in february.....	207
Table 5.5	Path loss value for different types of parabolic equation at height 10 m a.g.l., range 20 km for both stations in august.....	207
Table 5.6	Path loss value for different types of parabolic equation at height 20 m a.g.l., range 20 km for both stations in february.....	209

Table 5.7	Path loss value for different types of parabolic equation at height 20 m a.g.l., range 20km for both stations in august.....	209
-----------	---	-----

CHAPTER ONE

INTRODUCTION AND BASIC BACKGROUND STUDY OF RADIOCLIMATOLOGICAL MODELING

1.0 INTRODUCTION

Predictions of tropospheric propagation effects are mostly made either for the average worst month or the average year. In clear-air environments, the radioclimatological frameworks for such predictions are more than thirty years old, while for precipitation effects they are more than twenty years old [1]. Radioclimatological data needed to improve on the existing frameworks are sparse for some regions of the world including Africa. Radiosonde data that should be used to test the prediction techniques based on radioclimatological models are even sparser.

Recently, efforts have been made by the international community to update the radioclimatological data base for tropospheric propagation predictions. These efforts have increased the number of meteorological stations included in their analysis, new potential prediction variables have been included and mapping and other presentation procedure has significantly improved (see, for example, Olsen [1]). The use of sensors of variable quality in different parts of the world and shortage of data for certain regions has, however, hampered this effort. Lack of radio propagation data has hindered the full testing of the new radioclimatological models.

Significant progress in clear-air radioclimatological modeling in recent years has been stimulated by discussions and organization at the international level. Initial discussions began within the International Radio Consultative Committee (i.e. CCIR, the predecessor of the current ITU Radiocommunication sector, ITU-R). The discussions began in the late 1980's through the recognition of inadequacies in the then adopted global radioclimatological models for predictions of multipath fading distributions on terrestrial line-of-sight links and duct propagation transhorizon interference between terrestrial and satellite links sharing the same frequency bands.

The first conference in the URSI CLIMPARA (Climatic Parameters in Prediction of Radiowave Propagation Prediction) series [2] dealt with precipitation effects. It created a good climate for discussions and interaction between the scientific community and the CCIR community responsible

for adopting international radio standards. It had the distinction of bringing together scientist from Africa, South America and Australia directly concerned with propagation effects in tropical as well as in the temperate conditions.

The recent significant progress began around 1994, initially with the establishment of an ITU-R group to develop new global radioclimatological models in clear-air conditions [3]. Major participants, besides Norway, include Canada and the United Kingdom (UK). A parallel research effort within the framework of COST 235 was simultaneously conducted in Europe, with Norway and the UK as the major participants [4]. Two other parallel efforts supported by the European Space Agency (ESA) were carried out under contract with laboratories in Finland [5], [6] and Italy [7], [8].

More recently, the radioclimatic work undertaken by COST 235 and ESA has been continued and expanded under the framework of COST 255, with Canada as a participant and twenty European nations [9]. The progress has been chronicled and enhanced by a succession of URSI CLIMPARA workshops and similar conferences [10] – [13], the latter two of which have been held immediately prior to joint meetings of ITU-R Working Parties 3J and 3M [14]. Three types of data have been employed in the analysis: radiosonde data, surface data and numerical meteorological forecasts based on a combination of both types of data and sophisticated dynamical meteorological models.

Since radiosonde data were the basis for existing global radioclimatological models employing several refractivity statistics, they were naturally the subject of new analyses. Surface data were also analyzed since many more sensor locations are available and since they are obtained several times per day in contrast to the normally twice per day at radiosonde stations. It was also felt that such data could be used to help calibrate known differences in the radiosonde caused by the use of different sensor types in different regions [15].

Numerical meteorological predictions quickly became the subject of interest because they are based on both radiosonde and surface data as well as terrain and satellite information. This was because the initial results obtained by this predictions appeared promising [5],[16]. In order to effectively carry out the work, Norway and the UK analyzed the radiosonde data, Canada analyzed the surface data and ESA independently analyzed the numerical meteorological data.

The above exposition shows how the radioclimatological modeling framework has been developed by the international community using different types of data in different regions of the world. This

demonstrates that in order to do a significant radioclimatological modeling, there must be substantial radio propagation data available. The main challenge with this is that most times, this radio propagation data is not readily available for researchers in this field of study. The reason for this serious limitation is that measurement procedures involved in radioclimatological studies are very expensive and might not be easily affordable for growing economies that obtain in the African continent. Even when these measurements are available, they might not be available in the format that suits the researcher's interest. The reason for this might not be unconnected with the sources of the data. For instance a major source of radiosonde data might be from the meteorological weather stations; data from such sources sometimes do not exist in a format very useful for communication purposes.

This then imposed on the present researcher the need to manipulate the data to best suit the objectives of the thesis and in so doing introduce errors into the result generated at the end of the work. The solution to this challenge is one of the main focuses of this thesis. Hence the thesis seeks an alternative way of modeling which is not totally based on measurement. This brings to the study the development of an analytical technique that can incorporate radio propagation data of the region in question to bridge this challenging gap. The parabolic equation technique has been found to satisfy this quest.

The radiosonde data used in the thesis for model formulation was gathered in Maun, Botswana and Durban, South Africa for the periods ranging from (1996 – 1998) and (1985 – 1994). In addition, there was signal level measurement data over one year (2003 – 2004) for model validation and verification. Our proposed model was developed based on both this data.

1.1 Thesis Objective and proposed way to achieve stated objective

The main objective of the thesis is to develop a model that addresses the solution of radioclimatological problems in a clear-air environment in Southern Africa. In order to achieve this stated objective, the researcher studied different clear-air radioclimatological models that have been developed in different regions of the world.

Having done an in-depth study of this, these various models are tested using the local radio propagation data available in Southern Africa. The test results show which of these models will likely fit the Southern Africa data. This would be the beginning of developing an appropriate model

for Southern Africa. If any of these models fits the local Southern Africa data to some extent, the said model will be modified to account for the Southern Africa uniqueness, if none of these models fit the Southern Africa data, then a completely new model would be developed for Southern Africa.

1.2 Thesis Overview

The report presented in this thesis is organized as follows: Chapter one introduces the theoretical frameworks for the thesis. The initial work, which forms the state of the art in this field, especially the earlier CLIMPARA papers are cited in the beginning of the chapter. Also the main objective of the thesis is clearly stated in this chapter and the description of way this objective is achieved. The chapter then progresses by describing the thesis overview which gives the detail of the content of the remaining chapters in the thesis. The original contribution and the main achievements of the thesis are also given in this chapter and finally the list of publication during the production of the thesis is listed towards the end of the chapter.

Chapter two gave a brief overview of both clear-air multipath and diffraction modeling as review by different authors across the globe. The chapter then progresses by discussing in some detail the characterization of the LOS link path where signal level measurement used by the researcher for multipath model formulation is taken. The chapter discusses also in some detail the type and duration of data used in the thesis for model formulation. The challenges encountered with the available data and how these challenges have been combated is also discussed in this chapter. Notable among these challenges is the format of the data in terms of the height ranges. This format has created a significant data gap. The gaps were bridge by introducing the Inverse Distance Weighting (IDW) of the spatial interpolation technique. The chapter explained in detail how this technique has been used to predict the data in the appropriate usable format for the research interest. The chapter concludes by discussing the determination of different radioclimatic parameters such as refractivity gradients, geoclimatic factor and k-factor for the research location. The Kernel estimation techniques used to model the k-factor for the region is also discussed in the chapter.

Chapter three has extensively reviewed the various methods employed by different authors in different parts of the world to solve clear-air radioclimatological problems in their region. The chapter begins with general study of radio propagation both in clear-air and non clear-air environment. The chapter then progresses with an extensive review of the clear-air multipath fading modeling carried out by different authors from different part of the world. Notable among these approaches, are the

approaches by Morita and Kakita in Japan[29], Vigants[24] and Crombie[34] in the USA, Olsen and Segal [95] in Canada and Tjelta *et al* in western Europe[100]. All these approaches involve measurements of signal level and fade event statistics over microwave line-of-sight links set up across paths with different characteristics. These links allow the authors in their different approaches to take clear-air measurements for a reasonable period of time. These measurements are then used to develop models that can be used to predict occurrence probabilities of a particular signal fade depth as a function of the path characteristics such as: path length, terrain roughness, frequency, path inclination and path grazing angles.

Furthermore, the chapter reviews clear-air diffraction fading techniques adopted by different authors in different parts of the world. Diffraction fading characterization which is instrumental in proper path clearance is an important clear-air effect for clear-air radioclimatological modeling study. In this review, it is determined that significant modeling work has not been done in this area in the past. Instead a given k-factor value is normally used for path clearance depending on the path distance as given by the then CCIR (now ITU-R). For instance, a path that is designed for $k = 0.67$ km, becomes effectively $k = 1.0$ at 200km. On a longer path of about 240 km, effective value of $k = 4/3$ is recommended by the author in [83].

Notable modeling work done in this regard is found to be done in Africa. Among these is the work by Baker and Palmer [38-39, 74] in South Africa where they have used refractivity measurement statistics to model the cumulative distribution of the k factor in South Africa. They have gathered measurement in eight different locations in South Africa initially to come up with their model and later extend these stations to thirty for their model verification. Another significant effort in this regard is the work of Afullo and Odedina [44] in Southern Africa. In their own case, they have developed a framework for modeling the probability distribution of the effective earth radius factor (k-factor) using refractivity measurement data gathered for three years in Botswana and South Africa. They proposed an analytical model which predicts the probability density function of the k-factor for Southern Africa using data gathered from the stated two countries (i.e. South Africa and Botswana). These two efforts from Southern Africa have been able to develop a model using refractivity data in this region to determine the appropriate value of the k-factor for their region. Their effort helps to come up with a better value of the k-factor for LOS link design rather than the oversimplified value of $k = 4/3$ that was normally used in this region.

The chapter then concludes by looking at semi-empirical/ analytical approaches employed to solve clear-air radioclimatological propagation problems. The first of the two approaches reviewed is the work of Martin [103-104] from Australia who proposed a new multipath model based on Rayleigh distributed reflections and refractions. His approach includes consideration of the reflected /refracted signal amplitude, delay and time variability. The approach is characterized by two signals arriving at the receiver by different paths, a normalized direct signal and a second reflected / refracted Rayleigh distributed signal.

Finally, the parabolic equation technique for solving clear-air radioclimatic problems is reviewed. The parabolic equation is an analytical approach that was originally developed by Fock and Leontovich (1946) from the former USSR [109]. Hadin and Tappert later (1973) developed a practical implementation of the parabolic equation to find solution for complicated refractive environments [108]. This method, called split-step Fourier method, was originally applied to model acoustic propagation, but the radar community has since used the split-step algorithm to model propagation in the troposphere. After the work of Fock and Leontovich (1946) different authors now adapt various modifications of the parabolic equation using different numerical and computational approaches as seen in [110–118]. While some authors focus on improving the parabolic equation approach by using a more sophisticated modern numerical and computational techniques [110–111] which were not available during the time of Fock and Leontovich (1946), others focus on different applications that the technique could offer [112, 116–118]. Other authors even focus on improving the boundary condition that may be implemented with the parabolic equation [113–115].

Chapter four presents an extensive analysis of the clear-air signal level measurement across a line of sight link between Howard College Campus and Westville Campus of the University of KwaZulu-Natal. This analysis is very important in order to be able propose an appropriate clear-air radioclimatic model for Southern Africa. The measurement period spans eight months from February to December 2004. Measurements are taken across the LOS link at a frequency of 19.5 GHz. The analysis has been done in three phases. The first phase was done daily; the second phase was done monthly, and the last phase was done for all measurement periods.

Seven fade depth levels were analyzed in each of the phases. These fade depth levels are: fade depths, $A(\text{dB}) \geq 2 \text{ dB}$; $A(\text{dB}) \geq 5 \text{ dB}$; $A(\text{dB}) \geq 10 \text{ dB}$; $A(\text{dB}) \geq 15 \text{ dB}$; $A(\text{dB}) \geq 20 \text{ dB}$; $A(\text{dB}) \geq 30 \text{ dB}$; $A(\text{dB}) \geq 40 \text{ dB}$. The percentage of time that each of these fade depth levels is exceeded from the total measurement time – known as exceedance probability was determined at each phase of the analysis.

The analysis described above becomes the bedrock for determination of the proposed analytical model for clear-air radioclimatic study in Southern Africa. Having determined the exceedance probability of these different fade depths as discussed above, an analytical expression is proposed to model these exceedance probabilities as a function of fade depth. The proposed analytical model is a fourth order polynomial. The model can be used to predict the percentage of time that a particular fade depth is exceeded for different months and for the whole year in Southern Africa.

The second analytical model proposed in this study is the modified parabolic equation. This is an analytical model which captures the effect of the terrain characteristic of the study area. The standard parabolic equation (SPE) was modified to include the geoclimatic factor. This initial modification is called first modified parabolic equation (MPE1). The final modification includes the effective earth radius factor (k-factor). This final modification is called second modified parabolic equation (MPE2). Two different topographical terrains were chosen to test each of these modifications. The result obtained after the test shows that there is more signal loss due to multipath in Botswana, where the terrain is flat compared to the second location. MPE1 which incorporate geoclimatic factor was able to capture this effect. On the other hand, in Durban where the terrain is hilly and mountaneous, more signal loss is experienced due to diffraction fading. The second modification (MPE2) was able to capture this effect.

In chapter five, we have done a comparative analysis of some of the multipath propagation models presented by various authors, reviewed in chapter three. Based on our analysis and finding, one can convincingly say that no single model can accurately predict the line of sight propagation path in Southern Africa. The result of the analysis and subsequent comparison with practical measurement shows that while some of the models predict accurately well for some months, others do not. From the eight month measurement campaign in KwaZulu-Natal over a line-of-sight microwave link, we determine the analytical models for fade exceedance probability. The outage probability of 0.037% compares well with 0.060% from Morita's model for sea and coastal areas. It also compares reasonably well with outage values of 0.027% and 0.024% obtained from the model of ITU-R Recommendations P.530-8 and P.530-12, respectively [125].

However, it is observed that Vigants' model of the United States for coastal and over-water regions do not present a reasonable prediction for the link outage in South Africa, even with surface

roughness incorporated. It should be noted that while the proposed model presents a good start, a longer measurement campaign in South Africa will ensure a refinement of the model. This will take into account ducting and sea-breeze effects, which might possibly help explain the fifteen days of total outage during these measurements.

Finally a cross comparison was done among the different types of modified parabolic equation in this chapter. The results corroborate the earlier findings in chapter four. These findings show that signal loss is experience due to multipath fading in Botswana, while in South Africa; signal loss is due to diffraction fading. This result is due to the different topographical structures of these two Southern African countries. While Durban is of hilly rugged and mountainous terrain structure, Botswana on the other hand is of a flatter and gentler terrain.

The conclusions of this work, as well as recommendation for future work, are given in chapter six.

1.3 Original Contribution

The original contribution of thesis is evident by the various publications in section 1.7. Some of the contributions are further highlighted as follows. The clear-air signal level measurement analysis done in chapter four is a significant original contribution necessary for clear-air radioclimatic modeling and formulation. The analysis in this chapter helps us determine and propose a fourth order polynomial model that can be used to predict fade occurrence probabilities as a function of fade depth in Southern Africa. Still in chapter four we have proposed the parabolic equation to model clear-air radioclimatic problems. The standard parabolic equation (SPE) has been modified by including two clear-air parameters that have been discussed throughout the thesis. These two parameters are the geoclimatic factor and the k-factor. The geoclimatic factor caters for multipath effect on transmitted signal while k-factor caters for diffraction fading effects. These effects are tested using two terrain structures in two different locations of Southern Africa (i.e. Botswana and Durban). Also in this chapter, a new formulation for determination of geoclimatic factor is developed. In chapter five, various proposed multipath models by different authors across the globe are compared using the results of chapter four. This is another significant contribution as this helps to determine the applicability of the various models in Southern Africa. Also in chapter two, the effective earth radius factor was modeled using the kernel estimation technique in order to propose the right k-factor for Southern Africa. In this same chapter, we have used the spatial interpolation technique to fill the data gaps that exist in the measurement data, during the modeling of primary radioclimatic variables. A simplified statistical

approach is then proposed to model the height variability of primary radioclimatic variables of temperature, pressure and humidity.

1.4 Publications

1. P.K. Odedina and T.J. Afullo, "Use of Spatial Interpolation Technique for the Determination of the Geoclimatic Factor and Fade Depth Calculation for Southern Africa," Proceedings of IEEE AFRICON conference 2007 ISBN: 0 – 7803 – 8606 – X. IEEE Catalog number: 04CH37590C, September 26 – 28, 2007, Namibia.
2. P.K. Odedina and T.J. Afullo, "Estimation of Secondary Radioclimatic Variables and Its Application to Terrestrial LOS Link Design in South Africa," Proceedings of the Southern Africa Telecommunication Networks and Applications Conference (SATNAC 2008), Wild Coast Sun, South Africa, 7 – 10, September, 2008.
3. P.K. Odedina and T.J. Afullo, "Effective Earth Radius Factor Measurement and Modeling for Radio Link Design in Botswana," South Africa Institute of Electrical Engineers Research Journal Vol. 99 No.3 pp.77 – 86, September 2008.
4. P.K. Odedina and T.J. Afullo, "A Simplified Statistical Modeling of Radioclimatological Parameters for LOS Links in South Africa," Proceedings of Progress in Electromagnetic Research Symposium (PIERS) pp. 1483 – 1486 Beijing, China, 23 – 27 March, 2009.
5. P.K. Odedina and T.J. Afullo, "Alternative formulation for determination of geoclimatic factor using local radiosonde data from Southern Africa," Proceedings of Sixth IEEE IASTED Conference on Antennas, Radar and Wave Propagation, Banff, AB, Canada July 2009, ISBN 978 – 0 – 88986 – 975 – 6.
6. P.K. Odedina and T.J. Afullo, "Multipath Propagation Modeling and Measurement in a Clear-Air Environment for LOS Link Design Application," Proceedings of Southern Africa Telecommunications and Networks Application Conference (SATNAC 2009), Ezulwini, Swazi Royal Spa, Swaziland, August 31 – September 2 2009.

7. P.K. Odedina and T.J. Afullo, “Clear-Air Signal Level Measurement Analysis for Microwave Line-Of-Sight Link in South Africa,” Presently under review for SAIEE African Research Journal 2010.
8. P.K. Odedina and T. J. Afullo “Clear-Air Analysis of Fade Exceedance Probability Statistic for Microwave Line-Of-Sight Link in South Africa,” Accepted for presentation at the Proceedings of the Seventh IASTED International Conference on Antennas, Radar and Wave Propagation, Massachusetts, USA Nov. 1 – 3 2010.
9. P.K. Odedina and T.J. Afullo, “Application of Parabolic Equation to Solve Clear-Air Problems for Microwave LOS Link” Presently under review for PIERS / JEMWA Research Journal.

1.5 Chapter Summary

The chapter has introduced the theoretical frameworks for the thesis. The initial work, which forms the state of the art in this field, especially the earlier CLIMPARA papers are cited in the beginning of the chapter. Also the main objective of the thesis is clearly stated in this chapter, as well as the description of way this objective has been achieved. The chapter then progresses by describing the thesis overview which gives details of the content of the remaining chapters in the thesis. The original contribution and the main achievements of the thesis are also given in this chapter and, finally, the list of publications during the production of the thesis is listed towards the end of the chapter.

CHAPTER TWO

LITERATURE REVIEW

2.0 INTRODUCTION

A brief overview of clear-air multipath and diffraction modeling by different authors is given in this chapter. The detail discussion on this topics by different authors across the globe is presented in chapter three. The investigation study area where signal level measurement is done by the author for multipath model formulation is discussed in some detail in the chapter. The characteristic of the line-of-sight path and terrain configuration of the path is discussed. All these are discussed in preparation for the signal level analysis done in chapter three and proposed clear-air model formulation developed in chapter four. Also discussed in the chapter is the work of the author on geoclimatic factor, k-factor and the different techniques used by the author to model the clear-air secondary parameters.

2.1 Overview of Clear-Air Multipath Modeling

In clear-air conditions, prediction methods based on global radioclimatic models of the ITU-R can currently be made for three significant clear-air propagation effects on terrestrial line of sight links: multipath fading, distortion and depolarization [17]. In addition, such predictions can also be made for multipath fading on very-low-angle satellite links [18], and interference between terrestrial and satellite communications system resulting from duct propagation beyond the horizon [19],[20]. All these predictions explicitly or implicitly use worldwide contour maps of refractive index gradient statistics for the lower 100 meters of the atmosphere. Techniques for predicting the deep-fading range of the multipath fading distribution for average worst month have been available for several years [21]. Most of these techniques were based on empirical fits of Rayleigh-type distributions (i.e. with slopes of 10 dB/decade) to fading data for individual countries. The best known techniques in this regard are those of Moritas [22] for Japan, Barnette [23] and Vigants [24] for USA, Pearson [25] and Doble [26] for the United Kingdom, Nadenenko [27] for the former Soviet Union and that of International Radio Consultative Committee (CCIR now ITU-R) [28] for the North-West Europe.

The single-frequency or narrow-band prediction equations [21] were based on the power-law form originally introduced by Morita and Kakita [29] in 1958. They showed the influence of path length on the number of hours containing deep fading or so-called Rayleigh fading. Morita and Kakita [29] fitted

the number of measured hours with deep fading in the worst “season” to path length for 4 GHz links in Japan, but they did not make it clear how to relate the measured time with fade depth. Seven years later, Pearson [25] presented a set of curves for predicting the fade depth exceeded for 0.1% of the worst month at 4 GHz in the UK, taking the path length and terrain profile roughness s as predictor variables. Like the model of Morita and Kakita [29], his model gave a linear relationship between the fade depth expressed in decibels and the logarithmic path length (i.e. the power-law form in probability), but it did not give a linear dependence on terrain roughness. Pearson [25] also assumed a distribution slope of 10 dB/decade for fading exceeding 10 dB. Morita [22] added a dependence on frequency f later by analyzing new data for different frequencies. He used a partial regression technique, fitting the path length, d , dependence first and the frequency, f , dependence afterwards. Also he introduced discrete geoclimatic variability by giving geoclimatic factors for three regions: plains, mountains and coast. More detailed information about the Morita [29] approach is discussed in section 2.3.1.

Shortly afterwards, Barnett [23] introduced a very similar prediction equation based on data for USA. The reason for the large differences between the geoclimatic factors for the two methods have not been fully resolved, but Wheeler [30] provided an explanation which is consistent with the importance of the grazing angle observed is analyzed in [21]. Further discussions about the Wheeler [30] approach is given in section 2.3.2. Vigants [24] extended the prediction equation of Barnett [23] to include the terrain roughness variable introduced by Pearson [25], while maintaining a discrete climatic variation. Vigants [24, 31-33] approach is discussed further in chapter three. Doble *et al* [26] developed a more refined technique, fitting the UK data (29 links compared with Pearson’s 10 links) with a trial-and-error optimization approach to obtain *geographically dependent equations based on path length, frequency and terrain roughness*. The roughness here was defined as the root mean square (rms) of the difference between the angles of path profile segments (formed by the line between two adjacent profile points) and the mean angle rather than the standard deviation of the profile heights. The fitting technique included a more systematic way of determining geographical variation, since links close to each other were arranged in zones and a zone-dependent correction was added to minimize the mean error within the zone. Crombie [34] employed the multiple regression technique in analyzing 15 sets of data for frequencies above 11 GHz. He obtained a region-independent equation, introducing two new predictor variables (the geometric mean θ of the transmitting and receiving antenna beamwidths and the path clearance h) in addition to d and f . More details about the Crombie approach is discussed in chapter three.

Link designers from various countries have been faced with the *difficulty of choosing among these techniques, sometimes giving vastly different results for the same apparent climatic region* [35]. To overcome this problem, in 1988 Study Group 5 of the CCIR (now ITU-R) adopted two “worldwide” techniques for predicting the deep fading range of the multipath fading distribution [17]. The first method did not require detailed path profile information and was specified as best suited for preliminary planning or licensing purposes. It needed only path length, frequency and path inclination as input variables. The second method did require the path profile in order to obtain an additional link variable (the “average” grazing angle of the wave specularly reflected from the ground), and was specified as more appropriate for link design [35]. Multipath fading database of 246 links (including 34 over water) in 23 countries of the world are used to test and revise the two methods. Hence the geoclimatic model used in both methods was revised based on this database. The method for predicting the shadow-fading distribution was then adopted by ITU-R study group 3.

2.2 Overview of Clear-Air Diffraction Fading Modeling

For proper planning of terrestrial and earth-space radio links, it is necessary to have appropriate procedures for assessing the refractivity effects on radio signals [36]. This is required for the determination of both the Geoclimatic factor (K) and the effective earth radius factor (k-factor). Variations in atmospheric refractive index cause changes in the effective earth radius factor (k-factor) from its “median” value of $4/3$ for standard temperate atmosphere [37]. When the earth is sufficiently sub-refractive (that is, when k assumes low values), rays will be bent in such a way that the earth appears to obstruct the direct path, giving rise to diffraction fading [17]. Values of k exceeded 99.9% of the time (called the effective value of k, k_e) are thus vital for the determination of path clearance criteria. In Southern Africa, Baker and Palmer [38–39] proposed a model for the cumulative probability distribution of the k-factor. While using available data for South Africa and Namibia, they concluded from regression analysis that there are climatic factors that need to be incorporated into the basic model. They concluded that the model would assist in predicting large values of the k-factor that may only be exceeded relatively rarely in the inland summer rainfall areas [39].

Afullo *et al.* [40-41] also reported on radio refractivity and k-factor studies for Botswana. Using measurements taken over three years (1996 – 1998), the median value of k was determined to be 1.1, while the effective value, k_e being 0.7. On the other hand when ducting data were included, they found the median k to be 1.03, while k_e was 0.61. In [36] a framework for modeling the probability density function pdf, of k, $f(k)$, was developed and the model determined, based on radiosonde data collected in Botswana for the period 1996-1998. It is observed that at height spans 0-500m and 0-200m above

ground level (a.g.l), the all-year median value of k , μ_k is 1.12 and the standard deviation is found to vary between 0.13 – 0.16 in all months, except in August when the deviation becomes lower at 0.067. The effective value of k , k_e , is found from the analytical expression in [36] to be 0.7 for height span 0-500m a.g.l., while it is 0.61 for the lower span 0-200m a.g.l.

The data base used in [36] for the modeling of the probability density function (pdf) of k was expanded in [42] by incorporating one year data for Durban, South Africa. The median value of k for Durban, South Africa was found to be 1.21 over the height range 0-500m a.g.l. while the value of k exceeded 99.9% of the time is 0.5. Hence the median k -factor value for Durban is much closer to the “standard” temperate climate value of $4/3$ than the Botswana k -factor ranges. The k value obtained via the curve-fitting model for Botswana and Durban, South Africa were compared in [42]. Also compared were the median k -factor values and the values of k exceeded 99.9% of the time. Two design examples showed that the type of terrain plays a major role in diffraction fading resulting from k -factor variation. While designing with $k = 4/3$ only result in losses of 2dB and 5dB for Durban and Botswana links, respectively, multiple obstructions would result in higher fades. Moreover, the gentler terrain in Botswana results in lower losses that would have been the case if the k -factor for Durban had been 1.1 [43]. Also it was observed that 99.9% link availability would be harder to attain in Durban than in Botswana, due to the higher k -factor variability and hillier terrain in Durban [44].

2.3 Clear-Air Line of Sight Path Characterization

This section is devoted to the characterization of the path for the line of sight link set up in Durban. The investigation was carried out using clear-air signal level measurement on a terrestrial line of sight link set up between the Howard College and Westville Campuses of the University of KwaZulu Natal, Durban, South Africa for a period of one year in 2004.

2.3.1 Investigation Study Area

The investigation study area where the line-of-sight link was set up is Durban in KwaZulu Natal province of South Africa. Durban is located on the coast shore of Indian ocean (see Figure 2.1), on the geographical coordinate (Latitude $29^{\circ} 97' S$ and Longitude $30^{\circ} 95' E$) the climatic region is coastal savanna [45].

The line-of-sight link was established between the Howard College and the Westville campuses of the University of KwaZulu-Natal, Durban. The transmitting station was setup on the roof of the Science

building at the Westville campus on the azimuth angle of 30.980° and about 178 m above sea level and the receiving station on the roof of the Electrical Engineering building at Howard College campus on the azimuth angle of 30.943° and about 145 m above sea level [46, 47], as seen from the area photo in Figure 2.2.

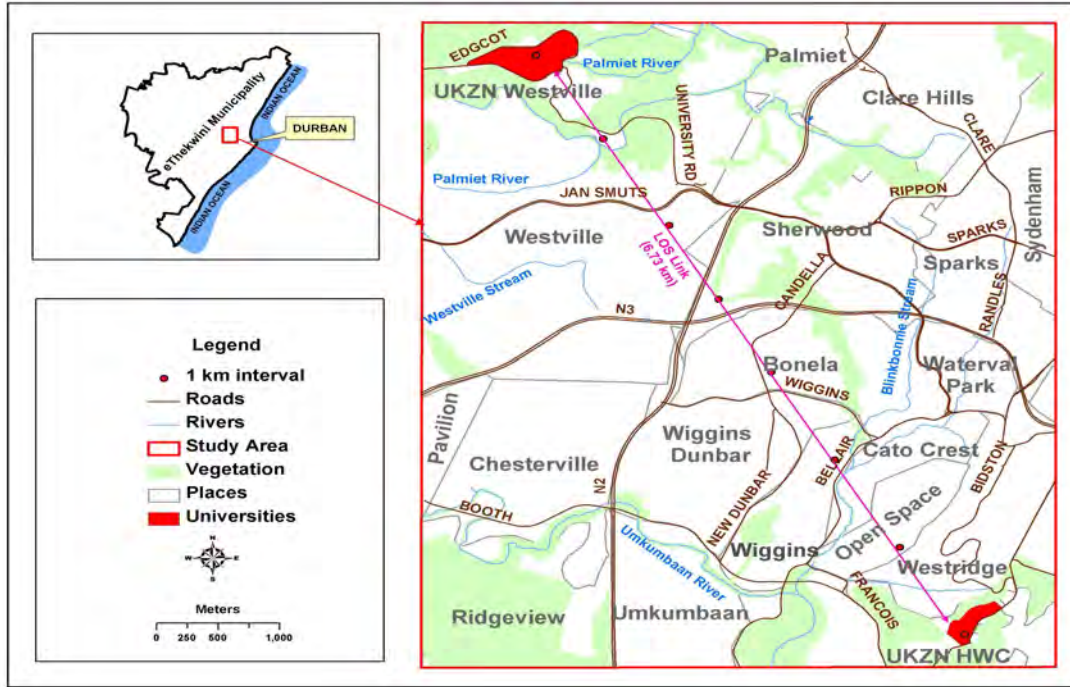


Figure 2.1 Location Map of the Study Area

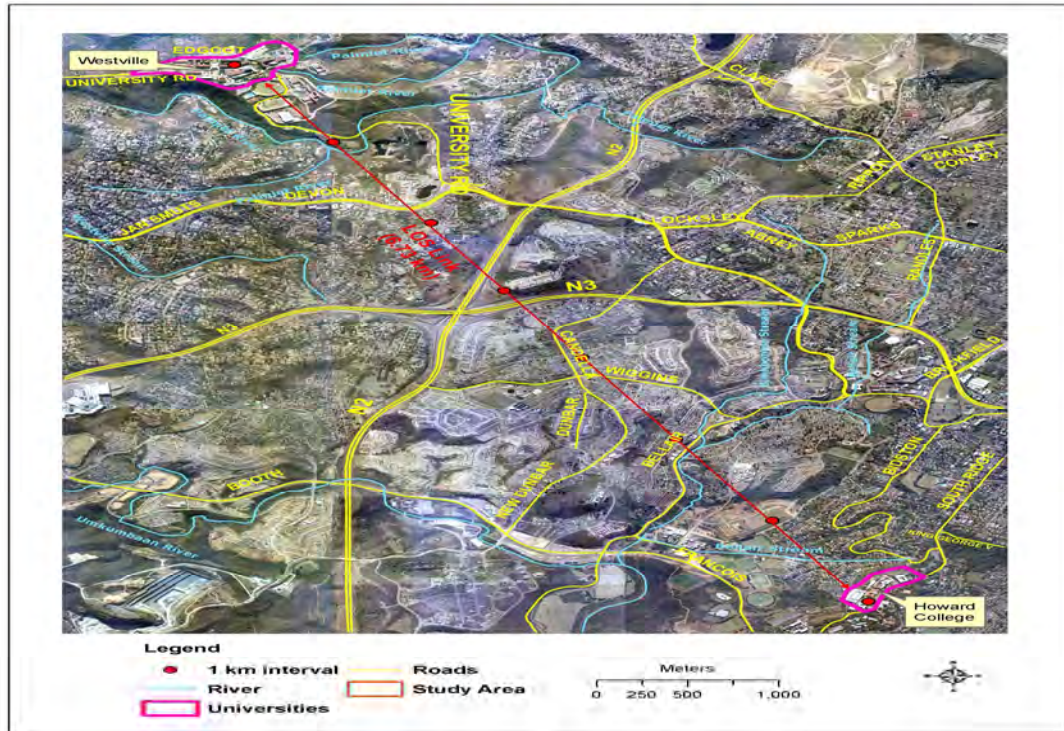


Figure 2.2 An areal photo of the study area

These heights were able to provide sufficient clearance for the link. The path clearance from the first Fresnel ellipsoid and the line-of-sight path are shown in Figure 2.3, with effective earth radius factor value of $4/3$. The link is horizontally polarized and centered at operating frequency of 19.5 GHz. The length of the link is 6.73 km and two Oregon Scientific WMR928N wireless professional weather stations were used along the path at both the receiver and the transmitter ends. The wireless equipments are used to measure 1-minute rainfall rate, out door temperature, relative outdoor humidity, outdoor dew point, temperature, outdoor pressure, wind speed and wind direction under the link [46, 47]. All these aforementioned radioclimatic parameters were measured for a period of one year in 2004.

A valuline WR43/R220 parabolic antenna of diameter 0.6 m with a 3 dB angle beam width of 1.9 degrees at 19.5 GHz is used at both the receiving and the transmitting stations [46, 47]. The antenna can operate within the 17.7 – 19.7 GHz and 21.2 – 23.6 GHz bands and provide a gain of 38.6 dBi.

The cabling consists of FSJI-50A superflexible coaxial cable which produces an attenuation of 2.2 dB per 100 m. At the transmitter, an agilent E8251A signal generator is used to provide the source signal and this can operate between 250 kHz – 20 GHz. This is used in conjunction with an agilent 83018A microwave system amplifier which can operate from 0.5 GHz to 25 GHz and provide a gain of up to 27 dB. This setup produces unmodulated continuous wave signals at the operating frequency of 19.5 GHz.

At the receiver, another agilent 83018A power amplifier is used to produce additional gain before feeding the signal into the Rhode & Schwarz FS1Q40 spectrum analyzer. More details on the link setup at the receiver and transmitter can be seen in [46, 47]. The terrestrial link parameters are shown in Table 2.1. The expected noise power in the receiver when no signal is transmitted lies between – 80.5 to – 80.2dBm [48].

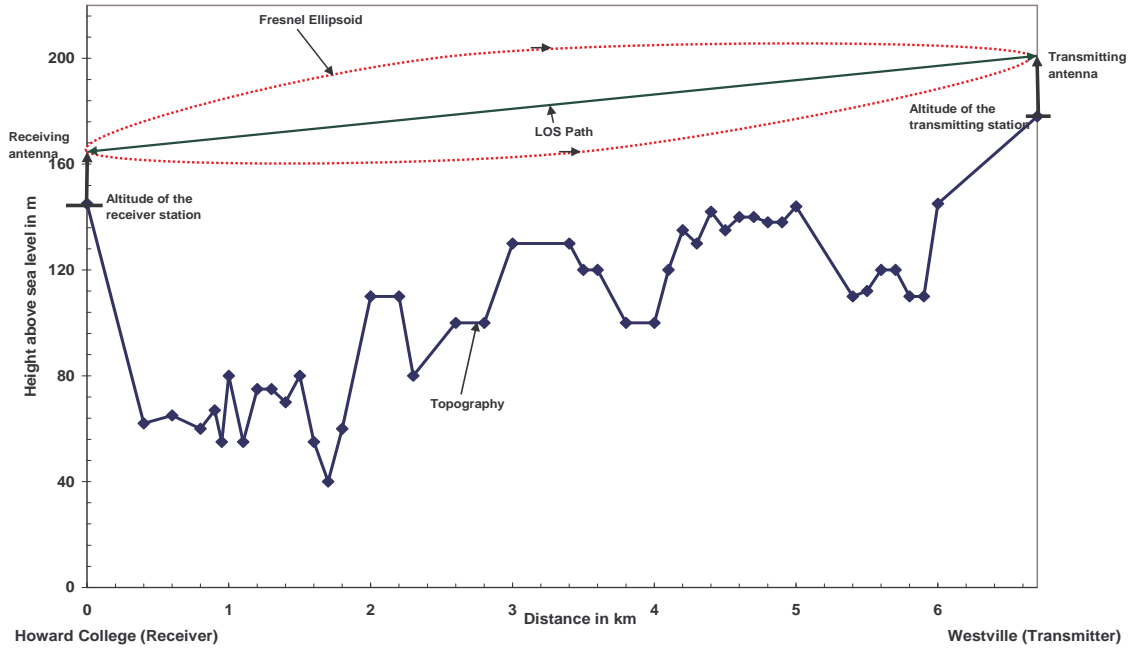


Figure 2.3 The Path Profile for 6.73 Km Terrestrial Line-Of-Sight Link from the Howard College Campus to the Westville Campus

Table 2.1 Terrestrial Link Parameters for the LOS SHF System [46]

Parameter	Description
Path Length	6.73 km
Height of transmitting antenna above the ground	24 m
Altitude of transmitter station	178 m
Height of receiving antenna above the ground	20 m
Altitude of receiver station	145 m
Carrier frequency	19.5 GHz
Bandwidth under investigation	200 MHz
Transmitting power	10 – 100 mW
Transmitting/receiver antenna gain	38.6 dBi
Transmitting/receiver beam width	1.9 degrees
Free space loss	135 dB
Total cabling and connection losses	≈ 2.2 dB
Clear-air attenuation	≈ 1dB
Receiver bandwidth	100 kHz – 1GHz

This defines the noise floor which is determined from the noise temperature of the antenna T_A of 206°K (with an estimated efficiency of 63.4%, equivalent background temperature of 150°K [49], and a maximum physical temperature of 303°K). The transmission line noise temperature is 93.4°K (with an attenuation of 2.2 dB per 100m); 83018A agilent amplifier (with a gain of 27 dB, and noise figure of about 9.5 dB at 19.5 GHz (see [50]) with noise temperature of 2398.5°K; thus resulting in total

receiver noise temperature of 3470.4°K, or a noise power of -80.2 dBm [51]. At the lower temperature of 287°K, the noise power is – 80.5 dBm to – 82 dBm. In the measurements, this value varied from – 79.5 dBm to – 82 dBm. The power received from the receiver end can be calculated as follows [48]:

$$P_r = P_t - \text{FSL} + G_{r \text{ ant}} + G_{t \text{ ant}} - \text{Losses} \quad (2.1)$$

Where:

P_t is Power transmitted (taken as 100mW = 20 dBm); FSL is Free space loss;

$G_{r \text{ ant}}$ is Receive antenna gain; $G_{t \text{ ant}}$ is Transmit antenna gain.

Thus the power received P_r expected at the receiver end of the link when transmitting power of 100 mW is employed between Howard College and Westville campuses should be – 41 dBm in a clear-air propagation condition.

2.3.2 Clear-Air Digital Terrain Characterization

In order to appropriately test the proposed model by various authors, there is a need to get the digital terrain model and contour mapping of our line-of-sight link study area. This is very necessary as the information from such map will enable us to determine the surface roughness of our LOS link path (this is a vital parameter in almost all the models to be tested). We have therefore used the Argis software tool to develop the digital elevation model (DEM) map and the contour map of our study area. These maps are shown in Figure 2.4 and Figure 2.5 respectively. The DEM of the study area shown in Figure 2.4 can broadly be defined as a digital representation of the continuous variation of elevation over space [52]. Elevation can be any continuous variable that depends on geographic coordinates [53]. It is also customary to use the term 'DEM' for what can be called 'gridded DEM' so that the more general term should then be 'Digital Terrain Model' (DTM).

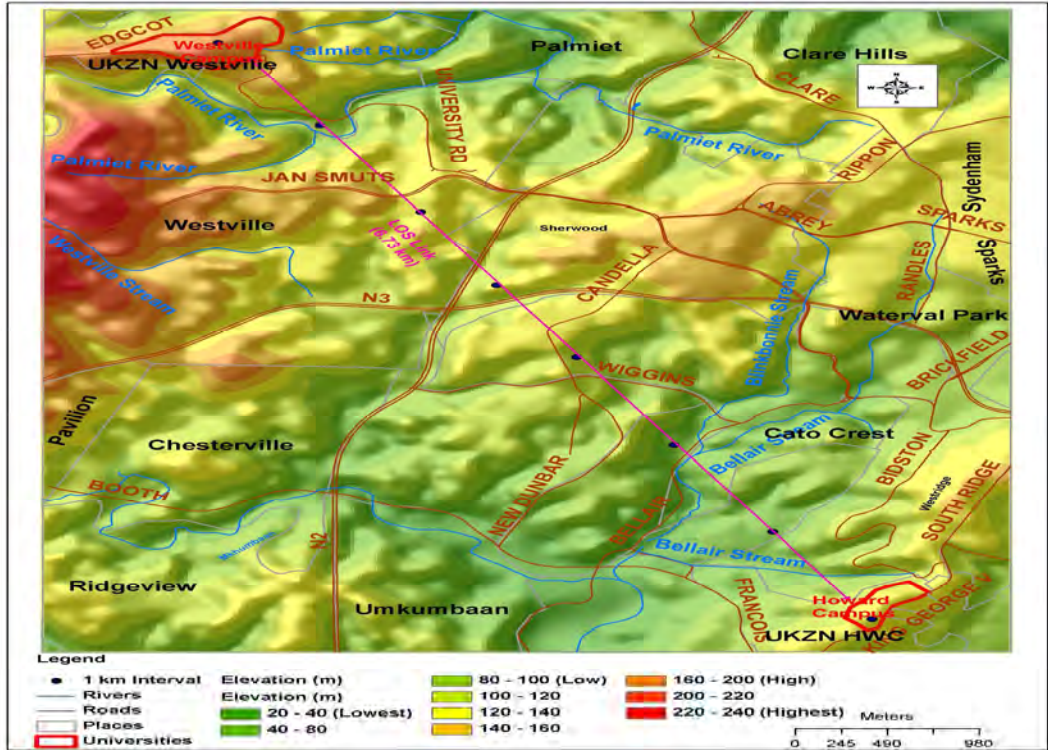


Figure 2.3 A digital elevation model (DEM) of the study area

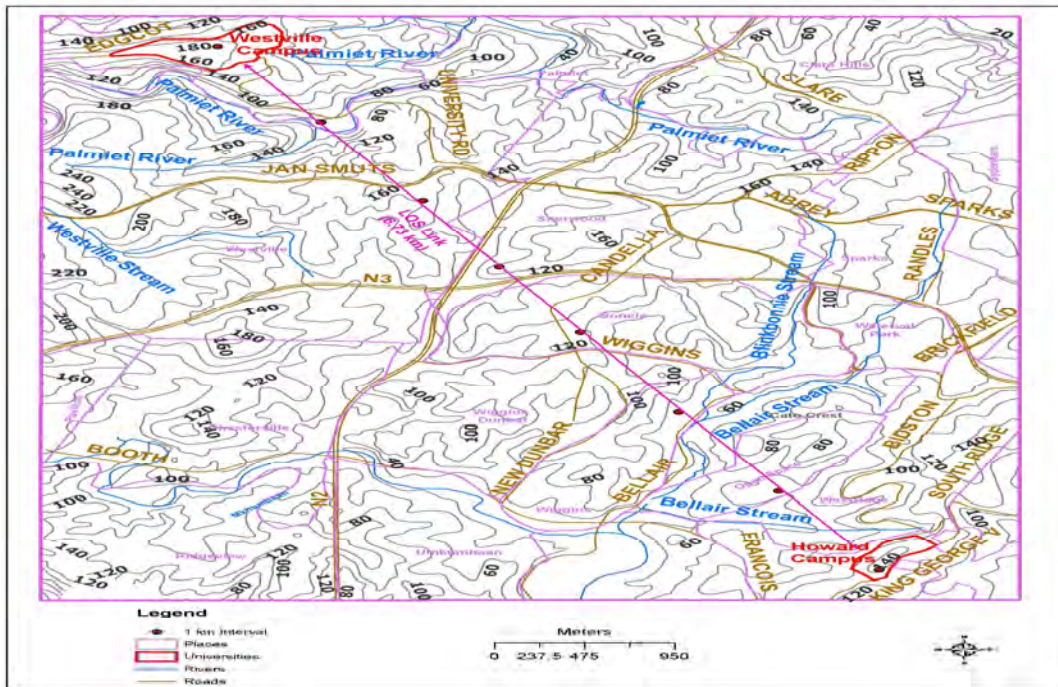


Figure 2.4 Contour Map of the Study Area

The digital elevation model is an extremely useful product of a geographic information system (GIS) for land evaluation and production of maps [53]. It can be seen that more detail information on the

topographical feature of our study area is revealed by the DEM map (see Figure 2.4). Our link is surrounded by different geographical features such as roads, rivers, vegetation and different undulating terrains as can be observed from Figure 2.4. All these contribute in various ways to the signal degradation as we observed from our clear-air signal level measurement over the 6.73 km, 19.5 GHz link [54]. Though one can get a rough estimate of terrain height distribution of our study area from the DEM, it is still difficult to get the exact height of each point on the DEM. This is why we have produced a contour map of our study area using the same software as shown in Figure 2.5. The contour map has the advantage of showing the exact height for each point in the study area.

We have divided our path length of 6.73 km into intervals of 1 km from the transmitter to the receiver as can be seen on the two plots. This is done so that the terrain surface roughness of the propagation path can be easily estimated, as most of the models will require the terrain roughness factor.

2.4 Refractivity, Refractivity Gradient and Geoclimatic Factor Determination

A significant parameter required for estimation of clear-air multipath propagation modeling is the geoclimatic factor. The geoclimatic factor cannot be determined on its own but relies on other propagation parameters such as refractivity and refractivity gradient [37]. The refractivity and refractivity gradient in turn will be determined from the clear-air primary radioclimatic variables such as temperature, pressure and humidity at a height range of less than 100 m a.g.l. according to ITU-R recommendations [37]. One of the greatest challenges of this study is to acquire these aforementioned primary parameters in the required height range. The process of acquiring this measurement is quite expensive and therefore, we resort to using secondary sources of data in most cases. Moreover, since these secondary sources (e.g. weather services department) are not gathering their measurement for communication purposes, a good portion of the data obtained from such sources might not be in the required height range for communication. To work around this problem, we apply some mathematical or statistical concepts on these data, in order to predict the data in the required range heights. One of the techniques applied to do this is the spatial interpolation technique which will be explained in more detail in the next subsection.

2.4.1 Spatial Interpolation Technique

Spatial interpolation technique is used in data analysis whereby data is sampled to provide a subset of information about all data. Spatial interpolation techniques therefore help to fill in the gaps between

data points where such gaps exist or to predict the intermediate data where the exact data point cannot be estimated from an existing data set [55].

There are different types of spatial interpolation techniques; these include the Inverse Distance Weight (IDW); Splining; Nearest Neighbor; and Kriging [55]. The approach employed in this thesis is known as Inverse Distance Weight (IDW). This approach is chosen because of its simplicity in application [56]. IDW interpolation explicitly implements the assumption that things that are close to one another are more alike than those that are farther apart. To predict a value for any unmeasured location, IDW will use the measured values surrounding the prediction location. Those measured values closest to the prediction location will have more influence on the predicted value than those farther away [55]. Thus IDW assumes that each measured point has a local influence that diminishes with distance. It weights the points closer to the prediction location greater than those farther away, hence the name inverse distance weighted. The formula used to calculate IDW is [55]:

$$Z = \frac{\sum_i^n \frac{x_i}{d_i}}{\sum_i^n d_i^{-1}} \quad (2.2)$$

Where

Z is the value we are trying to predict for position x, d_i is distance between the prediction position and i^{th} measured surrounding location, n is the number of measured sample points surrounding the prediction location that will be used in the prediction and x_i is the i^{th} measured value surrounding the prediction position that will be used in the prediction

2.4.2 Application of Spatial Interpolation Technique to Clear-air Study

We have implemented the spatial interpolation technique discussed in the previous section in clear-air study by using the three primary radioclimatic variable data available for Durban, South Africa. These data are the temperature, pressure and humidity. These basic variables are necessary to calculate the refractivity, refractivity gradient, k-factor and eventually geoclimatic factor. We have used radiosonde data for Durban, spanning a period of ten months. The challenge though is that, some data gaps exist in between this data set as the height increases from 0 – 500 m a.g.l.[57]. Also, we have similar data set for Durban spanning ten to twenty years, but this set of data exist in the height range of 1000 – 26000 m a.g.l. This height is far out of range for line of sight (LOS) link application. The challenge therefore rises again to derive an analytical expression to predict the existing

information in the usable height range of 0 – 100 m a.g.l which is normally used for LOS application. As stated earlier, the starting point of solving this problem is to use the spatial interpolation technique to estimate the missing data points in the data gaps for the ten months data. The data exist as shown in Tables 2.2 (a) and (b) before and after the implementation of spatial interpolation technique [57]. It should be noted from Tables 2.2 (a) and (b) that **bold** values are the data set that was available from measurement while the unbolded values are those obtained using the spatial interpolation technique.

It is observed in Tables 2.2 (a) and (b) that the missing data points are now filled with information at the corresponding heights after the implementation of spatial interpolation technique. The information shown in Tables 2.2 (a) and (b) is for the month of April 2004. Similar procedure was implemented for the remaining months as can be observed in the next section.

Table 2.2 (a) Data Set for Month of April 2004 before and after applying Spatial Interpolation Techniques

Height(m)	Pressure (hpa)	Temperature (Deg C)	Humidity (%)
14	1024.5	23.9	67.92115022
15	1024.3	23.868	67.5998
16	1024.2	23.8361	67.2784
17	1024	23.8042	66.9571
18	1023.8	23.7722	66.6357
.	.	.	.
.	.	.	.
.	.	.	.
84	1016.3	22.9129	65.8182
85	1016.2	22.9117	65.7973
86	1016.1	22.9106	65.7765
87	1015.9	22.9094	65.7557
.	.	.	.
.	.	.	.
.	.	.	.

Table 2.2 (b) Data Set for Month of April 2004 before and after applying Spatial Interpolation Techniques

Height(m)	Pressure (hpa)	Temperature (Deg C)	Humidity (%)
97	1014.8	22.8577	65.5684
98	1014.7	22.8365	65.5476
99	1014.5	22.8153	65.5268
100	1014.4	22.7942	65.506
.	.	.	.
.	.	.	.
.	.	.	.
309	990.2	20.8	59.9422

2.4.3 Application of Simplified Statistical Technique to Clear-Air Study

After the implementation of spatial interpolation technique, it was discovered that we need to improve on the expression equation that was formulated through this method. In order to do this, we implement the simplified statistical technique to make comparison with the proposed expression and the measured information so that the proposed model is improved further.

The data used in this section of the report has two parts, both of which are radiosonde measurements spanning different periods in Durban, KwaZulu-Natal Province of South Africa. The first part of the data is a one year radiosonde data measured over a height range of 0-500 m a.g.l., in 2004 [57]. From these set of data, parameters within the first 0-100 m height a.g.l were extracted. The second set of data is a radiosonde measurement for six years from (1990-1995) over a height range of 0-26000 m a.g.l. These sets of data come very handy in the statistical analysis for the model formulation [57].

The one year data was initially used to start the model formulation process; however more data is needed in the 0-100 m a.g.l. region since this is where signal loss is experienced most in terrestrial line of sight link design [37]. To fill in this data gap, the spatial interpolation techniques discussed in [58] was implemented for each of the twelve months in 2004 for 0-500 m a.g.l. Having done this, each of the parameters was plotted against height for the twelve months in order to obtain a model equation.

The process explained above gives an initial model equation for each of temperature, pressure and humidity for the twelve calendar months. The second process embarked on is to modify and improve on these initial model equations. To do this, a simplified statistical approach was used [57]. The initial

set of modeled equations was used to predict the missing parameters for the height range 0-26000 m a.g.l. Then the predicted parameters were matched against the measured parameters in order to observe how well the initially modeled equations predict the data points that exist from measurement [57]. It was observed from this exercise that the initially modeled equations were able to predict parameters fairly well with little disparity for the lower height ranges 0-200 m a.g.l.. The data points in the higher height ranges specifically above 1000 m a.g.l. were not properly estimated by the model. At this point it was concluded that another method will be required to predict the higher height range parameters.

Finally, the data set within the height range 0 – 200m a.g.l. for the six years were sorted and collated for both the measured and predicted parameters. The deviations between the measured and the predicted values for this data and the average of these deviations called mean temperature deviation (MTD), mean pressure deviation (MPD) and, mean humidity deviation (MHD), were determined [57]. Next, the standard deviation for these parameters namely: standard deviation of temperature deviation (SDTD), standard deviation of pressure deviation (SDPD) and standard deviation of humidity deviation (SDHD), were also computed. These standard deviations then become the compensation factors which were used to modify the initial set of modeled equations for the twelve months.

The mean deviations give an indication whether the initially modeled equation overestimated or underestimated the true measured values. If the mean deviation for a particular parameter in a certain month is negative for instance, it means that modeled equation overestimated the true value for that month by a value given as the standard deviation for that month. Hence this standard deviation value is subtracted from the constant value in the initial equation to get the finally modeled equation for that month and vice versa. The results obtained from this activity are presented in Tables 2.3 and 2.4. The equations used to arrive at the above solutions are stated below:

$$MTD = \frac{\sum(T_m - T_p)}{N} \quad (2.3)$$

$$MPD = \frac{\sum(P_m - P_p)}{N} \quad (2.4)$$

$$\text{MHD} = \frac{\sum(H_m - H_p)}{N} \quad (2.5)$$

Where T_m is the Measured temperature value ($^{\circ}\text{C}$), T_p is the Predicted temperature value ($^{\circ}\text{C}$), P_m is the Measured pressure value (hpa), P_p is Predicted pressure value (hpa), H_m is Measured humidity value (%), H_p is Predicted humidity value (%), N is Total Number of variables used in the analysis. Also for the compensation factor calculation, the following formulations are applicable:

$$\text{SDTD} = \sqrt{\frac{\sum(T_D - \text{MTD})^2}{(N-1)}} \quad (2.6)$$

$$\text{SDPD} = \sqrt{\frac{\sum(P_D - \text{MPD})^2}{(N-1)}} \quad (2.7)$$

$$\text{SDHD} = \sqrt{\frac{\sum(H_D - \text{MHD})^2}{(N-1)}} \quad (2.8)$$

$$T_D = T_m - T_p, \quad P_D = P_m - P_p, \quad H_D = H_m - H_p, \quad (2.9)$$

Where T_D is Temperature Deviation, P_D is Pressure Deviation and H_D is Humidity Deviation. It should be noted from Tables 2.3 and 2.4 that H means humidity while h is the height variable.

Having modeled the basic primary radioclimatic variables needed to determine the refractivity and refractivity gradients, the geoclimatic factor can now be determined. The radio refractivity, refractivity gradients and geoclimatic factor formulation as given by the ITU-R recommendation applies. The formulations quoted in ITU-R recommendation [37] are implemented in this section using local radio propagation data from Botswana and Durban, South Africa.

The refractivity data obtained from radiosonde measurement in both Durban and Botswana were used to calculate the refractivity gradient for the first 100 m a.g.l. of the atmosphere. From these data, the variable of interest dN_1 was determined. The procedure used to determine dN_1 was firstly to determine the frequency of occurrence of refractivity gradient in the first 100 m of the atmosphere for the gradients obtained. Then cumulative distributions of these gradients were determined as shown in

Figure 2.6. The value of dN_1 was estimated from the gradient distribution in Figure 2.6 for each month as displayed in Figure 2.7, for existing data points. However, where the needed data points cannot be estimated exactly from Figure 2.6, the IDW technique described in section 2.4.1 was applied.

Table 2.3 Compensation Factor for Temperature and Pressure Jan-Dec (1985-1990)[57]

Month	Temperature (DegC)				Pressure (hpa)			
	MTD		Initial Model	T =	MPD		Initial Model	P =
Jan	MTD	-0.37	Initial Model	T = -0.019h + 26.08	MPD	-5.88	Initial Model	P = -0.113h + 1019
	SDTD	2.68	Final Model	T = -0.019h + 23.4	SDPD	3.95	Final Model	P = -0.113h + 1015.05
Feb	MTD	-0.32	Initial Model	T = -0.014h + 25.89	MPD	-0.47	Initial Model	P = -0.112h + 1014
	SDTD	2.64	Final Model	T = -0.014h + 23.25	SDPD	4.07	Final Model	P = -0.112h + 1009.93
Mar	MTD	-1.99	Initial Model	T = -0.022h + 27.79	MPD	2.46	Initial Model	P = -0.112h + 1012
	SDTD	2.65	Final Model	T = -0.022h + 25.14	SDPD	4.22	Final Model	P = -0.112h + 1016.22
Apr	MTD	-0.52	Initial Model	T = -0.009h + 23.78	MPD	-9.55	Initial Model	P = -0.115h + 1026
	SDTD	2.95	Final Model	T = -0.009h + 20.83	SDPD	5.36	Final Model	P = -0.115h + 1020.64
May	MTD	-5.41	Initial Model	T = -0.032h + 28.88	MPD	5.68	Initial Model	P = -0.11h + 1013
	SDTD	4.16	Final Model	T = -0.032h + 24.72	SDPD	5.38	Final Model	P = -0.11h + 1018.38
Jun	MTD	-0.52	Initial Model	T = -0.040h + 22.69	MPD	-7.65	Initial Model	P = -0.120h + 1029
	SDTD	5.02	Final Model	T = -0.040h + 17.67	SDPD	6.50	Final Model	P = -0.120h + 1022.5
July	MTD	-2.17	Initial Model	T = -0.008h + 21.02	MPD	2.24	Initial Model	P = -0.111h + 1019
	SDTD	3.60	Final Model	T = -0.008h + 17.42	SDPD	5.74	Final Model	P = -0.111h + 1024.74
Aug	MTD	-0.58	Initial Model	T = -0.029h + 22.39	MPD	-4.36	Initial Model	P = -0.116h + 1025
	SDTD	3.99	Final Model	T = -0.029h + 18.4	SDPD	6.54	Final Model	P = -0.116h + 1018.46
Sep	MTD	-0.54	Initial Model	T = -0.029h + 22.39	MPD	-6.05	Initial Model	P = -0.116h + 1025
	SDTD	3.39	Final Model	T = -0.029h + 19	SDPD	6.68	Final Model	P = -0.116h + 1018.32
Oct	MTD	-3.55	Initial Model	T = -0.029h + 25.99	MPD	7.75	Initial Model	P = -0.112h + 1010
	SDTD	3.04	Final Model	T = -0.029h + 22.95	SDPD	6.05	Final Model	P = -0.112h + 1016.05
Nov	MTD	-2.23	Initial Model	T = -0.029h + 25.99	MPD	6.33	Initial Model	P = -0.112h + 1010
	SDTD	2.99	Final Model	T = -0.029h + 23	SDPD	5.59	Final Model	P = -0.112h + 1015.59
Dec	MTD	-1.57	Initial Model	T = -0.027h + 26.57	MPD	-7.19	Initial Model	P = -0.113h + 1021
	SDTD	2.56	Final Model	T = -0.027h + 24.01	SDPD	4.99	Final Model	P = -0.113h + 1016.01

Table 2.4 Compensation Factor for Humidity Jan-Dec (1985-1990)[57]

Month	Humidity (%)			
Jan	MHD	11.50	Initial Model	$H = -0.019h + 66.17$
	SDHD	10.99	Final Model	$H = -0.019h + 77.16$
Feb	MHD	-3.80	Initial Model	$H = -0.017h + 81.14$
	SDHD	11.77	Final Model	$H = -0.017h + 69.37$
Mar	MHD	5.35	Initial Model	$H = -0.031h + 72.36$
	SDHD	12.38	Final Model	$H = -0.031h + 84.74$
Apr	MHD	6.97	Initial Model	$H = -0.021h + 67.34$
	SDHD	13.12	Final Model	$H = -0.021h + 80.46$
May	MHD	26.77	Initial Model	$H = -0.040h + 44.49$
	SDHD	16.52	Final Model	$H = -0.040h + 61.01$
Jun	MHD	-4.11	Initial Model	$H = -0.033h + 68.44$
	SDHD	17.58	Final Model	$H = -0.033h + 50.86$
July	MHD	9.99	Initial Model	$H = -0.002h + 52.19$
	SDHD	16.83	Final Model	$H = -0.002h + 69.02$
Aug	MHD	24.08	Initial Model	$H = 0.009h + 43.10$
	SDHD	16.55	Final Model	$H = 0.009h + 59.65$
Sep	MHD	28.31	Initial Model	$H = 0.009h + 43.10$
	SDHD	14.09	Final Model	$H = 0.009h + 57.19$
Oct	MHD	-5.58	Initial Model	$H = -0.020h + 81.76$
	SDHD	12.72	Final Model	$H = -0.020h + 69.04$
Nov	MHD	-5.52	Initial Model	$H = -0.020h + 81.76$
	SDHD	11.47	Final Model	$H = -0.020h + 70.29$
Dec	MHD	7.29	Initial Model	$H = -0.033h + 71.37$
	SDHD	11.20	Final Model	$H = -0.033h + 82.57$

The corresponding geoclimatic factor (K) was then calculated and the results plotted in Figure 2.8. It can be observed (see Figure 2.7 and Figure 2.8) that a distinct relationship exists between the point refractivity gradient dN_1 and the geoclimatic factor (K): as the value of dN_1 becomes more negative, the geoclimatic factor increases.

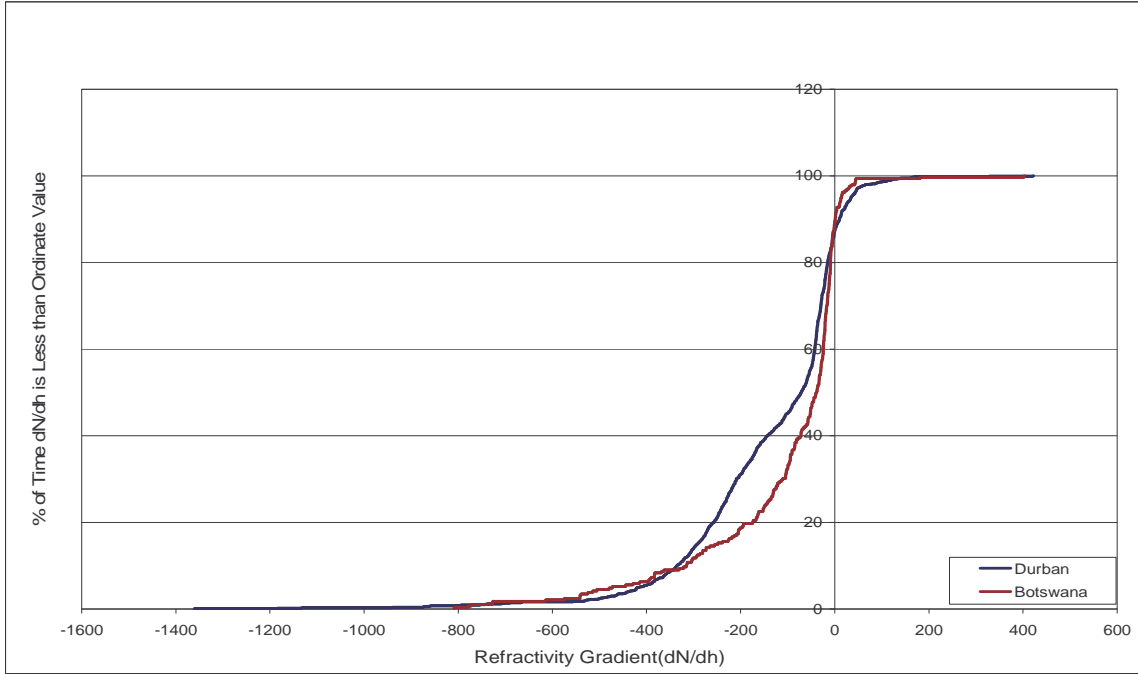


Figure 2.5 Cumulative Distribution of dN/dh for Durban and Botswana [58]

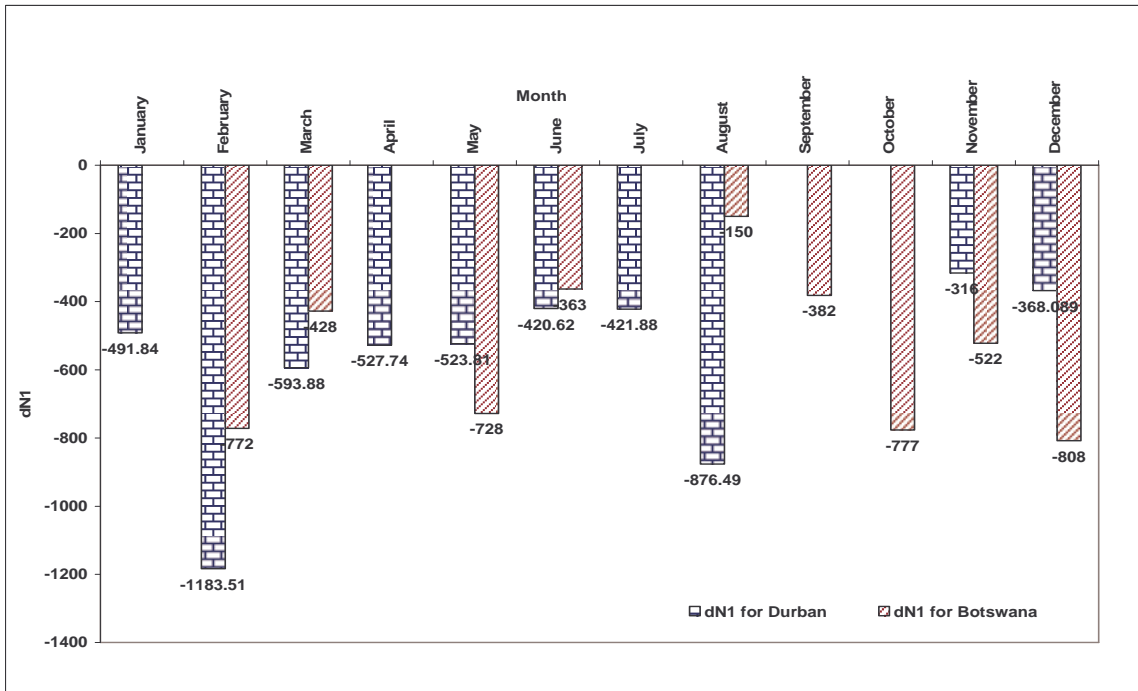


Figure 2.6 Point Refractivity Gradient for Durban and Botswana [58]

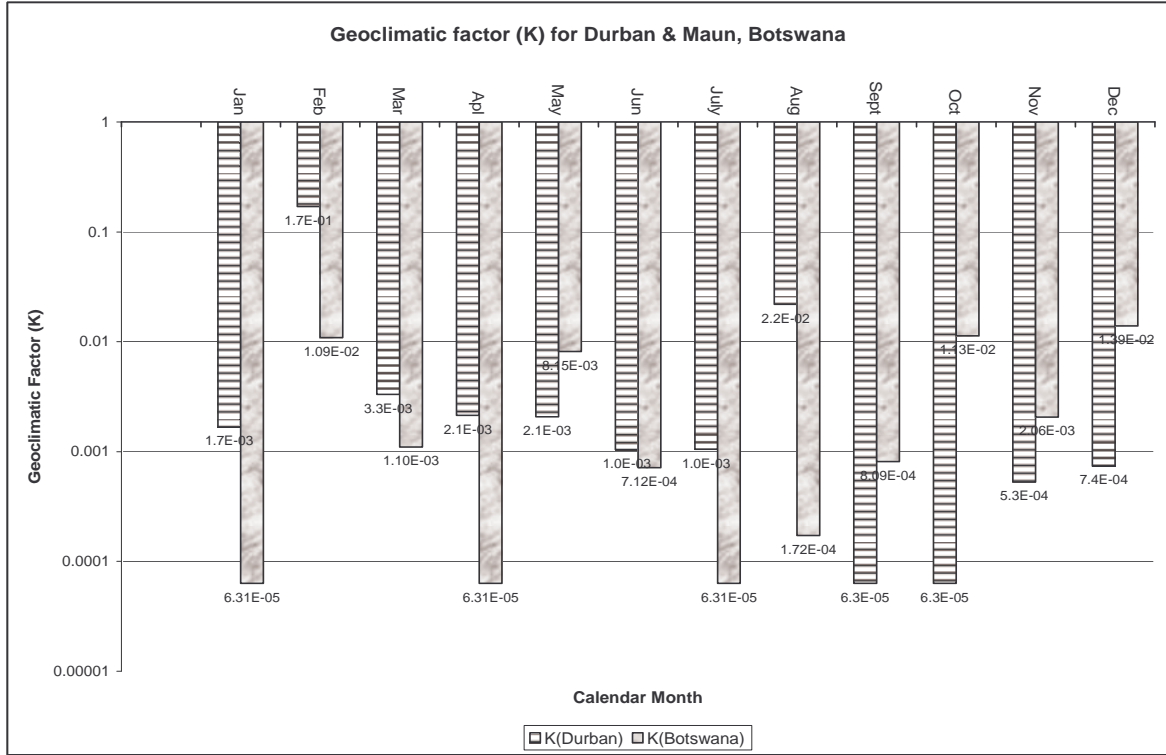


Figure 2.7 Geoclimatic Factor for Different Months for Durban and Botswana [58]

2.5 Kernel Estimation Technique

Another important clear-air parameter used to determine diffraction fading is the effective earth radius factor (k-factor) as mentioned earlier. The k-factor have been modeled the in [36] using the curve-fitting technique. Another interesting fitting technique that is better than the curve-fitting technique known as the kernel estimation technique is presented in this section. This discussion on the kernel estimator is based on Silverman [59]. One common approach to estimation of the pdf of a variable, apart from histograms, involves the use of a kernel function, $K(k)$, satisfying the condition [60]:

$$\int_{-\infty}^{\infty} K(k) dk = 1 \quad (2.10)$$

Then the kernel estimator for the pdf $f(k)$, with kernel K , is defined as:

$$f^*(k) = \frac{1}{nh} \sum_{i=1}^n K\left(\frac{k - X_i}{h}\right) \quad (2.11)$$

where h is the smoothing parameter, and n is the sample size, X_i is the i th sample or observation of the k factor. The kernel estimator is defined as a sum of “bumps” placed at observations: the kernel function $K(k)$ defines the shape of the bumps, while the smoothing parameter h determines the width of the bump. Note that if h is chosen too small, then spurious fine structures in the distribution become visible, while if h is chosen too large, then the actual nature of the distribution becomes obscured.

Provided the kernel $K(k)$ is everywhere non-negative and satisfies the condition in (2.10), (that is, it is a probability density function), it follows that $f^*(k)$ will itself be a probability density function. Furthermore, $f^*(k)$ will inherit all the continuity and differentiability properties of $K(k)$.

The most widely used measure of the global accuracy of $f^*(k)$ as an estimate of $f(k)$ is the integrated square error, ISE, defined as :

$$\text{ISE} = \int_{-\infty}^{\infty} [f^*(k) - f(k)]^2 dk \quad (2.12)$$

In order to make the ISE as small as possible, Silverman [59] determines that the most appropriate kernel $K(k)$ is the so-called Epanechnikov kernel, given by:

$$K(k) = \begin{cases} \frac{3}{4\sqrt{5}} \left(1 - \frac{1}{5}k^2\right), & -\sqrt{5} \leq k \leq \sqrt{5} \\ 0, & \text{elsewhere} \end{cases} \quad (2.13)$$

Thus the efficiency of any symmetric kernel $K(k)$ is determined by comparing it to the Epanechnikov kernel. Some of the kernels and their efficiencies are given in Table 2.5 [59]. It is observed that the efficiencies of the kernels are quite close to 1. There is thus very little to choose between the kernels on the basis of the ISE. Therefore it is legitimate that the choice of kernels be based on other considerations. For a Gaussian kernel, Silverman has determined that the optimum smoothing parameter, h_m , is given by:

$$h_m = \left(\frac{4}{3n} \right)^{1/5} \sigma \quad (2.14)$$

A quick way of choosing the optimum smoothing parameter in this case would be to estimate the standard deviation, σ , from the sample data and then substitute the same into (2.14).

Table 2.5 Typical kernels and their efficiencies (η) [59]

KERNEL	K(k)	$\eta(\%)$
Epanechnikov	$K(k) = \begin{cases} \frac{3}{4\sqrt{5}} \left(1 - \frac{1}{5}k^2\right)^2, & -\sqrt{5} \leq k \leq \sqrt{5} \\ 0, & \text{elsewhere} \end{cases}$	100%
Biweight	$K(k) = \begin{cases} \frac{15}{16} (1 - k^2)^2, & -1 \leq k \leq 1 \\ 0, & \text{elsewhere} \end{cases}$	99.4%
Triangular	$K(k) = \begin{cases} \frac{15}{16} (1 - k), & -1 \leq k \leq 1 \\ 0, & \text{elsewhere} \end{cases}$	98.6%
Gaussian	$K(k) = \frac{1}{\sqrt{2\pi}} e^{-\left(\frac{k^2}{2}\right)}, \quad -\infty < k < \infty$	95.1%

2.5.1 Results of Kernel Estimates

We plot pdf distributions of the k-factor for the height ranges 0-200 m and 0-500m a.g.l. Three kernels are used, namely, the biweight, the triangular, and the Gaussian kernels. For 200 m a.g.l., the total data samples were 740; therefore the optimum smoothing parameter according to (2.14), is $h_m \approx 0.26$. Similarly, for a height range 0-500 m a.g.l., there were 1600 data samples, with the corresponding optimum smoothing parameter found to be $h_m \approx 0.24$ [60].

Table 2.6 ISE for some kernels for best k-factor pdf, Botswana, 200 m agl, 740 samples

KERNEL K(k)	WINDOW WIDTH, h		
	h=0.1	h=0.25	h=0.8
Biweight	0.2600	0.1988	0.5717
Triangular	0.2360	0.2089	0.5818
Gaussian	0.2000	0.4427	0.9051

Table 2.7 Median values of the k-factor for Botswana, 200 m agl, 740 samples

KERNEL K(k)	WINDOW WIDTH, h		
	h=0.1	h=0.25	h=0.8
Biweight	1.120	1.126	1.119
Triangular	1.128	1.127	1.119
Gaussian	1.128	1.122	1.113

Table 2.8 Median values of the k-factor and ISE for Botswana, 500 m agl, 1600 samples

KERNEL (k)	WINDOW WIDTH, h			
	h=0.1		h=0.25	
	Mean	ISE	Mean	ISE
Biweight	1.094	0.3220	1.093	0.2863
Triangular	1.093	0.2970	1.093	0.3020
Gaussian	1.093	0.2870	1.090	0.6469

In Tables 2.6 to 2.8, we show the error values for each kernel and each smoothing parameter, h. In Table 2.6, while for the low values of h (h = 0.1), the Gaussian kernel gives the lowest error, as h rises to 0.25 and 0.8, the Gaussian kernel gives the highest value of ISE. It is observed that while initially the biweight kernel gives the highest error of 0.26 for h = 0.1, as h increases, it gives the lowest error. Also, the triangular and biweight kernels give progressively the same errors as h increases [60].

In Figures 2.9 and 2.10, one notices that it is almost impossible to discern the difference between biweight and triangular plots, especially around the centre of the curve. This could be attributed to the

fact that both these kernels are truncated for $|k| < 1$ [60]. Their difference with the Gaussian plot (Figure 2.11) is much more obvious, since the Gaussian kernel is defined even for $|k| > 1$. Notice from Figure 2.9 to Figure 2.11 that as h increases to values beyond 0.1, ($h = 0.25$ and 0.8), the resulting $f(k)$ takes the shape of the kernel for each of the three kernels, hence completely obscuring the actual shape of the k -factor distribution. This emphasizes the importance of the optimal choice of h [60].

From Tables 2.7 and 2.8, and Figures 2.9 to 2.13, one notices that for Botswana, the median value of k , μ_k , is about 1.12 for the height range 0-200 m, while it reduces to about 1.09 for the height range 0-500 m. This implies, as expected, that k distribution shifts slightly to lower ranges as the height range under consideration increases. These values are comparable to the value of 1.12 obtained from the curve-fitting model.

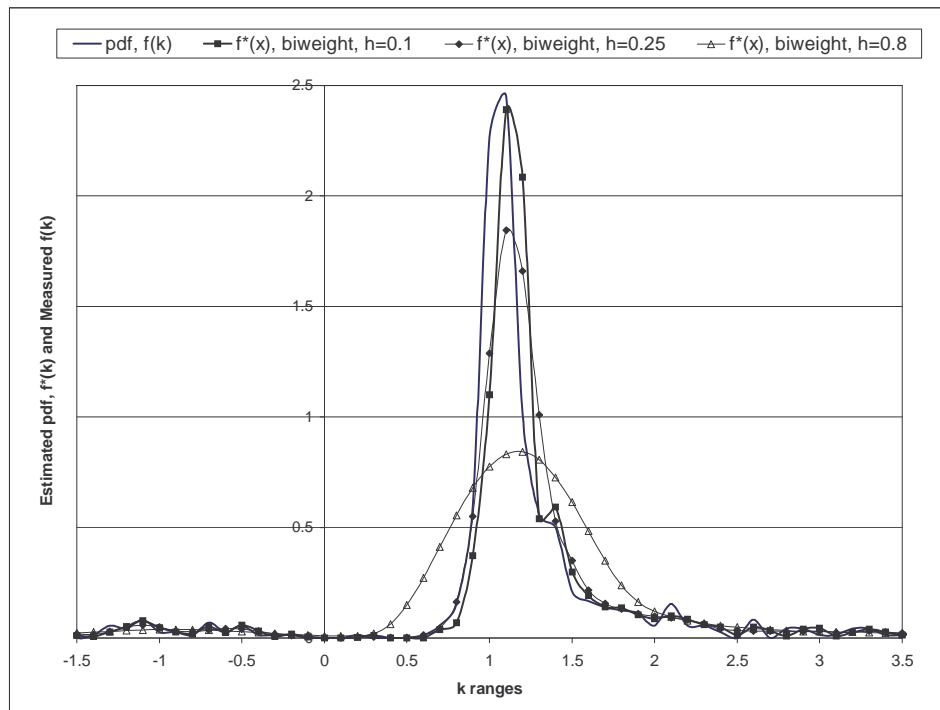


Figure 2.8 Biweight kernel estimates of the k -factor distribution, Botswana, 0-200m a.g.l.

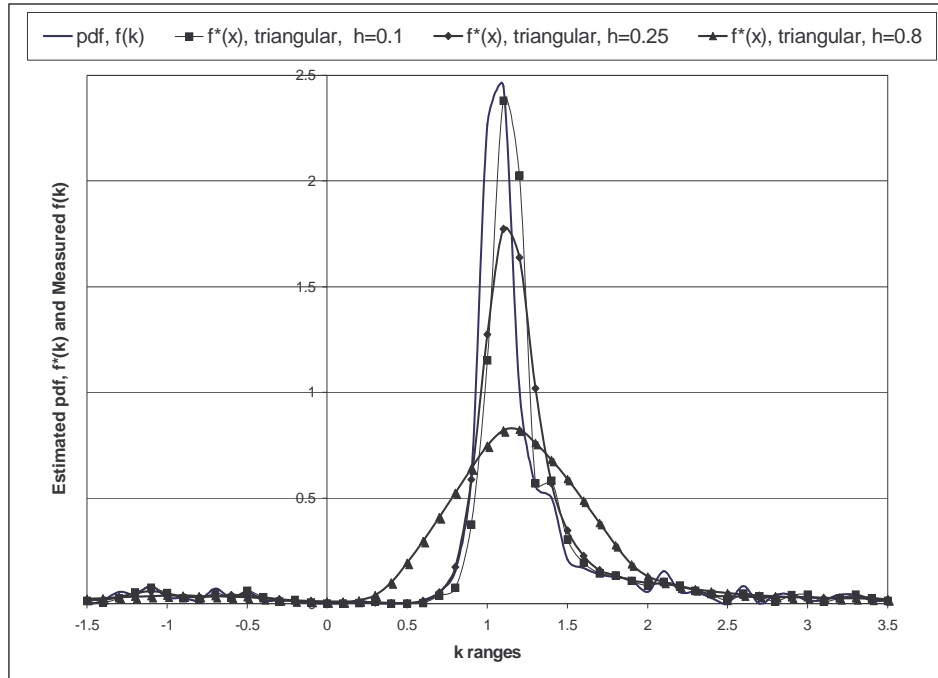


Figure 2.9 Triangular kernel estimates of the k-factor distribution, Botswana, 0-200m a.g.l.

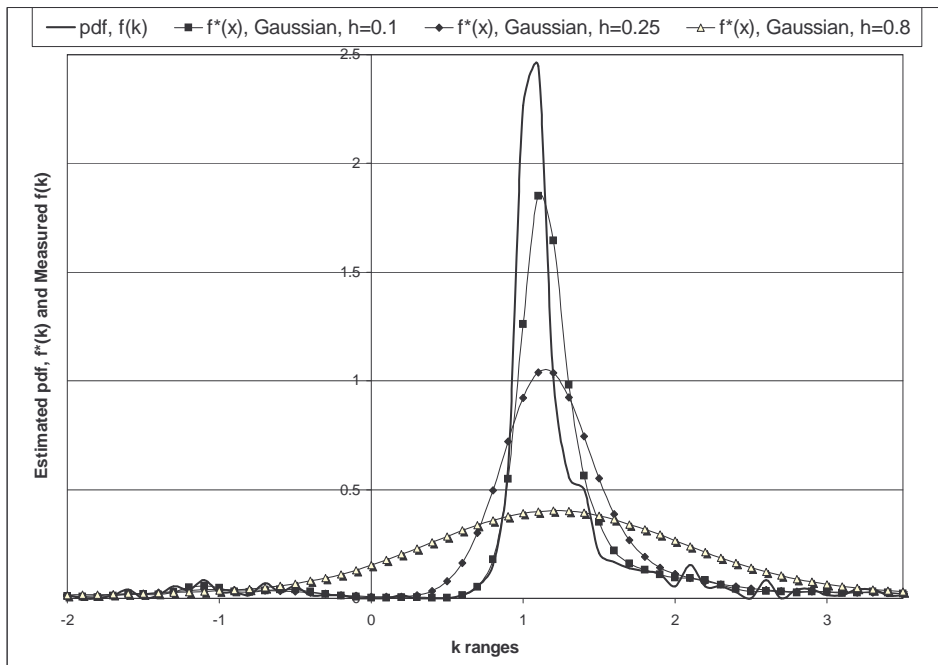


Figure 2.10 Gaussian kernel estimates of the k-factor distribution, Botswana, 0-200m a.g.l.

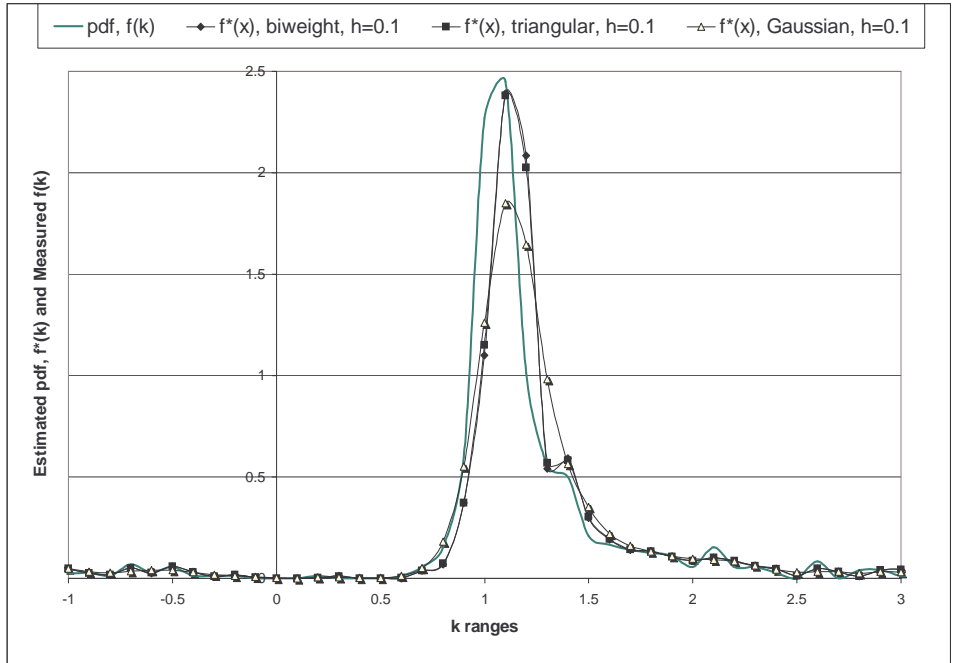


Figure 2.11 Comparison of kernel estimates of k-factor distribution, Botswana, 0-200m a.g.l., h=0.1

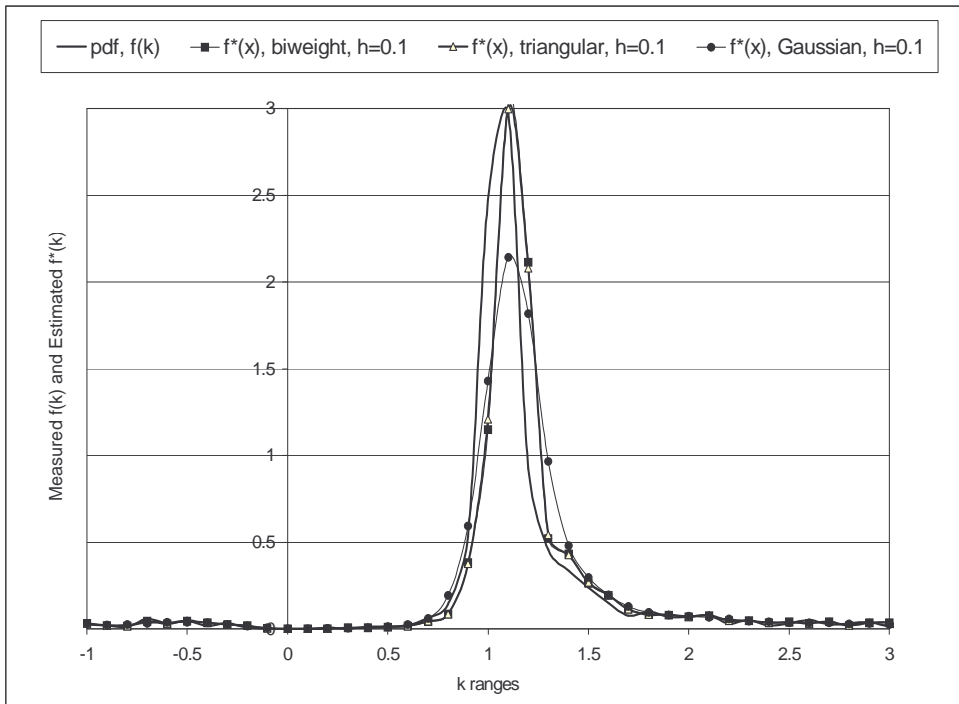


Figure 2.12 Comparison of kernel estimates of k-factor distribution, Botswana, 0-500 m a.g.l., h=0.1

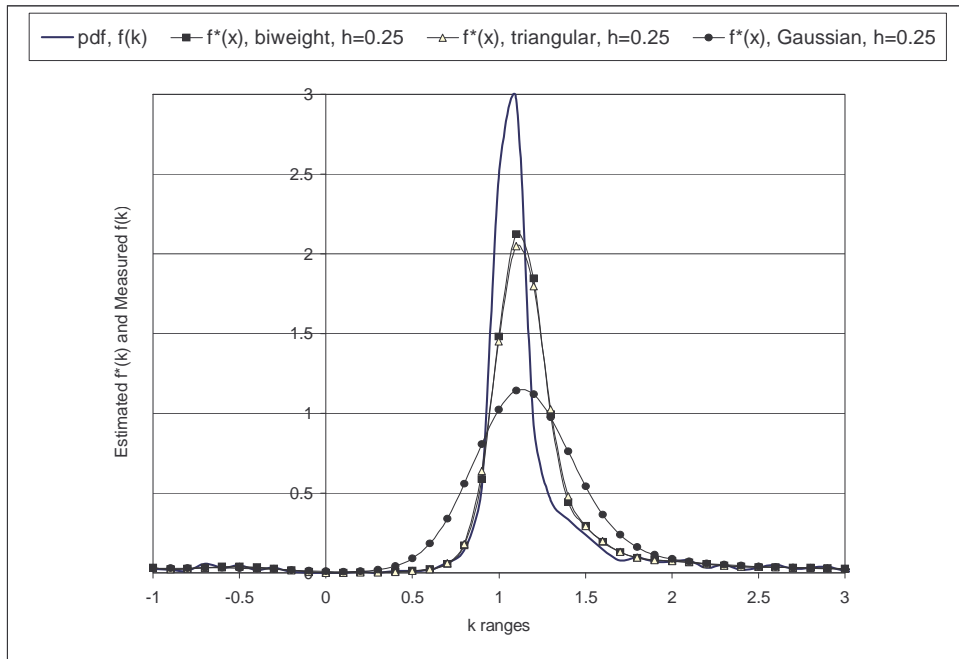


Figure 2.13 Comparison of kernel estimates of k-factor distribution, Botswana, 0-500 m a.g.l., $h=0.25$

2.6 Chapter Summary

This chapter has given a brief overview of both clear-air multipath and diffraction modeling as reviewed by different authors across the globe. The chapter then progresses by discussing in some detail the characterization of the LOS link path where signal level measurement used by the researcher for multipath model formulation is taken. The chapter discusses also in some detail the type and duration of data used in the thesis for model formulation. The challenges encountered with the available data and how these challenges have been combated is also discussed in this chapter. Notable among these challenges is the format of the data in terms of the height ranges. This format has created a significant data gap. The gaps were bridged by introducing the Inverse Distance Weighting (IDW) of the spatial interpolation technique. The chapter explained in detail how this technique has been used to predict the data in the appropriate usable format for the research interest. The chapter concludes by discussing the determination of different radioclimatic parameters such as refractivity gradients, geoclimatic factor and k-factor for the research location. The Kernel estimation techniques used to model the k-factor for the region is also discussed in the chapter.

CHAPTER THREE

BACKGROUND INFORMATION AND REVIEW OF CLAR-AIR RADIOCLIMATIC MODELING BY DIFFERENT AUTHORS

3.0 INTRODUCTION

General background information about radio propagation studies both in precipitation and clear-air environments is presented. The chapter then narrows down and discusses more material on clear-air radio propagation environment. Different authors in different parts of the world have adopted different methods to solve clear-air propagation problems. The methods can be grouped into three categories, namely: clear-air multipath modeling, clear-air diffraction fading and analytical or semi-empirical approach. The first two methods are purely statistical as they require, in most cases, a long time measurements of either signal level/fade event statistics or refractivity measurement statistics, or both. The third method on the other hand may require signal level measurements (semi-empirical) or purely analytical (in this case much measurement is not required). This chapter therefore focuses on reviewing these methods as adopted by different authors worldwide, and their approaches are summarized in the last section of the chapter. Some limitations of some of these approaches are also discussed.

3.1 Atmospheric Effects on Propagation for Line of Sight (LOS) Links

If a radio beam is propagated in free space, the path followed by the beam will be a straight line [61]. However, a radio ray propagated through the earth's atmosphere encounters variations in the atmospheric refractive index along its trajectory that causes the ray path to become curved [62, 36]. Refractivity of the atmosphere will affect not only the curvature of the ray (expressed by k-factor) but will also give some insight into the fading phenomenon [63].

Different propagation mechanisms are important at different frequencies. For frequencies below 3 GHz, path attenuation due to atmospheric gases, clouds, and rain is small and thus often neglected, whereas for terrestrial paths the relatively large vertical antenna beamwidths in use at these frequencies invite problems due to multipath propagation [64]. Atmospheric gases will absorb and

scatter the radio path energy, the amount of absorption and scattering being a function of frequency and altitude above sea level. Absorption and scattering do become serious contributors to transmission loss above 10GHz. At frequencies above 30 GHz, narrow beamwidth antennas may prevent multipath but path attenuation due to rain or antenna-pointing errors will be important.

In all, atmospheric propagation effects can be categorized into two categories depending on the causative agent or the frequency of propagation. These two categories are: precipitation effects (non clear-air) and clear-air effects.

3.1.1 Precipitation (non clear-air) Effect on Line of Sight (LOS) Links

The precipitation effects consist of hydrometeors in the atmosphere such as: rain, fog, cloud and snow [65]. In this section, we look at the effect of these hydrometeors on line of sight link design.

3.1.2 Rain

Rainfall is a natural and time varying phenomenon that varies from location-to-location and from year to year [48]. Above a certain threshold of frequency, attenuation due to rain becomes one of the most important limitations of the performance of line-of-sight microwave links [66, 67]. Rain affects the design of any communication or remote sensing system that relies on the propagation of electromagnetic waves through the lowest 10 km of Earth's atmosphere at frequencies above 1 GHz [68].

Communication systems may experience a loss of signal due to the attenuation caused by rain on a radio link and be temporarily unavailable for use. Scattering by rain may also introduce unwanted or interfering signals into a communication system receiver that may mask the desired signal. The problem for a system designer is the prediction or forecast of the effects of rain on radar, remote sensing, or communication system located anywhere on or above the surface of the earth.

At some time in the future, it may be possible to use numerical models for storm development and motion to predict the occurrence time, duration, and magnitude of a rain event producing attenuation on a radio link. At present, all that can be done is to predict the occurrence statistic of such events for a typical month or year as shown, for example, in [45].

3.1.3 Clouds and Fog

Scattering by the very small liquid water droplets that make up liquid water fogs near the earth's surface and liquid water clouds higher in the atmosphere can produce significant attenuation at the higher frequencies [64]. Clouds in the most active part of mid-latitude thunderstorms may have liquid water contents in excess of 5g/m^3 .

The liquid water cloud heights in the atmosphere can range from 0 km above ground (a fog) to 6 km above ground in the strong updrafts in convective clouds. For frequencies lower than 10GHz, cloud (or fog) attenuation can be ignored [64]. At a frequency above 30 GHz, cloud attenuation on a 50° elevation angle path may approach 3 to 4 dB. At a frequency of 120 GHz, this result translates to 30 to 40 dB.

3.1.4 Snow

Some parts of the world have no snow at all, while other parts have to face this problem most of the time. The attenuation in dry snow is an order of magnitude less than that in rain for the same precipitation rate. But attenuation by wet snow is comparable to that in rain and may even exceed that of rain at millimeter wavelengths [69]. It is difficult to specify the attenuation in any simple form.

3.2 Clear-Air Radioclimatic Effect on Line of Sight (LOS) Links

We define other parameters or factors that affect radiowave propagation in the line of sight domain different from the precipitation effects that has been explained in previous sections as clear-air radioclimatic effects. These clear-air effects can be categorized as either primary or secondary clear-air radioclimatic effects. Each of these is explained in the appropriate sub-sections below.

3.2.1 Primary Clear-Air Radioclimatic Effect

The primary clear-air radioclimatic effect is caused by three main radioclimatic variables namely: temperature, pressure and humidity (or water vapour pressure) [57]. These three parameters are called primary since other radioclimatic variables are derived directly from them [57]. These parameters are measured directly using different meteorological equipment. Temperature is measured by thermometers while pressure and humidity or water vapour pressure are measured by barometer. In cases where measuring equipment is not immediately available, use can be made of known measurements with application of statistical modeling techniques as discussed in [57] for research purposes. It has been established that each of these parameters decreases linearly with increasing altitude [61], except for temperature inversion situation which is not a normal propagation condition

[70].Therefore modeling these parameters is not a problem even if measuring equipment is not immediately available.

3.2.2 Secondary Clear-Air Radioclimatic Effect

Secondary radioclimatic data are derived from the primary radioclimatic variable explained above. Secondary radioclimatic data includes refractivity, refractivity gradient, ducting, geoclimatic factor, fading data and effective earth radius factor (k-factor) as explained in [51].

Each of the parameters mentioned above affect the radio propagation signal in one way or the other; this is why an appropriate procedure is required for proper planning of terrestrial line of sight links [51]. The propagation of electromagnetic waves around the earth is influenced by the properties of the earth and the atmosphere [17, 37, 35 & 71]. The earth is an inhomogeneous body whose electromagnetic properties vary considerably as we go from one point to another [72].

The changing nature of the atmosphere causes the refractive index of the troposphere to vary as the height increases from sea level [73] and this consequently has a significant effect on radio signal. The procedures recommended by the ITU-R for determining these variations are given in [37]. The atmospheric radio refractive index can be computed from the following formula:

$$n = \sqrt{\epsilon_r} = 1 + N \times 10^{-6} \quad (3.1)$$

N is the radio refractivity expressed as:

$$N = \frac{77.6}{T} \left(P + 4810 \frac{e}{T} \right) \quad (3.2)$$

$$M = N + 157h \quad (3.3)$$

Where

- P = Pressure in hectopascal (hpa)
- T = Temperature in Degree Kelvin (°K)
- e = Water vapour pressure in hectopascal (hpa)
- M = Modified refractivity
- h = height in m

The refractivity gradient is a measure of how the refractive index varies with increasing height. This is given as [51]:

$$\frac{dN}{dh} = 77.6 \frac{1}{T} \frac{dP}{dh} \left(\frac{77.6P}{T^2} + \frac{746512e}{T^3} \right) \frac{dT}{dh} + \frac{373256}{T^2} \frac{de}{dh} \quad (3.4)$$

The effective earth radius factor (k-factor) can be determined by [44]:

$$k = \frac{1}{1 - a/\rho} = \left(\frac{1}{1 + a \frac{d\epsilon_r/dh}{2}} \right) \quad (3.5)$$

Where $a = 6375$ km is the actual earth radius and ρ is the radius of curvature of the ray. The relative permittivity of troposphere at height h is defined as ϵ_r . Although a typical design values of $4/3$ is often used for k-factor in line of sight link design, the true value of k factor varies from place to place as shown in [36, 38-39, 70&74].

The geoclimatic factor, which is a measure of climatic and geographical condition of the terrain, is calculated using the following relation [58]:

$$K = 10^{-4.2 - 0.0029 \times dN_1/dh} \quad (3.6)$$

Where K is the geoclimatic factor and dN_1/dh is the point refractivity gradient in the lowest 65m of the atmosphere not exceeded for 1% of the average year.

The standard atmospheric model used in propagation studies is the one where the refractive index decreases linearly with height. The decreasing value of the refractivity causes the radio waves rays to curve downward [75]. In certain regions of the world, it often turns out that the index of refraction will have a rapid rate of decrease with height over a short distance that is sufficient to cause the rays to be refracted back to the surface of the earth. These rays are then reflected and refracted back and forth in such a manner that the field is trapped or guided within a thin layer of the atmosphere near the earth. This phenomenon is known as ducting [75]. Over a given height range, refractivity profiles

can be designed as sub-refractive, standard, super-refractive, or ducting, depending on the range dN/dh (or dM/dh) as shown in Table 3.1 below.

Table 3.1 Refractivity Profile for Different Atmospheric Condition [75]

Profile type	Refractivity Value
Sub-refraction	$dN/dh > -40$ or $dM/dh > 117$
Standard	$dN/dh \sim -40$ or $dM/dh \sim 117$
Super-refraction	$dN/dh < -40$ or $dM/dh < 117$
Ducting	$dN/dh < -157$ or $dM/dh < 0$

3.3 Other Line of Sight Link Design Issues

3.3.1 Multipath Propagation

There is no direct ray from the transmitter to the receiver in a wireless communication channel environment [76]. Rather what exists is the radiowave energy that travels through different paths from the transmitter to the receiver with different amplitude and phase characteristics as a result of ground reflection and possible obstruction on the path of the radio signal [76]. These different rays are combined either constructively or destructively at the receiver; hence the receiver is faced with the challenge of properly demodulating and decoding the signal into a replica of the original signal. The situation described above is called multipath propagation, which results in multipath fading.

Fading is defined as any time varying of phase, polarization, and level of the received signal. Multipath fading is the most common type of fading encountered, particularly on LOS radio links. For an explanation of atmospheric multipath fading, we refer to the refractive index gradient discussed in section 3.2.2 above. As the gradient varies, multipath fading results owing to the following factors (a) the interference between the direct rays and the specular component of a ground-reflected wave (see Figure 3.1); (b) the nonspecular component of the ground-reflected wave; (c) partial reflections from atmospheric sheets or elevated layers; or (d) additional direct wave paths (i.e. nonreflected paths) [61].

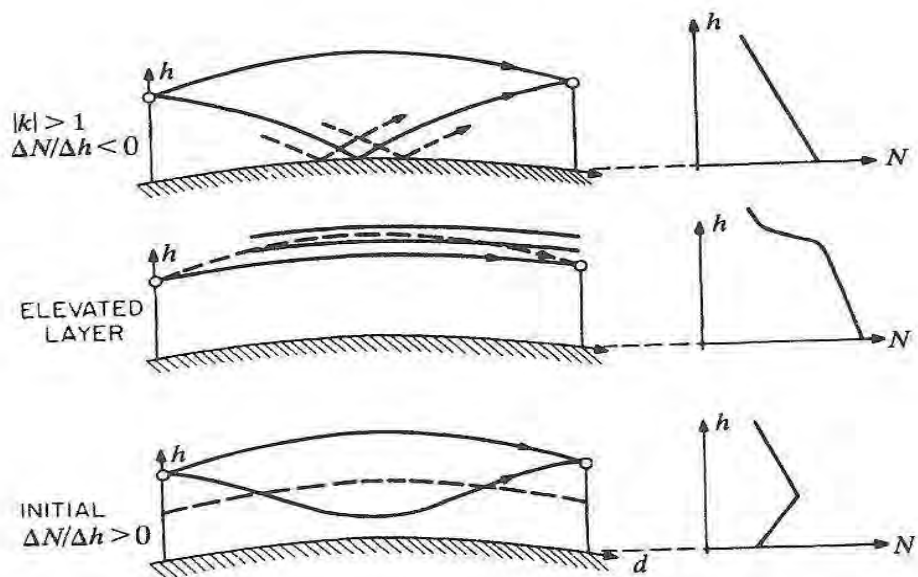


Figure 3.1 Mechanism of Multipath Fading

The radiolink designer is more interested in the fading rate (i.e. number of fades per time unit) and the fade depth (i.e. how much the signal intensity at the receiver varies from its free-space value) generally expressed in decibels. The four multipath fading mechanisms previously listed can operate individually or concurrently. Fade depths can exceed 20 dB, particularly on long LOS paths and more than 30 dB on the much longer troposcatter paths. Fade durations of up to several minutes or more can be expected [61].

Often multipath fading is frequency selective and the best technique for mitigation is frequency diversity [76]. For effective operation of frequency diversity, sufficient frequency separation is required between the two transmit frequencies to provide sufficient decorrelation. On most systems a 5% frequency separation is desirable [76]. However, on many installations such a wide separation may not be feasible owing to frequency congestion and local regulations [76]. In such cases it has been found that a 2% separation is acceptable [76].

No analytical equations have been obtained to give an accurate prediction of the radio propagation pathloss for multipath (or multipath models). But empirical and statistical representations are available for various scenarios [69]. Most of the popular outdoor pathloss prediction tools are based on Okumura and Hata's formulation, which are based on a huge amount of measured data for

frequencies between 100 MHz and 3 GHz [72]. For indoor scenarios, many researchers have shown that indoor pathloss actually obeys the distance power law as [72]:

$$L_p(d) = L_p(d_0) + 10n \log\left(\frac{d}{d_0}\right) + X, \text{ dB} \quad (3.7)$$

Where d_0 is the reference distance (normally 1m), the power index n depends on the frequency, surrounding, and building type, and X represents a normal random variable in dB having a standard deviation of σ dB. Typical values for various building are provided in Table 3.2.

Table 3.2 Pathloss exponent and standard deviation measured in different building [69]

Building	Frequency (MHz)	Index n	Standard deviation σ (dB)
Retail Stores	914	2.2	8.7
Office (hard partition)	1500	3.0	7.0
Office (soft partition)	1900	2.6	14.1
Office (soft partition)	915	2.0 – 2.8	9 – 14
Open-plan factory	1300	2.0 – 2.4	3.7 – 9.0
Suburban home	900	3.0	7.0

3.3.2 Diffraction Effects

Diffraction of radio wave fronts occur when the wave front encounters an obstacle that is large when compared to the wavelength of the ray. Below about 1000 MHz there is diffraction or bending from an obstacle with increasing attenuation as a function of obstacle obstruction. Above about 1000 MHz, with increasing obstruction of an obstacle, the attenuation increases even more rapidly such that the path may become unstable by normal transmission means than at lower frequencies. The actual amount of obstruction loss is dependent on the area of the beam obstructed in relation to the total frontal area of the energy propagated and to the diffraction properties of the obstruction [61].

3.3.3 Fresnel Zone Radius

Under normal transmission conditions (i.e. non diffraction), the objective for the system designer is to provide sufficient clearance of the obstacle without appreciable transmission loss due to the obstacle. Huygen's principle developed by Fresnel is employed to calculate the necessary obstacle clearance. When dealing with obstacle diffraction, we assume that the space volume is small enough that

gradient effects can be neglected so that the diffraction discussion can proceed as though in an homogeneous medium.

Considering Figure 3.2, the Huygens–Fresnel wave theory states that the electromagnetic field at point S_2 is due to the summation of the fields caused by radiation from small incremental areas over a closed surface about point S_1 , provided that S_1 is the only source of radiation. The field at a constant distance r_1 from S_1 , which is a spherical source, has the same phase over the entire surface since the electromagnetic wave travels at a constant phase velocity in all directions in free space. The constant phase surface is called a wave front. If the distances r_2 from the various points on the wave front to S_2 are considered, the contributions to the field at S_2 made up of components that add vectorially in accordance with their relative phase differences. Where the various values of r_2 differ by half-wavelength ($\lambda/2$), the strongest cancellation occurs. Fresnel zones distinguish between the areas on a closed surface about S_1 whose components add in phase.

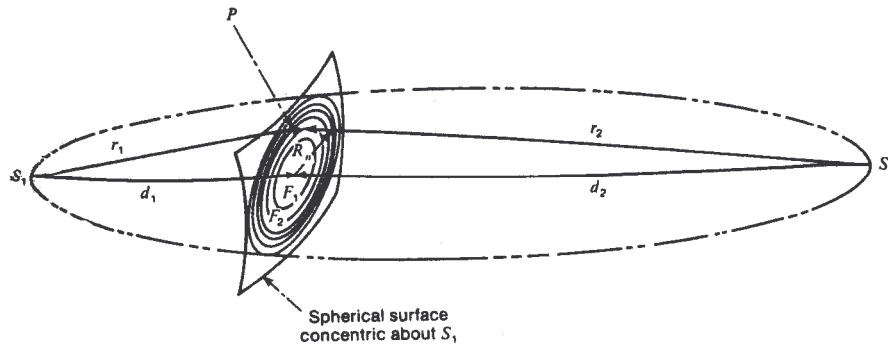


Figure 3.2 Fresnel Zone Geometry [61]

Let us consider a moving point P_1 in the region about the terminal antenna locations S_1 and S_2 such that the sum of the distances r_1 and r_2 from the antennas to P is constant. Such a point, then, will generate an ellipsoid with S_1 and S_2 as its foci. We now can define a set of concentric ellipsoidal shells so that the sum of the distances r_1 and r_2 differs by multiples of half-wavelength ($\lambda/2$). The intersection of these ellipsoids defines Fresnel zones on the surface as shown in Figure 3.2. Thus, on the surface of the wave front, a first Fresnel zone F_1 is defined as bounded by the intersection with the sum of the straight line segments r_1 and r_2 equal to the distance d plus one-half wavelength ($\lambda/2$). The second Fresnel is defined as the region where $r_1 + r_2$ is greater than $d + \lambda/2$ and less than $d + 2(\lambda/2)$. Thus the general case may now be defined where F_n is the region where $r_1 + r_2$ is greater than $d + (n-$

$1)\lambda/2$ but less than $d + n\lambda/2$. Field components from even Fresnel zones tend to cancel those from odd zones since the second, third, fourth, and fifth zones (etc.) are approximately of equal area.

Fresnel zone application to path obstacles may only be used in the far field. The minimum distance d_F where the Fresnel zone is applicable may be roughly determined by $d_F > 2D^2/\lambda$, where D is the antenna aperture measured in the same unit as λ . To calculate the radius of the n th Fresnel zone r_n on a surface perpendicular to the propagation path, the following equation provides a good approximation [61]:

$$r_n = \sqrt{n\lambda \left(\frac{d_1 d_2}{d_1 + d_2} \right)} \quad (3.8a)$$

or

$$r_n = 17.3 \sqrt{\frac{n}{F_{\text{GHz}}} \left(\frac{d_1 d_2}{d_1 + d_2} \right)} \quad (3.8b)$$

Here d_1 is the distance to the near end antenna and d_2 is the distance to the far end antenna from the obstacle. In equation (3.8b) all distances are in kilometers, the frequency of the emitted signal is in gigahertz and r_n is in meters. Conventionally we require 0.6 Fresnel zone clearance of the beam edge (3-dB point) due to obstacle in the path. This 0.6 Fresnel zone clearance is implemented in the design example discussed in section 3.3.5. Providing 0.6 Fresnel zone clearance is usually sufficient to ensure that attenuation due to obstacle near the ray beam path is negligible [61].

3.3.4 Knife – Edge Diffraction Loss

Consider a situation where a knife edge obstacle made up by a perfect conductor half plane, normal to the direction of propagation. In this ideal case the obstacle may be defined by a single non-dimensional parameter v given by [77]:

$$v = \pm h \sqrt{\frac{2d}{\lambda d_1 d_2}} \quad (3.9)$$

where h is the obstacle height above (plus sign) or below (minus sign) the direct ray between the transmitter and receiver antennas (see Figure 3.3), d is the distance between the antennas, d_1 and d_2

are the distances between the obstacle and each of the antennas, and λ is the wavelength corresponding to the operating frequency f . Parameter v may also be expressed as a function of the radius of the first Fresnel ellipsoid r_{1e} at the obstacle. From equations (3.8a) and (3.9) we get [77]:

$$v = \pm h \frac{\sqrt{2}}{r_{1e}} \quad (3.10)$$

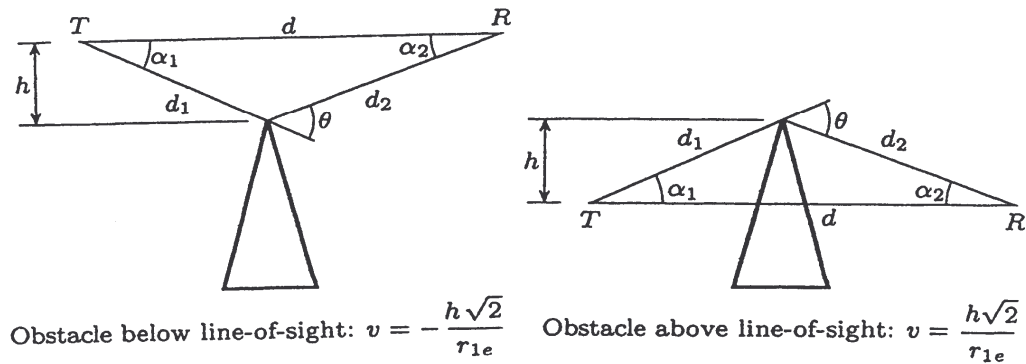


Figure 3.3 Definition of v for obstacles above and below line-of-sight [46]

Estimating the signal attenuation caused by diffraction of radio waves over hills and buildings is essential in predicting the signal strength in a given service area. The electric field strength E_d of a knife-edge diffraction wave is given in [78] as:

$$\frac{E_d}{E_0} = F(v) = \frac{(1+j)}{2} \int_v^{\infty} \exp(-j\pi t^2/2) dt \quad (3.11)$$

Where E_0 is the free space field strength in the absence of both the ground and the knife edge, and $F(v)$ is the complex Fresnel integral. The Fresnel integral, $F(v)$ is a function of the Fresnel-Kirchoff diffraction parameter v . The diffraction gain due to the presence of a knife-edge as compared to the free space electric field is given in [78] as:

$$G_d(\text{dB}) = 20 \log |F(v)| \quad (3.12)$$

In practice, graphical or numerical solutions are relied upon to compute diffraction gain. Rappaport [78] gives an approximate equation of G_d as follows:

$$\left. \begin{array}{ll} G_d \text{ (dB)} & v \\ 0 & v \leq -1 \\ 20\log (0.5-0.62v) & -1 \leq v \leq 0 \\ 20\log (0.5\exp(-0.95v)) & 0 \leq v \leq 1 \\ 20\log \left(0.4-\sqrt{0.1184-(0.38-0.1v)^2} \right) & 1 \leq v \leq 2.4 \\ 20\log \left(\frac{0.225}{v} \right) & v > 2.4 \end{array} \right\} \quad (3.13)$$

3.3.5 k-Factor Fading

As an example, a 48.28 km link is set up between Umlazi and Sherwood in Kwazulu-Natal Province of South Africa. The path profile diagram of the link is shown in Figure 3.4. A design value of $k = 1.33$ is assumed, as opposed to $k = 1.21$ which is the median k value for Durban. The link availability is examined using different values of k ranging between 0.5 and 1.33 [42].

The results in table 3.3 show that for the median k -value of 1.21, the diffraction loss (due to a knife-edge obstruction 18 km from Sherwood) is barely noticeable at 1.5 dB. On the other hand, for link design of 99.9% availability, we notice that for this particular link, a fade margin of 18 dB would suffice for the month of February, since the value of k exceeded 99.9% of the time would be 0.9 [42]. Yet this would be insufficient for the other times of the year. From fourth-order polynomial extrapolation (in order to ensure 99.9% link availability all year) the corresponding value of $k=0.5$ would require a fade margin exceeding 40 dB for this path.

A second example explores the 44-km Gaborone-Molepolole SHF link operating at 23 GHz, also designed for 60% clearance of the first Fresnel zone radius for $k=4/3$. In this case we note, from Figure 3.5, possible obstructions at points A, B, and C placed at 8 km, 38 km, and 42 km from Gaborone. These result in diffraction losses of 1.6 dB, 1.8 dB, and 1.5 dB, respectively, give a total loss of 4.9 dB at the median $k = 1.1$. However, for this same path, the total diffraction loss for $k = 0.6$ (for link availability of 99.9%) is 15.9 dB, from k -type fading [42].

The two design examples show that the type of terrain plays a major role in diffraction fading emanating from k-factor variation. While designing with $k = 4/3$ only results in losses of 2 dB and 5 dB for Durban and Botswana links, respectively, multiple obstructions would result in higher fades. Moreover, the gentler terrain in Botswana results in lower losses that would have been the case if the k-factor for Durban had been 1.1. Moreover, 99.9% link availability is harder to attain in Durban than in Botswana [42].

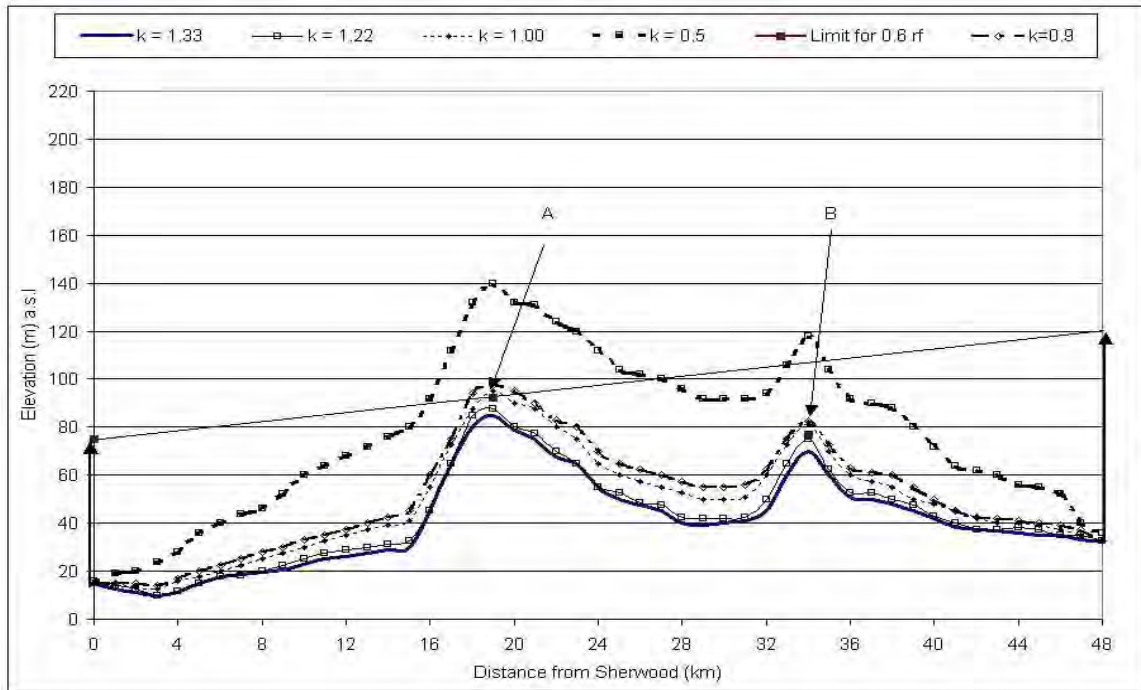


Figure 3.4 Path Profile for Radio Link between Sherwood and Umlazi: Antenna Heights for 60% clearance – Sherwood-60m, Umlazi-88m, $k=4/3$, $f=23$ GHz [42]

Table 3.3 k- Factor Variation with Diffraction Gain G (Sherwood – Umlazi) [42]

k	Point A		Point B		Total G(dB)
	h	G(dB)	h	G(dB)	
1.33	-7.35	+0.22	-36.00	0	+0.22
1.22	-4.85	-1.45	-31.00	0	-1.45
1.00	2.65	-10.15	-25.00	0	-10.15
0.90	5.15	-17.61	-23.50	0	-17.61
0.50	47.65	-27.76	12.00	-16.74	-44.50

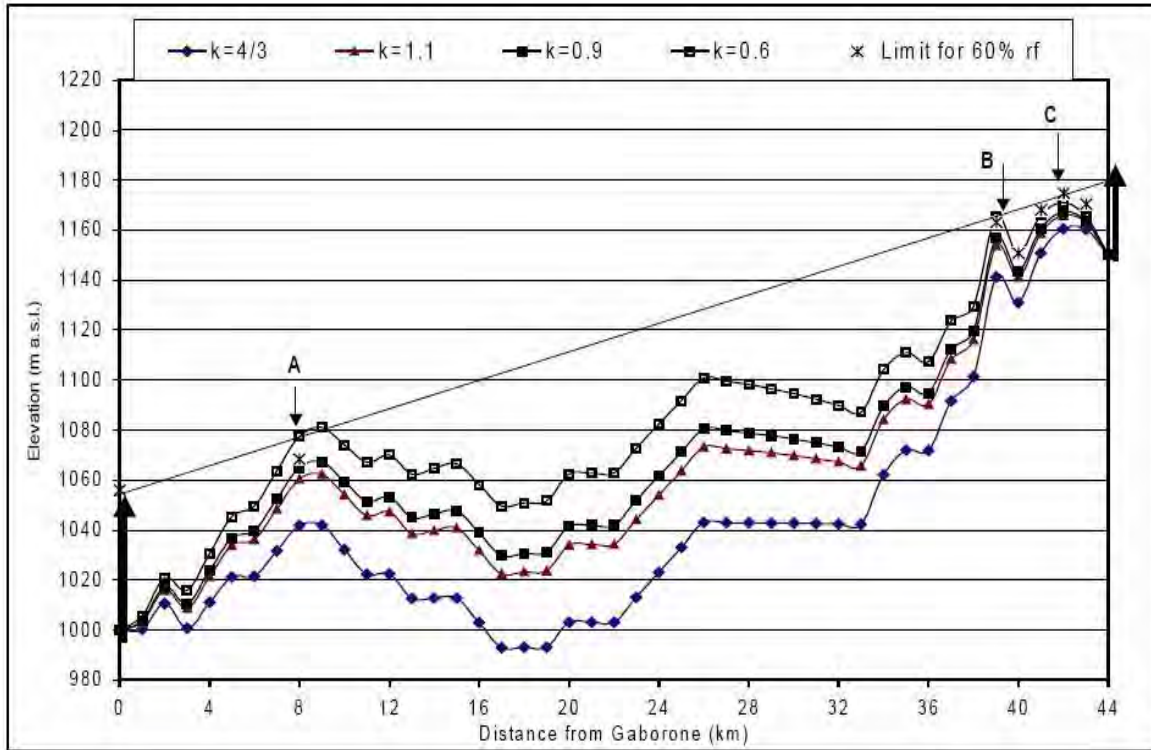


Figure 3.5 Gaborone-Molepolole Path Profile: Antenna Heights for 60% clearance – Gaborone-56m, Molepolole-30m, $k = 4/3$, $f = 23$ GHz [42]

Table 3.4 Effect of the k-factor variation on Diffraction Gain G for Gaborone-Molepolole Link [42]

k	Point A		Point B		Point C		Total G(dB)
	h	G(dB)	h	G(dB)	h	G(dB)	
1.1	-8	-1.6	-13	-1.8	-9.4	-1.5	-4.9
0.6	0	-6.0	0	-6.0	-3.8	-3.9	-15.9

3.3.6 Link Budget and Link Reliability

For a radio line of sight link, there are losses associated with the radio wave signal as it travels from the transmitter to the receiver. The total path loss associated with the transmitted signal is given by [43]:

$$L_{\text{tot}} = L_{\text{fs}} + K_1 + L_o + L_r + L_v + L_{\text{fad}} \quad (3.14)$$

Where:

- L_{fs} = Free Space Loss
- K_1 = Correction factor of free-space loss (medianloss) = -16dB for Raleigh-faded path
- L_o = oxygen loss ($\approx 50\text{ GHz}$)
- L_r = rain loss depends, on rain rate
- L_v = Water Vapour Loss ($>10\text{ GHz}$)
- L_{fad} = Fade margin, due to multipath effects.

If the link is non line-of-sight (NLOS) however, then we also include a diffraction loss, L_d . A design value of k which results in less than 60% clearance of first Fresnel zone results in some non-zero diffraction loss. If $k = k_1$ is used in the design, then earth bulge, b_1 , is experienced at point of maximum obstruction.

The link design is such that at maximum obstruction point, 60% of first Fresnel zone radius is achieved. However if the actual value of k is k_2 , the earth bulge is b_2 . Then there is obstruction of the first Fresnel zone if $b_2 > b_1$ (that is, more than 60% r_1 is obstructed). Fresnel zones explain the concept of diffraction loss as a function of path clearance around an obstruction. The discussion of Fresnel zones radius is detailed in section 3.3.3. It should be noted that the Fresnel zones are elliptical in shape with the transmitter and receiver at their foci [43].

3.4 Free Space Propagation

In order to define the loss between the transmitting and receiving antenna separated by a particular distance we assume that the transmission medium between the transmitter and receiver is a vacuum [70]. The antenna at each end of the link is assumed to be an isotropic one, so that we can say point A is an isotropic source¹. Let the total power in watts radiated by the source be P_T . The envelope containing the radiation around the source can be considered to be an expanding sphere of radius r . The net power flow through the surface of a sphere at its center point is also P_T , hence, it follows that the power flow per unit area through any portion of the sphere's surface is given by [61]:

$$P_{av} = \frac{P_T}{4\pi r^2} \quad (3.15)$$

An isotropic antenna may serve as either a transmitting antenna or receiving antenna. In the receive function, it absorbs power from the radiation field in which it is situated. Its effective aperture² determines the amount of power that the receiving antenna absorbs in relation to the RF

¹An isotropic source radiates uniformly in all directions (i.e. has a gain of 1 or 0 dB).

² Defined as the area of the incident wave front that has a power flux equal to the power dissipated in the load connected to the receive antenna output terminals.

power density of the field [61]. For an isotropic antenna, the effective area is $\lambda^2/4\pi$, where λ is the wavelength of incident radiation field. From equation (3.15) it then follows that an isotropic antenna situated in a radiation field with a power density P_{av} will deliver into its load a power P_R given by:

$$P_R = P_T \left(\frac{\lambda}{4\pi r} \right)^2 \quad (3.16)$$

Where r is the radius of the sphere. The transmission loss between transmit and receive antennas is defined as:

$$L_{dB} = 10 \log_{10} \frac{P_T}{P_R} \quad (3.17)$$

Combining equations (3.16) and (3.17), the free space loss becomes

$$FSL_{dB} = 21.98 + 20 \log_{10} \left(\frac{r}{\lambda} \right) \quad (3.18)$$

Equation (3.18) can be re-expressed in a more useful form:

$$FSL_{dB} = 32.45 + 20 \log r_{km} + 20 \log F_{MHz} \quad (3.19)$$

The chapter progresses by looking at the atmospheric effects on propagation for line of sight link design. These atmospheric effects are categorized into precipitation effects and clear-air radioclimatic effects. Precipitation effects consist of hydrometeors in the atmosphere such as: rain, fog, cloud and snow, while clear-air effects consist of all other effects outside hydrometeor. The clear-air effect is further categorized into primary and secondary radioclimatic effects. The primary clear-air radioclimatic effect is caused by three primary radioclimatic variables namely: temperature, pressure and humidity (or water vapour pressure). On the other hand, secondary radioclimatic data are derived from primary radioclimatic variable. Secondary radioclimatic data includes refractivity, refractivity gradient, ducting, geoclimatic factor, fading data and effective earth radius factor (k-factor). Each of the highlighted effects are detailed in the appropriated section of the chapter. The chapter then discusses diffraction effects and concludes with link budget design and planning for terrestrial line of sight (LOS) application. This was shown with two LOS design examples set up in both Durban and Botswana.

3.5 Clear-Air Multipath Propagation Modeling Techniques by Various Authors

3.5.1 The K. Morita and K. Kakita Model (Japan)

In their approach, Morita and Kakita [29] derived an empirical formulation for the occurrence probability (P_R) of Rayleigh fading as a result of propagation tests in the worst season for many years in Japan. This empirical formulation was derived by studying the dependence of P_R on propagation path distance, path height and inclination of propagation path etc., by using fading data on NTT microwave links [29, 79, 80]. Measured Rayleigh fading occurrence probability, P_R in the 4 GHz microwave links in Japan in the worst season, is tabulated in Table A.1 (see appendix A). Rayleigh fading occurrence on each hop was picked up, counting the total signal interruption time due to fading which is confirmed by operation of the squelch circuit [22]. Measured Rayleigh fading P_R occurrence probability for the propagation test paths is shown in Table A.2 (see appendix A). The empirical formula of P_R is derived using the measured values of P_R in Table A.1 (see appendix A) and studying the dependence of P_R on distance, propagation path condition, path height and inclination of propagation path. Comparison between the value of P_R estimated by the empirical formula and the measured P_R value was carried out on data from Tables A.1 and A.2 (see appendix A).

3.5.2 Distance Dependence of Rayleigh Fading Occurrence Probability

The distance dependence of the Rayleigh fading occurrence probability P_R on the data from Table A.2 (see appendix A) is shown in Figure 3.6. The P_R for propagation paths over the mountains, over plains and over the sea is shown in Figure 3.6. The explanation of these different path classifications is shown in Table 3.5. The P_R values of these three paths rapidly increase with increasing distance d . This distance dependence is approximately the 3.5th power of d ($P_R \propto d^{3.5}$). A constant is therefore obtained from the following equation [22]:

$$P_R = a d^{3.5} \quad (3.20)$$

Where a in (2.1) is a constant. Constant values of the respective propagation paths becomes the following: Over the mountains: $2.1 \times 10^{-9}(0.4)$; over the plains: $5.1 \times 10^{-9}(1.0)$; over the sea:

1.9×10^{-8} (3.7). The numerical values in the brackets show the relative values which are normalized with the value over the plain.

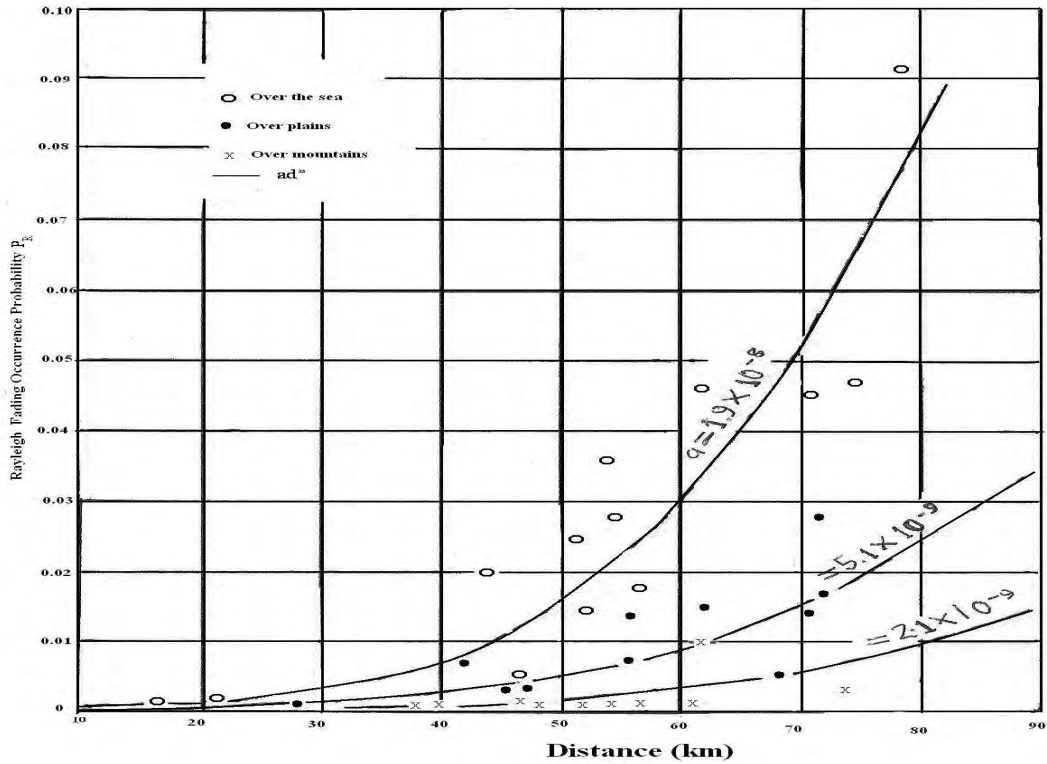


Figure 3.6 Distance dependence of Rayleigh fading occurrence probability [22]

Table 3.5 Classification of Propagation Path Condition [22]

Classification	Propagation Path Condition
Over mountains	Most of the path is over mountainous terrain.
Over plains	<ul style="list-style-type: none"> ▪ Most of the path is over plains. ▪ Most of the path over mountainous terrain and the rest is over water.
Over the sea	<ul style="list-style-type: none"> ▪ The path is over the sea. ▪ The path is over the coastal region (within about 10 km from the coast).

3.5.3 Relation between Path Height and Rayleigh Fading Occurrence Probability

The relation between average path height ($\bar{h} = (h_1 + h_2)/2$) and Rayleigh fading occurrence probability P_R is shown in Figs. 3.7 and 3.8. Each P_R in these two figures is reduce to $d = 50$ km,

after compensating for the characteristics of path distance effect ($P_R \propto d^{3.5}$). The P_R over the sea holds an approximate relation of $P_R \propto \sqrt{1/h}$. There is almost no correlation between h and P_R for the paths over the mountains and over the plains as shown in Figure 3.8.

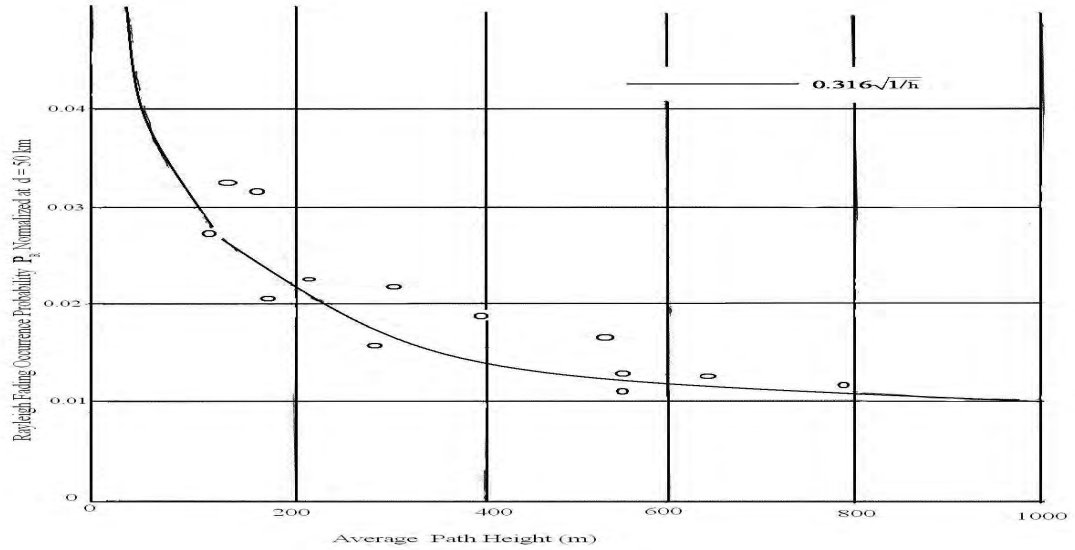


Figure 3.7 Relation between path height and Rayleigh fading occurrence probability over the sea [22]

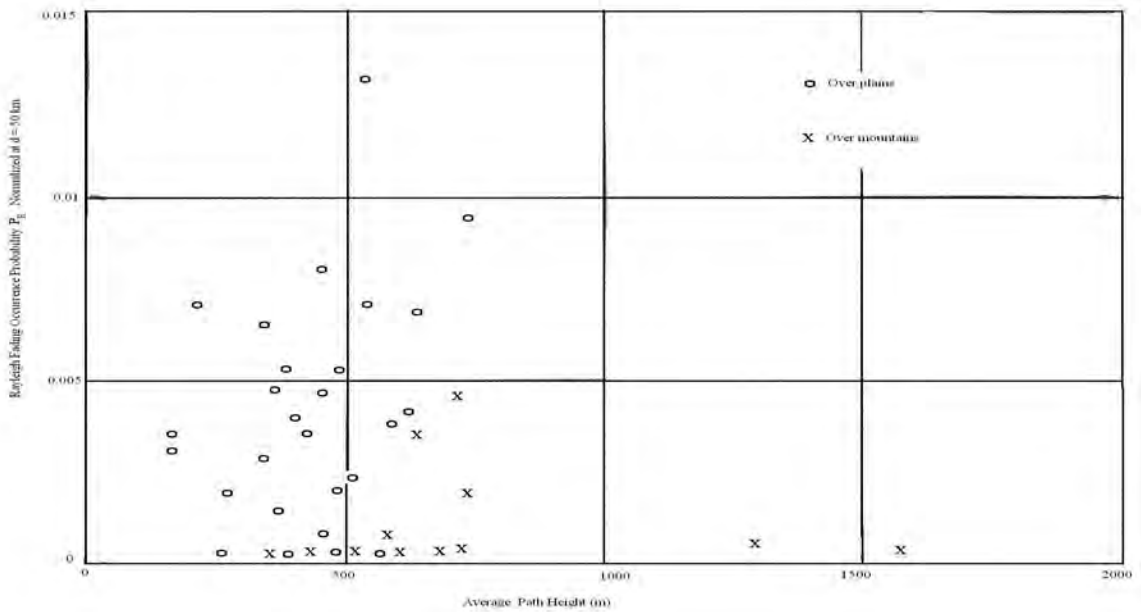


Figure 3.8 Relation between path height and Rayleigh fading occurrence probability [22]

3.5.4 Relation between Inclination of Propagation Path and Rayleigh Fading Occurrence Probability

The relation between the inclination of propagation path $\Delta h/d$ (Δh : difference of height between h_1 and h_2 , d : distance) and Rayleigh fading occurrence probability P_R is shown in Figure 3.9. As is obvious from the figure, there is very little correlation between $\Delta h/d$ and P_R for the propagation paths over the sea and coastal region and over the land. From this fact, it may be said that the inclination angle on each real microwave link is not sufficiently large ($\Delta h/d \leq 0.02$) to affect the P_R to decrease.

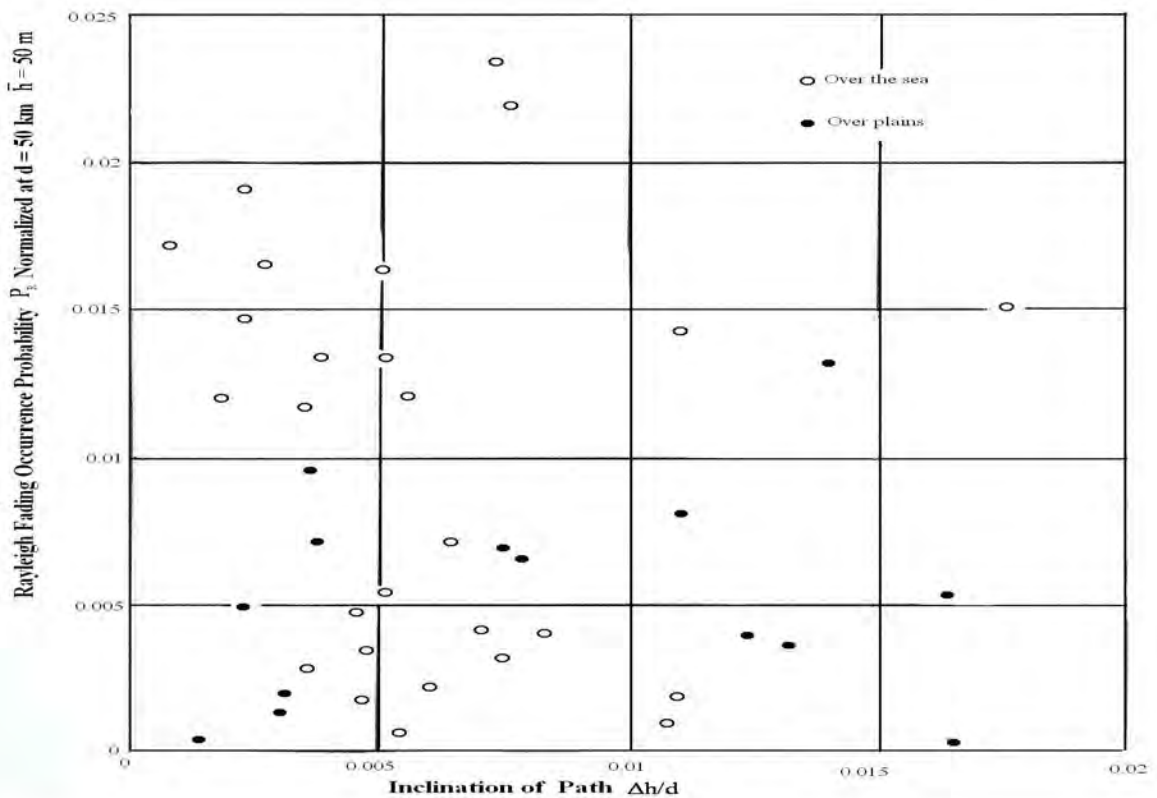


Figure 3.9 Relation between inclination of propagation path and Rayleigh fading occurrence probability [22]

3.5.5 Frequency Dependence of Rayleigh Fading Occurrence Probability

The frequency dependence of Rayleigh fading occurrence probability P_R can be obtained from fading data measured simultaneously at several different radio frequencies in various kinds of propagation paths. However, frequency dependence may depend on locality and propagation distance. Therefore, to obtain a universal conclusion of frequency dependence is very difficult. In their approach, Morita and Kakita [22, 29] obtain the frequency dependence of P_R using the following method.

It is known that short-period fading range is in proportion to a 1/2 exponent of frequency [81]. Therefore, if the distribution curve of short-period fading range is obtained empirically for one frequency, the frequency dependence of P_R can be obtained by using the fading range distribution curve. In Figure 3.10, the cumulative distribution curves of hourly fading range (10% to 90%), obtained on six paths of Togi – Odayama, Togi – Tsuneyama, Fukuso – Tsuneyama, Noro – Fukuso, Oginojo – Yakushi and Noboribetsu – Niyama, are shown.

In Rayleigh distribution, fading range (10% to 90%) F_r is approximately 13.4 dB. The percentage of $F_r \geq 13.4$ dB is obtained from the distribution curve in Figure 2.5, which gives the P_R at 4 GHz. For frequencies above 4 GHz, the P_R is obtained as the percentage of $F_r \geq \sqrt{4/f \times 13.4}$ (dB), where f is the frequency in GHz. Rayleigh fading occurrence probability P_R estimated by the above method is nearly proportional to $f^{1.2}$ [22].

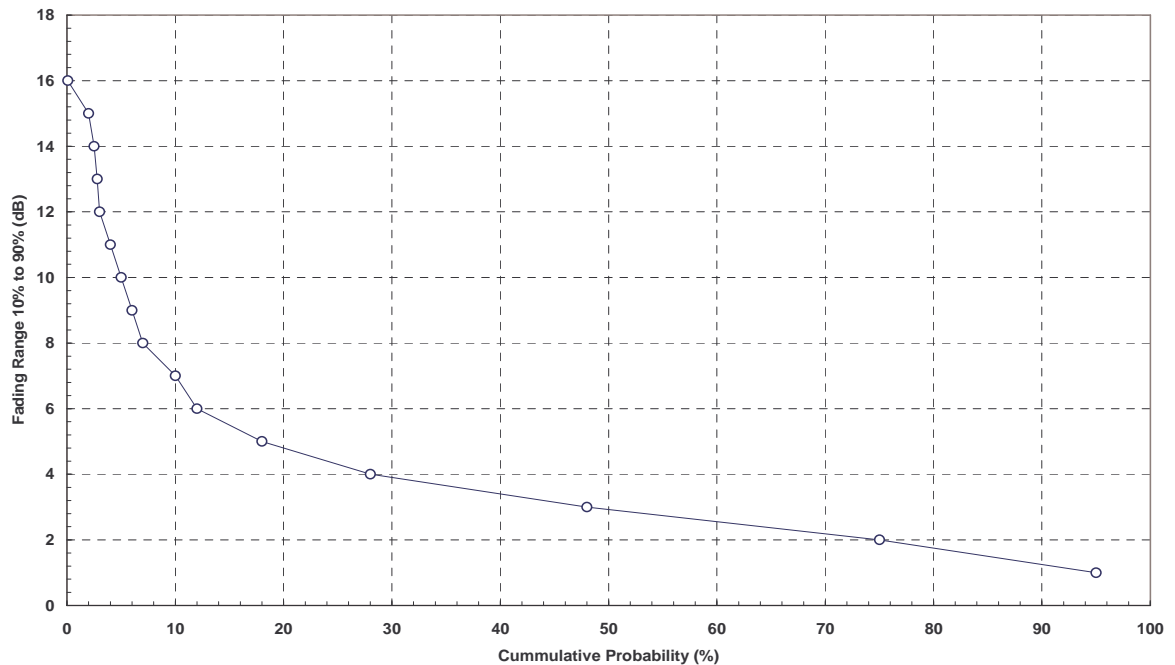


Figure 3.10 Cumulative distribution curve of the hourly fading range for six typical propagation paths [22].

3.5.6 Empirical Formula of Rayleigh Fading Occurrence Probability

The distance dependence of P_R , path condition dependence of P_R , relation between path height and P_R , relation between inclination of propagation path and P_R , and frequency dependence of P_R which

have all been explained above are all combined to formulate the empirical formula of Rayleigh fading occurrence probability. The empirical formula of P_R is given as follows [22]:

$$P_R = \left(\frac{f}{4}\right)^{1.2} \cdot Q \cdot d^{3.5} \quad (P_R \leq 0.3) \quad (3.21)$$

where f is frequency in GHz, $Q = 2.0 \times 10^{-9}$ (over the mountains), 5.1×10^{-9} (over the plains), $3.7 \times 10^{-7} \sqrt{1/\bar{h}}$ (over the sea), \bar{h} is the average path height in meters,

d is the path distance in kilometers. The empirical formula derived above may not be suitable for adaptation for a frequency band much greater than 4 GHz band. This is because the formula was derived based on data in the 4 GHz frequency band. This empirical formula is thought to be adaptable to the frequency bands between 2 to 15 GHz [22].

3.5.7 The M.S. Wheeler Model

In his model, Wheeler [61] examines three sources of microwave relay fade statistics to show that their differences may be explained on the basis of ground clearance at midpath. An empirical expression is suggested that combines the three sets of data into one that is useful over a considerable range of ground clearance. This is then used to calculate a microwave link composed of N hops between ground and tethered balloons. There are three primary sources of fading data in line of sight microwave relays. Data by Barnett [82] were taken at short range and small ground clearance in the United States. There is a large quantity of data taken by Morita [22] in Japan, much of it with large ground clearance and at relatively long distances. Some of the longest distances were measured by Battesti [83] at intermediate ground clearance in France. It is convenient to use a measure of terminal ground clearance as Morita [22], defined by the sum of antenna terminal heights above ground level divided by two:

$$\bar{h} = \frac{h_1 + h_2}{2} \quad (3.22)$$

This factor, together with the length of the link, is a rough measure of the clearance at the center of the path. Morita [22] has given the average antenna height and path length for many of the links used in his measurement. Morita's [22] links are shown in circles in Figure 3.10. Similarly, the Battesti [83] links are shown as crosses and the Barnett [23] links as squares.

These three sets of worst month-month data, as measured with a short time constant, differ considerably. It is convenient to compare them at the distance and frequency where a full Rayleigh statistic is produced. This level of fade is manageable by realizable transmitters and receivers. Moreover, at this level the usual diversity improvement is meaningful because not much ducting is usually present. The Morita [22] measurements have been approximated empirically by :

$$P_R = Q5.1 \times 10^{-9} (F/4)^{1.5} D^{3.5} \quad (3.23)$$

Where;

P_R = actual fade probability divided by the probability of obtaining a Rayleigh fade.

Q = terrain factor being 0.4 for mountains, 1.0 for plains, and $72/\sqrt{h}$ for sea or coastal areas.

F = frequency in gigahertz.

D = distance in kilometers.

Figure 3.11 shows the distance and frequency where Rayleigh fade is reached ($P_R = 1$). Similarly, the Barnett [23] measurements have been approximated by an empirical equation [84] which is rewritten here below in metric units for the worst month as:

$$P_R = a 2.4 \times 10^{-6} (F/4) D^3 \quad (3.24)$$

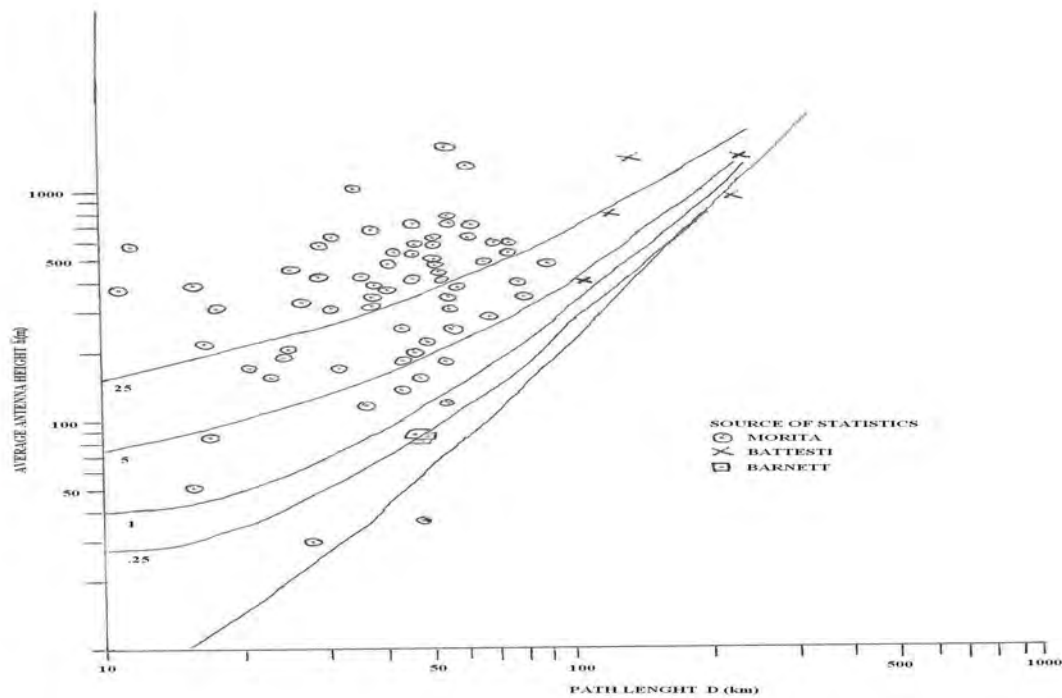


Figure 3.11 Path Length and average antenna height for which fade statistics have been measured [30]

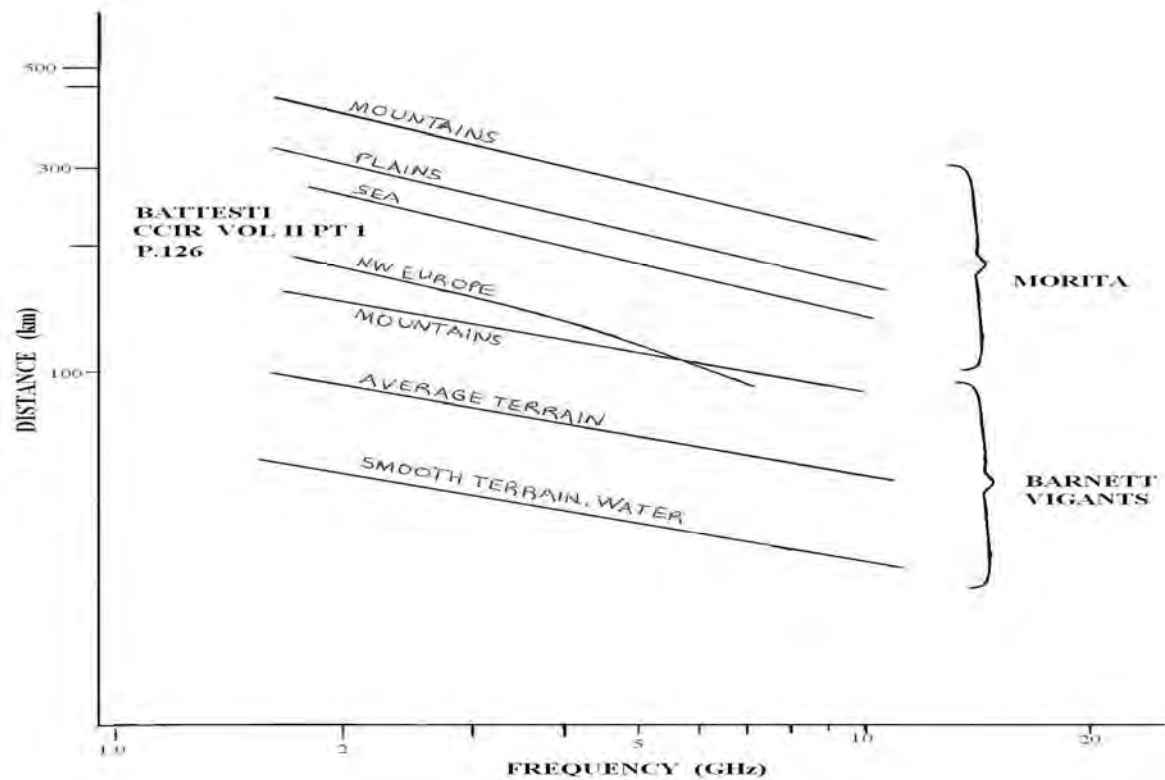


Figure 3.12 Distance at which Rayleigh fade is attained from three sources of data [30]

where a is a terrain factor being $1/4$ for mountains, 1.0 for average terrain, and 4 for smooth terrain including water. The Battesti data has not been written in this form but can be read graphically from [85]. Figure 3.12 also shows where both the Battesti and Barnett data reach a full Rayleigh fade.

3.5.8 The A. Vigants Model (USA)

Vigants in his model presented space-diversity engineering which encompasses estimation of fading, determination of the need for protection from transmission availability objectives, and calculation of the antenna separation needed to obtain the required transmission availability. In his description of fading, Vigants stated that the RF power received after transmission over a microwave radio hop is never absolutely constant; even at noon, when the atmosphere has “stabilized,” there can be fractional dB excursions (scintillations recurring a few times per second), as well as slower excursions of a dB or two [24]. During fading, the received RF power can be practically zero for seconds at a time. The terminology to describe this is shown in Figure 3.13 through an example in which the free space value is -30dBm and a single, idealized fade decreases the received power temporarily to -80dBm ; levels in dB relative to normal are denoted by $20\log L$. The time during which a signal is below a particular reference level is called the duration of fade of that level (the duration of a 40-dB fade is

illustrated in Figure 3.13) [24]. Average durations of fades are independent of microwave frequency and are proportional to L. Typical numerical values are given by [31]:

$$\langle t \rangle = 410 L \text{ seconds}, L < 0.1 \quad (3.25)$$

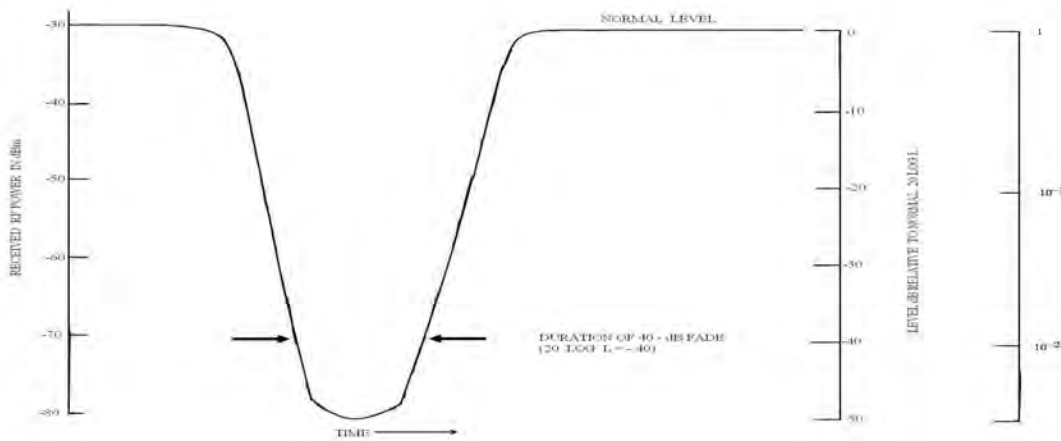


Figure 3.13 Definition of L and fade duration (- 30 dBm assumed normal as an example)[24]

The sum of the durations of all fades of a particular depth is called “time below level”. It is proportional to L^2 , since the number of fades is proportional to L, and its numerical values are given by [23]:

$$T = rT_0L^2, L < 0.1 \quad (3.26)$$

Where T_0 is the time period over which the summation of fade durations is made (a month, for example); the units of T are identical to that of T_0 (seconds are normally used). The fade occurrence factor r for heavy fading months is:

$$r = c(f/4)D^3 10^{-5} \quad (3.27)$$

where;

$c = 4$ over water and Gulf coast,
 $= 1$ average terrain and climate,
 $= \frac{1}{4}$ mountains and dry climate,
 f is frequency in GHz,
 and
 D is path length in miles.

The coefficient c in (3.27) incorporates the effect of both terrain and humidity and is adequate for first estimates of expected fading in many cases. Paths of identical climate but different terrain can be differentiated by introducing terrain roughness parameter [25]. This quantity shows that path over rough terrain experience fade less than paths over smooth terrain, because stable atmospheric layering is less likely to occur over rough terrain. Terrain roughness is calculated from terrain heights above a reference level (sea level, for example) obtained from the path profile at one-mile (1.6 km) intervals, with the ends of the path excluded. The standard deviation of the resulting set of numbers is the terrain roughness, denoted by w . Applicable values of w range from 20 feet (6.1 m) ("smooth") to 140 feet (42.7 m) ("rough"); values of 20 and 140 feet should be used when calculated values of w are less than 20 or larger than 140. Modified for roughness, the equations for c becomes:

$$\begin{aligned}
 c &= 2(w/50)^{-1.3}, & \text{coastal area,} \\
 &= (w/50)^{-1.3}, & \text{average climate,} \\
 &= 0.5 (w/50)^{-1.3}, & \text{dry climate,}
 \end{aligned} \tag{3.28}$$

where a roughness of 50 feet (15.25 m) has been defined as "normal."

3.5.9 The Space –Diversity Effect

During periods of multipath fading, deep fades of signals received on two vertically separated receiving antennas rarely overlap in time. The relatively few that do overlap give rise to simultaneous time below level (sum of durations of simultaneous fades, see Figure 3.14), which is proportional to L^4 and can be expressed as [32, 33, 86]:

$$T_s = T/I_0 \tag{3.29}$$

where T is the time below level of a signal received on the main antenna and I_0 is the available improvement, given numerically in practical units by the follow [33, 86]:

$$I_0 = 7 \times 10^{-5} v^2 s^2 f / DL^2, \quad s \leq 50 \tag{3.30}$$

where;

v = relative gain parameter (gain of secondary antenna relative to main antenna in dB is $20 \log v$),

s = vertical separation of receiving antennas in feet (or meters) , center-to-center,

f = frequency in GHz,

D = path length in miles (oo kilometers),

and

L = level parameter (level in dB relative to normal is $20 \log L$).

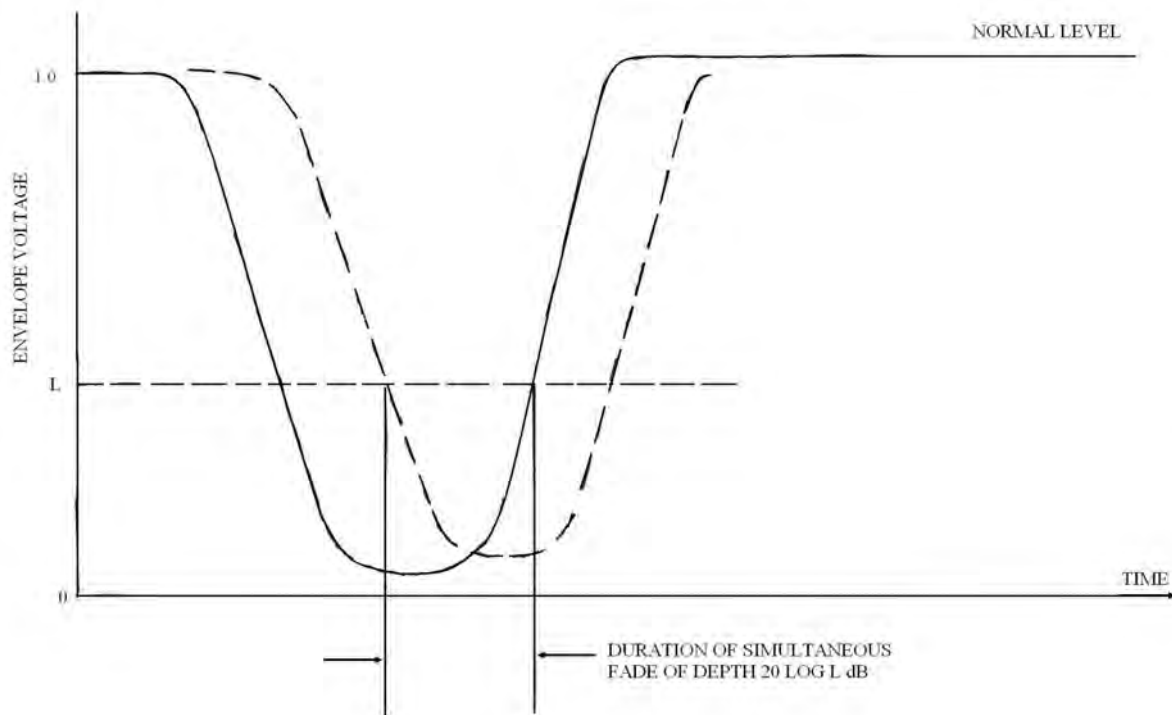


Figure 3.14 Definition of simultaneous fade [24]

Equation (3.30) applies only for the ranges of variables indicated on the nomogram in Figure 3.15. Extrapolation of the scales may lead to errors. For instance, under some conditions the increase in improvement due to an increase in separation over 50 feet may be small. Separations for which the available improvement is less than 10 should not be used; if possible, separations of at least 30 feet (9.2 m) should be used.

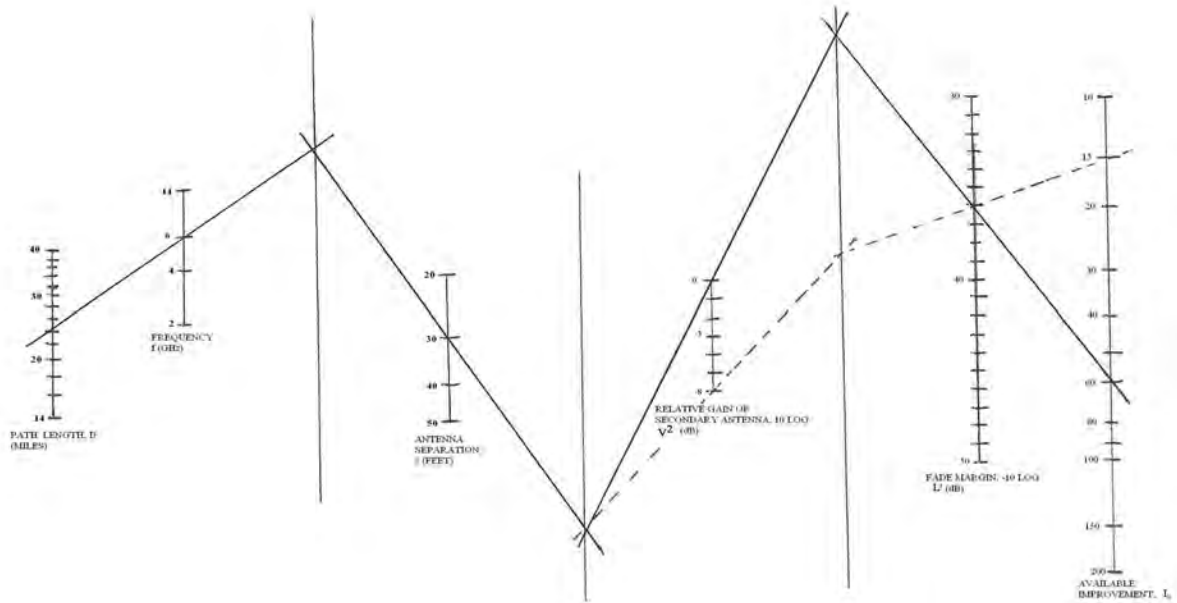


Figure 3.15 Nomogram for available improvement I_0 [24]

3.5.10 Comparison of Space and Frequency Diversity

Space diversity in its most common form provides a protection channel for every working channel (1×1 protection) on a per-hop basis. Frequency diversity usually provides one or two protection channels for m working channels ($1 \times m$ or $2 \times m$ protection) on the basis of switching sections that can contain as many as 10 hops in extreme cases. The most effective form of frequency diversity is 1×1 on a per-hop basis (which is restrict in use here at 4 and 6 GHz because of spectrum conservation); this can readily be compared to space diversity. For equal performance, the available improvements, I_0 , are equated. A convenient form for I_0 is:

$$I_0 = v^2 q L^{-2} \quad (3.31)$$

where for space diversity (from section.3.5.9);

$$q = 7 \times 10^{-5} s^2 f / D \quad S \leq 50 \quad (3.32)$$

and for frequency diversity;

$$q = 50 (\Delta f/f)/D \quad \Delta f < 0.5 \text{ GHz} \quad (3.33)$$

where f is frequency in GHz (4 or 6), and Δf is the difference of radio channel center frequencies, also in GHz ; D is the path length in kilometers. Values of separations in space and frequency providing equal performance (for antennas of equal size; $v^2 = 1$) are obtained by eliminating q from (3.32) and (3.33):

$$\begin{aligned} s &= 106 \sqrt{\Delta f} \quad \text{in the 4-GHz band} \\ &= 57.5 \sqrt{\Delta f} \quad \text{in the 6-GHz band} \end{aligned} \quad (3.34)$$

where s is in meters. A 9.2 m separation is equivalent to a Δf of about 0.08 GHz in the 4-GHz band and about 0.27 GHz in the 6 GHz band.

3.5.11 The Crombie Model (USA)

Crombie [34] in his approach published and analyzed data on the probability of multipath fading on different paths with lengths up to 45 km, at frequencies up to 37 GHz, measured in different countries [34]. In his analysis, Crombie [34] discovered that for paths which have probabilities greater than about 0.001% for 20 dB fades, the fading probability increases with antenna beam width. In addition, it is also found that increasing the clearance of the path above surrounding terrain reduces the fading probability. Crombie [34] affirms that inclusion of these two variables, in addition to frequency and path length, reduces the uncertainty in prediction of fading probability by a factor of 80 [34]. Barnett [23] and Ruthroff [87] developed a widely used model for predicting the probability of multipath fading as a function of path length and frequency, modifications of which have been adopted by the CCIR (now ITU-R) [88]. In the CCIR model, for fades greater than 15 dB, the probability $P\left(\frac{w}{w_o}\right)$, of a signal level less than w is given by [88]:

$$P\left(\frac{w}{w_o}\right) = KQ \frac{w}{w_o} d^B f^C \quad (3.35)$$

Where; d = path length (km)

- f = frequency (GHz)
- K = climate factor
- Q = terrain factor
- w = received signal power
- w_o = received power in non-fading conditions.

The formula in (3.35) may not be applicable for very small values of d [34]. Many values of B, C, K, and Q have been proposed for application in various parts of the world [88]. These values have been determined from analysis of empirical data. For example, the values of C range from 0.85 to 1.5; and B from 2.0 to 3.5. Values of the product K·Q show greater variability, and different functional forms have been used. In some cases, K·Q is identified as being dependent on the standard deviation of the terrain between antennas (measured at 1 km intervals) [24]. In other cases, K·Q is a function of the root mean square (RMS) value of the terrain slopes (in milli-radians) measured at 1 km intervals along the path [26].

Most of the empirical data used in defining B, C, and K·Q have been obtained at frequencies of 11 GHz or less. Crombie [34] in his approach has focused on obtaining a formula such as that shown in (3.35) which is applicable to frequencies of about 11 GHz or higher. Crombie also examined the possibility of eliminating the coefficients K and Q because of the great variability of the values suggested for these coefficients. Specifically, Crombie[34] investigated the effects of antenna beamwidth and of physical clearance of the center of the path above the ground. He investigated this in addition to the effects of path length and frequency. Thus Crombie[34] proposed a formula analogous to equation (3.35) as [34]:

$$P\left(\frac{w}{w_o}\right) = A\left(\frac{w}{w_o}\right) d^B f^C \theta^D h^E \quad (3.36)$$

Where A, D, E are constants, θ is a measure of antenna beamwidths, and h is the estimated height above the intervening terrain at the center of the path. The other symbols have the same meaning as in (3.35).

3.5.12 Data Used for Analysis

The data Crombie used for his model have been obtained from several sources. The primary source is the work of British Post Office [89]. This contains a very comprehensive set of long duration measurements at frequencies between 11 GHz and 37 GHz over path lengths ranging from 4 km to 58 km. Also used by Crombie[62] in addition to this is the earlier data obtained by the British Post Office on 11 GHz on two other paths [90]. Additional data obtained in the USA [23], Denmark [91], and Japan [92] were also used. The criteria Crombie[34] used in selection of data for analysis are:

- (i) Frequency of 11 GHz or greater.
- (ii) Antenna beamwidths known or obtainable.
- (iii) A measurable probability (of about 0.001%) for the worst month of fades ≥ 20 dB.
- (iv) Duration of measurements of at least one month.
- (v) No evidence that the terrain clearance would be less than 0.577 Fresnel zones when the effective earth radius factor k was $2/3$.
- (vi) Availability of path profiles.

The few available data that meet most of the highlighted criteria are listed in Table B.1 (see appendix B). Not all the criteria are met for some of the paths, but they are still included because of the need to maximize the data base for increasing the significance of the result; this data has been used for restricted models (however, data for three paths [89, 90] were omitted because the fading depth did not reach the 20 dB during measurements). The columns in Table B.1 contain the path number, path description, the % probability of fades of 20 dB or more, (P.01), for the worst month; the path length, d (km); the nominal frequency, f , in GHz; the nominal beamwidths, θ , in mR together with their geometric mean when not equal; and, reference to the source of the data.

3.5.13 Analysis of Data

Crombie [34] made an attempt to fit a limited equation of the type shown in (3.35) to the data of Table B.1 using linear regression. Equation (3.35) can be written as [34]:

$$\log P\left(\frac{w}{w_o}\right) = \log A' + \log (w/w_o) + B \log d + C \log f , \quad (3.37)$$

where the logarithms are base 10. The multipath fading probabilities shown in Table B.1 are for fades equal to or greater than 20 dB. Thus $\log (w/w_o)$ is a constant ($= -2$), and A' is a constant

representing the effective value of $K \cdot Q$ in (3.35) for all paths used. The terms in A and w/w_o can then be lumped together with:

$$\log A = \log A' + \log (w/w_o) \quad (3.38)$$

giving:

$$\log P(.01) = \log A + B \log d + C \log f \quad (3.39)$$

The data shown in Table B.1 was analyzed in three groups. The first group contains all the data. Information about the physical path clearances are missing for paths 14 – 16 (see appendix B). Thus, the analysis is confined to the effects of path length, frequency and beamwidths as discussed in sections 3.5.13(a) and 3.5.13(b). All the paths in this group, except two (i.e. paths 17 and 18 see appendix B) are believed to meet criterion (ii) of section 3.5.12. As a result, a further analysis is made in section 3.5.13(c) of the remaining 16 paths. Finally, analysis is made in section 3.5.13 (d) of the group of data (paths 1–13 together with paths 17 and 18) for which the physical clearance can be estimated. In that analysis, the effects of path clearance are included.

(a) Effects of Path Length and Frequency (All Paths)

Using information in the first three numerical columns of Table B.1 (see appendix B), the linear regression fit yields the coefficient values for A , B , and C shown in Table 3.6.

Table 3.6 Crombie Regression Results – All Paths, d , f , (Model 1) [34]

Coefficient	t	
$A_1 = -4.424$		$F_1 = 0.978$
$B_1 = 1.045$	1.31	$S_1 = 0.766$
$C_1 = 1.351$	1.11	$R_1^2 = 0.115$

where t and F are student's t and the variance ration statistics, respectively, and R is the multiple correlation coefficient. The fraction of the variation of $\log P(.01)$, which is due to regression, is equal to R^2 . Because there are two independent variables and fifteen degrees of freedom, the critical values of t and F for a 5% significance level are 2.13 and 3.68, respectively. Thus the regression is meaningless and the observed data cannot be represented by a model of the type shown in equation (3.35). A comparison between the predicted and measured fading probability is shown in Figure 3.16.

In addition to the use of the F statistic, a convenient means of visualizing the goodness of fit of the regression surface to the data is the standard error, s , given by [34]:

$$s = \sqrt{\sum_i (P_i - M_i)^2 / (n - k - 1)} \quad , \quad (3.40)$$

where M_i and P_i are measured and predicted values of $\log P(w)$ for the i^{th} path, n is the number of paths and k is the number of independent variables. With a large sample in which the residuals, $P_i - M_i$ are normally distributed, about 95% of the residuals will lie within $\pm 2s$ of the regression surface (measured in the P direction). These values of s are given for this and subsequent calculations.

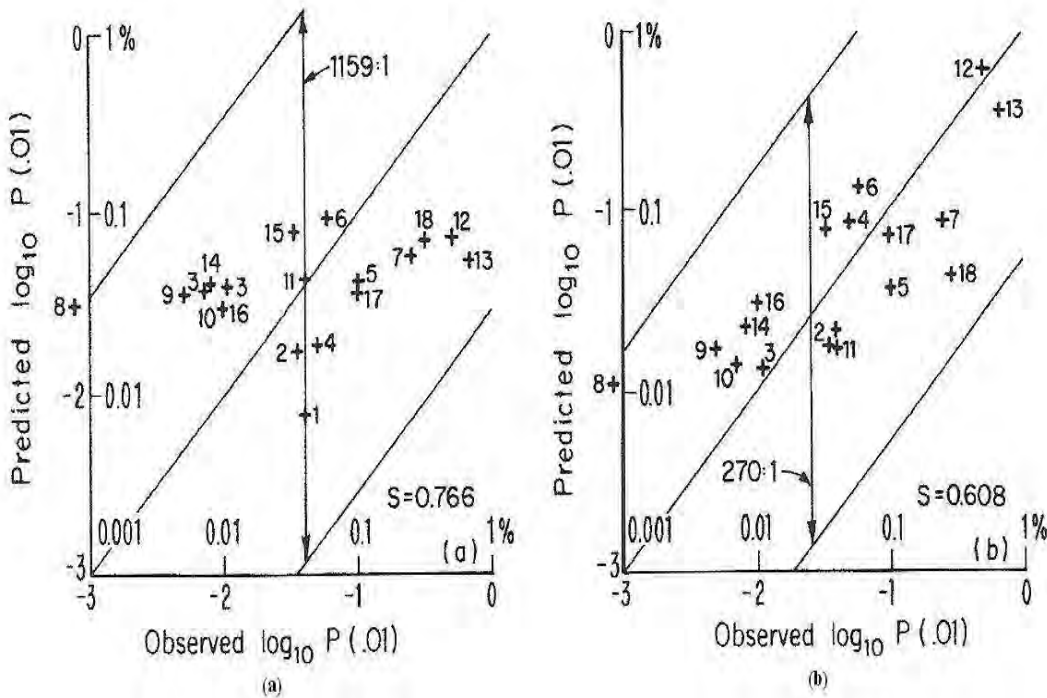


Figure 3.16 Comparison of observed and predicted probabilities of multipath fading ≥ 20 dB for all paths (a) d and f as independent variables (eq. 3.39, Table 3.6) (b) d , f , and θ as independent variables (Eq. (3.40), Table 3.7) [34]

(b) Effects of Antenna Beamwidth

Crombie investigated the effects of including antenna beamwidth, in view of the inadequacy of using only path length and frequency. The beamwidths of the antennas used on the various paths are listed

in Table B.1 (see appendix B), for both antennas on each path. For analysis, the geometric mean of the two beamwidths was used for the θ term of the new regression equation:

$$\log P\left(\frac{w}{w_0}\right) = \log A + B \log d + C \log f + D \log \theta \quad (3.41)$$

where $\theta = \sqrt{\theta_T \cdot \theta_R}$. The regression analysis yielded the results shown in Table 3.7 below.

Table 3.7 Crombie Regression Results – All Paths, d, f, θ (Model 2) [34]

Coefficient	t	
$A_2 = -10.162$		
$B_2 = 2.846$	3.32	$F_2 = 4.29$
$C_2 = 1.939$	1.97	$S_2 = 0.608$
$D_2 = 2.264$	3.12	$R_2^2 = 0.479$

With three independent variables and eighteen data sets, there are fourteen degrees of freedom. Thus, at 5% significance level, the critical value of t is 2.145 and F is 3.34. The overall regression is therefore quite significant (because $F_2 > 3.34$, see Table 3.7) even though the significance of the frequency coefficient is marginal.

(c) Analysis for Paths with Adequate Fresnel Zone Clearance

The data analyzed in section 3.5.13 (b) contain two paths [90] for which the Fresnel zone clearance (criterion No. V of section 3.5.12) may not always be achieved, although the physical clearance is known. Deletion of these paths yields a model for predicting the fading probability of paths with adequate Fresnel zone clearance. Analysis of the remaining data leads to the new set of coefficients shown in Table 3.8. Crombie [34] showed improvement on the fit by deleting the data for the two inconsistent paths as can be seen from comparing Tables 3.7 and 3.8 and Figures 3.16 and 3.17.

Table 3.8 Paths with Adequate Fresnel Zone Clearance – All Paths, d, f, θ (Model 3) [34]

Coefficient	t	
$A_3 = -12.230$		
$B_3 = 3.096$	4.88	$F_3 = 11.78$
$C_3 = 2.454$	3.42	$S_3 = 0.432$
$D_3 = 3.111$	5.53	$R_3^2 = 0.747$

In this case, there are three independent variables and twelve degrees of freedom. At the 5% significance level, the critical values of t and F are 2.179 and 3.49 respectively. As clearly shown in Figure 3.17b, the correlation is very marked, being significant at less than 0.5% level. Without the beamwidth term, the regression analysis (Figure 3.17 (a)) gives results which are very similar to those obtained for the whole data set. That is, there is no statistically meaningful dependence of fading probability on the path length and frequency [34].

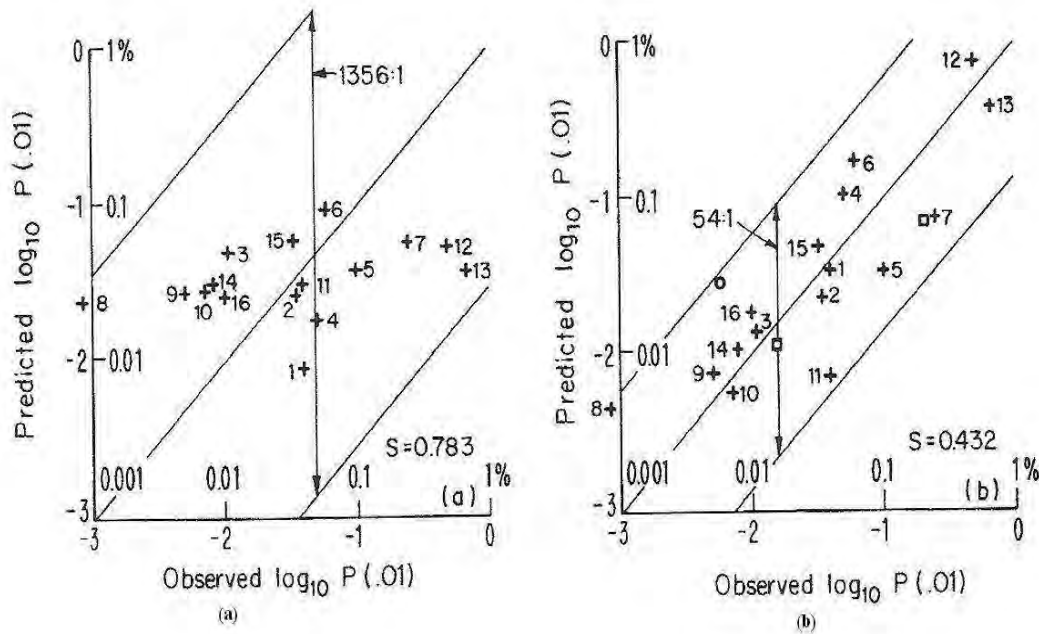


Figure 3.17 Comparison of observed and predicted probabilities of multipath fading ≥ 20 dB on paths with adequate Fresnel Zone clearance (a) d and f as independent variables (Eq. (3.39)) (b) d , f , and θ as independent variables (Eq. (3.40), Table 3.8)[34]

- + data from Table B.1 (appendix B)
- 11 GHz data from Lin [93]
- 11 GHz data from Butler [94]

(d) Effect of Physical Path Clearance

In view of the apparent importance of Fresnel Zone clearance stated above, the use of physical path clearance in some geographical areas, and other indications [30], Crombie did additional analysis using the path clearance term. In this case, the mean height, h , of the line-of-sight (assuming a $4/3$ earth radius) above the terrain at the center of the path was the variable used. This data was not available for paths 14, and 15, and the available data for path 16 was uncertain. As a result, these

three paths were omitted, leaving a total of fifteen paths and ten degrees of freedom. The new regression equation now becomes [34]:

$$\log P \left(\frac{w}{w_0} \right) = \log A + B \log d + C \log f + D \log \theta + E \log h. \quad (3.42)$$

The results of the analysis are shown in Table 3.9 and in Figure 3.17 (c).

Table 3.9 Paths with Known Clearance d, f, θ , h (Model 4) [34]

Coefficient	t	
$A_4 = -2.997$		
$B_4 = 2.487$	5.42	$F_4 = 20.18$
$C_4 = 0.840$	1.49	$S_4 = 0.298$
$D_4 = 1.190$	2.88	$R_4^2 = 0.889$
$E_4 = -2.440$	-5.89	

With four independent variables and ten degrees of freedom, the critical value of F at the 0.5% level is 7.34. Since the value calculated in Table 3.9 above (i.e $F_4 = 20.18$), is much greater than 7.34, the regression is even more significant. The statistical significance of each variable, except f, is also high [34]. Deletion of the fourth variable, h, gives the result shown in Tables 3.10 and Figure 3.17 (b) below.

Table 3.10 Paths with Known Clearance d, f, θ (Model 5) [34]

Coefficient	t	
$A_5 = -9.988$		
$B_5 = 2.931$	3.21	$F_5 = 3.78$
$C_5 = 1.860$	1.72	$S_5 = 0.635$
$D_5 = 2.171$	2.84	$R_5^2 = 0.507$

In this case, Crombie [34] used fifteen data sets and three independent variables giving eleven degrees of freedom. The critical value of F at the 5% level of significance is then 3.59 and the overall regression is thus significant at this level. The goodness of fit is, however, materially worse than that obtained when clearance is included. Removal of the third variable, θ , yields similar results to those obtained previously – in the absence of any significant correlation, as shown in Figure 3.18 (a).

Figure 3.18 also shows that inclusion of θ and h , in the regression equation, reduces the range of uncertainty in the predictions by a factor of about 80.

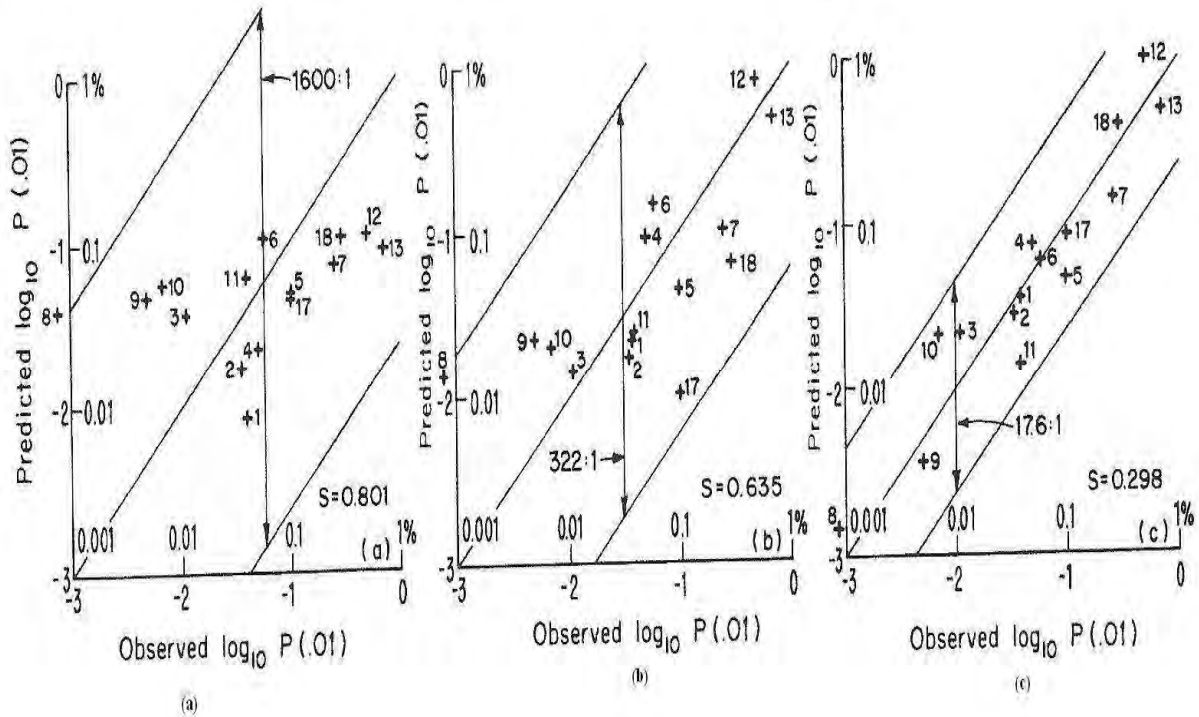


Figure 3.18 Comparison of observed and predicted probabilities of multipath fading ≥ 20 dB for paths with known physical clearance (a) d and f as independent variables (Eq. (3.39)), (b) d , f , and θ as independent variables (Eq. (3.41), Table 3.10), (c) d , f , θ , and h as independent variables (Eq. (3.42), Table 3.9) [34].

3.5.14 Summary of Crombie Model

The analysis discussed in Crombie’s [34] model suggests that multipath fading probability (on terrestrial paths at frequencies above 11 GHz) can be estimated without detailed knowledge of climate or terrain. Crombie [34] stated that such estimates require knowledge of path clearance and/or antenna beamwidths, in addition to path length and operating frequency. Without clearance and bandwidth information, as shown in Figs. 3.16(a), 3.17(a) and 3.18 (a), no meaningful correlation of fading probability with path length and frequency is found, using the data in Table B.1 (see appendix B). This data covers a wide range of operating frequencies and path lengths in several countries. Fading probability predictability increases when antenna beamwidths is included in Crombie’s analysis as shown in Figs. 3.16 – 3.18. Inclusion of path clearance shows (see Figs. 3.18 (a) and (b)) a further increase in predictability. In these two cases, the percentage of time for which multipath fading ≥ 20 dB, occurs in the worst month can be expressed in the following forms [34]:

Model 5 (variables used in analysis are d, f, θ) : $R = 0.71$

$$\begin{aligned} \text{Log } P(.01) &= -9.99 + 2.93 \log d + 1.86 \log f + 2.17 \log \theta \\ \text{or} \\ P(.01) &= 10^{-10} \cdot d^{2.93} \cdot f^{1.86} \cdot \theta^{2.17} \end{aligned} \tag{3.43}$$

Model 4 (variables used in analysis are d, f, θ, h) : $R = 0.94$

$$\begin{aligned} \text{Log } P(.01) &= -2.997 + 2.49 \log d + 0.84 \log f + 1.19 \log \theta - 2.44 \log h \\ \text{or} \\ P(.01) &= 10^{-3} \cdot d^{2.49} \cdot f^{0.84} \cdot \theta^{1.19} \cdot h^{-2.44} \end{aligned} \tag{3.44}$$

These formulas, and others developed above in Crombie analysis represent the behaviour of the paths described in Table B.1 (appendix B) fairly well. Thus the formula should be applicable to other paths having similar characteristics to those used in Table B.1 of appendix B.

3.5.15 The R.L. Olsen and B. Segal Approach (North America and Canada)

In this section, two methods are proposed for predicting the deep fading range of the average worst-month multipath fading distribution on line-of-sight links in the upper VHF, UHF and SHF bands in Canada.

3.5.16 Method for Initial Planning and Licensing Purposes

This method is for predicting the large fade depth range of the fading distribution for the average worst month. It should be used for planning and licensing purposes or when the path profile is not known. The step-by-step procedure of the method is as follows (see Olsen *et al* [95]):

For the path location in question, obtain the logarithmic geoclimatic factor G (in dB) for the average worst month from the map in Figure 3.19. This map shows contours of constant G , as well as estimated values for 47 radiosonde sites in Canada and adjacent parts of the United States. An approximate value for the path can be estimated by interpolation. If the path is above 60° latitude, add 5 dB to the value obtained from the map.

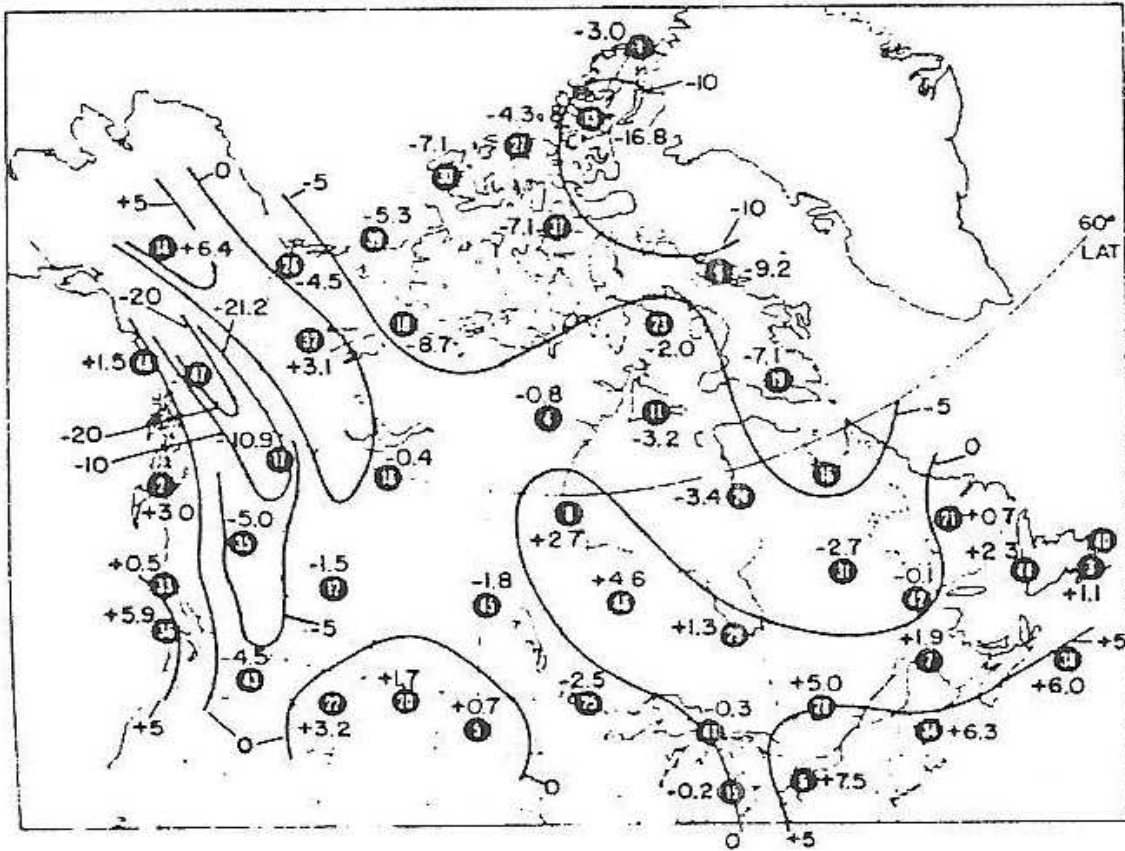


Figure 3.19 Contour map indicating logarithmic geoclimatic factor G for Canada [95]

If the path is over a medium-size body of water (see Figure 3.20), add 6 dB to the value of G obtained from the map (i.e. 5 + 6 dB above 60° latitude). Finally, if the path is over a large body of water, particularly one for which there are no adjacent hills that might give rise to duct-inhibiting turbulence (see Figure 3.20), add 14 dB to the value obtained from the map (5 + 14 dB above 60° latitude). In cases of uncertainty as to the size of the body of water in question, a 10 dB correction factor could be employed [95].



Figure 3.20 Map of Canada Showing Different Water Bodies and Provinces [96]

If the transmitting and receiving antenna heights, h_e and h_r (in meters above some reference height such as mean sea level), are known for the path length d (km), calculate the magnitude of the path inclination $|\epsilon_p|$ in milliradians from :

$$|\epsilon_p| = 1000 \text{Arctan} \left[\frac{h_r - h_e}{1000d} \right] \approx |h_r - h_e| / d \quad (3.45)$$

If the antenna height difference has not yet been established, assume $|\epsilon_p| = 0$ or some other appropriate value. Next calculate the percentage of time, P (%), that fade depth A (dB) is exceeded in the average worst month from the power-law expression:

$$P = Kd^{3.6} f^{0.89} (1 + |\epsilon_p|)^{-1.4} \cdot 10^{-A/10} \quad (3.46)$$

where K is the geoclimatic factor given by:

$$K = 10^{((G/10)-5.7)} \quad (3.47)$$

and;

$$G = 10 \log K + 57 \quad (3.48)$$

G is the logarithmic geoclimatic factor value for Canada obtained from the contour map of Figure 3.19 as stated earlier. Equation (3.46) was developed using data for path lengths in the range of 7.5 to 9.5 km, and frequencies in the range of 2 to 37 GHz.

3.5.17 Method Requiring Path Profile

This method is best suited for link design applications. In addition to the path length, d (km); frequency, f (GHz); and path elevation angle, ε_p (mrad), it requires that the grazing angle, ϕ (mrad), of the wave specularly reflected from the “average” path profile be known. This necessitates the availability of the actual path profile. It should be noted that Olsen[95] in his approach has incorporated the grazing angle parameter to cater for the effect of the terrain surface roughness used in Vigants approach [24] and average path height in Morita [22] approach. The step-by-step procedure is as follows:

Obtain the logarithmic geoclimatic factor G as discussed in section 3.5.16, including the over-water and/or Arctic correction factors if required. Also obtain the magnitude of the path inclination, $|\varepsilon_p|$ (mrad), as discussed in the same section.

From the profile of the terrain along the path, obtain the terrain heights, h , at intervals of 1 km, beginning 1 km from one terminal and ending 1 km to 2 km from the other. Using these heights, carry out a linear regression with the “method of least squares” to obtain the linear equation of the “average” profile:

$$h(x) = a_0 + a_1 x \quad (3.49)$$

where x is the distance along the path from the transmitter. The coefficients a_0 and a_1 can be calculated from the relations [97]:

$$a_0 = (\sum h - a_1 \sum x) / n \quad (3.50)$$

$$a_1 = \frac{\sum xh - (\sum x \cdot \sum h)/n}{\sum x^2 - (\sum x)^2/n} \quad (3.51)$$

where $\sum h$ is the sum of the height profile samples, and $\sum x$ is the sum of the distance samples. The summations are over the number, n , of profile height and distance samples. From (3.49), calculate $h(0)$ and $h(d)$, the heights of the average profile at the ends of the path, and the heights of the antennas above the average path profile:

$$h_1 = h_e - h(0) \quad (3.52a)$$

$$h_2 = h_r - h(d) \quad (3.52b)$$

For paths where the point of specular reflection is fairly obvious (such as on paths over water, partially over water, or partially over flat, level terrain), the height above the reflecting surface should be used for h_1 and h_2 . Also, on paths where a rigid application of the regression interval indicated above (i.e. to within 1 km of the ends of the path) would give obvious errors in the calculation of the “average” grazing angle (even though it is known to apply statistically [21]), it is suggested that a smaller regression interval over the path be chosen. On long paths, an increase in the profile sample distance to 2 km or more might be acceptable. If the path is so rough that it is obvious the main wave interaction with the ground would be one of diffraction from irregular mountain peaks rather than reflection from relatively flat surfaces, it may be meaningless to attempt to determine an appropriate value for the average grazing angle. For such a path, it is suggested that the first method be applied and that the value of G estimated from the map be reduced by 2 dB.

Next, calculate the “average” grazing angle ϕ (mrad), corresponding to a 4/3-earth radius model for refraction (i.e., $a_e = 8500$ km) from [35, 95]:

$$\phi = \frac{h_1 + h_2}{d} \left[1 - m(1 + b^2) \right] \quad (\text{mrad}) \quad (3.53)$$

where

$$m = \frac{d^2 10^3}{4a_e(h_1 + h_2)} \quad (3.54)$$

$$c = \frac{|h_1 - h_2|}{h_1 + h_2} \quad (3.55)$$

$$b = 2\sqrt{\frac{m+1}{3m}} \cos\left[\frac{\pi}{3} + \frac{1}{3}\text{Arcos}\left(\frac{3c}{2}\sqrt{\frac{3m}{(m+1)^3}}\right)\right] \quad (3.56)$$

Assume a minimum value for ϕ of 1 mrad. In calculation of the coefficients m and c , the variables a_e , d , h_1 and h_2 must be in the same units. The grazing angle ϕ will be in the desired units of milliradians if h_1 and h_2 are in meters and d in kilometers.

Finally, calculate the percentage of time, P , that the fade depth, A (dB), is exceeded in the average worst month using equation (3.57) below.

$$P = Kd^{3.3}f^{0.93}(1+|\varepsilon_p|)^{-1.1}\phi^{-1.2}\cdot 10^{-A/10} \quad (3.57)$$

where K is the geoclimatic factor given by;

$$K = 10^{((G/10)-4.6)} \quad (3.58)$$

$$\text{and } G = 10\log K + 46 \quad (\text{dB}) \quad (3.59)$$

The minimum ranges of variables over which equation (3.57) should apply is the same as those indicated in equation (3.46) with the addition of the range $\phi < 14$ mrad [21]. It should be noted that the latest revision of the ITU recommendation on the above subject has incorporated and embedded in equations (3.57) the grazing angle ϕ . By virtue of this latest revision, equations (3.57) now becomes (see [17]):

$$P = Kd^{3.2}\left(1+|\varepsilon_p|\right)^{-0.97} \times 10^{0.0032f - 0.00085h_L - A/10} \% \quad (3.60)$$

Where f is the frequency (GHz), h_L is the altitude of the lower antenna (i.e. the smaller of transmitter antenna altitude h_e and receiving antenna altitude h_r), and K is the geoclimatic factor.

3.5.18 Limitation and Accuracy of the First and Second Methods

Estimated means, standard deviations and maxima of prediction error for both methods are given in [95] for different groups of data. These were obtained from the differences between the predicted and observed values of G (see Table C.1(a) – (d) in appendix C). The grouping of overland links outside the two reference regions (Ottawa and Prince George) was included because it gives some measure of how well the “two-region fit” applies to overwater links in other temperate regions of the country. The grouping of all southern links does somewhat the same thing, but includes the result for the three over-water links which contain the 6 dB correction for links over medium-sized bodies of water.

The grouping for mountainous links in British Columbia includes the five reference links in Prince George area (see link nos.12-16 in Table C.1(b) in appendix C) , those in Salmo region (see link nos. 17 -19 in Table C.1 (b) – (c) in appendix B) and those in the Hope region (see link nos. 20 – 21 in Table C. 1(c) in appendix C). The lower standard deviations for the first method with respect to the second method, and for mountainous links with respect to all overland links (see Table 3.11), cannot be considered as statistically significant because of the small number of links involved. However they do suggest that the predictions for mountainous links should be as accurate as, or at least not significantly less accurate than, predictions for links over flatter terrain.

The results for the grouping of over-water paths show the effect of the respective 6 and 14 dB corrections for medium-sized and large bodies of water. Since seven of these paths are in the Arctic (see link nos. 26-33 in Table C.1(d) in appendix C), they also include the effect of the 5 dB correction for paths above 60° latitude. However, since the correction was derived from these results, they cannot be considered a true test of accuracy of the over-water correction. Additional results for an independent set of over-water links would likely show larger errors, but these could then be used to improve the over-water correction.

Again, since the correction factors were based on the results themselves, the results cannot be considered as a true measure of the accuracy of both methods in the Arctic. However, the fact that the mean error for the group of paths in the vicinity of Hudson Strait (see Figure 3.20) is close to that for the group in Viscount Melville Sound (see Figure 3.20) and the fact that the uncorrected G values for these two groups of paths based on radiosonde data are almost identical, lend some confidence to the prediction for over-water paths in the Arctic. Since there are no results yet for overland Arctic paths, the 5 dB correction factor (which was based on the results for three links in or at the entrance to Frobisher

Bay (see Figure 3.20) using the 6 dB correction for links over medium-sized bodies of water) remains to be fully tested.

Table 3.11 Summary of mean (m), standard deviation (s), and maximum (max) of prediction errors* (in dB) for various groupings of links [95]

Link Grouping	No. of Links	Method 1			Method 2		
		m	s	max	m	s	max
All links	33	-0.1	5.0	16.4	0.1	5.5	12.2
Reference**	15	0.4	3.9	8.1	0.0	4.1	7.2
Overland ⁺ , not including reference	6	0.6	5.1	11.4	-1.4	7.0	6.2
Overland ⁺	21	0.5	4.3	11.4	-0.4	4.8	7.2
Southern ⁺	24	0.8	4.2	11.4	-0.1	4.7	7.2
Mountainous	10	3.1	3.3	7.0	-0.1	3.9	5.2
Over-water	11	-1.2 (-8.6)	6.1 (7.8)	16.4	0.4 (-10.0)	7.1 (8.4)	12.2
Arctic	8	2.9 (-10.8)	7.0 (8.2)	16.4	0.1 (-11.9)	7.5 (8.7)	12.2
*	Predicted minus observed value of G.						
**	Includes all links in Ottawa area (excluding Kemptville-Avomore “near grazing” Link).						
+	Excluding Kemptville-Avomore “near grazing” link.						
Note:	Means and standard deviations using uncorrelated values of G indicated in parenthesis.						

A comparison of the standard deviations of error of 4.8 and 4.3 dB on overland links for both methods, respectively, with the corresponding values of 3.4 and 2.9 dB for the 47 overland links in France and the UK [21] might suggest that some accuracy has been lost in “transporting” the basic prediction equations to Canada. However, it must be remembered that the Canadian figures are all based on a mixture of one-year worst-month fade depths, whereas the European figures are based on a mixture of one-year statistics and averages taken over two, three and four years.

Such a mixture will inevitably reduce the standard deviation of error, since a finite but unknown component of the error is due to year-to-year statistic variability and not to intrinsic errors in the prediction equations. Furthermore, the proportion of unusual paths (i.e. very short or very rough) is

larger in the Canadian data base. Considering that the predictions for six of the 21 overland paths are also based on geoclimatic factors scaled from refractivity gradient data, it is satisfying that the errors are as small as they are.

The British-French paths on which the model coefficients were based had an average clearance at midpath of 106m (standard deviation of 70m) and average clearance to dominant obstacles of 31m under 4/3-earth refractivity conditions. Although the ϕ variable in the second method allows accuracy to be maintained over large clearance ranges, some inaccuracy is introduced when clearances are outside the range in the data base.

3.5.19 Approach of T. Tjelta, T.G. Hayton, B.Segal , E. Salomen, R. Olsen. and L. Martin (Western Europe)

Over recent years much effort has been directed into analyzing the clear-air climatic variables that could be suitable for radiowave prediction purposes [3]. A ten year set of radiosonde data from meteorological observation have been studied in [98]. Numerical atmosphere models have also provided useful insight into propagation on a limited scale [16]. Initial correlations between multipath data and both the old and new radiosonde data showed that there was scope for deriving better predictor variables from the climatic data source [99]. Multipath fading time series in particular proved to be highly correlated with large negative gradients in the lowest part of the atmosphere as described by the numerical model [16]. This study [100] presents the results of correlation and multiple regression analyses using the most recent and largest multipath fading data base available yet and the new climatic information on a worldwide scale. It shows that a linear combination of up to six climatic variables from all available sources can be used. This has been shown [100] to be successful for predicting the multipath fading distribution for the average worst month [100]. Tjelta *et al* in their second approach, present the results of an extensive systematic analysis of average worst month multipath fading data for 47 overland links in France and the United Kingdom [21].

3.5.20 Correlation of Multipath Occurrence Parameters Derived from radiosonde, Surface Stations and Numerical Atmospheric Model

This section gives the results of correlation and multiple regression analyses using the most recent and largest multipath fading database yet available and the new climatic information on a worldwide scale.

It shows that a linear combination of up to six variables from all available sources for predicting the multipath fading distribution for the average worst month is possible. The propagation data used in this approach have been collected over several years from measurement results published since the late fifties until present.

The tail fade, $A_{0.01}$ (dB) describes the deep-fade range of the distribution, which on average follows a Rayleigh-slope of 10 dB/decade. The point at the highest percentage from the straight portion of the tail is called the first tail point [17] and is used in the analysis, but transferred or normalized to 0.01% of the time. The data available for describing the radioclimatic conditions were derived from standard meteorological measurements and numerical models. On a worldwide scale there seems to be currently three sources of interest: radiosonde measurements, surface measurements and results from numerical atmosphere models, the latter containing a mixture of measured and predicted data.

A large number of variables have been investigated over the years. Those used in the current ITU prediction method are included in this approach along with new candidates describing the terrain and climate. The variables are described below in three groups depending on how they are derived: link variable, terrain variable and radioclimatic variables.

Link variables: The only variable that has been used since the first prediction method was developed in the late fifties is the path length d (km). It has defended a place in the prediction methods since. Frequency f (GHz) was added at a later stage, in practice when new frequency bands were introduced. Path inclination is defined as the angle the line between transmitter and receiver antennas forms with the horizontal plane, $\varepsilon_p \approx (h_r - h_t)/d$ (mrad). The lower terminal (antenna) height h_t (m) is measured from sea level.

Terrain Variables: The roughness parameters S_t and S_a (m) are defined as the standard deviation of all heights in an approximately 110×110 km² square area centered at the midpath of the radio link. The subscript t or a denoted calculation based, respectively, on the terrain data alone and on all data (including sea surface). The digital terrain data have a resolution of about 1 x1 km. The fraction of terrain from this area, denoted by r_t ranges from 0 to 1, becoming larger the more land there is in the square. Several regional methods use path profile roughness. However it was recently found that measures of area roughness are better predictor than the simpler roughness derived from the path profile [101].

Radioclimatic Variables: The radioclimatic variables all make use of the refractivity N. Three different sources of data have been used: radiosonde observations, surface measurements and data from numerical modeling of the atmosphere. For the actual analysis, the predictor variables are refractivity gradient statistics, duct variables and variables related to the refractivity at the surface of the earth. The refractivity gradient variable β_o is defined for the lowest 100 m of the atmosphere as the occurrence of dN/dz values equal or less than -100 N-units/km with $dz = 100$ m. Neither radiosondes nor numerical atmosphere models give N values exactly at 100 m, but the values at ground are available. To obtain the values at 100 m, linear interpolations were used for radiosondes. For the numerical model only, the first altitude was employed giving a separation of about 65 m.

Multiple regression models

A systematic approach combining multiple regressions with correlation on residual errors provides a means of finding the best combination of variables. In the multiple regressions, the normalized tail fade depth $A_{0.01}$ is the dependent variable;

$$A_{0.01} = a_0 + \sum_i a_i F(x_i) \quad (3.61)$$

where the sum of $F(x_i)$ represents a selection among the independent variables, and the a_i 's are the regression coefficients. The first model is simply the average of $A_{0.01}$, with no independent variables. Once a model is derived, its residuals are correlated with the potential new variables. The variables having the highest correlation are then combined with the earlier variables in the multiple regressions. The detailed result of the regression analysis using (3.61) is given in [100]. Eleven variables were used in the multiple regression analysis, six variables are derived from clear-air climatic data and five from the link itself and the surrounding terrain.

3.5.21 Systematic Development of New Multivariable Techniques for Predicting the Distribution of Multipath Fading on Terrestrial Microwave Links

In this approach, multipath fading data obtained from 47 terrestrial microwave line-of-sight links in France and the United Kingdom are analyzed to derive narrow-band prediction equations for the deep

fading range of the cumulative distribution for the average worst month. A large number of possible predictor variables based on typical radio link parameters are investigated in their approach and equations are developed which reduce the standard error of prediction to less than half that of the previous techniques for this part of Europe.

Generalized Prediction Equation

In their analysis, the earlier power law equations [21] are generalized to:

$$P = K_g \prod_i F_i^{\alpha_i}(x_i) \cdot 10^{-A/10} \quad (3.62)$$

where the F_i are appropriate functions of the variables x_i . Linear multiple regressions [97] is employed to obtain the best values of the exponent α_i . For such calculations, it is more convenient to work with the logarithmic form:

$$A = G + a_0 + \sum_i (a_i \log[F_i(x_i)]) - 10 \log(P) \quad (3.63)$$

Where $a_i = 10\alpha_i$ and $G + a_0 = 10 \log(K_g)$. Here it is assumed that the a_i 's are fixed over the entire region of the database and that G is a geoclimatic factor that in general varies within this region. In some cases, $F_i(x_i) = x_i$ are employed in the regression. In cases where functions F_i are used, they are obtained by a combination of physical intuition and trial and error, the least systematic aspect of the overall procedure, but perhaps one for which there is no alternative. Although it might be desirable to use functions of the x_i that give physically reasonable behaviour as the $x_i \rightarrow 0$, this has been found to not always be essential in order to obtain empirical equations that give good results down to fairly small values of x_i . For some variables, or functions of variables, regressions are carried out both with $W_i = \log(F_i)$ and $W_i = \log(10^{F_i}) \equiv F_i$ as the regression variables.

Calculation of the Geoclimatic Factor

In order to obtain the geoclimatic factor G using a finite amount of fading data, it is assumed that this factor is a constant G_j within geographical zones smaller than the overall region (the index j denoting the zone), each zone containing several of the experimental links. The G_j and the regression coefficients a_i are obtained by an "iterative multiple regression" on

$$A_{0.01} - G_j = a_0 + \sum a_i W_i(x_i) \quad (3.64)$$

In equation (3.64), $A_{0.01}$ is the fade depth at 0.01% of the time. This is done by setting all $G_j = 0$ in (3.64) and performing the first regression. The mean prediction errors are then computed for all the links in each zone, and these values are given to G_j . A new regression is done with $A_{0.01} - G_j$ as the dependent variable. For each additional regression the mean prediction errors for the links within each zone are added to the previous values of G_j . This is continued until the mean errors are negligible in each geoclimatic zone, allowing the final values of G_j to be interpreted as zonal geoclimatic factors.

Predictor Variable Selection

The initial selection of variables is based on both physical intuition and historical considerations (e.g., the use of d, f, and s). However, once the initial variables are selected for consideration, a systematic procedure involving partial regression and correlation on regression residuals is employed to determine the best combinations of these variables.

Procedure for the Selection of the Predictor Variables

(a) Distribution Slope

The prediction equations for the distribution tail are based on the assumption of “Rayleigh type” fading for small percentages of the time, with a distribution slope of 10 dB/decade. A mean distribution slope of 10.2 dB/decade was calculated for the 38 links for which both tails points were available. The estimated standard deviation is 1.5 dB, giving 95% confidence limits of ± 0.5 dB/decade (i.e. twice the standard error). The fairly large standard deviation, however, indicates quite a large variation in the sample distribution slopes at the lowest probabilities.

(b) Choice of Geoclimatic Zones

The links were grouped into eight geoclimatic zones with the number of links in each zone varying from four to eight. The four zones in the UK were chosen under the constraint of geographical proximity of links and are identical to those used by Doble [26]. Although other four-zone groupings of

links in the UK were investigated, this was found to be the most reasonable grouping in terms of minimizing the errors for the prediction models considered.

(c) Correlation Analysis

From the correlation analysis, the results for nine single variables or group of variables are presented. These variables are: path length, frequency, beamwidth, terrain profile roughness, clearance, path and terrain inclination, grazing angle, height above sea level, and relative reduction in combined antenna directivities in the direction of the specular reflection point. Some groups include several variables that are closely related. As seen in [21] the variables in general cannot be assumed to be statistically independent since several pairs have a large correlation coefficient. This includes path length, frequency and terrain roughness, not a completely surprising result since the experiments from which the data were obtained were not designed to minimize such correlation.

(d) Regression Analysis

Results were given in [21] for multiple regression models from one to six variables. In addition, the results of several standard statistical tests on each model are presented. The goodness of fit is best indicated by the standard error of regression σ . The overall statistical significance of each model is indicated by the values of the variance ratio statistic F and the multiple determination coefficient R^2 (or multiple correlation coefficient R). The statistical significance of the individual variables in a model is indicated by the values of the Student's t statistics. With a large enough sample in which the residual errors (predicted minus measured fade depths) are normally distributed, about 95% of measured fade depth will lie within $\pm 2\sigma$ of the predicted fade depths. For a given number of variables, the higher the value of F in relation to the critical value of 95% confidence, the more statistically significant is the overall regression. For any number of variables, this is also true the closer R^2 approaches 100%. For any variable in a model, the larger the value of $|t|$ statistic in relation to the critical value $|t|_{95\%}$ for 95% confidence that its regression coefficient is not zero, the more statistically significant is that variable.

3.5.22 Limitation of the Approach

Despite the marked success of the approach described in this sub-section, further analysis would be desirable to refine the prediction techniques even for North West Europe. These should include:

- Analysis of data for mountainous and overwater paths in addition to that for a larger number of paths in flat and hilly terrain,

- correlation and regression analysis of grazing angles for path profile segments that are believed to be most highly reflecting and
- correlation and regression analyses of meteorological variables.

In particular, analyses are required on data for other parts of the world.

3.6 Clear-Air Diffraction Fading Techniques by different Authors

3.6.1 The M.S. Wheeler Approach

Clearance of the direct line of sight is provided against varying atmospheric refraction down to an effective earth radius factor of $k = 0.67$. The author in [84] recommends that a Fresnel zone clearance of 0.3 should be provided down to $k = 0.67$ for a wideband, high reliability system. For comparison, CCIR (now ITU-R) [85] indicates that a 0.6 clearance down to $k = 0.7$ is used in the United States and the United Kingdom. With respect to water reflections, the path would ideally be free of water-like reflection for a range of k from 0.67 to ∞ (i.e. $2/3$ to flat earth). When these methods, applicable to short paths, are used for the design of longer paths, however, the requirements for the range of k are less severe, because the extreme refractive conditions tend to be localized, and affect only a small part of a long path at any particular time. Typically, a path that is designed for $k = 0.67$ at 27 km, becomes effectively $k = 1.0$ at 200 km. This information for minimum effective k from CCIR [85] is reproduced in Figure 3.21 together with an algebraic approximation. Similarly, on a long path, the maximum effective k is reduced for the same reason. Battesti and Baithias [83] suggest using merely the normal $k = 4/3$ for path work at 240 km.

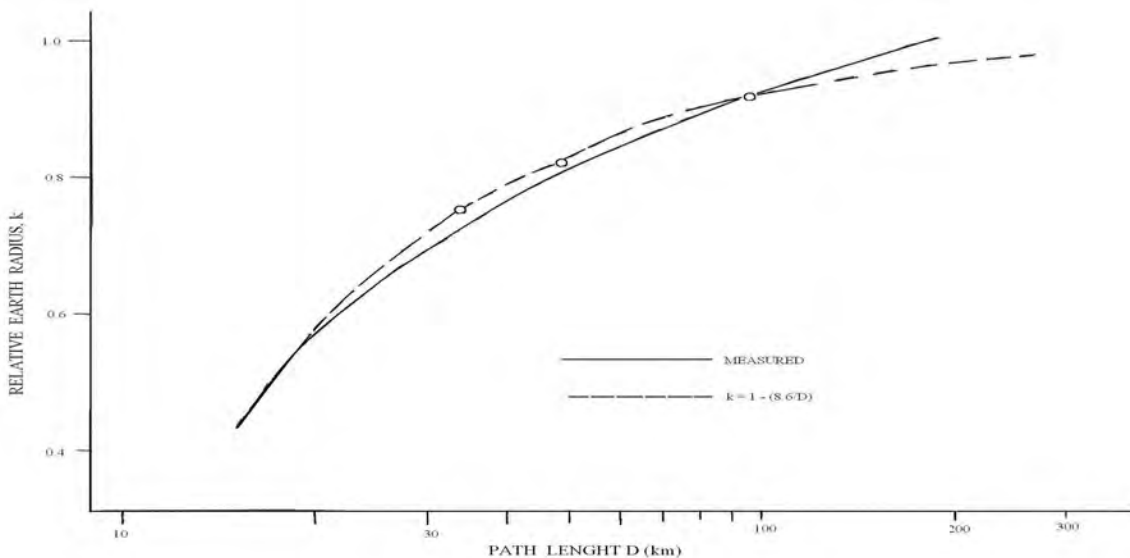


Figure 3.21 Minimum effective earth radius k exceeded 99.9 percent of time in continental temperate climate [30]

3.6.2 The D.C. Baker and A.J. Palmer Approach

Baker and Palmer [38-39] proposed a model for k-factor determination in South Africa. They use available South African and Namibia data to test their model. They use the regression analysis method with data obtained from eight different stations in South Africa, namely: Alexander Bay, Cape Town, Durban, Upington, Port Elizabeth, Bloemfontein, Pretoria and Windhoek. In their analysis, they report that k-factor comprises of both a “dry” term and a “wet” term. It is proposed that the cumulative distribution describing the probability that the k-factor exceeds a particular value, say k' could be approximated by [38]:

$$\Psi(k \geq k') = \exp\left\{-\frac{(k-1)^2}{2\sigma^2}\right\} \quad (3.65)$$

where σ is the variance of k. Expression (3.65) gives rise to a formula, which in turn could be used in a regression analysis, namely [38]:

$$\sqrt{\ln(1/\Psi)} = \frac{(k-1)}{\sqrt{2}\sigma} + c \quad (3.66)$$

where c is constant.

3.6.3 The “Dry – Wet” Model

The observed cumulative data seemed to be the result of two separate cumulative distributions, assumed to be independent. Baker and Palmer [39] therefore proposed to represent the effective cumulative distribution as the product of two statistically independent cumulative distributions so that [39]:

$$\Psi_{\text{eff}}(k \geq k') = \Psi_{\text{dry}} \times \Psi_{\text{wet}} \quad (3.67)$$

Where

$$\Psi_{\text{dry}} = \exp\left\{-\frac{(k-1)^2}{2\sigma_{\text{dry}}^2}\right\} \quad (3.68)$$

and

$$\Psi_{\text{wet}} = \exp\left\{-\frac{(k-k_{\text{ref}})^2}{2\sigma_{\text{wet}}^2}\right\} \quad (3.69)$$

The reference value of k , k_{ref} , was determined during regression analysis of data. Equations (3.67), (3.68) and (3.69) were manipulated to develop a regression formula of the form [39]:

$$\ln \sqrt{1/\psi} = c + m_1 k + m_2 k \text{Abs}(k - k_{ref}) \quad (3.70)$$

It was found that this form compressed the resultant data for values of k close to unity too much, resulting in significant loss of sensitivity of the method for these values. It was therefore decided to use the same basic form as in equation (3.66), namely:

$$\sqrt{\ln(1/\psi)} = c + m_1 k + m_2 k \text{Abs}(k - k_{ref}) \quad (3.71)$$

The results thus obtained from regression analysis were statistically only marginally worse than those from equation (3.70), but did retain the desired sensitivity for values of the k -factor close to unity. They report that on the basis of the results obtained, it has been possible to generate contour maps of South Africa showing the expected k -factor for a given cumulative distribution. Further, they note in [38] that the basic model reported appears to account mainly for the “dry” component of the refractive index, as reflected in the k -factor. They conclude from this research that the model will assist in predicting large values of k -factor that may only be exceeded rarely in the inland summer rainfall area [38].

Their research has been further extended to incorporate thirty stations instead of the previous eight [74]. In this new study, they use ground base data to test their model and are able to show that their results agree with the earlier work when they used radiosonde data except for the station at Alexander Bay. In [102] they use the model developed in [38-39] to predict the cumulative earth radius factor (k -factor) for different months as a function of height [102]. Comparisons between predicted and observed results were presented in [102]. It can be observed from [102] that the k -factor varies between 1.12 and 1.21 for all months at occurrence probability of 99.99% for the observed value in Pretoria, while it varies between 1.14 and 1.20 for all months at occurrence probability of 99.999% for the predicted values in the same location [102]. A median value of $k = 1.5$ was observed for Durban at a height 8 m a.g.l. while the predicted mean value is $k = 1.46$ a.g.l. at the same height [102].

3.6.4 The T.J. Afullo et al Approach

Afullo et al developed a framework for modeling the probability distribution of the effective earth radius factor (k-factor) using refractivity measurement data gathered for three years in Botswana and South Africa [36, 44, and 70]. In their method, an analytical model was proposed which predicts the probability density function of the k-factor for Southern Africa using data gathered from these two countries. A comprehensive derivation of the k-factor using refractivity data is given in [70]. From their previous work [40, 41], it was concluded that the distribution of k is bell-shaped, centered almost symmetrically about a median value μ_k . Therefore the following pdf, f(k) was proposed in [36]:

$$f(k) = Ae^{-\alpha(k-\mu_k)^2} \quad (3.72)$$

The parameter A is the value of f(k) at the mean, μ_k while the parameter α determines the girth of f(k). The task was therefore to determine A, μ_k , and α . The following conditions needed to be satisfied:

$$\int_{-\infty}^{\infty} f(k)dk = \int_{-\infty}^{\infty} Ae^{-\alpha(k-\mu_k)^2} dk = 1 \quad (3.73)$$

$$E\{k\} = \int_{-\infty}^{\infty} kAe^{-\alpha(k-\mu_k)^2} dk = \mu_k \quad (3.74)$$

In order to ascertain f(k) as the “best” approximation for g(k), there is need to optimize a cost function related to the error, $\varepsilon(k)$. The cost function used in their model is the integral of the square error (ISE).

$$\begin{aligned} \varepsilon(k) &= [f(k) - g(k)] \\ \text{ISE} &= \int_{-\infty}^{\infty} [f(k) - g(k)]^2 dk \end{aligned} \quad (3.75)$$

Therefore, the minimum value of the square of the error in (3.75) will determine the optimum choice of $f(k)$ parameters A , μ_k , and α . An algorithm was developed in [36] for determination of the parameters A , μ_k , and α , which gave the minimum error in (3.75). The algorithm is as follows:

- (a) As a first estimate, choose μ_k from the plot of $g(k)$.
- (b) Next, choose A such that:

$$A = g(k) \Big|_{k=\mu_k} \quad (3.76)$$

- (c) Now determine the corresponding α to fulfill the conditions (3.73) and (3.74).
- (d) Calculate the ISE from (3.75).
- (e) Keeping the mean constant at μ_k , vary A and α to satisfy conditions (3.73) and (3.74).

For each combination (A, α) , determine the ISE.

- (f) From the procedure stated in (e) above, identify the combination (μ_k, A_m, α_m) such that ISE is a minimum.

- (g) Keeping (A_m, α_m) at fixed value, vary the mean, μ_k until the lowest ISE is achieved.

This gives the optimum combination of $(A_m, \alpha_m, \mu_{km})$.

- (h) The best estimate for the pdf then becomes:

$$f(k) = A_m e^{-\alpha_m (k - \mu_{km})^2} \quad (3.77)$$

The assumption of their model is that there exist a global minimum, hence this is the limitation of the algorithm. Using the procedure described above, they obtained the optimum $f(k)$ (which gives the best estimate of $g(k)$ for the seasonal months of February, May, August, and November). The overall $f(k)$ for the whole year was also determined. Initially, their results were restricted to data within the height range 0–500m above ground level. Thereafter, height range 0–200m above ground level was considered [70]. Results were obtained for Botswana and South Africa for this stated height ranges and seasonal months as shown in Tables 3.12 and 3.13 and Figures. 3.22 and 3.23 respectively [70].

Table 3.12 Values of μ_k , A, and ISE for Botswana [70]

Period	Initial measurements estimates, g(k)			Next measurement estimates from calculation, f(k)			Final estimates from calculation, optimum f(k)		
	μ_k	A	ISE	μ_k	A	ISE	μ_k	A	ISE
February (0-500m a.g.l.)	1.04	2.922	0.891411	1.05	2.5	0.858813	1.08	2.5	0.81061
May (0-500m a.g.l.)	1.024	2.19	2.56045	1.024	3	2.42482	1.11	3	1.70535
August (0-500m a.g.l.)	1.16	3.557	1.89227	1.16	6	1.76622	1.14	6	1.35817
November (0-500m a.g.l.)	1.1055	2.2284	0.59136	1.1055	2.5	0.57031	1.13	2.5	0.55026
All Year (0-500m a.g.l.)	1.06	2.986	0.61699	1.12	2.78	0.42157	1.12	3	0.39895
All Year (0-200m a.g.l.)	1.15	1	0.63618	1.12	3	0.45520	1.12	2.5	0.40279

Table 3.13 Values of μ_k , A, and ISE for Durban [70]

Period	Initial measurements estimates, g(k)			Next measurement estimates from calculation, f(k)			Final estimates from calculation, optimum f(k)		
	μ_k	A	ISE	μ_k	A	ISE	μ_k	A	ISE
February (0-500m a.g.l.)	1.055	1.2	0.1925	1.055	1.1	0.1898	1.12	1.2	0.12958
May (0-500m a.g.l.)	1.036	1.3	0.25377	1.036	1.2	0.2517	1.15	1.4	0.18918
August (0-500m a.g.l.)	1.154	1.5	0.938	1.154	2.1	0.8562	1.26	3.7	0.29147
November (0-500m a.g.l.)	0.9603	0.75	0.4453	0.9603	1	0.4117	1.18	1.7	0.07737
All Year (0-500m a.g.l.)	1.046	1.2	0.28785	1.046	1.25	0.28757	1.21	1.75	0.09965

The optimum distributions for Botswana are determined to be [70]:

February (0–500m a.g.l.)	$f(k) = 2.5e^{-19.635(k-1.08)^2}$
May (0–500m a.g.l.)	$f(k) = 3e^{-28.28(k-1.11)^2}$
August (0-500m a.g.l.)	$f(k) = 6e^{-113.12(k-1.14)^2}$
November (0-500m a.g.l.)	$f(k) = 2.5e^{-19.635(k-1.13)^2}$
All Year (0–500m a.g.l.)	$f(k) = 3e^{-28.28(k-1.12)^2}$
All Year (0–200m a.g.l.)	$f(k) = 2.5e^{-19.635(k-1.12)^2}$

(3.78)

The optimum distributions for Durban are determined to be [70]:

February (0–500m a.g.l.)	$f(k) = 1.2e^{-4.5(k-1.12)^2}$
May (0–500m a.g.l.)	$f(k) = 1.4e^{-6.16(k-1.15)^2}$
August (0–500m a.g.l.)	$f(k) = 3.7e^{-43.01(k-1.26)^2}$
November (0–500m a.g.l.)	$f(k) = 1.7e^{-9.08(k-1.18)^2}$
All Year (0–500m a.g.l.)	$f(k) = 3e^{-28.28(k-1.12)^2}$
All Year (0–200m a.g.l.)	$f(k) = 1.75e^{-9.62(k-1.21)^2}$

(3.79)

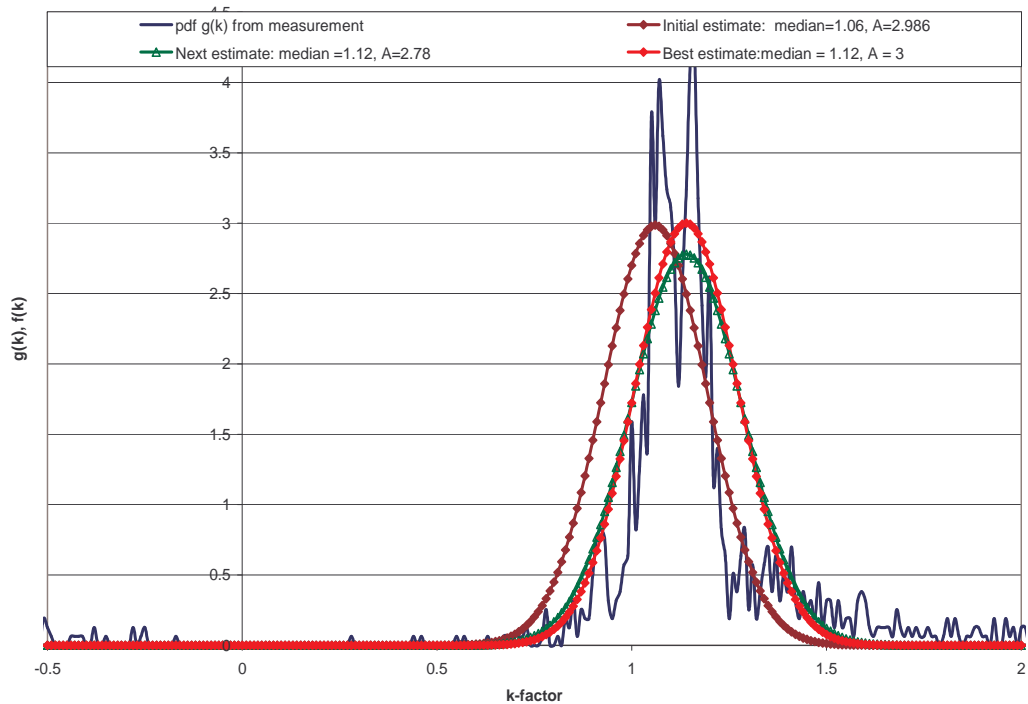


Figure 3.22 Measured and estimate pdf $g(k)$ and $f(k)$ All Year (0-500m a.g.l.) Botswana[70]

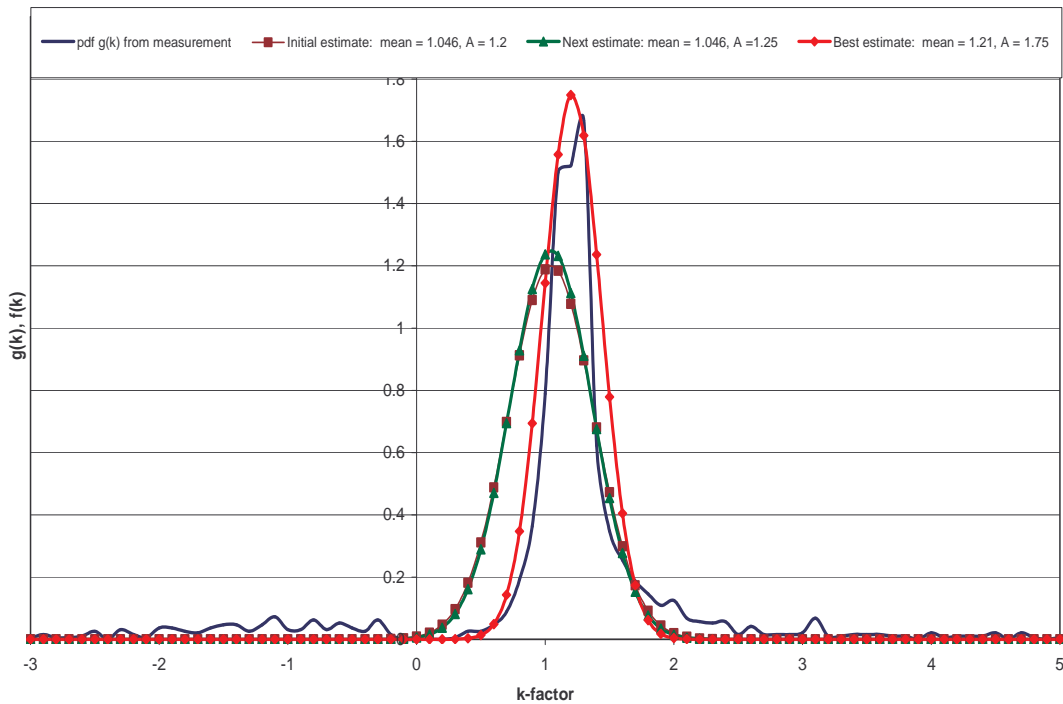


Figure 3.23 Measured and estimate pdf $g(k)$ and $f(k)$ All Year (0-500m a.g.l.) Durban [70]

3.7 Analytical or Semi-Empirical Approach to Solving Clear-Air Radioclimatic Problems

3.7.1 Martin's Analytical / Semi-Empirical Approach (Australia)

This approach presents a new multipath model based on Rayleigh distributed reflections and refractions and includes consideration of the reflected/refracted signal amplitude, delay and time variability. This multipath model is able to describe all the effects observed on paths that are dominated by reflective and refractive mechanisms. The model is characterised by two signals arriving at the receiver by different paths, a normalized direct signal and a second reflected/refracted Rayleigh distributed signal which gives a channel transfer function of:

$$Y(f, t) = 1 + b(t)e^{-j(2\pi f\tau + \phi(t))} \quad (3.80)$$

where f is the operating frequency, $b(t)$ is the time varying, Rayleigh distributed amplitude of the second signal relative to the direct signal and $\phi(t)$ is the uniformly distributed, time varying phase of the second signal [103].

The second signal can arise from reflections from the ground, water or ground based ducts or from refractions from ground based or elevated ducts. The delay difference between the direct signal and the second signal τ , is determined by the path geometry and the position of the reflecting / refracting point. The time variability of the second signal is related to the variations in the specular nature of the reflecting/refracting surface. These time variations are characterized by a Rayleigh low pass filter with a cut off frequency that can be from the order of about micro Hz up to approximately 0.5 Hz [104].

The time varying Rayleigh characteristic of the second signal arises from the specular nature of the refracting surface. The surfaces that refract cause several signals to arrive at the receiver with different phases and amplitudes. These signals from the refracting or reflecting surface add together, resulting in the second signal having Rayleigh amplitude distribution and a uniform phase distribution. As the refracting or reflecting surface is unstable, it will cause the refracted or reflected signals to vary in their amplitude and phase. The resulting signal at the receiver will thus show time variability in both its amplitude and phase leading to the well known time variability of fading [104].

The time variability of the surface depends critically on the amount and rate of agitation of the surface. For water surfaces, the specular reflection depends on the surface agitation with the fastest rates of change being measured from such surfaces. Duct surfaces on the other hand apparently have much slower rate of change [104]. Under some circumstances, the surface rate of change drops to the point where the reflection is dominant and the surface acts like mirror. In these cases, the specularly reflected signal is characterized by the special case of a signal with amplitude of 1.0 and a phase shift of 180 degrees at the reflection point. This case can arise from very still water or from a very intense ground based duct.

The time delay difference between the direct signal and the second reflected/refracted signal depends on the geometry of the path in relation to the reflection/refraction point. For accurate designs of space diversity arrangements and wideband systems, a detailed knowledge of the delay is required. In particular, the height of the reflecting/refracting duct and its radiometeorological characteristics are

required to make an accurate assessment of the probable delays that will be associated with severe fading on a given path.

3.7.2 The Parabolic Equation Method

There have been many publications in recent years on the development of the split-step parabolic equation method as applied to electromagnetic wave propagation [105-108]. The parabolic equation method was originally developed by Fock in 1946 [109], but it was not until 1973 that a practical solution for complicated refractive environments was developed by Hadin and Tappert [108], called the split step Fourier method [108]. This method was originally applied to model acoustic propagation, but the radar community has since used the split-step algorithm to model propagation in the troposphere.

The exposition in [109] presents a solution to the propagation of electromagnetic waves along the earth surface using a method of parabolic equation proposed by Leontovich [109]. The first section of the paper considered the earth surface to be a plane and the well known Weyl-van der Pol formula is deduced. This formula turns out to be the exact solution of the parabolic equation with corresponding boundary conditions. In the second section, the surface is considered to be spherical, and the resulting formula coincides with that obtained by Fock by the method of summation of infinite series representing the rigorous solution of the problem.

After the work of Fock and Leontovich [109] different authors now adapt various modifications of the parabolic equation using different numerical and computational approaches as seen in [110–118]. While some authors focus on improving the parabolic equation approach by using a more sophisticated modern numerical and computational techniques [110–111] which were not available during the time of Fock [109] and Leontovich [109], others focus on different applications that the technique could offer [112, 116 – 118]. Other authors even focus on improving the boundary condition that may be implemented with the parabolic equation [113 – 115]. A brief introduction of the parabolic equation method will be reviewed in the following sub-sections.

3.7.3 Parabolic Equation Framework

In the succeeding sections, we assume $\exp(-i\omega t)$ time-dependence of the fields, where ω is the angular speed frequency. Initially we work with Cartesian coordinates (x, y, z) . We concern ourselves with two-dimensional electromagnetic problems where the fields are independent of the transverse

coordinate y . There are then no depolarization effects, and all the fields can be decomposed into horizontally and vertically polarized components propagating independently.

For horizontal polarization, the electric field \mathbf{E} only has one non-zero component E_y , while for vertical polarization, the magnetic field \mathbf{H} only has one non-zero component H_y . The appropriate field component is defined by:

$$\psi(x, z) = E_y(x, z) \quad (3.81)$$

for horizontal polarization and;

$$\psi(x, z) = H_y(x, z) \quad (3.82)$$

for vertical polarization.

We will be solving the wave equation in a domain where the refractive index $n(x, z)$ has smooth variations, assuming that suitable boundary conditions can be defined at the domain boundaries. Typically the bottom boundary is the air/ground interface and the top boundary extends to infinity. We are interested in solving problems where energy propagates at small angles from a preferred direction, called the paraxial direction. Following the convention in radiowave propagation problems, we choose the x -direction as the paraxial direction. If the propagation medium is homogeneous with refractive index n , the field component ψ satisfies the two-dimensional scalar wave equation:

$$\frac{\partial^2 \psi}{\partial x^2} + \frac{\partial^2 \psi}{\partial z^2} + k^2 n^2 \psi = 0 \quad (3.83)$$

Where the wave number in vacuum is $k = \omega/c$, c is the group velocity of propagation and n is the refractive index of the medium and may vary with the coordinates. For the start, we assume a constant value of n , $n \equiv 1$ [119]. In general, the refractive index varies with range x and height z , and equation (3.83) is not exact [120]. It is however a good approximation provided the variations of n remain slow on the scale of a wavelength.

3.7.4 Numerical Methods of Parabolic Equations

Equation (3.83) is written for a two-dimensional case of the propagation since this case is the one that is most widely considered in applications of the split-step approximation. Equation (3.83) can be factorized as follows:

$$\left[\frac{\partial}{\partial x} + i\sqrt{k^2 + \frac{\partial^2}{\partial z^2}} \right] \times \left[\frac{\partial}{\partial x} - i\sqrt{k^2 + \frac{\partial^2}{\partial z^2}} \right] \psi = 0 \quad (3.84)$$

representing the forward and backward propagating waves respectively. We introduce the reduced function associated with the paraxial direction x :

$$u(x, z) = e^{ikx} \psi(x, z) \quad (3.85)$$

The reason for using this reduced function is that it is slowly varying in range for energy propagating at angles close to the paraxial direction, which gives it convenient numerical properties. The truncated and factorized equation for amplitude u takes the following form:

$$\left[\frac{\partial}{\partial x} + ik \left(1 + \sqrt{1 + \frac{1}{k^2} \frac{\partial^2}{\partial z^2}} \right) \right] \times \left[\frac{\partial}{\partial x} + ik \left(1 - \sqrt{1 + \frac{1}{k^2} \frac{\partial^2}{\partial z^2}} \right) \right] u = 0 \quad (3.86)$$

By retaining only the forward propagating wave, we obtain the following forward parabolic equation

$$\left[\frac{\partial}{\partial x} + ik \left(1 - \sqrt{1 + \frac{1}{k^2} \frac{\partial^2}{\partial z^2}} \right) \right] u = 0 \quad (3.87)$$

which has a formal solution;

$$u(x + \Delta x) = \exp \left\{ ik\Delta x \left[\sqrt{1 + \frac{1}{k^2} \frac{\partial^2}{\partial z^2}} - 1 \right] \right\} u(x) \quad (3.88)$$

where Δx is a range increment. As can be seen from equation (3.88), the forward propagating wave at range $x+\Delta x$ can be obtained from values of the wave amplitude at the previous distance x by applying the exponential operator in equation (3.88). In order to calculate the wave field, the exponential operator in equation (3.88) should be approximated in a form suitable for computations. Let us introduce a notation:

$$Z = \frac{1}{k^2} \frac{\partial^2}{\partial z^2} \quad (3.89)$$

Depending on the type of approximation, we obtain three known types of the split-step approximation to parabolic equations, which are:

- (a) The standard or narrow angle approximation, obtained by expanding the square root in the exponent into a Taylor series and retaining the linear term:

$$\sqrt{1+Z} = 1 + \frac{Z}{2} \quad (3.90)$$

This approximation is used in a split-step Fourier method and it is normally valid for narrow angles of propagation relative to the paraxial axis x , not exceeding $15^\circ - 20^\circ$.

- (b) The Claerbout approximation is in the following form:

$$\sqrt{1+Z} \approx \frac{1 + \frac{3}{4}Z}{1 + \frac{Z}{4}} \quad (3.91)$$

this method is reported to be valid for wider angles up to $30^\circ - 40^\circ$ [121, 122].

- (c) The split-step Padé approximation, where the exponential is expanded into series

$$\exp\left[ik\Delta x\sqrt{1+Z}-1\right] \approx 1 + \sum_{m=1}^M \frac{a_m}{1+b_m Z} \quad (3.92)$$

where the coefficients a_m , b_m are determined numerically in the complex plane using the approach developed in [121]. The split-step Padé approximation is reported in [122, 114] to be valid for angles of propagation relative to the x-axis of up to 90° .

All the above methods have been realized in a very powerful computational technique well suited for parallel computing and widely used in numerous applications. With regard to the problem of radio wave propagation in the earth's troposphere, the most established computational approach is based on the split-step Fourier method, equivalent to a standard narrow angle approximation of the square root in the exponential operator. The wide angle approximations, such as Claerbout and Padé approximation have been used to solve scattering problems in radiowave free-space propagation [122, 123].

3.7.5 Parabolic Approximation Method of Parabolic Equation

Considering that in the propagation of an electromagnetic field, the azimuthal symmetry was assumed. In the far-field approximation, the outgoing part of the amplitude satisfies the one-way outgoing wave equation:

$$\frac{\partial u}{\partial x} = ik_0(-1 + \sqrt{1+X})u \quad (3.93)$$

where k_0 is the wave number in free space, $X = (1/k_0^2)(\partial^2/\partial z^2) + (n^2 - 1)$ and n is the refractive index. In order to solve equation (3.93), the square root operator $\sqrt{1+X}$ needs to be approximated. The standard approximation consist of the following writing:

$$\sqrt{1+X} \cong 1 + \frac{1}{2}X \quad (3.94)$$

This yields the standard parabolic equation (SPE), which has been shown to be valid only for propagation within 15° – 20° of horizontal. The first step leading to the split-step parabolic (SSP) solution consist of solving equation (3.93) as an ordinary differential equation in x . This gives

$$u(x + \Delta x, z) = e^{ik_0\Delta x(-1 + \sqrt{1+X})} u(x, z) \quad (3.95)$$

A Padé approximation is then applied to the exponential operator such that

$$e^{ik_0\Delta x(-1+\sqrt{1+X})} \cong 1 + \sum_{j=1}^{N_p} \frac{a_j N_p X}{1 + b_j N_p X} \quad (3.96)$$

where the two N_p coefficients ($a_j N_p$, $b_j N_p$) are determined numerically in the complex plane using the approach in [124]. Substituting the Padé approximation equation (3.96) into equation (3.95) leads to the SSP solution:

$$u(x + \Delta x, z) = u(x, z) + \sum_{j=1}^{N_p} a_j N_p X (1 + b_j N_p X)^{-1} u(x, z) \quad (3.97)$$

If we define N_p functions q_j by

$$q_j(x + \Delta x, z) = a_j N_p X (1 + b_j N_p X)^{-1} u(x, z) \quad (3.98)$$

$$\forall j = 1, 2, \dots, N_p$$

then equation (3.97) can be written as

$$u(x + \Delta x, z) = u(x, z) + \sum_{j=1}^{N_p} q_j(x + \Delta x, z) \quad (3.99)$$

It can be seen that equation (3.99) is solved at the advanced range by solving equation (3.98) for each $j = 1, 2, \dots, N_p$. This can be done separately for each j and therefore makes the SSP solution suitable for parallel processing.

3.8 Chapter Summary

This chapter has extensively reviewed the various methods employed by different authors in different parts of the world to solve clear-air radioclimatological problems in their region. The chapter begins with general study of radio propagation both in clear-air and non clear-air environment. The chapter then progresses with an extensive review of the clear-air multipath fading modeling carried out by different authors from different part of the world. Notable among these approaches, are the approaches by Morita and Kakita in Japan [29], Vigants [24] and Crombie [34] in the USA, Olsen and Segal [95] in Canada and Tjelta et al in western Europe[100]. All these approaches involve measurements of signal level and fade event statistics over microwave line-of-sight links set up across paths with different characteristics. These links allow the authors in their different approaches to take clear-air measurements for a reasonable period of time. These measurements are then used to develop models that can be used to predict occurrence probabilities of a particular signal fade depth as a

function of the path characteristics such as: path length, terrain roughness, frequency, path inclination and path grazing angles.

Furthermore, the chapter reviews clear-air diffraction fading techniques adopted by different authors in different parts of the world. Diffraction fading characterization which is instrumental in proper path clearance is an important clear-air effect for clear-air radioclimatological modeling study. In this review, it is determined that significant modeling work has not been done in this area in the past. Instead a given k-factor value is normally used for path clearance depending on the path distance as given by the then CCIR (now ITU-R). For instance, a path that is designed for $k = 0.67$ at 27 km, becomes effectively $k = 1.0$ at 200 km. On a longer path of about 240 km, effective value of $k = 4/3$ is recommended by the author in [83].

Notable modeling work done in this regard is found to be done in Africa. Among these is the work by Baker and Palmer [38-39, 74] in South Africa where they have used refractivity measurement statistics to model the cumulative distribution of the k factor in South Africa. They have gathered measurement in eight different locations in South Africa initially to come up with their model and later extend these stations to thirty for their model verification. Another significant effort in this regard is the work of Afullo and Odedina [44] in Southern Africa. In their own case, they have developed a framework for modeling the probability distribution of the effective earth radius factor (k-factor) using refractivity measurement data gathered for three years in Botswana and South Africa. They proposed an analytical model which predicts the probability density function of the k-factor for Southern Africa using data gathered from the stated two countries (i.e. South Africa and Botswana). These two efforts from Southern Africa allowed develop a model using refractivity data in this region to determine the appropriate value of the k-factor for their region. Their effort helps to come up with better value of the k-factor for LOS link design rather than the oversimplified value of $k = 4/3$ that was normally used in this region.

The chapter then concludes by looking at semi-empirical/ analytical approaches employed to solve clear-air radioclimatological propagation problems. The first of the two approaches reviewed is the work of Martin [103-104] from Australia who proposed a new multipath model based on Rayleigh distributed reflections and refractions. His approach includes consideration of the reflected /refracted signal amplitude, delay and time variability. The approach is characterized by two signals arriving at the receiver by different paths, a normalized direct signal and a second reflected / refracted Rayleigh distributed signal. Finally, the parabolic equation technique for solving clear-air radioclimatic

problems is reviewed. The parabolic equation is an analytical approach that was originally developed by Fock and Leontovich (1946) from the former USSR [109]. Hadin and Tappert later (1973) developed a practical implementation of the parabolic equation to find solution for complicated refractive environments [108]. This method, called split-step Fourier method, was originally applied to model acoustic propagation, but the radar community has since used the split-step algorithm to model propagation in the troposphere. After the work of Fock and Leontovich (1946) different authors now adapt various modifications of the parabolic equation using different numerical and computational approaches as seen in [110–118]. While some authors focus on improving the parabolic equation approach by using a more sophisticated modern numerical and computational techniques [110–111] which were not available during the time of Fock and Leontovich (1946), others focus on different applications that the technique could offer [112, 116–118]. Other authors even focus on improving the boundary condition that may be implemented with the parabolic equation [113–115].

Consequently, it is imperative however to note that none of these methods highlighted above have been implemented in this chapter. It would have been interesting to implement most, if not all, the techniques highlighted in this chapter in the thesis, but for want of resources to do so. Almost all the approaches highlighted in the first and second category make use of at least ten (10) to fifty (50) operational line-of-sight (LOS) links set up over different terrain types for measurements. This allows measurements at different frequencies and over paths with different characteristics. The present research has only one (1) such link over a single path and the link is not presently operational. This poses a serious limitation on the robustness of the present research as one cannot do a detailed regression analysis as carried out by some of the techniques highlighted above. In spite of the above stated fact, the limited resources available for the research will be put into good use. For instance, measurements have been taken over this single LOS link for a period of one year. This is signal level measurements and it is appropriate for model verification purposes. To this end, some of the models highlighted above will be tested using refractivity measurements available for South Africa and Botswana and the signal level measurement mentioned earlier can then be used for model verification. This will help to check which of the models highlighted above will best suit South African region or better still if a new model will be proposed. This is the focus of the subsequent chapters.

CHAPTER FOUR

A PROPOSED MODEL OF CLEAR-AIR RADIOCLIMATIC STUDY

4.0 INTRODUCTION

In chapter three, an in depth review of different models proposed by researchers across different regions of the world was presented. These various models of clear-air radioclimatic study were given based on clear-air signal level measurement statistic over a considerable period of time. In order to test the applicability of these various models in South Africa, we first need to establish a standard measurement background based on information from Southern Africa. To this end, the present chapter focuses on proposing a workable model of clear-air radioclimatological study in Southern Africa. Before such a model can be proposed there is need to do an extensive analysis on clear-air signal level measurement carried out between the Westville campus and Howard College campus of University of KwaZulu-Natal in 2004. After this analysis has been done, then proposition can be made of workable clear-air radioclimatic study for this region.

4.1 Basic information on Data used for Analysis and Model Formulation

The measurement period is eight months which spans from February 2004 to December 2004; information is not available for January, September, October and November. The total measurement days are 153, which details are shown in Table 4.1 below.

Table 4.1 Measurement information for Model Formulation

Month	Days	Hours	Minutes
February	8	192	11318
March	22	528	31633
April	25	592	35448
May	31	736	44081
June	16	368	22077
July	12	260	15621
August	16	376	22591
December	23	552	33039
Total	153	3604	215808

It should be noted that not all the days of the months are available in the measurements and sometimes not all the 24 hours in a day are available (see appendix D). We have chosen to do the analyses in minutes since these values are moderate in size.

4.2 Daily Signal Level Analysis for Percentage of Time that a Particular Fade Depth is Exceeded

The measurement days are categorized into seven different fade depth levels for the analysis. These seven fade depth levels are: fade depth $A(\text{dB}) \geq 2$ dB; fade depth $A(\text{dB}) \geq 5$ dB; fade depth $A(\text{dB}) \geq 10$ dB; fade depth $A(\text{dB}) \geq 15$ dB; fade depth $A(\text{dB}) \geq 20$ dB; fade depth $A(\text{dB}) \geq 30$ dB; fade depth $A(\text{dB}) \geq 40$ dB. Before we start the analysis for each fade depth level for different months, we pool together all the available measurement for the particular month in question. We then plot a probability distribution of all this data, and later use a curve fitting procedure described in section 3.6.4 to estimate the average signal level for that month. Obviously the mean of the estimation with the lowest integral square error (ISE) value is our chosen average signal level for that month. This chosen average signal level then becomes the minimum threshold value for the month. Any signal level value lower than this minimum threshold is considered to be a faded signal and counted as such. This is the procedure we have used to isolate the number of faded signal in a particular day of any particular month at any time.

4.2.1 Daily Signal Level Analysis for February

For the month of February 2004, there are eight (8) days of clear-air signal level measurement available for analysis. The threshold values estimated from the pdf plot for this month is - 42.84 dBm as described in section 4.2. This distribution is shown in Figure 4.1 below:

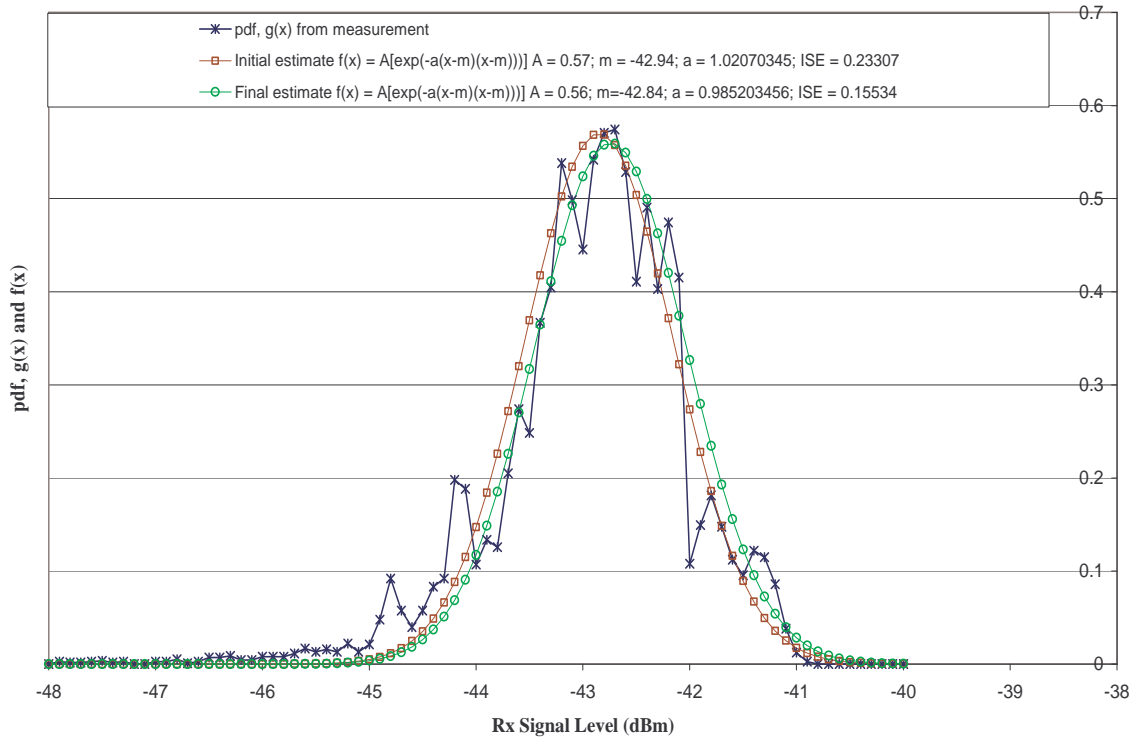


Figure 4.1 Measured and Estimated pdf, $g(x)$ and $f(x)$ for Rx Signal Level Measurement, February 2004

4.2.2 February 20 2004

From the signal level measurement and analysis, the following information is obtainable for this particular day of the month:

Probability (Fade depth ≥ 2 dB) $\triangleq P(A_{2\text{dB}}, A_{2\text{dB}}$ is exceeded for 6 minutes;

Probability (Fade depth ≥ 5 dB) $\triangleq P(A_{5\text{dB}}, A_{5\text{dB}}$ is exceeded for 6 minutes;

Probability (Fade depth ≥ 10 dB) $\triangleq P(A_{10\text{dB}}, A_{10\text{dB}}$ is exceeded for 6 minutes;

Probability (Fade depth ≥ 15 dB) $\triangleq P(A_{15\text{dB}}, A_{15\text{dB}}$ is exceeded for 6 minutes;

Probability (Fade depth ≥ 20 dB) $\triangleq P(A_{20\text{dB}}, A_{20\text{dB}}$ is exceeded for 6 minutes;

Probability (Fade depth ≥ 30 dB) $\triangleq P(A_{30\text{dB}}, A_{30\text{dB}}$ is exceeded for 3 minutes;

Probability (Fade depth ≥ 15 dB) $\triangleq P(A_{15\text{dB}}, A_{15\text{dB}}$ is exceeded for 0 minutes.

We can see from above that for this particular day, signal fading is experienced at all the fade depth levels. We therefore determine the percentage of time that these fade depths (A) occur from the total measurement for this day as follows [134]:

$$P(A \geq F_L (\text{dB})) = \frac{F_m}{T_m} \times \frac{100}{1} \quad \% \quad (4.1)$$

where:

$P(A)$ is the percentage of exceedance probability of certain fade depth $A(\text{dB})$, A is Any fade depth level (dB), F_L is the fade depth level being analyzed (dB), F_m is the total faded minutes for the fade depth under analysis (mins), and T_m is the total faded minutes for the month being analyzed (mins).

Using equation (4.1) therefore, for February 20th 2004, the percentage of time that a fade depth of 2 dB to 30 dB is exceeded from the total measurement for that day is 0.472%, while for the same day, a fade depth of 40 dB or more is exceeded for 0.236% of the time.

4.2.3 February 28 2004

Following similar procedure as explained in section 4.2.2, for February 28 2004, the following information is obtainable for this day:

Probability (Fade depth ≥ 2 dB) $\triangleq P(A_{2\text{dB}})$, $A_{2\text{dB}}$ is exceeded for 29 minutes;
 Probability (Fade depth ≥ 5 dB) $\triangleq P(A_{5\text{dB}})$, $A_{5\text{dB}}$ is exceeded for 2 minutes;
 Probability (Fade depth ≥ 10 dB) $\triangleq P(A_{10\text{dB}})$, $A_{10\text{dB}}$ is exceeded for 0 minutes;
 Probability (Fade depth ≥ 15 dB) $\triangleq P(A_{15\text{dB}})$, $A_{15\text{dB}}$ is exceeded for 0 minutes;
 Probability (Fade depth ≥ 20 dB) $\triangleq P(A_{20\text{dB}})$, $A_{20\text{dB}}$ is exceeded for 0 minutes;
 Probability (Fade depth ≥ 30 dB) $\triangleq P(A_{30\text{dB}})$, $A_{30\text{dB}}$ is exceeded for 0 minutes;
 Probability (Fade depth ≥ 15 dB) $\triangleq P(A_{15\text{dB}})$, $A_{15\text{dB}}$ is exceeded for 0 minutes.

For this particular day, the signal fading is experienced at two fade depth levels. The percentage of time that these fade depth levels are exceeded from the total measurement time for the day is calculated as follows using equation (4.1) and the result is stated as follows:

For February 28 2004, the percentage of time that a fade depth of 2 dB or more is exceeded from the total measurement time for the day is 2.016%, while at a fade depth of 5 dB or more, the percentage of signal loss is 0.139%. The procedure is repeated for all the eight days in February and the result obtained after this exercise is displayed in Table 4.2 below:

Table 4.2 Percentage of Exceedance Probabilities for the Days in February 2004 Measurement

Date	Percentage of Time P(A) that a Particular Fade Depth A(dB) is Exceeded from the Total Measurement time						
	P(A _{2dB}) %	P(A _{5dB}) %	P(A _{10dB}) %	P(A _{15dB}) %	P(A _{20dB}) %	P(A _{30dB}) %	P(A _{40dB}) %
19 / 02	0	0	0	0	0	0	0
20 / 02	0.472	0.472	0.472	0.472	0.472	0.472	0.236
21 / 02	3.127	0.486	0	0	0	0	0
22 / 02	1.459	0	0	0	0	0	0
23 / 02	15.705	0	0	0	0	0	0
24 / 02	0.972	0	0	0	0	0	0
25 / 02	8.2	0	0	0	0	0	0
28 / 02	2.016	0.139	0	0	0	0	0

4.2.4 Daily Signal Level Analysis for March

There exist twenty-two (22) days of clear-air signal level measurement data for analysis for the month of March 2004. We follow the same procedure as was done for the month of February. The minimum threshold average signal level value for this month is determined to be -42 dBm as shown in Figure 4.2 below. Using this signal level, we determine the percentage time P(A) that a particular fade depth A(dB) is exceeded for the twenty-two different days as was done before. The same seven fade depth levels used for February is used here and repeated for all the analysis for uniformity. We show below (in sections 4.2.5 and 4.2.6) the calculation for two sample days of the twenty-two days:

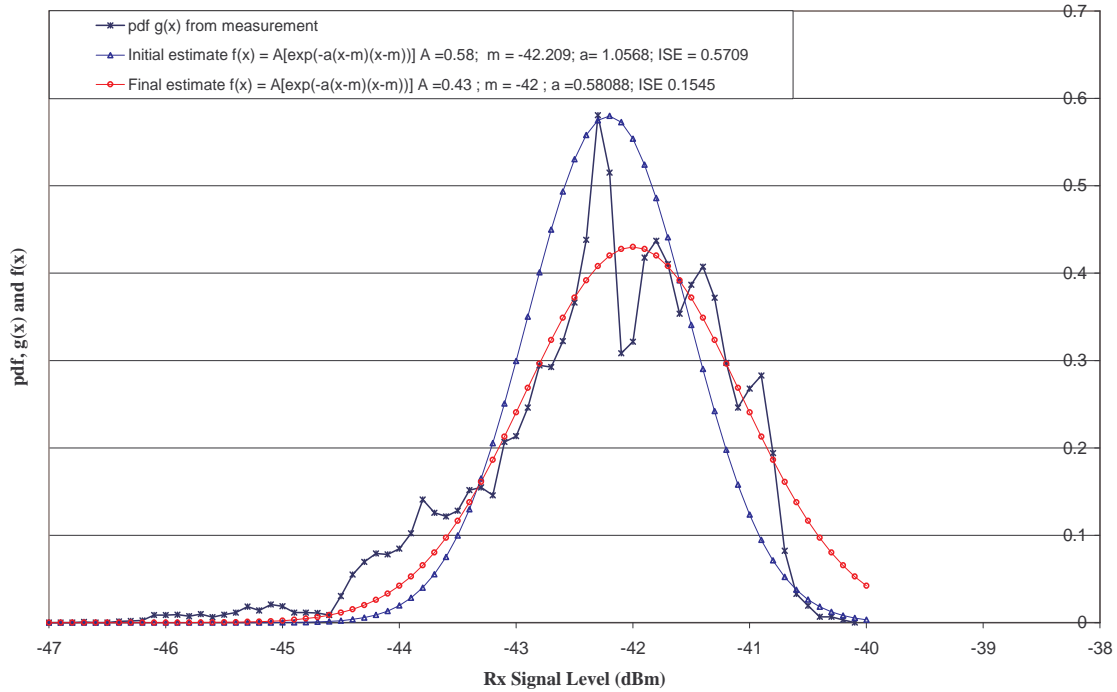


Figure 4.2 Measured and Estimated pdf, $g(x)$ and $f(x)$ for Rx Signal Level Measurement, March 2004

4.2.5 March 6 2004

From the signal level measurement and analysis the following information is obtainable for March 6 2004:

Probability (Fade depth ≥ 2 dB) $\triangleq P(A_{2\text{dB}})$, $A_{2\text{dB}}$ is exceeded for 7 minutes;

Probability (Fade depth ≥ 5 dB) $\triangleq P(A_{5\text{dB}})$, $A_{5\text{dB}}$ is exceeded for 0 minutes;

Probability (Fade depth ≥ 10 dB) $\triangleq P(A_{10\text{dB}})$, $A_{10\text{dB}}$ is exceeded for 0 minutes;

Probability (Fade depth ≥ 15 dB) $\triangleq P(A_{15\text{dB}})$, $A_{15\text{dB}}$ is exceeded for 0 minutes;

Probability (Fade depth ≥ 20 dB) $\triangleq P(A_{20\text{dB}})$, $A_{20\text{dB}}$ is exceeded for 0 minutes;

Probability (Fade depth ≥ 30 dB) $\triangleq P(A_{30\text{dB}})$, $A_{30\text{dB}}$ is exceeded for 0 minutes;

Probability (Fade depth ≥ 15 dB) $\triangleq P(A_{15\text{dB}})$, $A_{15\text{dB}}$ is exceeded for 0 minutes.

Only one fade depth level is recorded for this day. The exceedance probability of this fade depth is determined using (4.1).

Hence, for March 6, 2004, the percentage of time that a fade depth of 2 dB or more is exceeded from the total measurement time is 0.487 %.

4.2.6 March 16 2004

Similar procedure as explain in section 3.1.2.1 is followed for March 16 2004 and the following information can be gathered for this day:

Probability (Fade depth \geq 2 dB) \triangleq P(A_{2dB}), A_{2dB} is exceeded for 128 minutes;

Probability (Fade depth \geq 5 dB) \triangleq P(A_{5dB}), A_{5dB} is exceeded for 0 minutes;

Probability (Fade depth \geq 10 dB) \triangleq P(A_{10dB}), A_{10dB} is exceeded for 0 minutes;

Probability (Fade depth \geq 15 dB) \triangleq P(A_{15dB}), A_{15dB} is exceeded for 0 minutes;

Probability (Fade depth \geq 20 dB) \triangleq P(A_{20dB}), A_{20dB} is exceeded for 0 minutes;

Probability (Fade depth \geq 30 dB) \triangleq P(A_{30dB}), A_{30dB} is exceeded for 0 minutes;

Probability (Fade depth \geq 15 dB) \triangleq P(A_{15dB}), A_{15dB} is exceeded for 0 minutes.

Only one fade depth level is recorded for this day. The exceedance probability of this fade depth is determined using equation (4.1). This analysis was done for the twenty-two days and the results are presented in Table 4.3 below:

Table 4.3 (a) Percentage of Exceedance Probabilities for the Days in March 2004 Measurement

Date	Percentage of Time P(A) that a Particular Fade Depth A(dB) is Exceeded from the Total Measurement time						
	P(A _{2dB}) %	P(A _{5dB}) %	P(A _{10dB}) %	P(A _{15dB}) %	P(A _{20dB}) %	P(A _{30dB}) %	P(A _{40dB}) %
06 / 03	0.487	0	0	0	0	0	0
07 / 03	0	0	0	0	0	0	0
08 / 03	0	0	0	0	0	0	0
09 / 03	0.903	0	0	0	0	0	0
10 / 03	1.806	1.806	1.806	1.806	1.806	1.806	0
13 / 03	0	0	0	0	0	0	0
14 / 03	0	0	0	0	0	0	0
15 / 03	0	0	0	0	0	0	0
16 / 03	8.914	0	0	0	0	0	0

Table 4.3 (b) Percentage of Exceedance Probabilities for the Days in March 2004 Measurement

Date	Percentage of Time P(A) that a Particular Fade Depth A(dB) is Exceeded from the Total Measurement time						
	P(A _{2dB}) %	P(A _{5dB}) %	P(A _{10dB}) %	P(A _{15dB}) %	P(A _{20dB}) %	P(A _{30dB}) %	P(A _{40dB}) %
17 / 03	3.833	0	0	0	0	0	0
18 / 03	21.821	0	0	0	0	0	0
19 / 03	80.976	48.502	48.502	48.502	48.502	48.502	20.627
20 / 03	100	100	100	100	100	100	57.093
21 / 03	100	100	100	100	100	100	57.789
22 / 03	100	100	100	100	100	100	58.733
25 / 03	100	100	100	100	100	100	55.702
26 / 03	100	100	100	100	100	100	54.520
27 / 03	100	100	100	100	100	100	54.735
28 / 03	100	100	100	100	100	100	55.872
29 / 03	100	100	100	100	100	100	55.532
30 / 03	100	100	100	100	100	100	58.513
31 / 03	100	100	100	100	100	100	57.342

It can be observed from Table 4.2 that there is total signal loss for the period from March 19 till the end of the month. In these days, the LOS link is not running, so the system is down and this will be put to consideration when we do monthly analysis in section 4.3.

4.2.7 Daily Signal Level Analysis for April

The analysis for the month of April is not so different from the previous months. For this month twenty-five (25) days of clear-air signal level measurement data is available for analysis (see appendix D, Table D.3). For this data, we determine the average minimum threshold signal level for the month to be -42.86 dBm as seen from Figure 4.3 below. Next we determine the percentage of time P(A) that a particular fade depth A(dB) level occurs from the total measurement time. We use the same seven fade depth levels that were used for the previous analysis. This analysis was done for all the available 25 days in this month. We have shown only two samples of the calculations here, while the results for the remaining days are shown in Table 4.4 below:

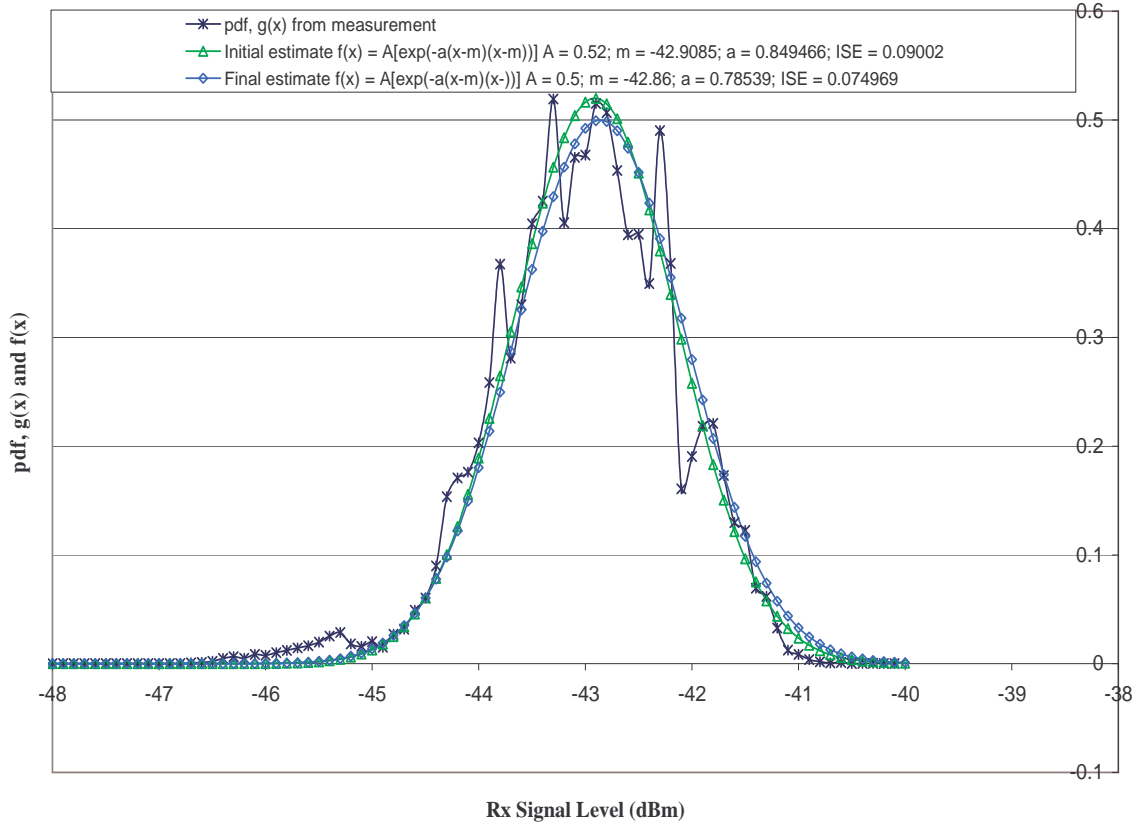


Figure 4.3 Measured and Estimated pdf, $g(x)$ and $f(x)$ for Rx Signal Level Measurement, April 2004

4.2.8 April 15 2004

The clear-air signal level for April 15 2004 shows the following information:

Probability (Fade depth ≥ 2 dB) $\triangleq P(A_{2\text{dB}}, A_{2\text{dB}}$ is exceeded for 357 minutes;

Probability (Fade depth ≥ 5 dB) $\triangleq P(A_{5\text{dB}}, A_{5\text{dB}}$ is exceeded for 0 minutes;

Probability (Fade depth ≥ 10 dB) $\triangleq P(A_{10\text{dB}}, A_{10\text{dB}}$ is exceeded for 0 minutes;

Probability (Fade depth ≥ 15 dB) $\triangleq P(A_{15\text{dB}}, A_{15\text{dB}}$ is exceeded for 0 minutes;

Probability (Fade depth ≥ 20 dB) $\triangleq P(A_{20\text{dB}}, A_{20\text{dB}}$ is exceeded for 0 minutes;

Probability (Fade depth ≥ 30 dB) $\triangleq P(A_{30\text{dB}}, A_{30\text{dB}}$ is exceeded for 0 minutes;

Probability (Fade depth ≥ 15 dB) $\triangleq P(A_{15\text{dB}}, A_{15\text{dB}}$ is exceeded for 0 minutes.

This shows that only one fade depth level is recorded for this day.

4.2.9 April 22 2004

Similar procedure to the one described in section 4.2.7 is adopted here and the following information is determined for April 22 2004.

Probability (Fade depth ≥ 2 dB) $\triangleq P(A_{2\text{dB}})$, $A_{2\text{dB}}$ is exceeded for 1 minute;

Probability (Fade depth ≥ 5 dB) $\triangleq P(A_{5\text{dB}})$, $A_{5\text{dB}}$ is exceeded for 0 minutes;

Probability (Fade depth ≥ 10 dB) $\triangleq P(A_{10\text{dB}})$, $A_{10\text{dB}}$ is exceeded for 0 minutes;

Probability (Fade depth ≥ 15 dB) $\triangleq P(A_{15\text{dB}})$, $A_{15\text{dB}}$ is exceeded for 0 minutes;

Probability (Fade depth ≥ 20 dB) $\triangleq P(A_{20\text{dB}})$, $A_{20\text{dB}}$ is exceeded for 0 minutes;

Probability (Fade depth ≥ 30 dB) $\triangleq P(A_{30\text{dB}})$, $A_{30\text{dB}}$ is exceeded for 0 minutes;

Probability (Fade depth ≥ 15 dB) $\triangleq P(A_{15\text{dB}})$, $A_{15\text{dB}}$ is exceeded for 0 minutes.

Only one fade depth level is recorded for this day. The result of the analysis for all the days in this month is shown in Table 4.4 below.

Table 4.4 (a) Percentage of Exceedance Probabilities for the Days in April 2004 Measurement

Date	Percentage of Time P(A) that a Particular Fade Depth A(dB) is Exceeded from the Total Measurement time						
	P($A_{2\text{dB}}$) %	P($A_{5\text{dB}}$) %	P($A_{10\text{dB}}$) %	P($A_{15\text{dB}}$) %	P($A_{20\text{dB}}$) %	P($A_{30\text{dB}}$) %	P($A_{40\text{dB}}$) %
01 / 04	100	100	100	100	100	100	31.549
02 / 04	100	100	100	100	100	100	32.453
03 / 04	100	100	100	100	100	100	31.176
04 / 04	100	100	100	100	100	100	30.042
05 / 04	0.107	0	0	0	0	0	0
09 / 04	0	0	0	0	0	0	0
10 / 04	0	0	0	0	0	0	0
11 / 04	0	0	0	0	0	0	0
12 / 04	0	0	0	0	0	0	0

Table 4.4 (b) Percentage of Exceedance Probabilities for the Days in April 2004 Measurement

Date	Percentage of Time P(A) that a Particular Fade Depth A(dB) is Exceeded from the Total Measurement time						
	P(A _{2dB}) %	P(A _{5dB}) %	P(A _{10dB}) %	P(A _{15dB}) %	P(A _{20dB}) %	P(A _{30dB}) %	P(A _{40dB}) %
13 / 04	0	0	0	0	0	0	0
14 / 04	0	0	0	0	0	0	0
15 / 04	24.826	0	0	0	0	0	0
16 / 04	0.348	0	0	0	0	0	0
17 / 04	0	0	0	0	0	0	0
18 / 04	0	0	0	0	0	0	0
19 / 04	0.139	0	0	0	0	0	0
20 / 04	0.069	0	0	0	0	0	0
21 / 04	0	0	0	0	0	0	0
22 / 04	0.069	0	0	0	0	0	0
23 / 04	0.905	0	0	0	0	0	0
24 / 04	0.208	0	0	0	0	0	0
25 / 04	6.319	0	0	0	0	0	0
28 / 04	0	0	0	0	0	0	0
29 / 04	0	0	0	0	0	0	0
30 / 04	17.954	0	0	0	0	0	0

It can be observed from Table 4.4 above that the early days in April (i.e. April 1st – April 4th) has 100 % exceedance probability at almost all the fade depths. This shows that the LOS link is down and not running for this period. This will be put into consideration when analyzing this month in section 4.3.

4.2.10 Daily Signal Level Analysis for May

The analysis for the month of May follow the same trend as discussed for the previous months. For this month, there exist thirty-one (31) days of clear-air signal level measurement for analysis. This

shows that every day in this month is a clear-air day and available for analysis. The probability distribution is determined for the value of power -43.82 dBm where its maximum value occurs (see Figure 4.4). Five fade depth levels is also analyzed for this month as was done for the other months. Determination of the percentage of exceedance for these five fade depths is shown for two days here, while the results for the remaining twenty-nine days is shown in Table 4.5 (a) and (b) below.

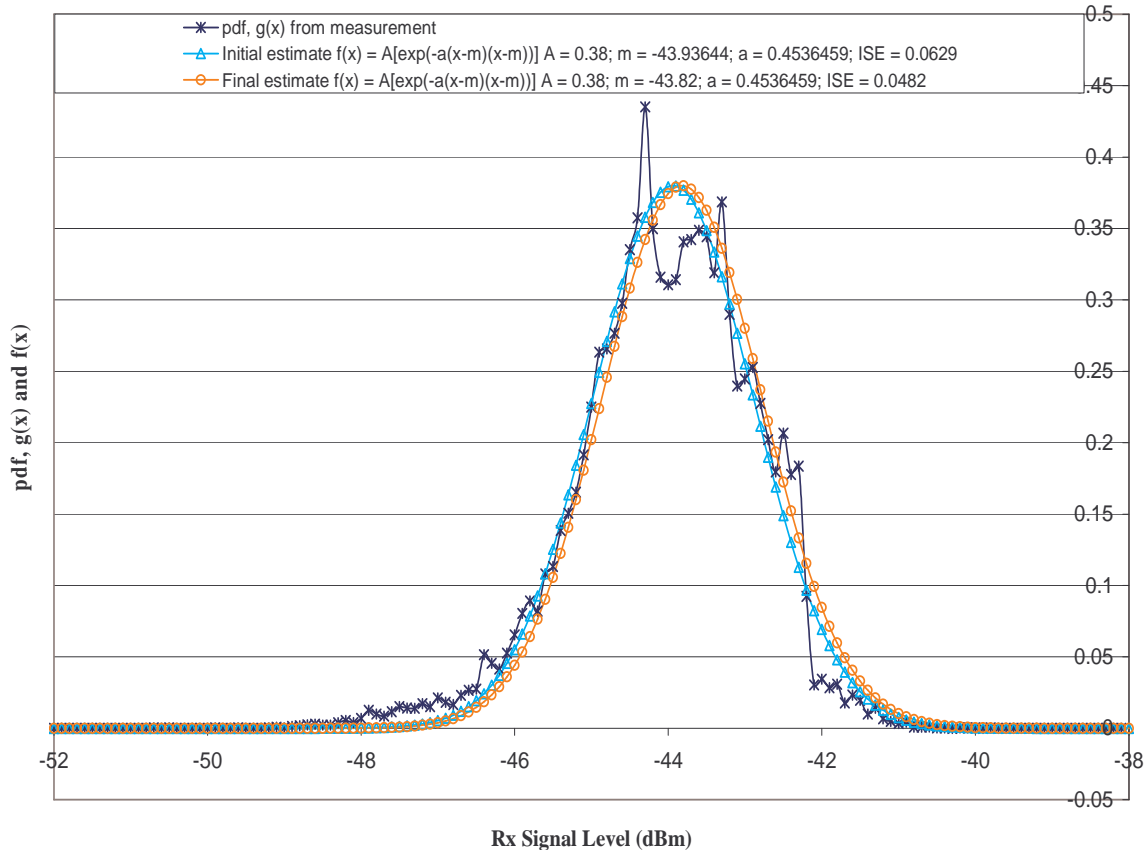


Figure 4.4 Measured and Estimated pdf, $g(x)$ and $f(x)$ for Rx Signal Level Measurement, May 2004

4.2.11 May 3 2004

From the signal level measurement and analysis, the following information is obtainable for May 3 2004.

Probability (Fade depth ≥ 2 dB) $\triangleq P(A_{2\text{dB}})$, $A_{2\text{dB}}$ is exceeded for 0 minute;

Probability (Fade depth ≥ 5 dB) $\triangleq P(A_{5\text{dB}})$, $A_{5\text{dB}}$ is exceeded for 0 minutes;

Probability (Fade depth ≥ 10 dB) $\triangleq P(A_{10\text{dB}})$, $A_{10\text{dB}}$ is exceeded for 0 minutes;

Probability (Fade depth ≥ 15 dB) $\triangleq P(A_{15\text{dB}})$, $A_{15\text{dB}}$ is exceeded for 0 minutes;

Probability (Fade depth ≥ 20 dB) $\triangleq P(A_{20\text{dB}})$, $A_{20\text{dB}}$ is exceeded for 0 minutes;
 Probability (Fade depth ≥ 30 dB) $\triangleq P(A_{30\text{dB}})$, $A_{30\text{dB}}$ is exceeded for 0 minutes;
 Probability (Fade depth ≥ 15 dB) $\triangleq P(A_{15\text{dB}})$, $A_{15\text{dB}}$ is exceeded for 0 minutes.

There is no faded signal for this day. The entire signals transmitted are within the average minimum threshold for the month. Hence, all the transmitted signals are received for this day.

4.2.12 May 27 2004

Similar procedure to that used in section 4.2.11 is used for calculation for May 27. The information available for this day is as follows:

Probability (Fade depth ≥ 2 dB) $\triangleq P(A_{2\text{dB}})$, $A_{2\text{dB}}$ is exceeded for 316 minute;
 Probability (Fade depth ≥ 5 dB) $\triangleq P(A_{5\text{dB}})$, $A_{5\text{dB}}$ is exceeded for 52 minutes;
 Probability (Fade depth ≥ 10 dB) $\triangleq P(A_{10\text{dB}})$, $A_{10\text{dB}}$ is exceeded for 52 minutes;
 Probability (Fade depth ≥ 15 dB) $\triangleq P(A_{15\text{dB}})$, $A_{15\text{dB}}$ is exceeded for 50 minutes;
 Probability (Fade depth ≥ 20 dB) $\triangleq P(A_{20\text{dB}})$, $A_{20\text{dB}}$ is exceeded for 50 minutes;
 Probability (Fade depth ≥ 30 dB) $\triangleq P(A_{30\text{dB}})$, $A_{30\text{dB}}$ is exceeded for 50 minutes;
 Probability (Fade depth ≥ 15 dB) $\triangleq P(A_{15\text{dB}})$, $A_{15\text{dB}}$ is exceeded for 0 minutes.

There exist six different fade depth levels recorded for this day as observed from the above. The percentage of exceedance probabilities for these six fade depths and for the remaining days in the month are calculated using (4.1) and displayed in Table 4.5 below.

Table 4.5 (a) Percentage of Exceedance Probabilities for the Days in May 2004 Measurement

Date	Percentage of Time P(A) that a Particular Fade Depth A(dB) is Exceeded from the Total Measurement time						
	P(A _{2dB}) %	P(A _{5dB}) %	P(A _{10dB}) %	P(A _{15dB}) %	P(A _{20dB}) %	P(A _{30dB}) %	P(A _{40dB}) %
01 / 05	0	0	0	0	0	0	0
02 / 05	1.739	0	0	0	0	0	0
03 / 05	0	0	0	0	0	0	0
04 / 05	0	0	0	0	0	0	0
06 / 05	0	0	0	0	0	0	0
07 / 05	9.812	0	0	0	0	0	0
08 / 05	12.847	0	0	0	0	0	0
09 / 05	23.066	0	0	0	0	0	0
10 / 05	17.778	0	0	0	0	0	0
11 / 05	8.826	0	0	0	0	0	0
12 / 05	6.964	0	0	0	0	0	0
13 / 05	0	0	0	0	0	0	0
14 / 05	0	0	0	0	0	0	0
15 / 05	0	0	0	0	0	0	0
16 / 05	0.278	0	0	0	0	0	0
17 / 05	0.695	0	0	0	0	0	0
18 / 05	19.541	17.803	17.803	17.803	17.803	17.803	1.391
19 / 05	35.421	35.282	35.282	35.282	35.282	35.282	2.923
20 / 05	8.820	2.550	2.550	2.550	2.550	2.550	0.106

Table 4.5 (b) Percentage of Exceedance Probabilities for the Days in May 2004 Measurement

Date	Percentage of Time P(A) that a Particular Fade Depth A(dB) is Exceeded from the Total Measurement time						
	P(A _{2dB}) %	P(A _{5dB}) %	P(A _{10dB}) %	P(A _{15dB}) %	P(A _{20dB}) %	P(A _{30dB}) %	P(A _{40dB}) %
21 / 05	8.705	3.343	3.343	3.203	3.203	3.064	0
22 / 05	4.169	3.544	3.475	3.475	3.475	3.475	0
23 / 05	11.482	11.065	11.065	11.065	11.065	10.856	0
24 / 05	33.426	19.805	19.805	19.805	19.805	19.805	0
25 / 05	33.704	17.721	17.651	17.651	17.651	17.512	0
26 / 05	41.475	4.941	4.941	4.871	4.871	4.802	4.802
27 / 05	21.975	3.616	3.616	3.477	3.477	3.477	0
28 / 05	5.003	4.169	4.169	4.169	4.169	4.100	0
29 / 05	7.794	3.827	3.827	3.688	3.688	3.688	0
30 / 05	10.556	3.819	3.75	3.75	3.75	3.611	0
31 / 05	17.606	1.322	1.322	1.322	1.322	1.322	0

4.2.13 Daily Signal Level Analysis for June

The analysis for the month of June is not different from the previous months. The average minimum threshold clear-air signal level for this month determined from the probability distribution (see Figure 4.5) is -45.8 dBm. The total clear-air signal measurement days available for analysis in June is sixteen days (see appendix D, Table D.5). Analyses are done for all the sixteen days but only two days are shown here while results of the remaining fourteen days are presented in Table 4.6.

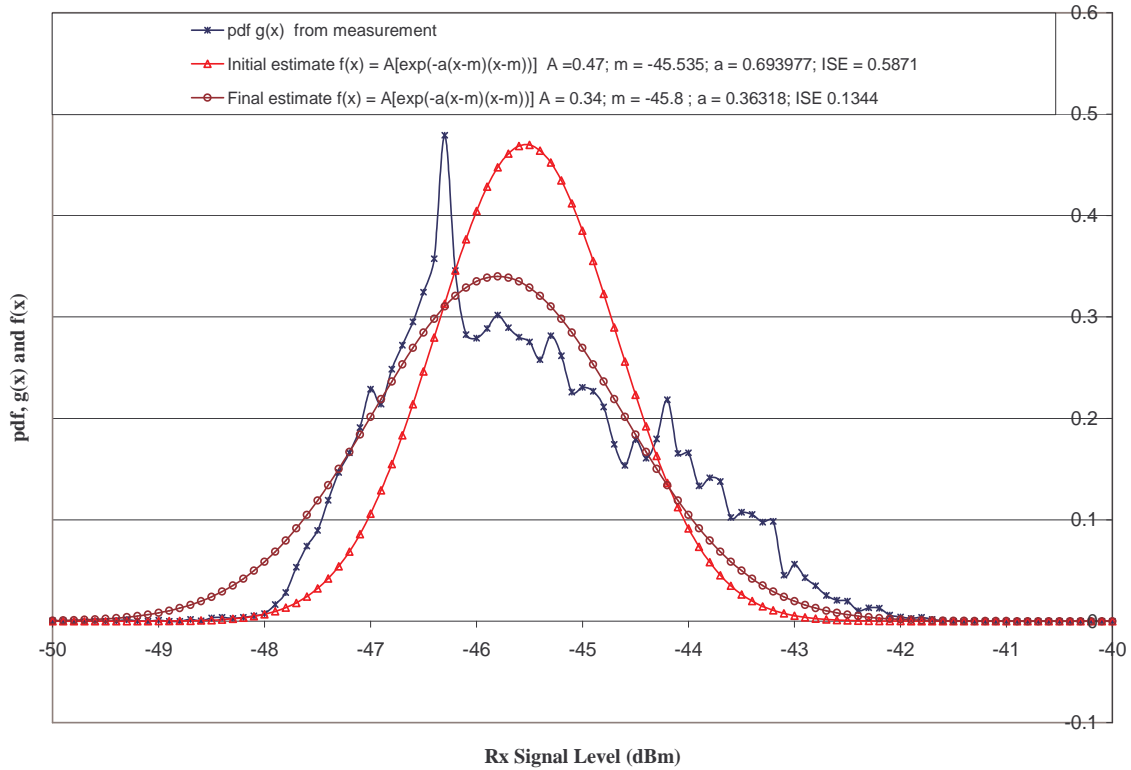


Figure 4.5 Measured and Estimated pdf, $g(x)$ and $f(x)$ for Rx Signal Level Measurement, June 2004

4.2.14 June 3 2004

The information available for the analysis carried out for June 3 is as follows:

Probability (Fade depth ≥ 2 dB) $\triangleq P(A_{2\text{dB}}, A_{2\text{dB}}$ is exceeded for 231 minute;

Probability (Fade depth ≥ 5 dB) $\triangleq P(A_{5\text{dB}}, A_{5\text{dB}}$ is exceeded for 231 minutes;

Probability (Fade depth ≥ 10 dB) $\triangleq P(A_{10\text{dB}}, A_{10\text{dB}}$ is exceeded for 230 minutes;

Probability (Fade depth ≥ 15 dB) $\triangleq P(A_{15\text{dB}}, A_{15\text{dB}}$ is exceeded for 229 minutes;

Probability (Fade depth ≥ 20 dB) $\triangleq P(A_{20\text{dB}}, A_{20\text{dB}}$ is exceeded for 229 minutes;

Probability (Fade depth ≥ 30 dB) $\triangleq P(A_{30\text{dB}}, A_{30\text{dB}}$ is exceeded for 229 minutes;

Probability (Fade depth ≥ 15 dB) $\triangleq P(A_{15\text{dB}}, A_{15\text{dB}}$ is exceeded for 0 minutes.

There exist six different fade depth levels recorded for this day as observed from the above.

4.2.15 June 20 2004

Similar procedure to that used in section 4.2.14 is used to do the calculation for June 20. The information available for this day is as follow:

Probability (Fade depth ≥ 2 dB) $\triangleq P(A_{2\text{dB}})$, $A_{2\text{dB}}$ is exceeded for 121 minute;
 Probability (Fade depth ≥ 5 dB) $\triangleq P(A_{5\text{dB}})$, $A_{5\text{dB}}$ is exceeded for 0 minutes;
 Probability (Fade depth ≥ 10 dB) $\triangleq P(A_{10\text{dB}})$, $A_{10\text{dB}}$ is exceeded for 0 minutes;
 Probability (Fade depth ≥ 15 dB) $\triangleq P(A_{15\text{dB}})$, $A_{15\text{dB}}$ is exceeded for 0 minutes;
 Probability (Fade depth ≥ 20 dB) $\triangleq P(A_{20\text{dB}})$, $A_{20\text{dB}}$ is exceeded for 0 minutes;
 Probability (Fade depth ≥ 30 dB) $\triangleq P(A_{30\text{dB}})$, $A_{30\text{dB}}$ is exceeded for 0 minutes;
 Probability (Fade depth ≥ 15 dB) $\triangleq P(A_{15\text{dB}})$, $A_{15\text{dB}}$ is exceeded for 0 minutes.

There exists only one fade depth level for this particular day. The result of the analysis for all the days in the month of June is calculated using (4.1) and presented in Table 4.6 below.

Table 4.6 (a) Percentage of Exceedance Probabilities for the Days in June 2004 Measurement

Date	Percentage of Time P(A) that a Particular Fade Depth A(dB) is Exceeded from the Total Measurement time						
	P($A_{2\text{dB}}$) %	P($A_{5\text{dB}}$) %	P($A_{10\text{dB}}$) %	P($A_{15\text{dB}}$) %	P($A_{20\text{dB}}$) %	P($A_{30\text{dB}}$) %	P($A_{40\text{dB}}$) %
01 / 06	10.385	10.385	10.385	10.385	10.385	10.192	0
03 / 06	16.075	16.075	16.006	15.936	15.936	15.936	0
06 / 06	16.134	16.134	16.134	16.064	16.064	16.064	0
08 / 06	17.189	15.588	15.588	15.588	15.588	15.588	0
09 / 06	9.243	9.173	9.173	9.104	9.104	9.034	0
10 / 06	0.625	0	0	0	0	0	0
12 / 06	0.139	0	0	0	0	0	0
13 / 06	0	0	0	0	0	0	0
14 / 06	0	0	0	0	0	0	0

Table 4.6 (b) Percentage of Exceedance Probabilities for the Days in June 2004 Measurement

Date	Percentage of Time P(A) that a Particular Fade Depth A(dB) is Exceeded from the Total Measurement time						
	P(A _{2dB})	P(A _{5dB})	P(A _{10dB})	P(A _{15dB})	P(A _{20dB})	P(A _{30dB})	P(A _{40dB})
	%	%	%	%	%	%	%
15 / 06	0.069	0	0	0	0	0	0
20 / 06	8.409	0	0	0	0	0	0
21 / 06	3.614	0	0	0	0	0	0
22 / 06	0.069	0	0	0	0	0	0
24 / 06	0.140	0	0	0	0	0	0
29 / 06	3.561	0	0	0	0	0	0
30 / 06	2.575	0	0	0	0	0	0

4.2.16 Daily Signal Level Analysis for July

Analysis for the month of July follows similar trend to the previous months that were analyzed. The average minimum threshold received signal level estimated from the probability distribution plot as observed from Figure 4.6 is – 45.4 dBm. There exist twelve days or data set available for analysis for this month as observed from appendix D (see Table D.6). The analysis was done to determine the percentage of time P(A) that a particular fade depth A(dB) occurs from total measurement time. Five different fade depth levels are analyzed as was done for the other months. The calculation for two of the eight days analyzed is shown here (see sections 4.2.17 and 4.2.18) while the results for the remaining days are shown in Table 4.7.

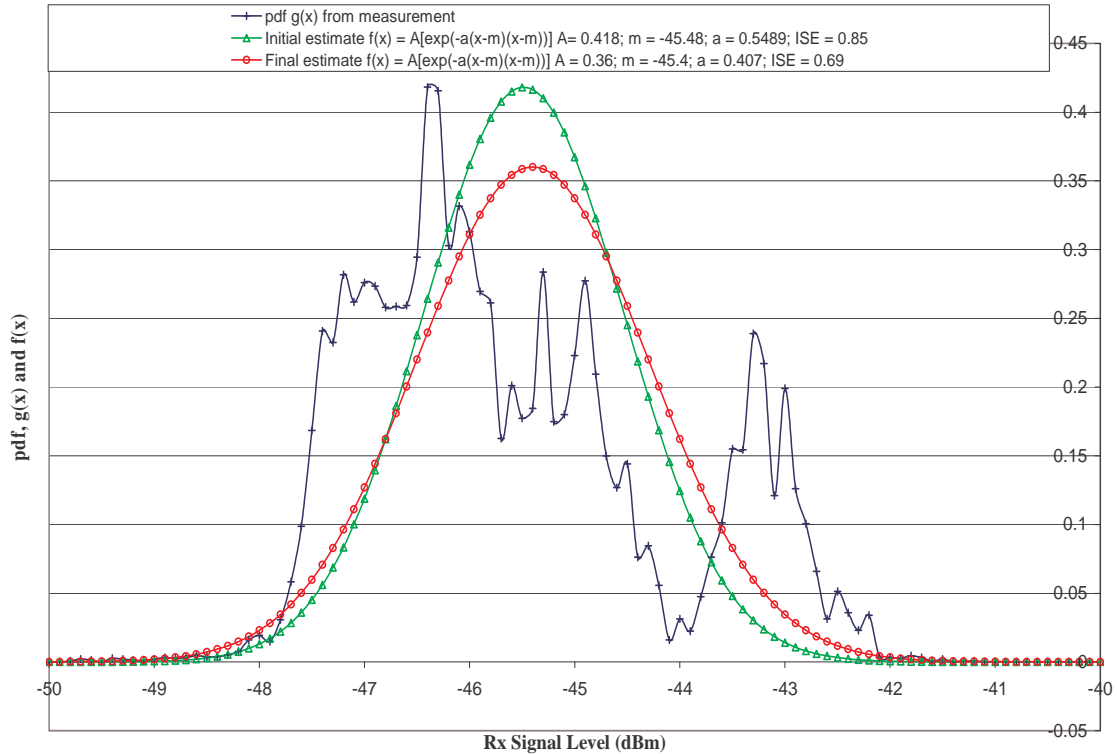


Figure 4.6 Measured and Estimated pdf, $g(x)$ and $f(x)$ for Rx Signal Level Measurement, July 2004

4.2.17 July 4 2004

The information available for the analysis done for July 4 are the following:

- Probability (Fade depth ≥ 2 dB) $\triangleq P(A_{2\text{dB}}, A_{2\text{dB}}$ is exceeded for 598 minutes;
- Probability (Fade depth ≥ 5 dB) $\triangleq P(A_{5\text{dB}}, A_{5\text{dB}}$ is exceeded for 33 minutes;
- Probability (Fade depth ≥ 10 dB) $\triangleq P(A_{10\text{dB}}, A_{10\text{dB}}$ is exceeded for 5 minutes;
- Probability (Fade depth ≥ 15 dB) $\triangleq P(A_{15\text{dB}}, A_{15\text{dB}}$ is exceeded for 0 minutes;
- Probability (Fade depth ≥ 20 dB) $\triangleq P(A_{20\text{dB}}, A_{20\text{dB}}$ is exceeded for 0 minutes;
- Probability (Fade depth ≥ 30 dB) $\triangleq P(A_{30\text{dB}}, A_{30\text{dB}}$ is exceeded for 0 minutes;
- Probability (Fade depth ≥ 15 dB) $\triangleq P(A_{15\text{dB}}, A_{15\text{dB}}$ is exceeded for 0 minutes.

Three fade depth levels are recorded for this day as seen above.

4.2.18 July 22 2004

The information available for this day as obtained from the analysis done for the day is as follows:

Probability (Fade depth ≥ 2 dB) $\triangleq P(A_{2\text{dB}})$, $A_{2\text{dB}}$ is exceeded for 17 minutes;
 Probability (Fade depth ≥ 5 dB) $\triangleq P(A_{5\text{dB}})$, $A_{5\text{dB}}$ is exceeded for 0 minutes;
 Probability (Fade depth ≥ 10 dB) $\triangleq P(A_{10\text{dB}})$, $A_{10\text{dB}}$ is exceeded for 0 minutes;
 Probability (Fade depth ≥ 15 dB) $\triangleq P(A_{15\text{dB}})$, $A_{15\text{dB}}$ is exceeded for 0 minutes;
 Probability (Fade depth ≥ 20 dB) $\triangleq P(A_{20\text{dB}})$, $A_{20\text{dB}}$ is exceeded for 0 minutes;
 Probability (Fade depth ≥ 30 dB) $\triangleq P(A_{30\text{dB}})$, $A_{30\text{dB}}$ is exceeded for 0 minutes;
 Probability (Fade depth ≥ 15 dB) $\triangleq P(A_{15\text{dB}})$, $A_{15\text{dB}}$ is exceeded for 0 minutes.

Only one fade depth level is recorded for this day as seen above. The percentage of exceedance for all the days in this month is calculated using (4.1) and presented in Table 4.7

Table 4.7 Percentage of Exceedance Probabilities for the Days in July 2004 Measurement

Date	Percentage of Time P(A) that a Particular Fade Depth A(dB) is Exceeded from the Total Measurement time						
	P($A_{2\text{dB}}$) %	P($A_{5\text{dB}}$) %	P($A_{10\text{dB}}$) %	P($A_{15\text{dB}}$) %	P($A_{20\text{dB}}$) %	P($A_{30\text{dB}}$) %	P($A_{40\text{dB}}$) %
01 / 07	19.319	0	0	0	0	0	0
02 / 07	12.161	0	0	0	0	0	0
03 / 07	4.378	0	0	0	0	0	0
04 / 07	41.557	2.293	0.347	0	0	0	0
06 / 07	0.278	0	0	0	0	0	0
07 / 07	0.069	0	0	0	0	0	0
08 / 07	0	0	0	0	0	0	0
21 / 07	0.769	0	0	0	0	0	0
22 / 07	1.181	0	0	0	0	0	0
23 / 07	0.905	0	0	0	0	0	0
30 / 07	0	0	0	0	0	0	0
31 / 07	0	0	0	0	0	0	0

4.2.19 Daily Signal Level Analysis for August

The month of August has sixteen days for analysis (see appendix D, Table D.7). The analysis for August follow similar trend as for the previous months analyzed. Five fade depth levels are analyzed for August. The average minimum threshold signal level estimated from the probability distribution

in Figure 4.7 for August is -44.65 dBm. Two sample analyses for two different days in the month is shown here (see sections 4.2.20 and 4.2.21) while the results for the remaining fourteen days are displayed in Table 4.8.

4.2.20 August 1 2004

On the 1st of August, the measurement information available after analysis is as follows:

Probability (Fade depth \geq 2 dB) \triangleq $P(A_{2\text{dB}}, A_{2\text{dB}}$ is exceeded for 0 minute;

Probability (Fade depth \geq 5 dB) \triangleq $P(A_{5\text{dB}}, A_{5\text{dB}}$ is exceeded for 0 minutes;

Probability (Fade depth \geq 10 dB) \triangleq $P(A_{10\text{dB}}, A_{10\text{dB}}$ is exceeded for 0 minutes;

Probability (Fade depth \geq 15 dB) \triangleq $P(A_{15\text{dB}}, A_{15\text{dB}}$ is exceeded for 0 minutes;

Probability (Fade depth \geq 20 dB) \triangleq $P(A_{20\text{dB}}, A_{20\text{dB}}$ is exceeded for 0 minutes;

Probability (Fade depth \geq 30 dB) \triangleq $P(A_{30\text{dB}}, A_{30\text{dB}}$ is exceeded for 0 minutes;

Probability (Fade depth \geq 15 dB) \triangleq $P(A_{15\text{dB}}, A_{15\text{dB}}$ is exceeded for 0 minutes.

There is no faded signal for all the seven fade depth levels for this day as can be observed above. This means that the entire received signals are within the minimum average threshold for the month in this day.

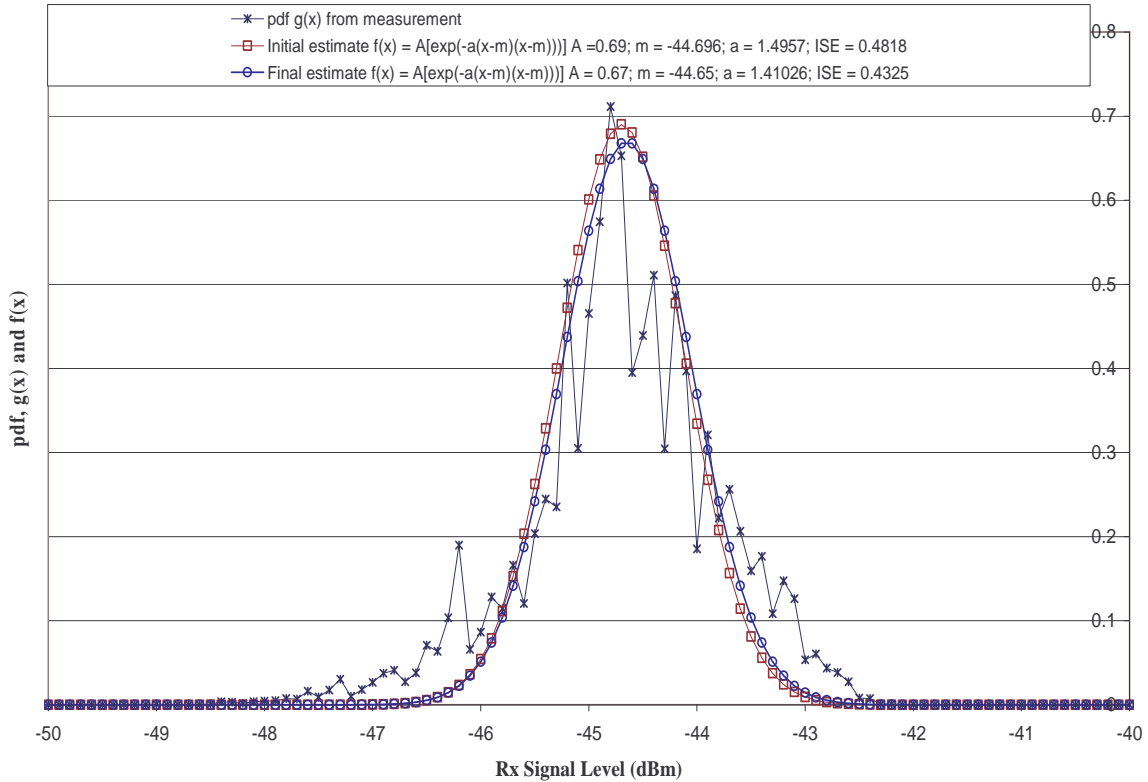


Figure 4.7 Measured and Estimated pdf, $g(x)$ and $f(x)$ for Rx Signal Level Measurement, August 2004

4.2.21 August 21 2004

The information available for the 21st of August after analysis from excel spread sheet is as follows:

Probability (Fade depth ≥ 2 dB) $\triangleq P(A_{2\text{dB}}, A_{2\text{dB}}$ is exceeded for 60 minutes;

Probability (Fade depth ≥ 5 dB) $\triangleq P(A_{5\text{dB}}, A_{5\text{dB}}$ is exceeded for 0 minutes;

Probability (Fade depth ≥ 10 dB) $\triangleq P(A_{10\text{dB}}, A_{10\text{dB}}$ is exceeded for 0 minutes;

Probability (Fade depth ≥ 15 dB) $\triangleq P(A_{15\text{dB}}, A_{15\text{dB}}$ is exceeded for 0 minutes;

Probability (Fade depth ≥ 20 dB) $\triangleq P(A_{20\text{dB}}, A_{20\text{dB}}$ is exceeded for 0 minutes;

Probability (Fade depth ≥ 30 dB) $\triangleq P(A_{30\text{dB}}, A_{30\text{dB}}$ is exceeded for 0 minutes;

Probability (Fade depth ≥ 15 dB) $\triangleq P(A_{15\text{dB}}, A_{15\text{dB}}$ is exceeded for 0 minutes.

Only one fade depth level is recorded for this day. The percentage of exceedance for all the days in this month is calculated using (4.1) and presented in Table 4.8 below.

Table 4.8 Percentage of Exceedance Probabilities for the Days in August 2004 Measurement

Date	Percentage of Time P(A) that a Particular Fade Depth A(dB) is Exceeded from the Total Measurement time						
	P(A _{2dB}) %	P(A _{5dB}) %	P(A _{10dB}) %	P(A _{15dB}) %	P(A _{20dB}) %	P(A _{30dB}) %	P(A _{40dB}) %
01 / 08	0	0	0	0	0	0	0
02 / 08	0	0	0	0	0	0	0
03 / 08	15.358	0	0	0	0	0	0
05 / 08	0	0	0	0	0	0	0
06 / 08	0	0	0	0	0	0	0
07 / 08	0	0	0	0	0	0	0
08 / 08	0.139	0	0	0	0	0	0
09 / 08	0.069	0	0	0	0	0	0
10 / 08	0.139	0	0	0	0	0	0
12 / 08	0.695	0	0	0	0	0	0
15 / 08	8.061	0	0	0	0	0	0
16 / 08	6.185	0	0	0	0	0	0
17 / 08	10.076	0	0	0	0	0	0
18 / 08	0	0	0	0	0	0	0
19 / 08	10.007	0	0	0	0	0	0
21 / 08	5.970	0	0	0	0	0	0

4.2.22 Daily Signal Level Analysis for December

Twenty-three (23) days or data is available for analysis for the month of December. Seven fade depth levels are analyzed. The estimated average minimum threshold received signal level from the probability distribution plot of Figure 4.8 is -43.75 dBm for this month. The analysis follows similar trend to the previous months analyzed. Analysis of two sample days are shown here, while the result of the analysis for the remaining twenty-one days are presented in Table 4.9 below.

4.2.23 December 12 2004

From the signal level measurement and analysis done, the following information is obtainable for December 12 2004.

Probability (Fade depth ≥ 2 dB) $\triangleq P(A_{2\text{dB}})$, $A_{2\text{dB}}$ is exceeded for 0 minute;
 Probability (Fade depth ≥ 5 dB) $\triangleq P(A_{5\text{dB}})$, $A_{5\text{dB}}$ is exceeded for 0 minutes;
 Probability (Fade depth ≥ 10 dB) $\triangleq P(A_{10\text{dB}})$, $A_{10\text{dB}}$ is exceeded for 0 minutes;
 Probability (Fade depth ≥ 15 dB) $\triangleq P(A_{15\text{dB}})$, $A_{15\text{dB}}$ is exceeded for 0 minutes;
 Probability (Fade depth ≥ 20 dB) $\triangleq P(A_{20\text{dB}})$, $A_{20\text{dB}}$ is exceeded for 0 minutes;
 Probability (Fade depth ≥ 30 dB) $\triangleq P(A_{30\text{dB}})$, $A_{30\text{dB}}$ is exceeded for 0 minutes;
 Probability (Fade depth ≥ 15 dB) $\triangleq P(A_{15\text{dB}})$, $A_{15\text{dB}}$ is exceeded for 0 minutes.

There is no faded signal for all the seven fade depth levels for this day as can be observed above. This means that the entire received signals are within the minimum average threshold for the month in this day.

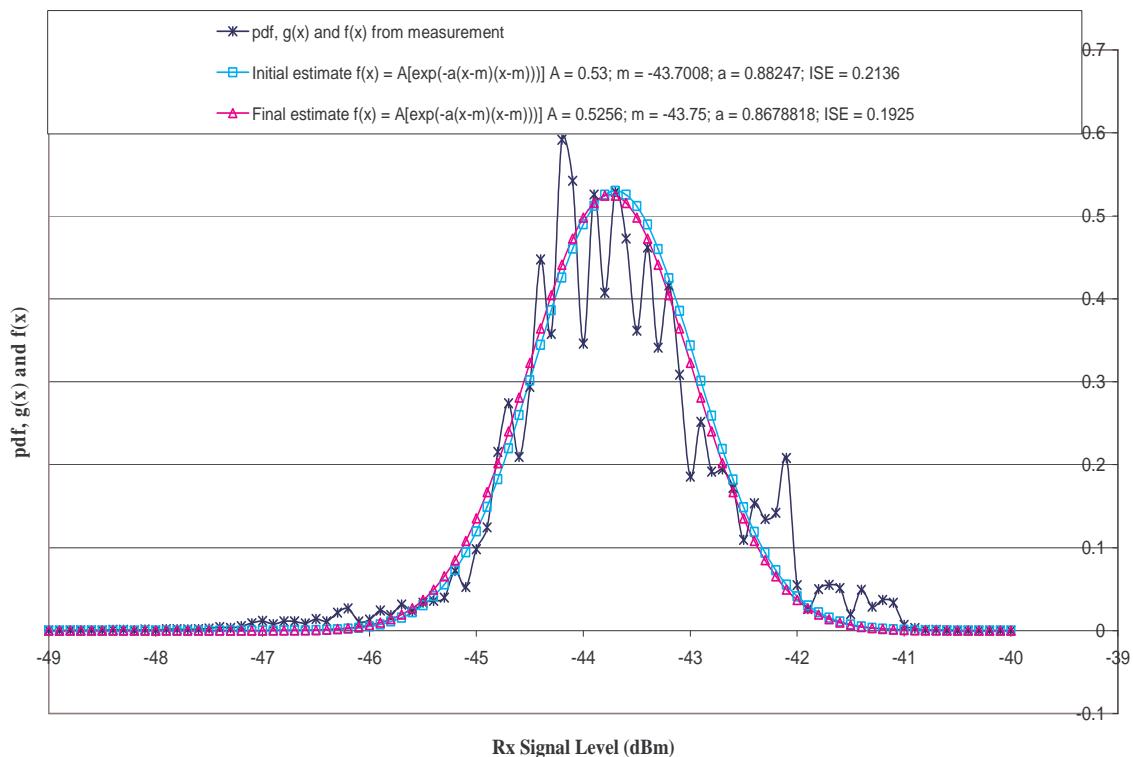


Figure 4.8 Measured and Estimated pdf, g(x) and f(x) for Rx Signal Level Measurement, December 2004

4.2.24 December 30 2004

The information available for the 30th of December after analysis from excel spread sheet is as follows:

- Probability (Fade depth \geq 2 dB) \triangleq P(A_{2dB}), A_{2dB} is exceeded for 326 minute;
- Probability (Fade depth \geq 5 dB) \triangleq P(A_{5dB}), A_{5dB} is exceeded for 202 minutes;
- Probability (Fade depth \geq 10 dB) \triangleq P(A_{10dB}), A_{10dB} is exceeded for 202 minutes;
- Probability (Fade depth \geq 15 dB) \triangleq P(A_{15dB}), A_{15dB} is exceeded for 202 minutes;
- Probability (Fade depth \geq 20 dB) \triangleq P(A_{20dB}), A_{20dB} is exceeded for 202 minutes;
- Probability (Fade depth \geq 30 dB) \triangleq P(A_{30dB}), A_{30dB} is exceeded for 123 minutes;
- Probability (Fade depth \geq 15 dB) \triangleq P(A_{15dB}), A_{15dB} is exceeded for 0 minutes.

There exist six different fade depth levels recorded for this day as observed from above. This is not a very promising day over the LOS link, as six out of the seven fade depth levels recorded signal fading. The percentage of exceedance probabilities for all the days in this month is calculated using (4.1) and the results are shown in Table 4.9 below.

Table 4.9 (a) Percentage of Exceedance Probabilities for the Days in December 2004 Measurement

Date	Percentage of Time P(A) that a Particular Fade Depth A(dB) is Exceeded from the Total Measurement time						
	P(A _{2dB}) %	P(A _{5dB}) %	P(A _{10dB}) %	P(A _{15dB}) %	P(A _{20dB}) %	P(A _{30dB}) %	P(A _{40dB}) %
02 / 12	0	0	0	0	0	0	0
03 / 12	0	0	0	0	0	0	0
04 / 12	14.941	0	0	0	0	0	0
05 / 12	0	0	0	0	0	0	0
09 / 12	0.347	0	0	0	0	0	0
10 / 12	0	0	0	0	0	0	0
11 / 12	0	0	0	0	0	0	0

Table 4.9 (b) Percentage of Exceedance Probabilities for the Days in December 2004 Measurement

Date	Percentage of Time P(A) that a Particular Fade Depth A(dB) is Exceeded from the Total Measurement time						
	P(A _{2dB}) %	P(A _{5dB}) %	P(A _{10dB}) %	P(A _{15dB}) %	P(A _{20dB}) %	P(A _{30dB}) %	P(A _{40dB}) %
12 / 12	0	0	0	0	0	0	0
13 / 12	0.069	0	0	0	0	0	0
14 / 12	10.445	0	0	0	0	0	0
15 / 12	2.431	0	0	0	0	0	0
16 / 12	0	0	0	0	0	0	0
17 / 12	1.599	0	0	0	0	0	0
19 / 12	0	0	0	0	0	0	0
20 / 12	0	0	0	0	0	0	0
21 / 12	9.040	0	0	0	0	0	0
22 / 12	3.127	1.250	0	0	0	0	0
25 / 12	1.597	0.069	0	0	0	0	0
26 / 12	0	0	0	0	0	0	0
28 / 12	4.861	0	0	0	0	0	0
29 / 12	0.069	0	0	0	0	0	0
30 / 12	22.639	14.028	14.028	14.028	14.028	8.542	0
31 / 12	6.042	0	0	0	0	0	0

4.3 Monthly Signal Level Analysis for Percentage of Time that a Particular Fade Depth is Exceeded

The next phase of the analysis is to scrutinize the available data and determine the percentage of exceedance probabilities for the seven fade depth levels from the total measurement time for each month. In order to achieve this stated goal, we check the total number of minutes that a particular fade depth occurs in a certain month. We then determine what percentage of the total measurement time for the month this is. We repeat this for each month in this section.

4.3.1 Monthly Signal Level Analysis for February

The signal level measurement plot for all the days in February is shown in Figure 4.9 below. One can see immediately from this figure whether there is signal squelching or not for the month. If there is, then this means the link is down within this squelching period. The total number of days that this squelching happen will be deducted from the total available measurement days for this month before further analysis is done. The procedure explained above is only done if the squelching is over an extended period (e.g. greater than 60 minutes in a day).

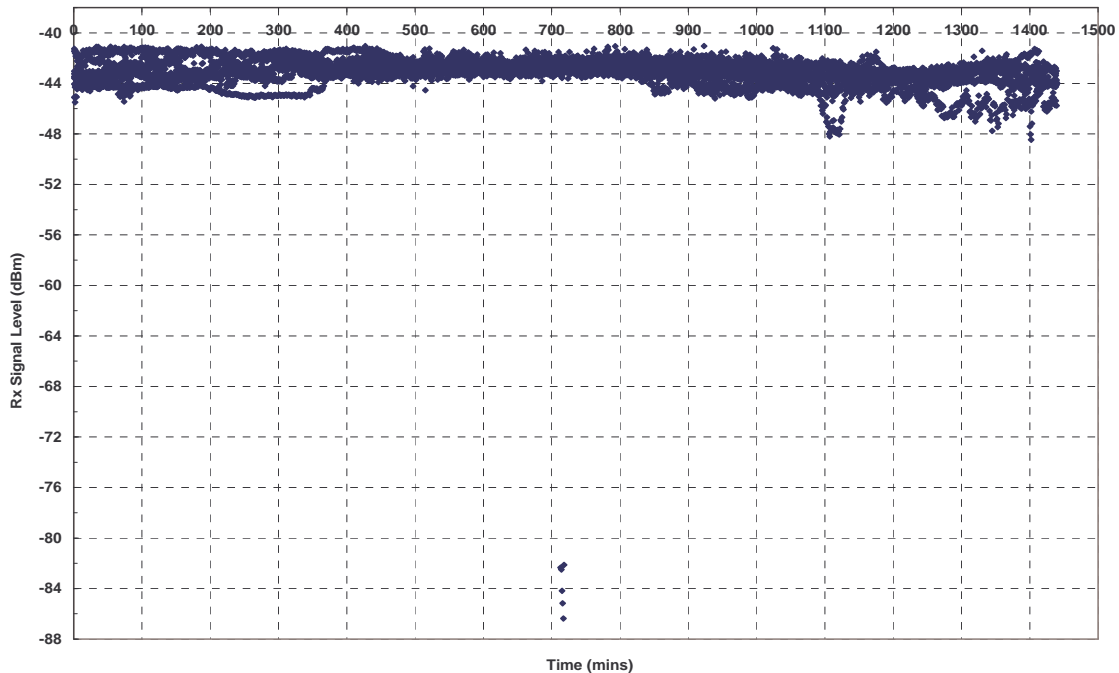


Figure 4.9 Clear-Air Signal Level Variation over 24hrs, February 2004, Durban

Table 4.10 Estimates of Measurement time at different Fade Depths in February 2004

Date	Total Measurement time at different Fade Depths for the Month						
	A _{2dB} (mins)	A _{5dB} (mins)	A _{10dB} (mins)	A _{15dB} (mins)	A _{20dB} (mins)	A _{30dB} (mins)	A _{40dB} (mins)
19 / 02	0	0	0	0	0	0	0
20 / 02	6	6	6	6	6	6	3
21 / 02	45	7	0	0	0	0	0
22 / 02	21	0	0	0	0	0	0
23 / 02	226	0	0	0	0	0	0
24 / 02	14	0	0	0	0	0	0
25 / 02	118	0	0	0	0	0	0
28 / 02	29	2	0	0	0	0	0
Total	459	15	6	6	6	6	3

As one can see from Figure 4.9 above, there is no squelching in the month of February 2004, we therefore continue with the analysis. Total measurement time in minutes for the seven fade depth levels for different days in the month of February is estimated as shown in Table 4.10 above.

Hence the percentages of time that the different fade depth levels occur from total measurement time in the month of February are shown in Figure 4.10 below.

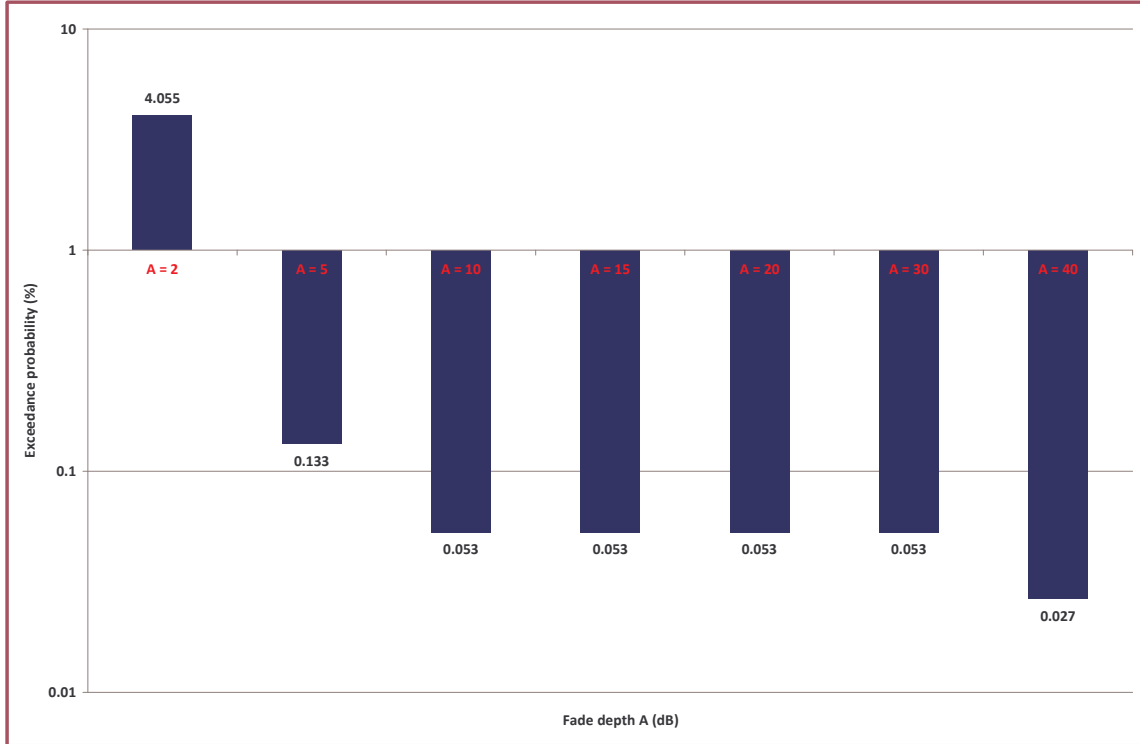


Figure 4.10 Fade Depth Exceedance Probability (%) for February 2004

The last stage is to compare the values of the required fade depth, for certain availability specification as given by ITU-R for Durban, with the measurement results over the link for this month. In order to achieve this, we check for the 99.99 % (or $A_{0.01}$) link availability specification. This is done by deducting the signal noise level (see Figure 3.9) from the average minimum signal threshold for the month (see. Figure 4.1) as follows:

$$A_{0.01} = -42.84 - (-82.14) = 39.3 \text{ dB}$$

This value of 39.3dB is quite comparable to the value of 40 dB determined Gopichund in [76] over a different for this specification over a similar link in Durban. This shows that for the month of February 99.99 % link availability is guarantee over this line-of-sight link.

4.3.2 Monthly Signal Level Analysis for March

A Similar procedure is adopted for the analysis in the month of March. The signal level measurement plot for all the days in March is shown in Figure 4.11 below.

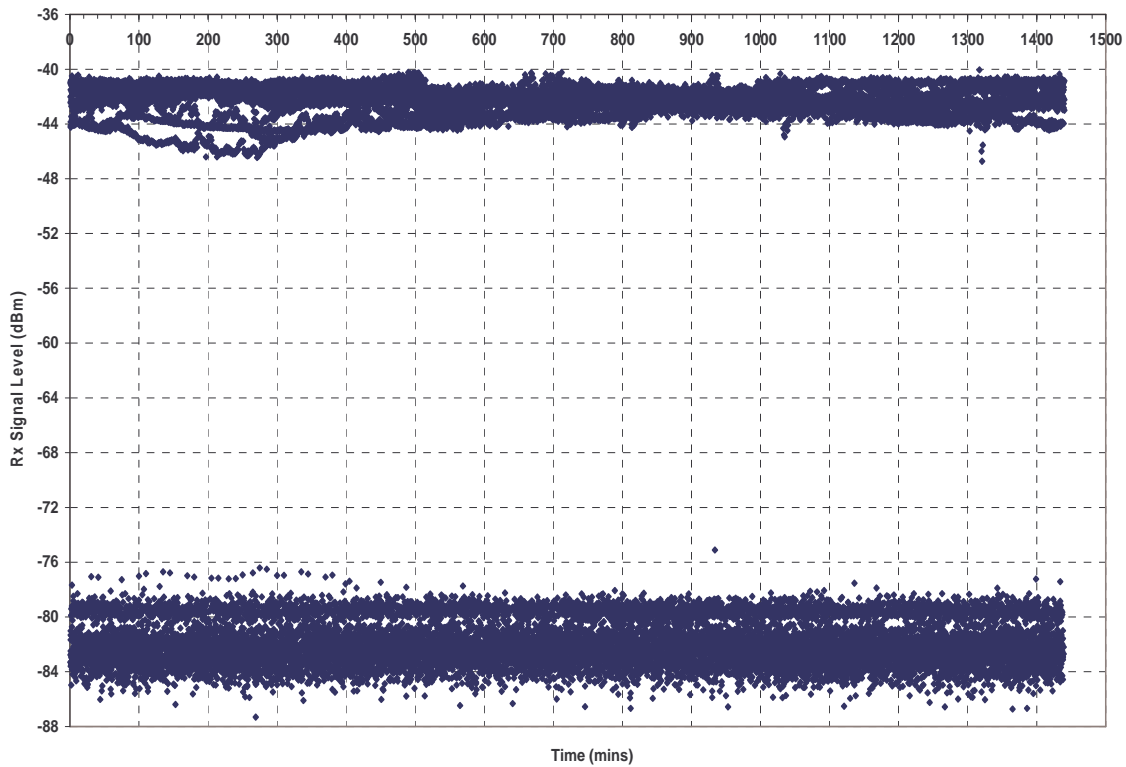


Figure 4.11 Clear-Air Signal Level Variation over 24hrs, March 2004, Durban

It can be observed that there is deep squelching for the month of March as defined by the noise floor level observed in Figure 4.11 above. We therefore take this into consideration in our analysis for this month as explained earlier in section 4.2.6. Total measurement time in minutes for the seven fade depth levels for different days in the month of March is estimated as shown in Table 4.11 (a) and (b) below.

Table 4.11 (a) Estimates of Measurement time at different Fade Depths in March 2004

Date	Total Measurement time at different Fade Depths for the Month						
	A _{2dB} (mins)	A _{5dB} (mins)	A _{10dB} (mins)	A _{15dB} (mins)	A _{20dB} (mins)	A _{30dB} (mins)	A _{40dB} (mins)
06 / 03	7	0	0	0	0	0	0
07 / 03	0	0	0	0	0	0	0
08 / 03	0	0	0	0	0	0	0

Table 4.11 (b) Estimates of Measurement time at different Fade Depths in March 2004

Date	Total Measurement time at different Fade Depths for the Month						
	A _{2dB} (mins)	A _{5dB} (mins)	A _{10dB} (mins)	A _{15dB} (mins)	A _{20dB} (mins)	A _{30dB} (mins)	A _{40dB} (mins)
09 / 03	13	0	0	0	0	0	0
10 / 03	26	26	26	26	26	26	0
13 / 03	0	0	0	0	0	0	0
14 / 03	0	0	0	0	0	0	0
15 / 03	0	0	0	0	0	0	0
16 / 03	128	0	0	0	0	0	0
17 / 03	55	0	0	0	0	0	0
18 / 03	314	0	0	0	0	0	0
19 / 03	1162	696	696	696	696	696	296
20 / 03	1438	1438	1438	1438	1438	1438	821
21 / 03	1438	1438	1438	1438	1438	1438	831
22 / 03	1437	1437	1437	1437	1437	1437	844
25 / 03	1438	1438	1438	1438	1438	1438	801
26 / 03	1438	1438	1438	1438	1438	1438	784
27 / 03	1436	1436	1436	1436	1436	1436	786
28 / 03	1439	1439	1439	1439	1439	1439	804
29 / 03	1437	1437	1437	1437	1437	1437	798
30 / 03	1439	1439	1439	1439	1439	1439	842
31 / 03	1437	1437	1437	1437	1437	1437	824
Total	543	26	26	26	26	26	0

The squelching period is observed to be from March 19 till the end of the month (see Table 4.11). These days are not included in the calculation of the total minutes in the last row of Table 4.11 because the link is down over these days. The percentages of time that the different fade depth levels occur from total measurement time in the month of March are shown in Figure 4.12 below.

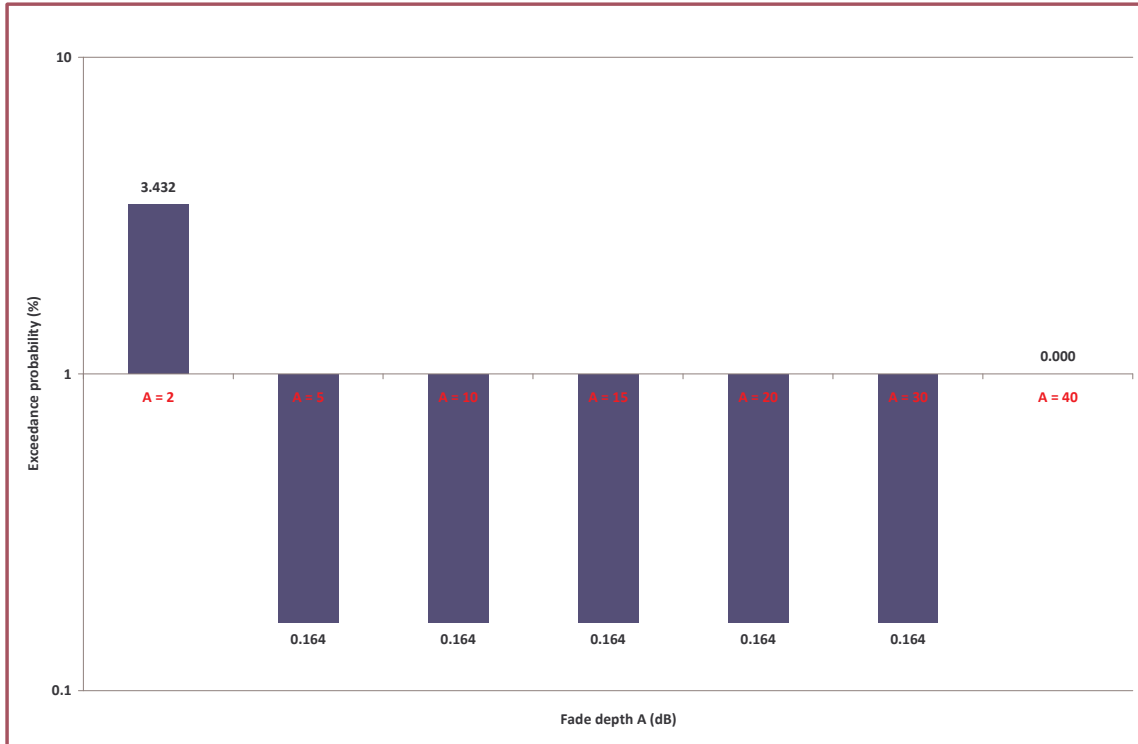


Figure 4.12 Fade Depth Exceedance Probability (%) for March 2004

We now compare the values of the required fade depth, for certain availability specification as given by ITU-R for Durban, with the measurement results over the link for this month. In order to achieve this, we check for the 99.99 % (or $A_{0.01}$) link availability specification. This is done by deducting the signal noise level (see Figure 4.11) from the average minimum signal threshold for the month (see Figure 4.2) as follows:

$$A_{0.01} = -42 - (-82) = 40 \text{ dB}$$

This value of 40 dB is the same value determined by Gopichund in [76] for this specification over similar link in Durban. This shows that for the month of March 99.99 % link availability is guaranteed over this line-of-sight link. In addition Figure 4.12 above shows 100 % link availability for the month of March for $A = 40$ dB.

4.3.3 Monthly Signal Level Analysis for April

For the month of April, we have adopted similar procedure for the analysis. The signal level measurement plot for all the days in April is shown in Figure 4.13 below.

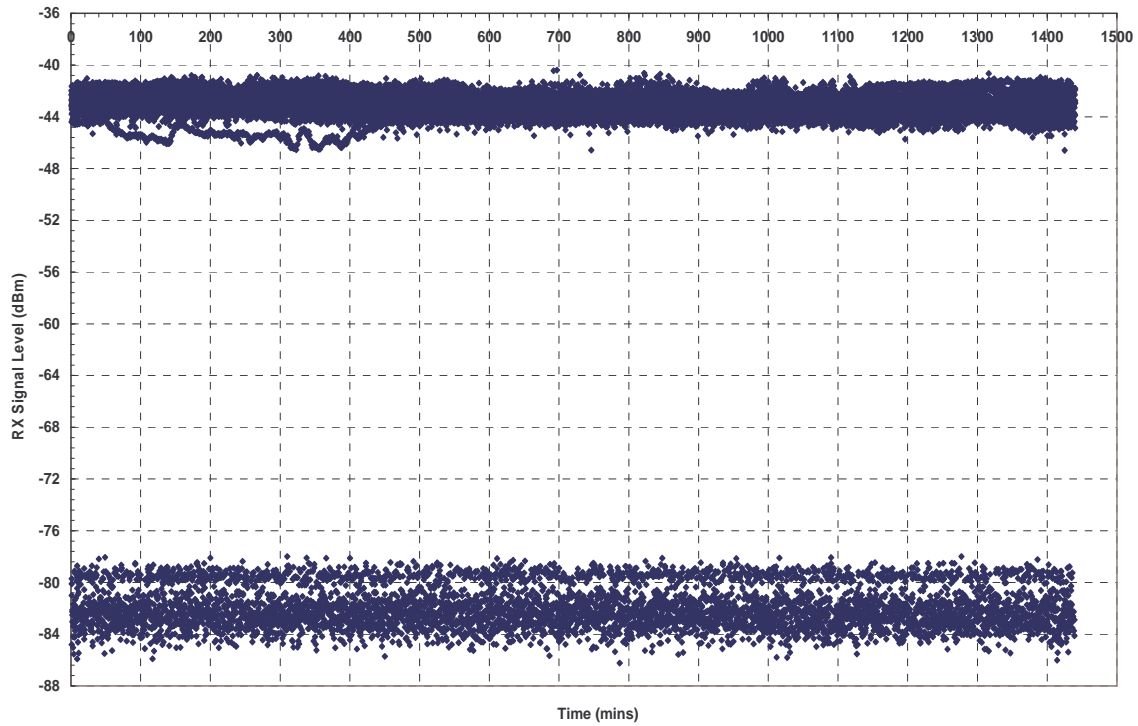


Figure 4.13 Clear-Air Signal Level Variation over 24hrs, April 2004, Durban

It can be observed again, that there is extreme squelching for the month of April as defined by the noise floor level observed in Figure 4.13 above. We therefore take this into consideration in our analysis for this month as explained earlier in section 4.2.6. Total measurement time in minutes for the seven fade depth levels for different days in the month of April is estimated as shown in Table 4.12 (a) and (b) below.

From this table, one can see the number of days during which this squelching occurs, and we will use this information to determine the link availability at 99.99 % specification.

Table 4.12 (a) Estimates of Measurement time at different Fade Depths in April 2004

Date	Total Measurement time at different Fade Depths for the Month						
	A _{2dB} (mins)	A _{5dB} (mins)	A _{10dB} (mins)	A _{15dB} (mins)	A _{20dB} (mins)	A _{30dB} (mins)	A _{40dB} (mins)
01 / 04	1439	1439	1439	1439	1439	1439	454
02 / 04	1439	1439	1439	1439	1439	1439	467
03 / 04	1437	1437	1437	1437	1437	1437	448
04 / 04	1438	1438	1438	1438	1438	1438	432
05 / 04	1	0	0	0	0	0	0
09 / 04	0	0	0	0	0	0	0
10 / 04	0	0	0	0	0	0	0
11 / 04	0	0	0	0	0	0	0
12 / 04	0	0	0	0	0	0	0
13 / 04	0	0	0	0	0	0	0
14 / 04	0	0	0	0	0	0	0
15 / 04	357	0	0	0	0	0	0
16 / 04	5	0	0	0	0	0	0
17 / 04	0	0	0	0	0	0	0
18 / 04	0	0	0	0	0	0	0
19 / 04	2	0	0	0	0	0	0
20 / 04	1	0	0	0	0	0	0
21 / 04	0	0	0	0	0	0	0
22 / 04	1	0	0	0	0	0	0
23 / 04	13	0	0	0	0	0	0
24 / 04	3	0	0	0	0	0	0

Table 4.12 (b) Estimates of Measurement time at different Fade Depths in April 2004

Date	Total Measurement time at different Fade Depths for the Month						
	A _{2dB} (mins)	A _{5dB} (mins)	A _{10dB} (mins)	A _{15dB} (mins)	A _{20dB} (mins)	A _{30dB} (mins)	A _{40dB} (mins)
25 / 04	91	0	0	0	0	0	0
28 / 04	0	0	0	0	0	0	0
29 / 04	0	0	0	0	0	0	0
30 / 04	258	0	0	0	0	0	0
Total	727	0	0	0	0	0	0

The squelching period is observed to be from April 1 to April 4 (see Table 4.12 (a) and (b)) signifying total outage. These days are not included in the calculation of the total minutes in the last row of Table 4.12 because the link is deemed to be down during the days. The percentages of time that the different fade depth levels occur from total measurement time in the month of April are shown in Figure 4.14 below.

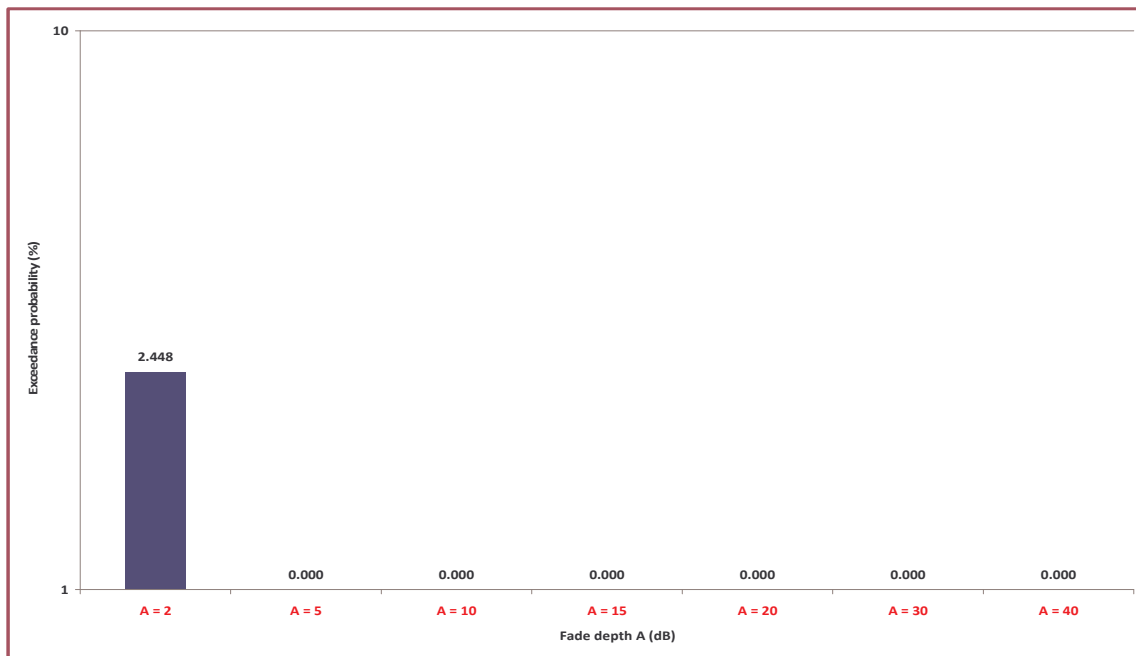


Figure 4.14 Fade Depth Exceedance Probability (%) for April 2004

The next task is to compare the values of the required fade depth, for certain availability specification as given by ITU-R for Durban, with the measurement results over the link for this month. In order to

achieve this, we check for the 99.99 % (or $A_{0.01}$) link availability specification. This is done by deducting the signal noise level (see Figure 4.13) from the average minimum signal threshold for the month (see. Figure 4.3) as follows:

$$A_{0.01} = -42.86 - (-82) = 39.14 \text{ dB}$$

This value of 39.14 dB is quite comparable to the value of 40 dB determined by simulation by Gopichund in [76] for a similar link in Durban. This shows that for the month of April 99.99 % link availability is guarantee over this line-of-sight link. In fact Figure 4.14 above shows 100 % link availability at fade depths of $A = 5$, $A = 10$, $A = 15$, $A = 20$, $A = 30$ and $A = 40$.

4.3.4 Monthly Signal Level Analysis for May

The analysis continues with similar trend for the month of May as for the previous months. The signal level measurement plot for all the days in May is shown in Figure 4.15 below.

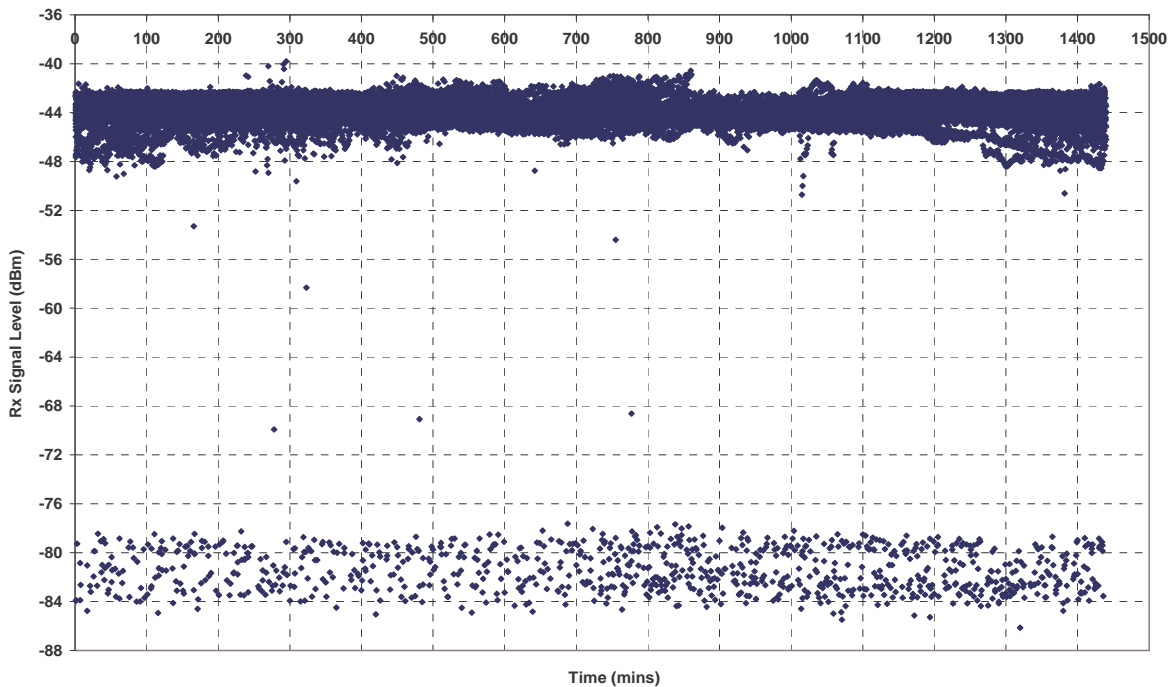


Figure 4.15 Clear-Air Signal Level Variation over 24hrs, May 2004, Durban

It can be observed that there is no total squelching for this month unlike, the months of March and April seen earlier. However, there are deep fades embedded in some days of the month as seen from Figure 4.15 above. We therefore use this noise floor to determine the 99.99 % link availability as we

have done earlier. Total measurement time in minutes for the seven fade depth levels for different days in the month of May is estimated as shown in Table 4.13 (a) and (b) below.

In order to check for the 99.99 % (or $A_{0.01}$) link availability specification, we deduct the signal noise level (see Figure 4.15) from the average minimum signal threshold for the month (see. Figure 4.4) as follows:

$$A_{0.01} = -43.82 - (-82) = 38.18 \text{ dB}$$

This value of 38.18 dB is lower than the value of 40 dB determined by the Gopichund in [76]. This shows that for the month of May 99.99 % link availability can not be achieved over this line-of-sight link; from Figure 4.16 for a fade depth of 40 dB, only 99.5 % link availability can be guaranteed over this link for the month of May. We can therefore say that May is the worst month over this measurement period.

Table 4.13 (a) Estimates of Measurement time at different Fade Depths in May 2004

Date	Total Measurement time at different Fade Depths for the Month						
	$A_{2\text{dB}}$ (mins)	$A_{5\text{dB}}$ (mins)	$A_{10\text{dB}}$ (mins)	$A_{15\text{dB}}$ (mins)	$A_{20\text{dB}}$ (mins)	$A_{30\text{dB}}$ (mins)	$A_{40\text{dB}}$ (mins)
01 / 05	0	0	0	0	0	0	0
02 / 05	25	0	0	0	0	0	0
03 / 05	0	0	0	0	0	0	0
04 / 05	0	0	0	0	0	0	0
06 / 05	0	0	0	0	0	0	0
07 / 05	141	0	0	0	0	0	0
08 / 05	185	0	0	0	0	0	0
09 / 05	331	0	0	0	0	0	0
10 / 05	256	0	0	0	0	0	0

Table 4.13 (b) Estimates of Measurement time at different Fade Depths in May 2004

Date	Total Measurement time at different Fade Depths for the Month						
	A _{2dB} (mins)	A _{5dB} (mins)	A _{10dB} (mins)	A _{15dB} (mins)	A _{20dB} (mins)	A _{30dB} (mins)	A _{40dB} (mins)
11 / 05	127	0	0	0	0	0	0
12 / 05	100	0	0	0	0	0	0
13 / 05	0	0	0	0	0	0	0
14 / 05	0	0	0	0	0	0	0
15 / 05	0	0	0	0	0	0	0
16 / 05	4	0	0	0	0	0	0
17 / 05	10	0	0	0	0	0	0
18 / 05	281	256	256	256	256	256	20
19 / 05	509	507	507	507	507	507	42
20 / 05	83	24	24	24	24	24	1
21 / 05	125	48	48	46	46	44	0
22 / 05	60	51	50	50	50	50	0
23 / 05	165	159	159	159	159	156	0
24 / 05	481	285	285	285	285	285	0
25 / 05	485	255	254	254	254	252	0
26 / 05	596	71	71	70	70	69	69
27 / 05	316	52	52	50	50	50	0
28 / 05	72	60	60	60	60	59	0
29 / 05	112	55	55	53	53	53	53
30 / 05	152	55	54	54	54	52	0
31 / 05	253	19	19	19	19	19	0
Total	4869	1897	1894	1887	1887	1876	185



Figure 4.16 Fade Depth Exceedance Probability (%) for May 2004

The percentages of time that the different fade depth levels occur from total measurement time in the month of May are shown in Figure 4.16 above.

4.3.5 Monthly Signal Level Analysis for June

The analysis for the month of June is not different from the previous months. The signal level measurement plot for all the days in June is shown in Figure 4.17 below.

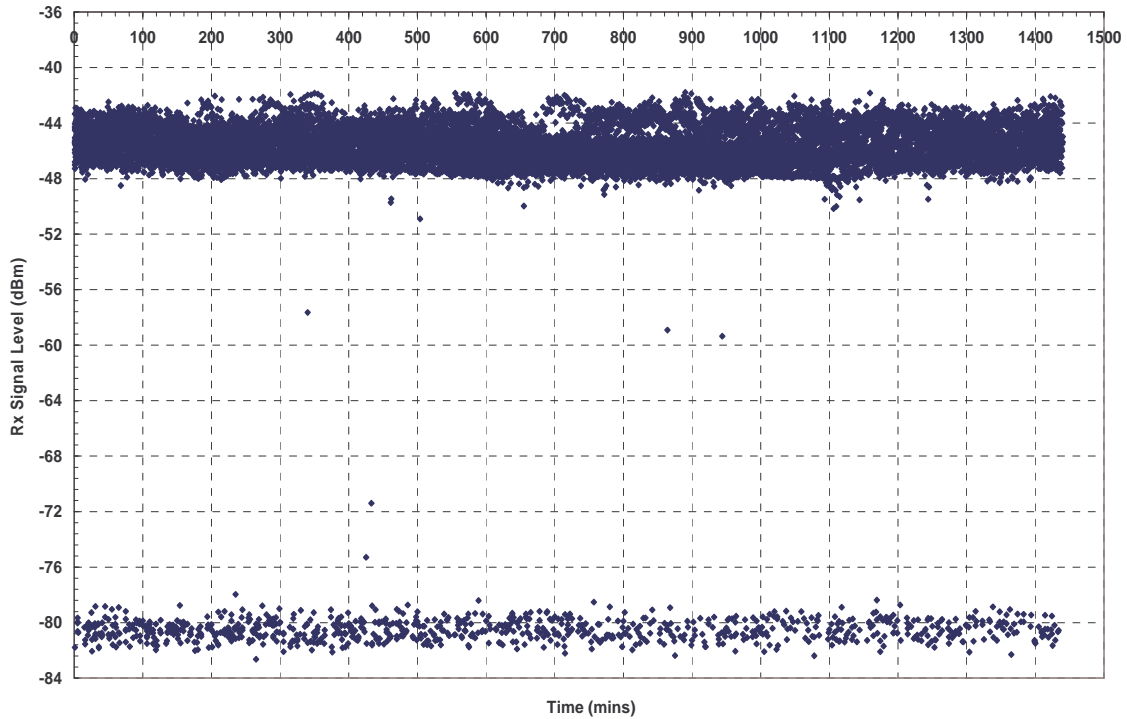


Figure 4.17 Clear-Air Signal Level Variation over 24hrs, June 2004, Durban

It can be observed that there is no extreme squelching for this month unlike other months discussed earlier. However, there are noises embedded in some days of the month as seen from Figure 4.17 above. We therefore use this noise floor to determine the 99.99 % link availability as we have done earlier. Total measurement time in minutes for the seven fade depth levels for different days in the month of June is estimated as shown in Table 4.14 below.

We now compare the values of the required fade depth, for certain availability specification as given by ITU-R for Durban, with the measurement results over the link for this month. In order to achieve this, we check for the 99.99 % (or $A_{0.01}$) link availability specification. This is done by deducting the signal noise level (see Figure 4.17) from the average minimum signal threshold for the month (see Figure 4.5) as follows:

$$A_{0.01} = -45.82 - (-82) = 36.18 \text{ dB}$$

Table 4.14 Estimates of Measurement time at different Fade Depths in June 2004

Date	Total Measurement time at different Fade Depths for the Month						
	A _{2dB} (mins)	A _{5dB} (mins)	A _{10dB} (mins)	A _{15dB} (mins)	A _{20dB} (mins)	A _{30dB} (mins)	A _{40dB} (mins)
01 / 06	54	54	54	54	54	53	0
03 / 06	231	231	230	229	229	229	0
06 / 06	232	232	232	231	231	231	0
08 / 06	247	224	224	224	224	224	0
09 / 06	133	132	132	131	131	130	0
10 / 06	9	0	0	0	0	0	0
12 / 06	2	0	0	0	0	0	0
13 / 06	0	0	0	0	0	0	0
14 / 06	0	0	0	0	0	0	0
15 / 06	1	0	0	0	0	0	0
20 / 06	121	0	0	0	0	0	0
21 / 06	52	0	0	0	0	0	0
22 / 06	1	0	0	0	0	0	0
24 / 06	2	0	0	0	0	0	0
29 / 06	51	0	0	0	0	0	0
30 / 06	37	0	0	0	0	0	0
Total	1173	873	872	868	868	866	0

This value of 36.18 dB is lower than the value of 40 dB determined in [76]. This shows that for the month of June 99.99 % link availability can be achieved if $A > 36.18$ (see Figure 4.18). The percentages of time that the different fade depth levels occur from total measurement time in the month of June are shown in Figure 4.18 below.



Figure 4.18 Fade Depth Exceedance Probability (%) for June 2004

4.3.6 Monthly Signal Level Analysis for July

The analysis for the month of July follows similar trend to the months analyzed before July. The signal level measurement plot for all the days in July is shown in Figure 4.19 below. It can be observed from Figure 4.19 below that there is no squelching of the signal in this month. This month therefore is one of the best months across the LOS link as most of the transmitted signals are received by the receiver with little or no fading. To determine the 99.99 % availability for the different fade depths in this month, we therefore refer to Figure 4.20 below. It can be observed that 99.99 % availability is guaranteed across the link for the month of July. A quick glance at Figure 4.20 actually shows 100 % link available from the fade depth $A \geq 15$ dB. The total measurement time in minutes at the seven fade depth levels for this month is shown in Table 4.15 below:

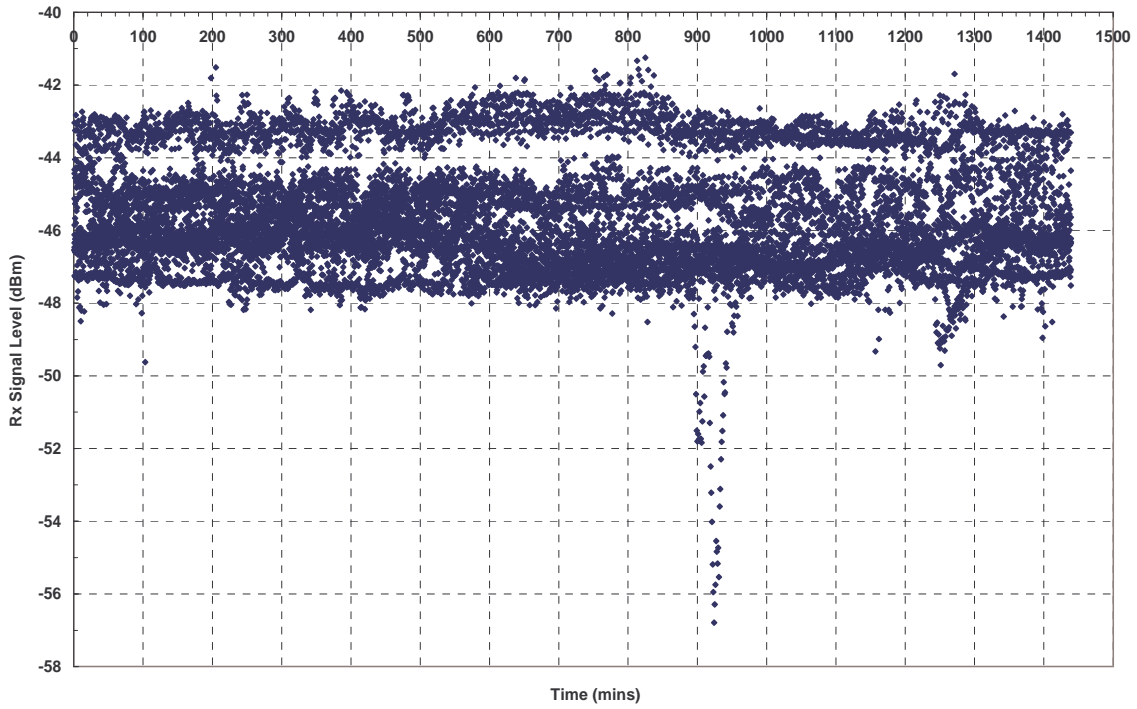


Figure 4.19 Clear-Air Signal Level Variation over 24hrs, July 2004, Durban

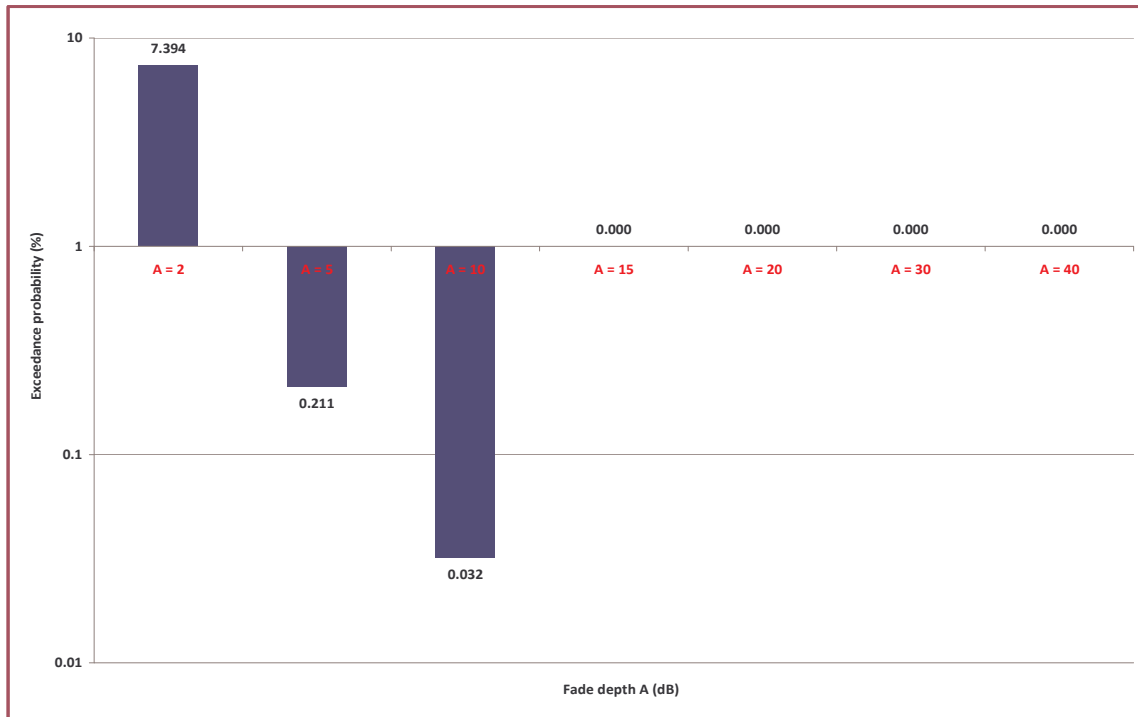


Figure 4.20 Fade Depth Exceedance Probability (%) for July 2004

Table 4.15 Estimates of Measurement time at different Fade Depths in July 2004

Date	Total Measurement time at different Fade Depths for the Month						
	A _{2dB} (mins)	A _{5dB} (mins)	A _{10dB} (mins)	A _{15dB} (mins)	A _{20dB} (mins)	A _{30dB} (mins)	A _{40dB} (mins)
01 / 07	278	0	0	0	0	0	0
02 / 07	175	0	0	0	0	0	0
03 / 07	63	0	0	0	0	0	0
04 / 07	598	33	5	0	0	0	0
06 / 07	4	0	0	0	0	0	0
07 / 07	1	0	0	0	0	0	0
08 / 07	0	0	0	0	0	0	0
21 / 07	6	0	0	0	0	0	0
22 / 07	17	0	0	0	0	0	0
23 / 07	13	0	0	0	0	0	0
30 / 07	0	0	0	0	0	0	0
31 / 07	0	0	0	0	0	0	0
Total	1155	33	5	0	0	0	0

4.3.7 Monthly Signal Level Analysis for August

We do similar analysis for the month of August. The signal level measurement plot for all the days in August is shown in Figure 4.21 below. It can be observed from Figure 4.21 that there is no squelching of the signal in this month. This month therefore is one of the best months across the LOS link as most of the transmitted signals are received with little or no fading. To determine the 99.99 % availability for the different fade depths in this month, we therefore refer to Figure 4.22 below. It can be observed that 99.99 % availability is guaranteed across the link for the month of August. A quick glance at Figure 4.22 actually shows 100 % link available for $A \geq 5$ dB. The total measurement time in minutes at the seven fade depth levels for this month is shown in Table 4.16 below:

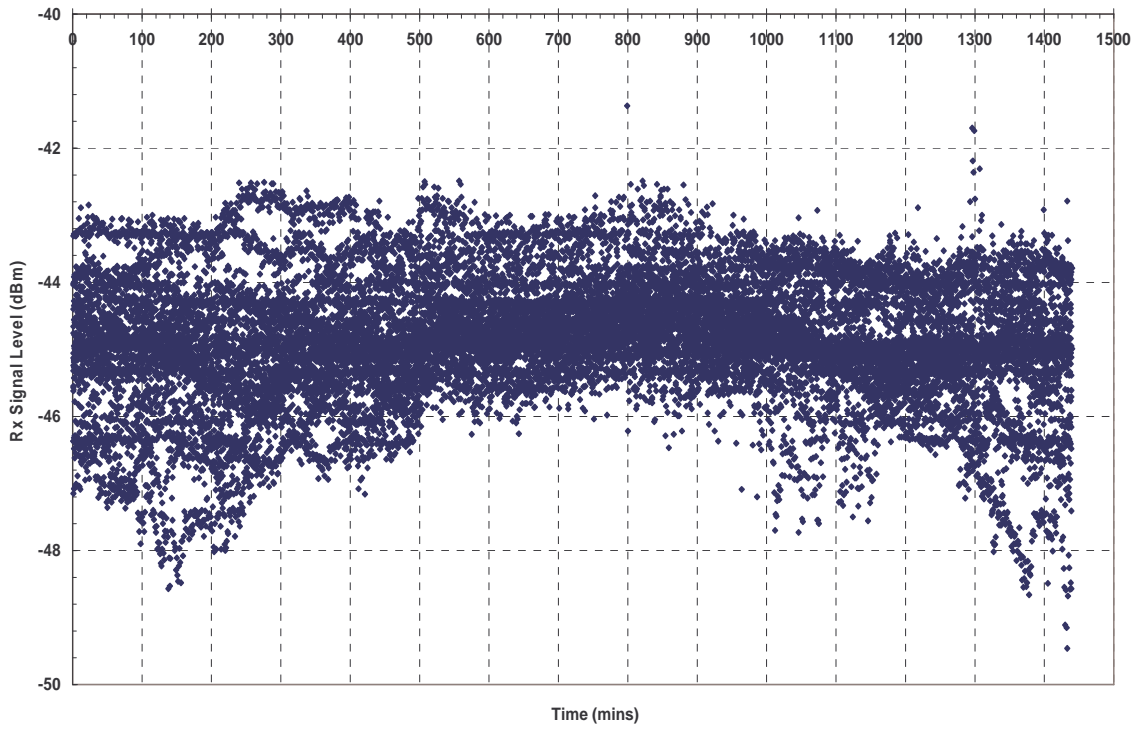


Figure 4.21 Clear-Air Signal Level Variation over 24hrs, August 2004, Durban



Figure 4.22 Fade Depth Exceedance Probability (%) for August 2004

Table 4.16 Estimates of Measurement time at different Fade Depths in August 2004

Date	Total Measurement time at different Fade Depth for the Month						
	A _{2dB} (mins)	A _{5dB} (mins)	A _{10dB} (mins)	A _{15dB} (mins)	A _{20dB} (mins)	A _{30dB} (mins)	A _{40dB} (mins)
01 / 08	0	0	0	0	0	0	0
02 / 08	0	0	0	0	0	0	0
03 / 08	221	0	0	0	0	0	0
05 / 08	0	0	0	0	0	0	0
06 / 08	0	0	0	0	0	0	0
07 / 08	0	0	0	0	0	0	0
08 / 08	2	0	0	0	0	0	0
09 / 08	1	0	0	0	0	0	0
10 / 08	2	0	0	0	0	0	0
12 / 08	10	0	0	0	0	0	0
15 / 08	116	0	0	0	0	0	0
16 / 08	89	0	0	0	0	0	0
17 / 08	145	0	0	0	0	0	0
18 / 08	0	0	0	0	0	0	0
19 / 08	144	0	0	0	0	0	0
21 / 08	60	0	0	0	0	0	0
Total	790	0	0	0	0	0	0

4.3.8 Monthly Signal Level Analysis for December

Finally we do similar analysis for the month of December. The signal level measurement plot for all the days in December is shown in Figure 4.23 below. It can be observed that there is no complete squelching for this month, unlike other months discussed earlier. We therefore use the noise floor to determine the 99.99 % link availability as we have done earlier. Total measurement time in minutes for the seven fade depth levels for different days in the month of December is estimated as shown in Table 4.17 (a) and (b) below.

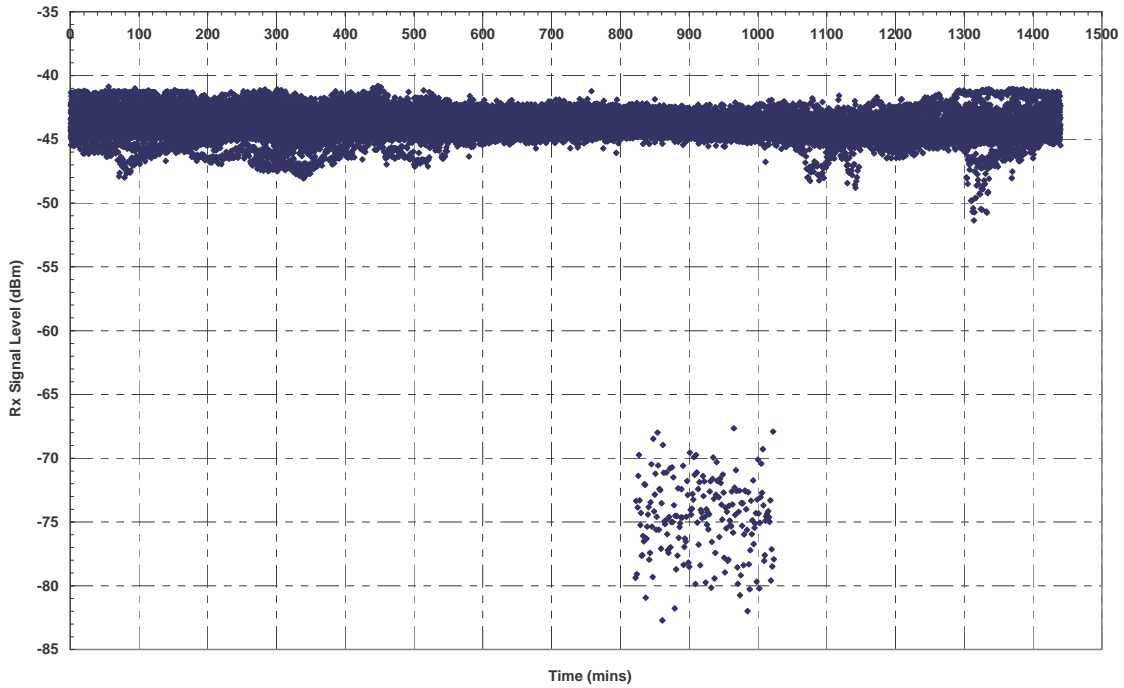


Figure 4.23 Clear-Air Signal Level Variation over 24hrs, December 2004, Durban

Table 4.17 (a) Estimates of Measurement time at different Fade Depths in December 2004

Date	Total Measurement time at different Fade Depths for the Month						
	A _{2dB} (mins)	A _{5dB} (mins)	A _{10dB} (mins)	A _{15dB} (mins)	A _{20dB} (mins)	A _{30dB} (mins)	A _{40dB} (mins)
02 / 12	0	0	0	0	0	0	0
03 / 12	0	0	0	0	0	0	0
04 / 12	215	0	0	0	0	0	0
05 / 12	0	0	0	0	0	0	0
09 / 12	5	0	0	0	0	0	0
10 / 12	0	0	0	0	0	0	0
11 / 12	0	0	0	0	0	0	0

Table 4.17 (b) Estimates of Measurement time at different Fade Depths in December 2004

Date	Total Measurement time at different Fade Depths for the Month						
	A _{2dB} (mins)	A _{5dB} (mins)	A _{10dB} (mins)	A _{15dB} (mins)	A _{20dB} (mins)	A _{30dB} (mins)	A _{40dB} (mins)
12 / 12	0	0	0	0	0	0	0
13 / 12	1	0	0	0	0	0	0
14 / 12	148	0	0	0	0	0	0
15 / 12	35	0	0	0	0	0	0
16 / 12	0	0	0	0	0	0	0
17 / 12	23	0	0	0	0	0	0
19 / 12	0	0	0	0	0	0	0
20 / 12	0	0	0	0	0	0	0
21 / 12	130	0	0	0	0	0	0
22 / 12	45	18	0	0	0	0	0
25 / 12	23	1	0	0	0	0	0
26 / 12	0	0	0	0	0	0	0
28 / 12	70	0	0	0	0	0	0
29 / 12	1	0	0	0	0	0	0
30 / 12	326	202	202	202	202	123	0
31 / 12	87	0	0	0	0	0	0
Total	1109	221	202	202	202	123	

We now compare the values of the required fade depth, for certain availability specification as given by ITU-R for Durban, with the measurement results over the link for this month. In order to achieve this, we check for the 99.99 % (or A_{0.01}) link availability. This is done by deducting the signal noise level (see Figure 4.23) from the average minimum signal threshold for the month (see. Figure 4.8) as follows:

$$A_{0.01} = -43.75 - (-82) = 38.25 \text{ dB}$$

This value shows that for the month of December 99.99 % link availability can be achieved over this line-of-sight link for A > 38.25 dB. The percentages of time that the different fade depth levels occur from total measurement time in the month of December are shown in Figure 4.24 below.

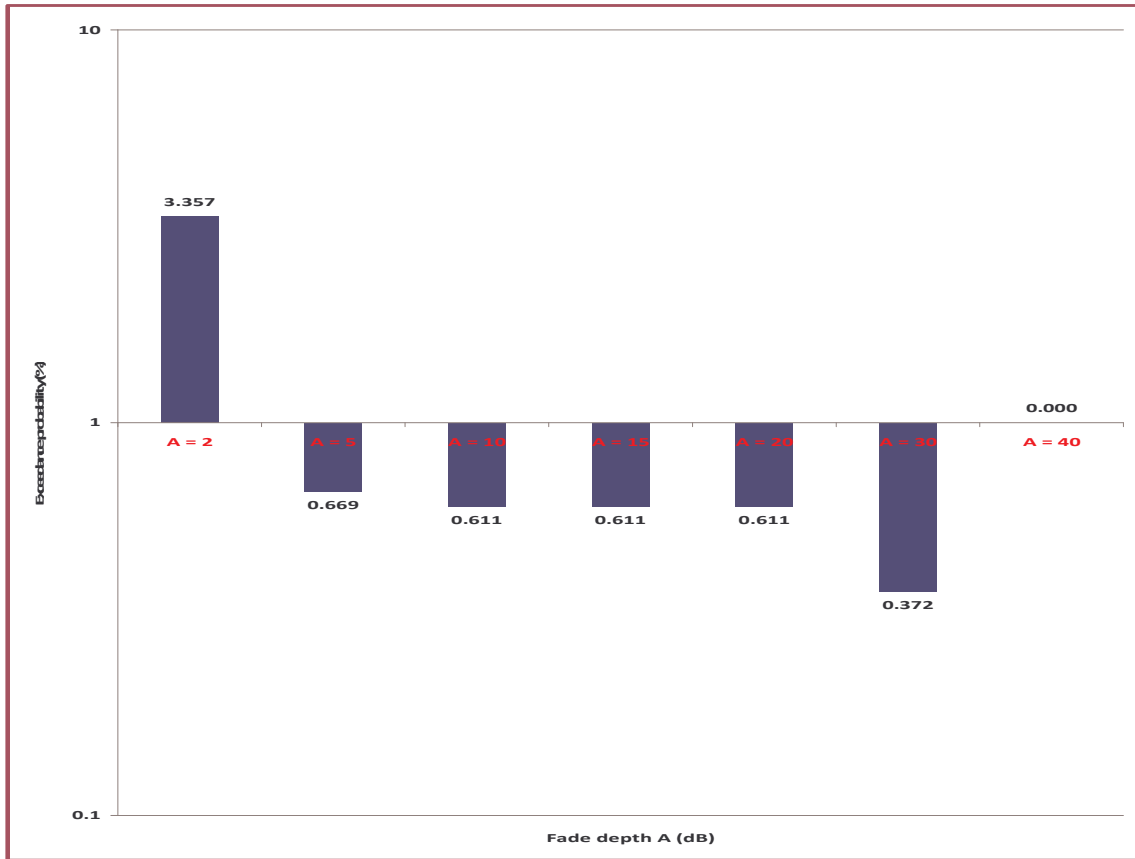


Figure 4.24 Fade Depth Exceedance Probability (%) for December 2004

4.4 Total Signal Level Analysis for Percentage of Time that a Particular Fade Depth is Exceeded

The last phase of the analysis is to determine the exceedance probabilities for each of the seven fade depth levels from the total measurement time over all the eight months. This is what we are doing in this section, and in order to achieve this, we first create a measurement time table for all the months. The measurement time table, created to achieve the stated goal is similar to the tables in the section 4.2. The measurement time for the different fade depth for whole year is shown in Table 4.18 below. Also shown in Table 4.19 are the corresponding exceedance probabilities for these seven fade depths for the whole year.

Table 4.18 Estimates of Measurement time at different Fade Depths for whole Year

Month	Total Measurement time at different Fade Depths for the Whole Year						
	A _{2dB} (mins)	A _{5dB} (mins)	A _{10dB} (mins)	A _{15dB} (mins)	A _{20dB} (mins)	A _{30dB} (mins)	A _{40dB} (mins)
February	459	15	6	6	6	6	3
March	543	26	26	26	26	26	0
April	727	0	0	0	0	0	0
May	4869	1897	1894	1887	1887	1876	185
June	1173	873	872	868	868	866	0
July	1155	33	5	0	0	0	0
August	790	0	0	0	0	0	0
December	33039	1109	221	202	202	123	
Total	10825	3065	3005	2989	2989	2897	188

Table 4.19 Percentage of Exceedance Probabilities at different fade depths for whole year

Month	Percentage of Time P(A) that a Particular Fade Depth A(dB) is Exceeded from the Total Measurement time for whole year						
	P(A _{2dB}) %	P(A _{5dB}) %	P(A _{10dB}) %	P(A _{15dB}) %	P(A _{20dB}) %	P(A _{30dB}) %	P(A _{40dB}) %
February	4.055	0.133	0.053	0.053	0.053	0.053	0.027
March	3.43	0.164	0.164	0.164	0.164	0.164	0
April	2.45	0	0	0	0	0	0
May	11.046	4.303	4.297	4.281	4.281	4.256	0.420
June	5.313	3.954	3.950	3.932	3.932	3.923	0
July	7.394	0.211	0.032	0	0	0	0
August	3.497	0	0	0	0	0	0
December	3.357	0.669	0.611	0.611	0.611	0.372	0
Total	5.573	1.578	1.547	1.539	1.539	1.491	0.097

The year long exceedance probability for the different fade depth levels is therefore shown in Figure 4.25 below.

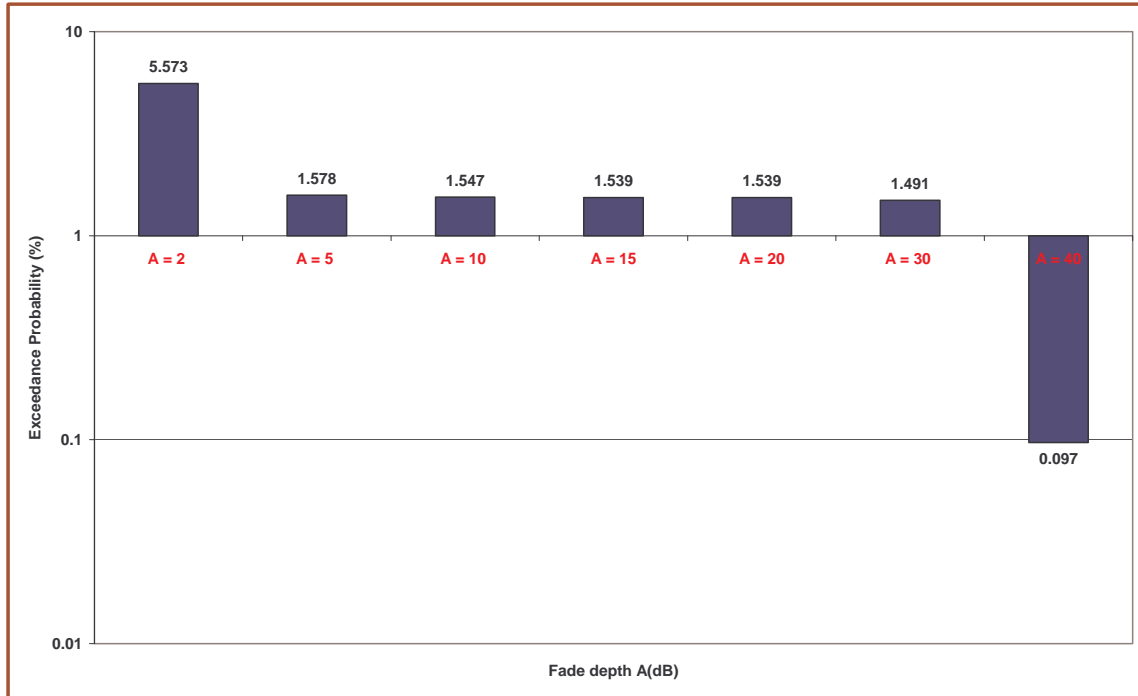


Figure 4.25 Fade Depth Exceedance Probability (%) for whole Year

Result of the analysis at fade depth $A \geq 5$ dB shows that this fade depth level occurs about 1.578 % of the total measurement time. This shows that 99.99 % link availability can not be achieved at this fade depth level in most of the month. Fade depths of $A \geq 10$ dB, $A \geq 15$ dB, $A \geq 20$ dB, and $A \geq 30$ dB shows similar characteristics over whole years measurements (Figure4.25). Fade depth of $A \geq 40$ dB has exceedance probability value of 0.097 % (see Figure 4.25) over the whole year. This still cannot guarantee 99.99 % link availability; this is as a result of contribution of the very high fading experience in the worst months of May and June (see Figure 4.16, Figure 4.19 and Table 4.18). From the daily and monthly analysis carried out, most of the days in almost all the months can guarantee 99.99% availability at fade depths of $A \geq 5$ dB. The worst months over the link are May and June (see Table 4.19) while the best months over the link are April and August (see Table 4.19).

4.5 Proposed Analytical Model for Clear-Air Radioclimatic Study in Southern Africa

The previous sections gave an extensive analysis of the clear-air signal level measurement over the line of sight terrestrial link between Howard College and Westville Campuses of the University of KwaZulu-Natal (UKZN). Our proposed analytical expression to model clear-air radioclimatic study

in Southern Africa is based on the above analysis. The proposed analytical representation for the percentage of exceedance probability as a function of fade depth is developed as follows:

As seen from the analysis done in section 4.2 to 4.4, all the available measurement data for the month in question were pooled together. We then determine the probability that a certain fade depth A is exceeded for a given month by summing all the measurement minutes during which that fade depth is exceeded, and dividing this by the total measurement minutes for that month. The fade depth for a given month, M , for a signal level P_{Mj} measured in the j th minute of that month is determined as follows [125]:

$$A_{Mj} = P_M - P_{Mj} \quad (4.2)$$

where P_M in (4.2) is the average clear-air signal level for month M . For example, for February, $P_M = -42.84$ dBm; for March, $P_M = -42$ dBm; for April, $P_M = -42.86$ dBm; et cetera. The resulting exceedance plots are shown in Figures 4.26a and 4.26b. As expected, the lower the value of A , the higher the probability of exceedance. In Figure 4.26a, the months with the best performance for the range $A = 5 - 15$ dB are April and August, which give exceedance values below 0.001%. The poorest performers for this range of A are the months of May and June, with exceedance levels of 5 % [125].

For $A = 30$ dB, again the best performance is obtained in the months of April, July and August. March and December give poor percentages just above 0.1%, with February only slightly better. Yet again, the greatest culprits are the months of May and June, which each gave a probability of exceedance just below 5 %. This implies that there is something else occurring during these two months, which needs further investigation. Finally, for $A = 40$ dB, all the other months perform well save for the months of May and February, which give exceedance probabilities of 0.42 % and 0.027% respectively. This high exceedance probability in May for a fade margin as high as 40 dB, drives one to surmise that some other events, like ducting and sea-breeze effects, must be playing a role here, and must be taken into account in future studies [125].

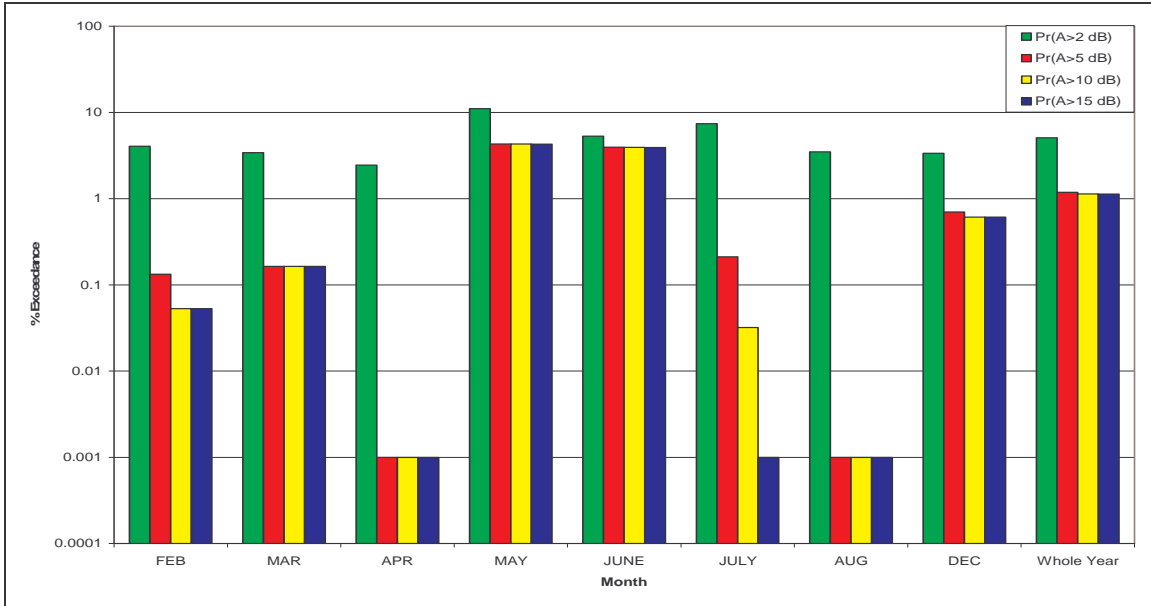


Figure 4.26a Percentage of Time that Fade depth A(dB) is exceeded; A = 2, 5, 10 and 15 dB

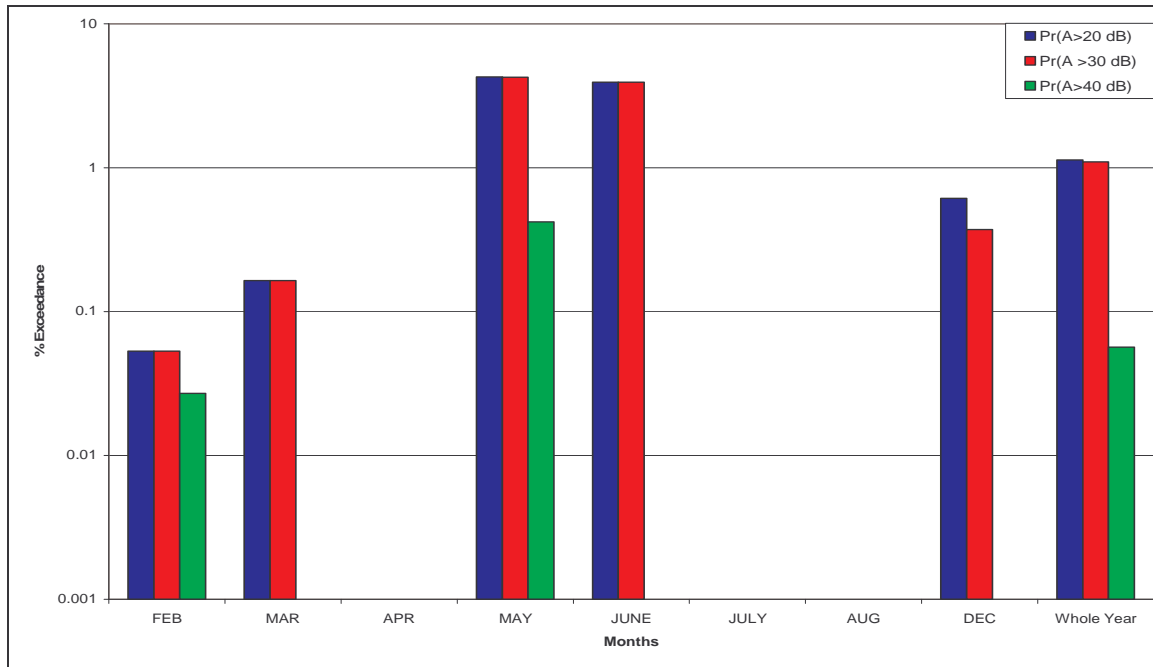


Figure 4.26b Percentage of Time that Fade depth A(dB) is exceeded; A = 20, 30 and 40 dB

For the exceedance plots shown in Figure 4.26, we now proceed to develop analytical expressions as a function of A (dB). The plots of the exceedance probability for different fade depths in the months of May, June and for the whole year are shown in Figures 4.27 – 4.29 below.

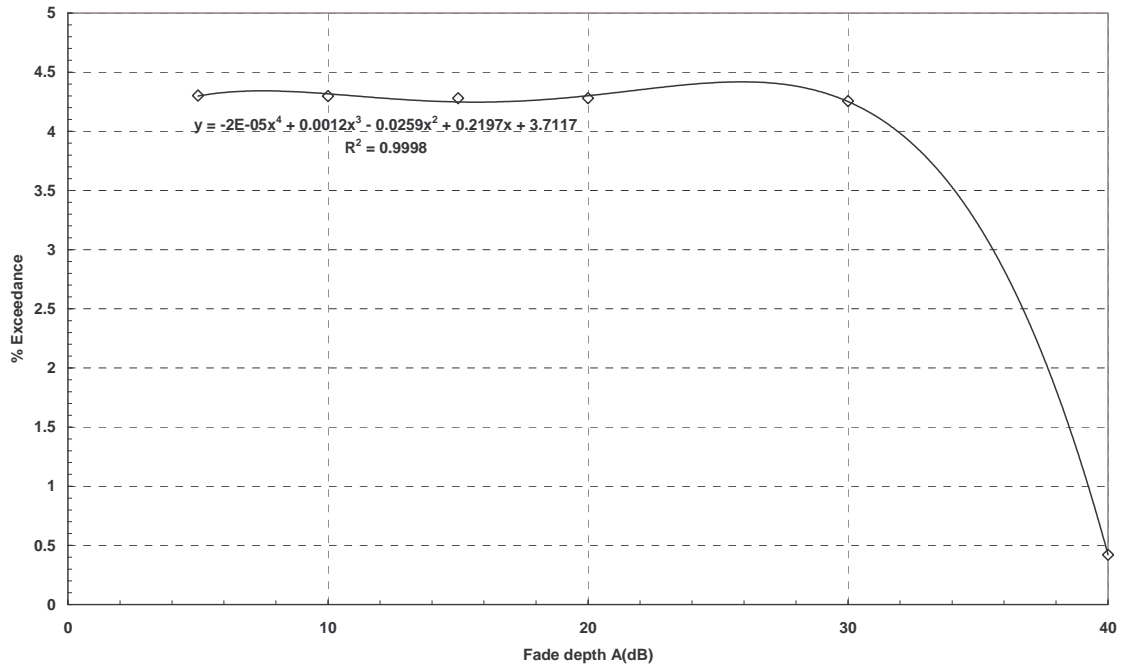


Figure 4.27 Analytical Model for Exceedance Probability plot for May 2004

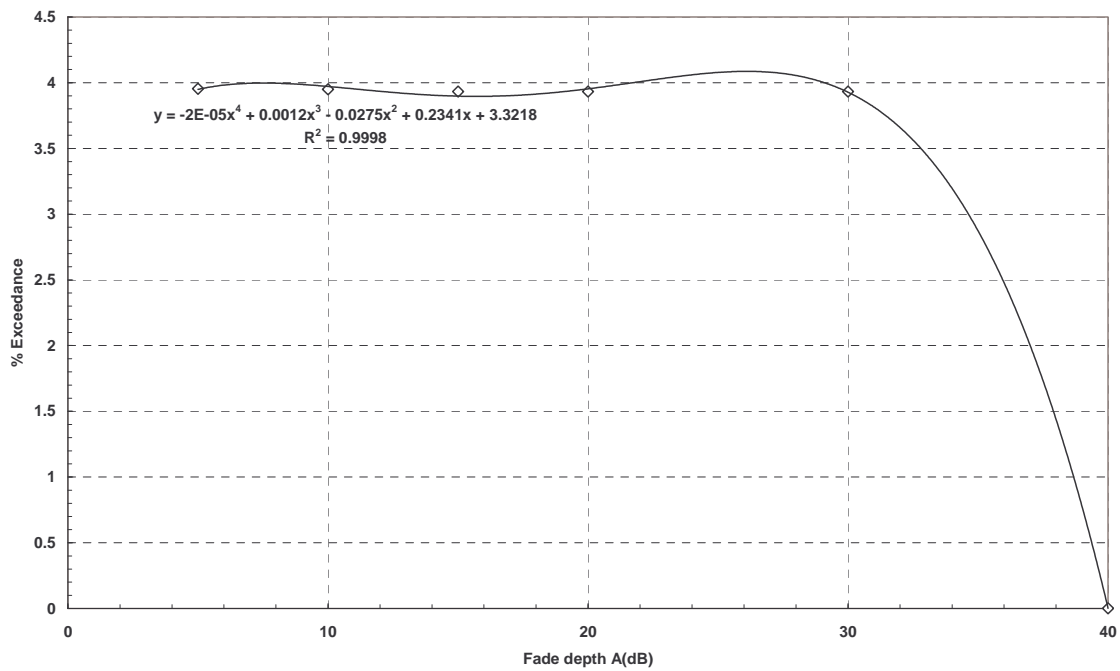


Figure 4.28 Analytical Model for Exceedance Probability plot for June 2004

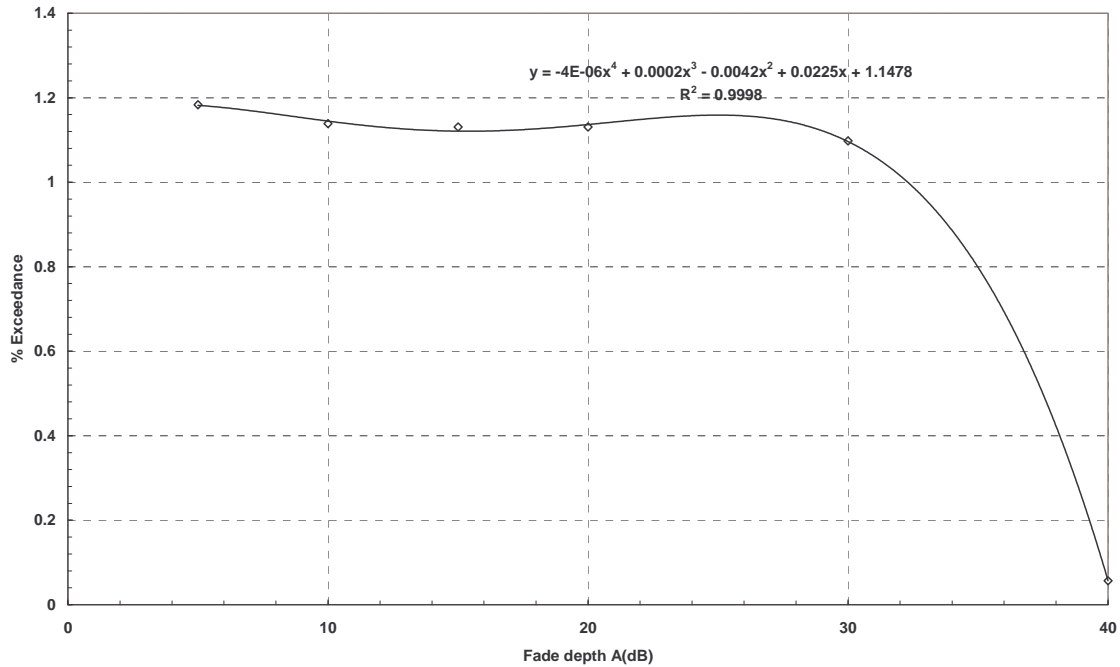


Figure 4.29 Analytical Model for Exceedance Probability plot for whole year 2004

It is observed from the three figures that over the link, the percentage of time that a certain fade depth A(dB) is exceeded can be modeled as a fourth order polynomial for May, June and whole year. These are given by the following expressions, for a given fade depth A:

$$P_{\text{May}}(A) = 0.00002A^4 + 0.0012A^3 - 0.0259A^2 + 0.2197A + 3.7117$$

$$P_{\text{June}}(A) = -0.00002A^4 + 0.0012A^3 - 0.0275A^2 + 0.2341A + 3.3218 \quad (4.3)$$

$$P_{\text{Year}}(A) = -0.000004A^4 + 0.0002A^3 - 0.0042A^2 + 0.0225A + 1.1478$$

These and other expressions, for all the measurement months of the year, are presented in Table 4.20 below.

Table 4.20: Analytical expressions of Percentage exceedance probabilities for the different months

Month	Analytical Expression
February	$P_A = 0.000001A^4 - 0.0001A^3 + 0.004A^2 - 0.057A + 0.3309$
March	$P_A = -0.0000008A^4 + 0.00005A^3 - 0.0011A^2 + 0.0096A + 0.138$
April	$P_A = 0.5868A^{-2.1162}$
May	$P_A = -0.00002A^4 + 0.0012A^3 - 0.0259A^2 + 0.2197A + 3.7117$
June	$P_A = -0.00002A^4 + 0.0012A^3 - 0.0275A^2 + 0.2341A + 3.3218$
July	$P_A = 0.00009A^4 - 0.0085A^3 + 0.2656A^2 - 3.2166A + 12.165$
August	$P_A = 0.00005A^4 - 0.0042A^3 + 0.1293A^2 - 1.554A + 5.7859$
December	$P_A = 0.000003A^4 - 0.0003A^3 + 0.0091A^2 + 0.1067A + 1.0428$
Whole Year	$P_A = -0.000004A^4 + 0.0002A^3 - 0.0042A^2 + 0.0225A + 1.1478$

4.6 Application of Parabolic Equation to Clear-Air Radioclimatological Study

The finite-difference method discussed in [126-128] is applied to solve the standard parabolic equation (SPE). This is later modified to incorporate clear-air propagation phenomena. We present the finite-difference of the Crank-Nicolson type. We assume that the lower boundary is horizontal, located at $z = 0$. The integration grid is defined, which is fixed in the vertical direction, but not in range, so that it can adapt to the terrain shape. Let

$$z_j = j\Delta z, \quad j = 0, N \quad (4.4)$$

be the vertical grid points and let x_0, \dots, x_m be the successive integration ranges. In order to advance the solution from range x_{m-1} to range x_m , we consider the midpoint :

$$\xi_m = \frac{x_{m-1} + x_m}{2} \quad (4.5)$$

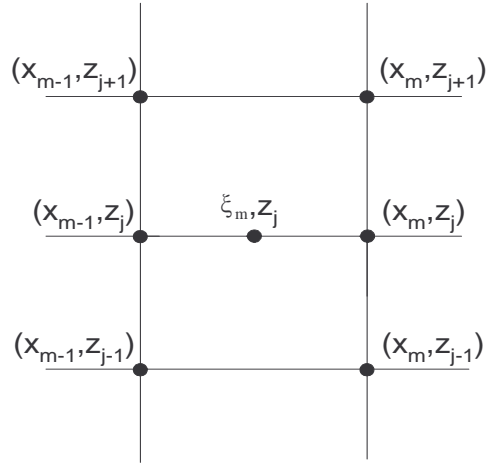


Figure 4.30 Finite difference grid for Crank-Nicolson scheme

The basic idea is to write finite difference expressions for the partial derivatives at point (ξ_m, z_j) , involving only values of the function u at the corners of adjacent rectangles as shown in Figure 4.30. The central finite-difference approximation of the derivative in range is given by:

$$\frac{\partial u}{\partial x}(\xi_m, z_j) = \frac{u(x_m, z_j) - u(x_{m-1}, z_j)}{\Delta x_m} \quad (4.6)$$

Where

$$\Delta x_m = x_m - x_{m-1} \quad (4.7)$$

The central finite-difference approximation of the second order derivative in height is given by:

$$\frac{\partial^2 u}{\partial z^2}(\xi_m, z_j) = \frac{u(\xi_m, z_{j+1}) + u(\xi_m, z_{j-1}) - 2u(\xi_m, z_j)}{\Delta z^2} \quad (4.8)$$

It should be noted that this expression would be more meaningful if all the points involved were inside the integration domain; this means that j cannot be 0 or N .

4.6.1 The Narrow-angle Code

Combining equations (4.6) and (4.8) with the standard parabolic equation, thus gives

$$\frac{u(\xi_m, z_{j+1}) + u(\xi_m, z_{j-1}) - 2u(\xi_m, z_j)}{\Delta z^2} + 2ik \frac{u(x_m, z_j) - u(x_{m-1}, z_j)}{\Delta x_m} + k^2 (n^2(\xi_m, z_j) - 1) u(\xi_m, z_j) = 0 \quad (4.9)$$

The final step is to approximate u at range ξ_m by averaging values at ranges x_{m-1} and x_m . Proper manipulation of equation (4.9) is necessary to achieve this. If we multiply equation (4.9) by Δz^2 and substitute equation (4.4) we get:

$$u\left(\frac{x_{m-1} + x_m}{2}, z_{j+1}\right) + u\left(\frac{x_{m-1} + x_m}{2}, z_{j-1}\right) - 2u\left(\frac{x_{m-1} + x_m}{2}, z_j\right) + 2ik \frac{\Delta z^2}{\Delta x_m} (u(x_m, z_j) - u(x_{m-1}, z_j)) + k^2 (n^2(\xi_m, z_j) - 1) \Delta z^2 u\left(\frac{x_{m-1} + x_m}{2}, z_j\right) = 0 \quad (4.10)$$

Multiplying through equation (4.10) by 2, expand further and collect terms of the same factor in z yields:

$$u(x_{m-1}, z_{j+1}) + u(x_m, z_{j+1}) + u(x_{m-1}, z_{j-1}) + u(x_m, z_{j-1}) - 2u(x_{m-1}, z_j) - 2u(x_m, z_j) + 4ik \frac{\Delta z^2}{\Delta x_m} u(x_m, z_j) - 4ik \frac{\Delta z^2}{\Delta x_m} u(x_{m-1}, z_j) + k^2 (n^2(\xi_m, z_j) - 1) \Delta z^2 u(x_{m-1}, z_j) + k^2 (n^2(\xi_m, z_j) - 1) \Delta z^2 u(x_m, z_j) = 0 \quad (4.11)$$

If we let

$$u_j^m = u(x_m, z_j)$$

$$b = 4ik \frac{\Delta z^2}{\Delta x} \quad (4.12a)$$

$$a_j^m = k^2 (n^2(\xi_m, z_j) - 1) \Delta z^2$$

and noting also that

$$\begin{aligned}
\mathbf{u}_{j+1}^{m-1} &= \mathbf{u}(x_{m-1}, Z_{j+1}) \\
\mathbf{u}_{j-1}^m &= \mathbf{u}(x_m, Z_{j-1}) \\
\mathbf{u}_{j-1}^{m+1} &= \mathbf{u}(x_{m+1}, Z_{j-1}) \\
\mathbf{u}_{j-1}^{m-1} &= \mathbf{u}(x_{m-1}, Z_{j-1}) \\
\mathbf{u}_{j+1}^{m+1} &= \mathbf{u}(x_{m+1}, Z_{j+1})
\end{aligned} \tag{4.12b}$$

Substituting equations (4.12a) and (4.12b) into equation (4.11) yields:

$$\mathbf{u}_{j+1}^{m-1} + \mathbf{u}_{j+1}^m + \mathbf{u}_{j-1}^{m-1} + \mathbf{u}_{j-1}^m - 2\mathbf{u}_j^{m-1} - 2\mathbf{u}_j^m + b\mathbf{u}_j^m - b\mathbf{u}_j^{m-1} + a_j^m \mathbf{u}_j^{m-1} + a_j^m \mathbf{u}_j^m = 0 \tag{4.13}$$

Collecting like terms and factorizing equation (4.13) gives

$$\mathbf{u}_j^m (-2 + b + a_j^m) + \mathbf{u}_{j+1}^m + \mathbf{u}_{j-1}^m = \mathbf{u}_j^{m-1} (2 + b - a_j^m) - \mathbf{u}_{j+1}^{m-1} - \mathbf{u}_{j-1}^{m-1} \tag{4.14}$$

for $j = 1, \dots, N-1$. Equation (4.14) provides $N-1$ equations. In order to complete the system, we need to include equations at the top and bottom of the domain. The finite difference method is very flexible for the treatment of boundary conditions. We thus treat the simplest possible case here as we assume a perfectly conducting ground. The field u must be zero at the bottom of the domain. For the moment we impose $u(x, z_N) = 0$, using an absorbing layer as in the sine transform model to avoid parasitic reflections at the top of the domain (then $N \rightarrow \infty$).

We have now expressed values at range x_m as a function of values at x_{m-1} in the form of a linear system. The solution is not explicitly given, but only implicitly, since we need to invert a matrix to obtain u at range x_m . This implicit scheme is of Crank-Nicolson type [127]. The scheme can be given in matrix form as:

$$\mathbf{A}_m \mathbf{U}_m = \mathbf{V}_m \tag{4.15}$$

Where U_m is the vector giving the field at range x_m

$$U_m = \begin{pmatrix} u_0^m \\ \vdots \\ u_N^m \end{pmatrix} \quad (4.16)$$

and A_m is the tridiagonal matrix

$$A_m = \begin{pmatrix} 1 & 0 & 0 & 0 & 0 & \dots & 0 & 0 \\ 1 & \alpha_1^m & 1 & 0 & 0 & \dots & 0 & 0 \\ 0 & 1 & \alpha_2^m & 1 & 0 & \dots & 0 & 0 \\ \vdots & & & & & & & \vdots \\ 0 & \dots & & 0 & 1 & \alpha_{N-1}^m & 1 \\ 0 & \dots & & 0 & 0 & 0 & 1 \end{pmatrix} \quad (4.17)$$

where

$$\alpha_j^m = -2 + b + a_j^m \quad (4.18)$$

The right hand side of equation (4.15), V_m , is obtained from the field U_{m-1} at the previous range by the matrix multiplication:

$$V_m = \begin{pmatrix} 1 & 0 & 0 & 0 & 0 & \dots & 0 & 0 \\ -1 & \beta_1^m & -1 & 0 & 0 & \dots & 0 & 0 \\ 0 & -1 & \beta_2^m & -1 & 0 & \dots & 0 & 0 \\ \vdots & & & & & & & \vdots \\ 0 & \dots & & 0 & -1 & \beta_{N-1}^m & -1 \\ 0 & \dots & & 0 & 0 & 0 & 1 \end{pmatrix} U_{m-1} \quad (4.19)$$

where

$$\beta_j^m = 2 + b - a_j^m, \quad j = 1, \dots, N-1 \quad (4.20)$$

Since the matrix A_m is tridiagonal, inversion with a Gaussian elimination scheme is straightforward provided A_m is non-singular. The superscript m is omitted for simplicity's sake in what follows. In a first sweep, the lower subdiagonal is eliminated, with the forward loop:

$$\begin{aligned}\Gamma_0 &= \frac{V_0}{\alpha_0} \\ \Gamma_j &= \frac{V_j - \Gamma_{j-1}}{\alpha_j}, \quad j = 1, \dots, N\end{aligned}\tag{4.21}$$

The upper subdiagonal is then eliminated with a back solving loop, giving the solution as:

$$\begin{aligned}U_N &= \Gamma_N \\ U_j &= \Gamma_j - \frac{U_{j+1}}{\alpha_j}, \quad j = N-1, \dots, 0\end{aligned}\tag{4.22}$$

The number of operations is of order N .

4.6.2 Path Loss

The results of the parabolic equation is given in terms of path loss [129-130]. The path loss is defined as the ratio between boresight equivalent isotropic radiated power for the actual antenna and the power received by an isotropic antenna with the same polarization, assuming that there are no system losses [131]. The boresight equivalent isotropic radiated power (e.i.r.p.) of an antenna is the power P_{iso} required at the input of an isotropic antenna to produce the same far-field power flux density in the boresight direction as the actual antenna radiating in vacuum. It should be noted that the definition of P_{iso} does not take ground effects into account. At distance r from the source, the power flux density S_{iso} radiated by equivalent isotropic antenna is:

$$S_{iso} = \frac{P_{iso}}{4\pi r^2}\tag{4.23}$$

The power flux density S_b in the boresight direction is related to the boresight far-field beam pattern for the electric field by:

$$S_b = \frac{|B_{\max}|^2}{2Z_0 r^2} \quad (4.24)$$

Since we are working in ratios, we may choose the value of B_{\max} by working with the normalization:

$$B_{\max} = \frac{1}{\sqrt{2\pi}} \quad (4.25)$$

which correspond to unity gain in the boresight direction. The boresight equivalent isotropic radiated power is then given by :

$$P_{\text{iso}} = \frac{1}{Z_0} \quad (4.26)$$

Where Z_0 is the impedance of a vacuum. We now relate the parabolic equation output to the path Loss L_p . We first look at the case of horizontal polarization, then we solve for the reduced function u corresponding to the azimuth component E_ϕ of the electric field. The power flux density at the point of coordinates (X, Z) is:

$$S = \frac{1}{2Z_0} |E_\phi(X, Z)|^2 \quad (4.27)$$

If the received antenna is treated as an isotropic point source, the received power P_r is given by:

$$P_r(X, Z) = \frac{\lambda^2}{4\pi} S \quad (4.28)$$

From equation (4.27) we have

$$Z_0 = \frac{1}{2S} |E_\phi(X, Z)|^2$$

$$\frac{P_{\text{iso}}}{P_r(X, Z)} = \frac{4\pi}{\frac{1}{2} |E_\phi(X, Z)|^2 \lambda^2}$$

$$\text{but } E_\phi = \frac{1}{\sqrt{kx \sin\theta}} \psi_h(X, Z)$$

$$|E_\phi|^2 = \frac{1}{kx \sin\theta} |\psi_h(X, Z)|^2$$

$$\text{and } X = x \sin\theta, \quad k = \frac{2\pi}{\lambda}$$

$$\therefore |E_\phi(X, Z)|^2 = \frac{\lambda}{2\pi X} |\psi_h(X, Z)|^2$$

$$\text{substitute into } \frac{P_{\text{iso}}}{P_r(X, Z)}$$

$$\text{we have from } \frac{P_{\text{iso}}}{P_r(X, S)} = \frac{4\pi}{\frac{1}{2} |E_\phi(X, Z)|^2 \lambda^2}$$

$$\frac{P_{\text{iso}}}{P_r(X, Z)} = \frac{4\pi}{\frac{\lambda}{4\pi X} |\psi_h(X, Z)|^2 \lambda^2}$$

$$= \frac{(4\pi)^2 X}{\lambda^3 |\psi_h(X, Z)|^2}$$

$$\therefore \frac{P_{\text{iso}}}{P_r(X, Z)} = \frac{(4\pi)^2}{\lambda^3} X |\psi_h(X, Z)|^{-2} \quad (4.29)$$

Writing equation (4.29) in the log format which is usually used for the decibel unit of path loss, we proceed as follows:

$$L_p(\text{dB}) = 10 \log_{10} \left(\frac{P_{\text{iso}}}{P_r(X, Z)} \right)$$

$$L_p(\text{dB}) = 10 \log_{10} \left(\frac{(4\pi)^2}{\lambda^3} \cdot x \cdot |\psi_h(X, Z)|^{-2} \right)$$

$$L_p(\text{dB}) = 10 \log_{10} (4\pi)^2 - 10 \log_{10} \lambda^3 + 10 \log_{10} x + 10 \log_{10} |\psi_h(X, Z)|^{-2}$$

$$L_p(\text{dB}) = -20 \log_{10} |\psi_h(X, Z)| + 20 \log_{10} (4\pi) + 10 \log_{10} x - 30 \log_{10} (\lambda)$$

We can write this last equation in terms of the reduced field u as follows:

$$L_p(x, z) = -20 \log |u(x, z)| + 20 \log(4\pi) + 10 \log(x) - 30 \log(\lambda) \quad (4.30)$$

Where λ is the wavelength of the propagating radio wave, and x is the path length or coverage range of the transmitting signal. In order to properly modify the SPE to include the geoclimatic factor, we have proposed a new formulation for determination of the geoclimatic factor. This new formulation is different from the ITU-R formulation. The reason for this new formulation is that the ITU-R formulation is of differential form and the parabolic equation too is a second order differential equation. The idea is to replace the refractive index aspect of the parabolic equation with the geoclimatic factor. However, the refractive index aspect that is to be replaced is already within a differential loop, placing another differential equation within this loop will complicate the solution procedure. In order to avoid this complication, we have proposed an alternative formulation for determination geoclimatic factor in the next section. This new formulation is a simple linear equation that can be placed in a differential equation and the numerical procedure described in section 4.6.1 above can be applied to solve the new parabolic equation.

4.7 Alternative Formulation (AF) for Determination of Geoclimatic Factor

In this section, we present a newly proposed formulation for determination of geoclimatic factor. The ITU-R formulation for determination of geoclimatic factor has been reported and applied to terrestrial line of sight link design in the previous chapters. This section gives an alternative formulation used to determine the geoclimatic factor. This formulation is quite easily adaptable to the solution of clear-air problems if a computational or numerical procedure is to be applied [132]. The ITU-R formulation discussed earlier is best used when a statistical procedure is to be used.

The derivation of the alternative formulation for determination of geoclimatic factor requires the calculation of refractive index from the local radio propagation data. A distribution of this refractive index is then plotted from which an optimum value is estimated using a kernel estimation technique

[132]. It is in view of this we present an alternative formulation to calculate the geoclimatic factor as follows:

$$G_F = a_F * (n_{opt}^2 - 1) \quad (4.31)$$

Where G_F is the geoclimatic factor, a_F is the adjustment factor determinable from ITU-R version of geoclimatic factor and is region depended, and n_{opt} is optimum refractive index value gotten from the kernel estimate. It should be noted that a standard value of a_F will be determined for the region of interest and it also varies for different months. Typical value of a_F for the different months in Durban and Botswana is shown in Table 4.20 below. It should be noted that the empty rows in Table 4.20 are the months for which no measurement information exist.

The optimum refractive index is determined from the local radiosonde data using the kernel estimation procedure discussed in the chapter two. Hence in order to choose a refractive index value as the optimum, it must be a refractive index value with the optimum smoothing parameter when Kernel estimation algorithm program is run. The population sample size of the refractive indices used in the kernel estimation is 4933 for Durban and 1643 for Botswana data. The kernel estimation program was run for different types of kernel initially, in order to choose the appropriate kernel type. The kernel with the minimum ISE compared to the rest was chosen as the appropriate kernel (see Figure 4.31 and Figure 4.32).

The plots in figures 4.31 – 4.32 show that the Biweight kernel has the minimum ISE. This is the reason why we choose the Biweight kernel for further analysis of the data in Durban and Botswana. The next challenge is to choose the appropriate smoothing parameter that will give the distribution needed to obtain the optimum refractive index value for our new formulation. In order to do this, the kernel program was ran several times with different values of the smoothing parameter ‘h’ starting with that predicted by Silverman in equation (2.14). The result of such activity is displayed in Figure 4.33 and Figure 4.34.

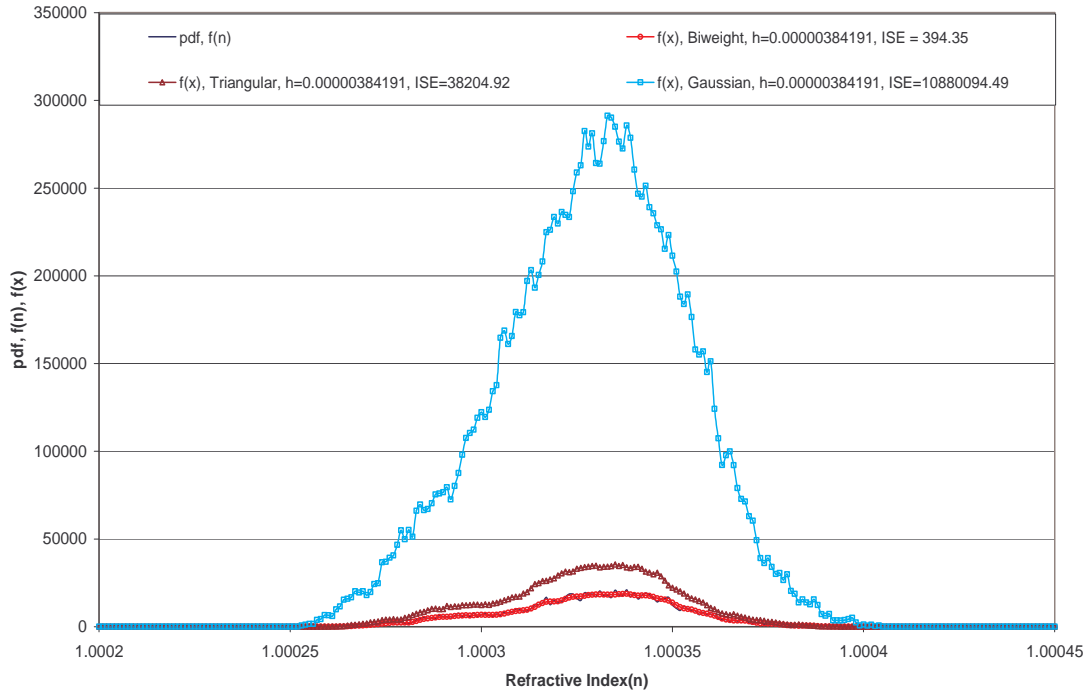


Figure 4.31 Probability Distribution of Refractive Index for different Kernels, Nov'03-Aug'04, Durban

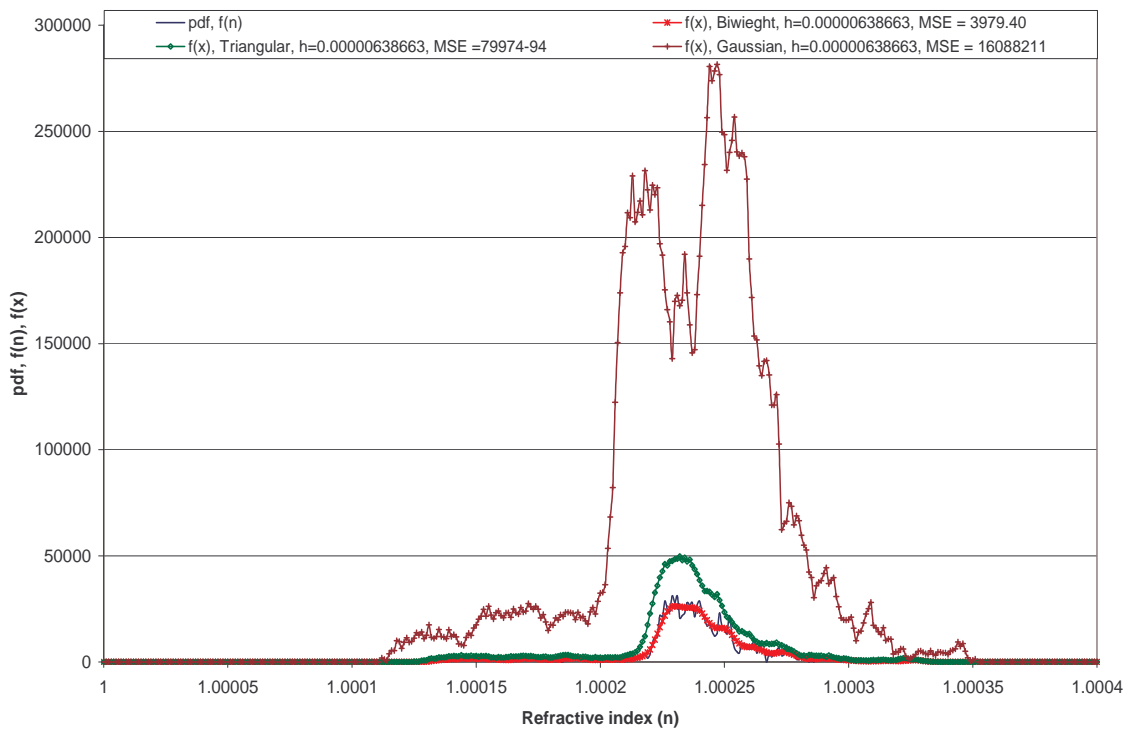


Figure 4.32 Probability Distribution of Refractive Index for different Kernels, Feb-Dec'96, Maun Botswana

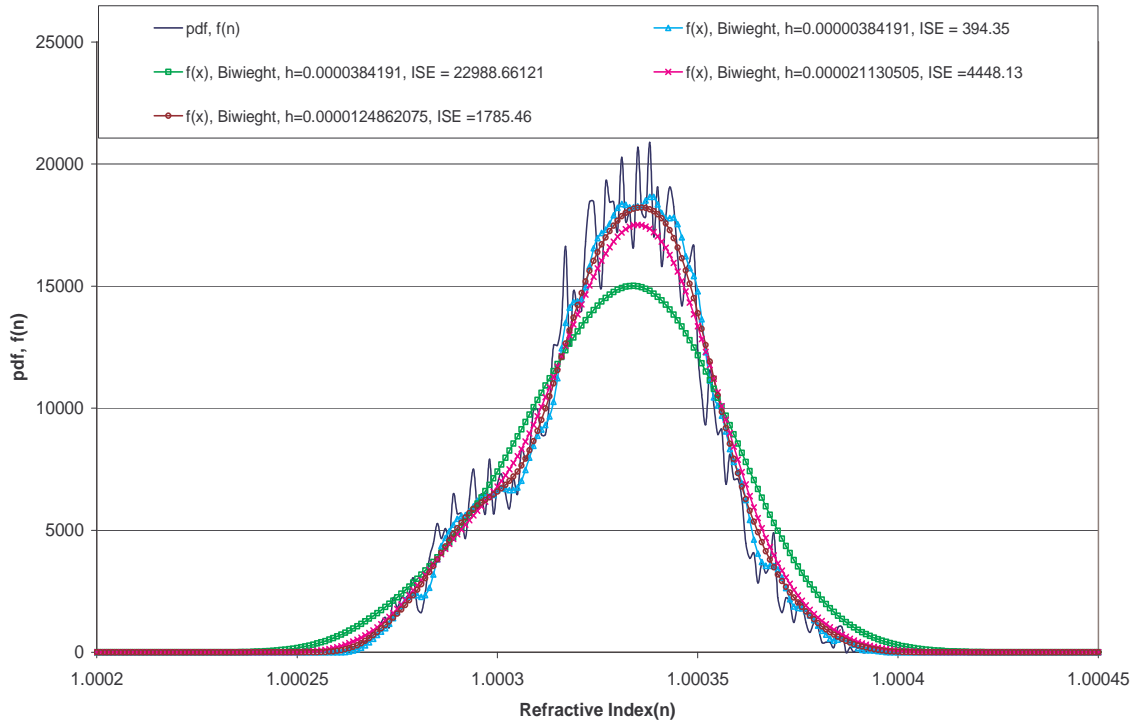


Figure 4.33 Probability Distribution of Refractive Index for Biweight Kernels, Nov'03-Aug'04, Durban

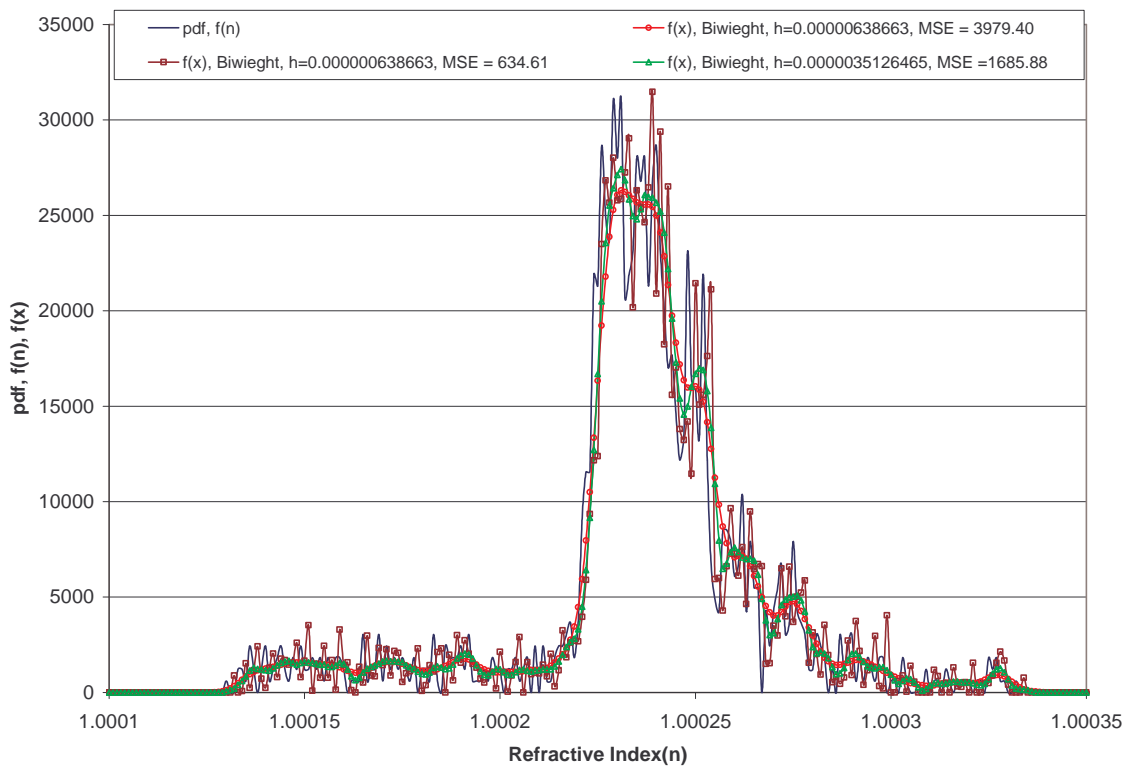


Figure 4.34 Probability Distribution of Refractive Index for Biweight Kernels, Feb-Dec'96, Maun, Botswana

Finally, using this new formulation in (4.31), the geoclimatic factor is estimated for different months in both Durban and Botswana. The result obtained using the new formulation is compared with those obtained using the standard ITU-R procedure. These results are displayed in Table 4.21.

Table 4.21 Calculated Geoclimatic Factor(K) for Durban and Botswana using ITU-R and the new Alternative Formulation Approach (AFA)

Month	Durban (K) 2003/2004			Botswana (K) 1996		
	ITU-R approach	AF approach	% deviation	ITU-R approach	AF approach	% deviation
January	0.001684	0.001670	0.8314			
February	0.170679	0.159465	6.5702	0.010935	0.010091	7.7183
March	0.003329	0.003173	4.6864	0.001010	0.001082	7.1287
April	0.002140	0.002141	0.0467			
May	0.002085	0.002003	3.9328	0.008151	0.007338	9.9742
June	0.001047	0.000982	6.2082	0.000712	0.000686	3.6517
July	0.001055	0.001010	4.2654			
August	0.021970	0.022697	3.3091	0.000172	0.000172	0
September				0.000809	0.000731	9.6415
October				0.011306	0.010335	8.5884
November	0.000521	0.000480	7.8695	0.002060	0.001959	4.9029
December	0.000737	0.000736	0.1357	0.013906	0.014177	1.9488

4.8 First Modified Parabolic Equation (MPE1) (Takes into account the effect of multipath)

The modified parabolic equation (MPE) is a standard parabolic equation that has been slightly modified to include some clear-air radioclimatic propagation parameters. The two basic parameters that were included in the modifications are the geoclimatic factor and the effective earth radius factor (popularly known as k-factor). Geoclimatic factor is the basic parameter needed to implement the effect of multipath propagation in a clear-air environment [54, 58]. On the other hand, k-factor variable is needed for diffraction fading modeling in clear-air radioclimatic studies [42, 44, 60].

The geoclimatic factor as determined in equation (4.31) of section 4.7 is incorporated into equation (3.93) in chapter three in order to come up with the first modified parabolic equation MPE1. Equation (3.93) is restated as equation (4.31) below:

$$\frac{\partial u}{\partial x} = ik_o \left(-1 + \sqrt{1 + X} \right) u \quad (4.32)$$

where k_o is the wave number in free space, $X = \left(1/ k_o^2 \right) \left(\partial^2 / \partial z^2 \right) + (n^2 - 1)$ and n is the refractive index. It will be noted in equation (4.32) that the variable X is a function of refractive index. So in MPE1 the refractive index portion of variable X is replaced with the geoclimatic factor G_F , equation (4.31) which is also a function of refractive index. Then equation (4.32) now becomes:

$$\frac{\partial u_{G_F}}{\partial x} = ik_o \left(-1 + \sqrt{1 + X_{G_F}} \right) u \quad (4.33)$$

Where u_{G_F} is the reduced field component of the first modified parabolic equation (MPE1), X_{G_F} is $X_{G_F} = \left(1/ k_o^2 \right) \left(\partial^2 / \partial z^2 \right) + G_F$. The solution of the MPE1 is very similar to that of SPE detailed in previous section. Since G_F can be determined numerically, from the radio propagation data available for the research; the remaining task of the solution is resolved by the M-File MATLAB software code developed to implement the solution.

The features of this modification can better be observed by plotting path loss against height and path loss against range separately. This is done in the next set of plots for the two stations and for different seasonal months. Figures 4.35 (a) and (b) below shows the path loss against height for Durban and Botswana in the summer months of February while figures 4.36 (a) and (b) shows path loss against height plots for Durban and Botswana in the winter months of August.

In figures 4.35 and 4.36 where path loss versus height is plotted at two coverage ranges (i.e. 10km and 20km), it can be observed that for all the plots in this section at a range of 10km from the transmitting source, path loss increases initially slowly as the height increases for the first 0 –10m above ground level (a.g.l.) and exponentially later above 10m above ground level (a.g.l.). On the other hand, at a longer range of 20km, the behaviour of the plot is quite different from what is explained above as one observes from figures 4.35 – 4.36. In this case, path loss decreases initially slowly from

a maximum value of about 5.5 dB to a value ranging from 2.85dB – 4dB depending on the location and season. It then starts to increase slowly initially from this minimum value for the first 4m height and increase exponentially beyond 10 m a.g.l.

This behaviour of the plot at 20km range shows duct occurrence probability, ducting is a very significant phenomena in clear-air study because it has the effect of trapping signal as if propagating in a wave guide. The duct depth and thickness varies from season to season and for different locations as seen from figures 4.35 – 4.36.

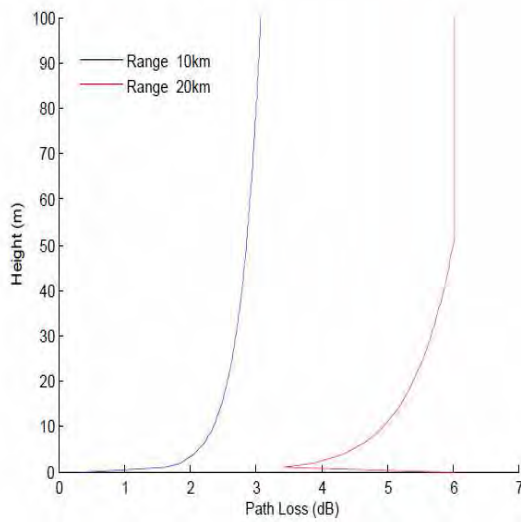


Figure 4.35 (a) Path Loss against Height at 19.5 GHz for MPE1 February 2004 Durban

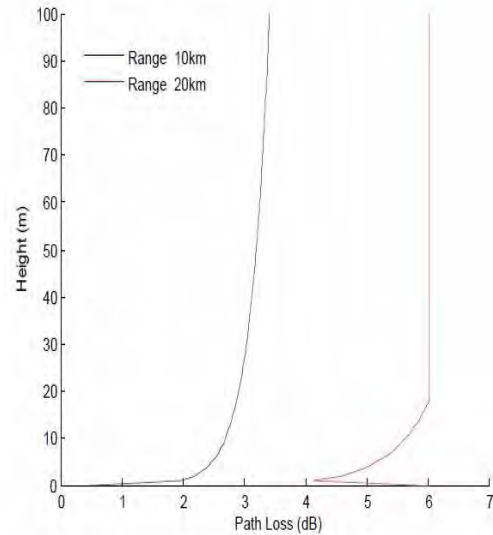


Figure 4.35(b) Path Loss against Height at 19.5 GHz for MPE1 February 1996 Botswana

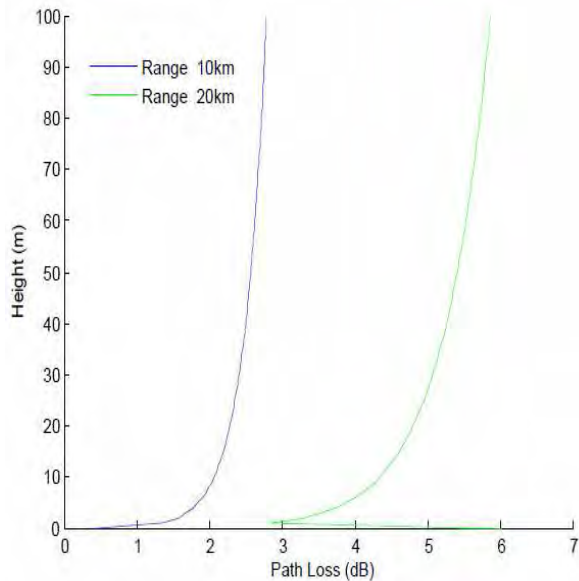


Figure 4.36(a) Path Loss against Height at 19.5 GHz for MPE1 August 2004 Durban

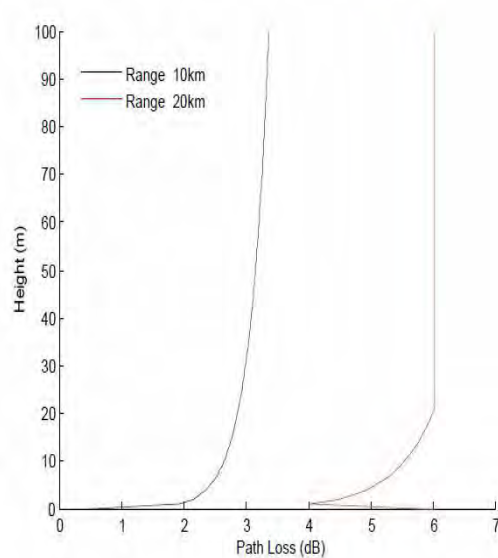


Figure 4.36(b) Path Loss against Height at 19.5 GHz for MPE1 August 1996 Botswana

We are just considering MPE1 modification of parabolic equation in these plots, and MPE1 modification is arrived at by incorporating only the geoclimatic factor variable into the parabolic equation. We now look at the effect of geoclimatic factor as captured by our plot, geoclimatic factor is the clear-air variable which is used for multipath fading modeling, it is therefore expected that multipath fading effect should be more prominent in a flat terrain such as Botswana as compared to an hilly terrain like Durban where diffraction fading should be more prominent.

Further analysis of the plots reveals the following: at a height of 10 m a.g.l and range 10 km, a path loss value of 2.5 dB is observed in Durban while at the same height and range, a value of 2.6 dB is observed in Botswana during the summer months of February (see Figure 4.35(a) and (b)). While still at the same height level of 10m a.g.l but now moving to a longer range of 20 km, a path loss value of 5 dB is observed for Durban while that of Botswana is 5.6dB during the summer months of February (see Figure 4.35 (a) and (b)).

Moving to a higher height level of 30m a.g.l for the same months (i.e. February) and at a range of 10 km shows that Durban has 2.8dB path loss while Botswana has a higher path loss value of 3 dB. If we now increase the coverage range to a distance of 20 km at the same height level of 30 m a.g.l for this

same summer month of February, our result will be as follows: Durban has a path loss value of 5.6 dB while Botswana has a higher value of 6 dB.

Doing the same analysis for the winter months of August in the two stations shows similar trends to our discussion above with slight differences in values. At the height level of 10 m a.g.l and coverage range of 10 km, Durban has a path loss value of 2 dB while Botswana has a higher value of 2.6 dB. Taking a longer range of 20 km at the same height level of 10 m a.g.l gives Durban a path loss value of 4.3 dB while that of Botswana is 5.5 dB (see Figure 4.36 (a) and (b)).

At a higher height level of 30 m a.g.l in the winter month of August, the result is as follows: for a coverage range of 10 km, Durban has a path loss value of 2.5 dB while Botswana records a path loss value of 2.9 dB. If a longer range of 20 km is considered, then the results will be as follows: Durban has a path loss value of 5.1 dB while Botswana has a path loss value of 6 dB at this range and height level (see Figure 4.36(a) and (b)).

All the discussions above show that for the two seasonal months considered, Botswana always has a higher path loss value at the selected ranges and height levels. This is not surprising since we are at this stage dealing with the first modification of parabolic equation which incorporates multipath fading effect and Botswana being a flatter terrain than Durban is expected to have more fading due to multipath than Durban as explained earlier.

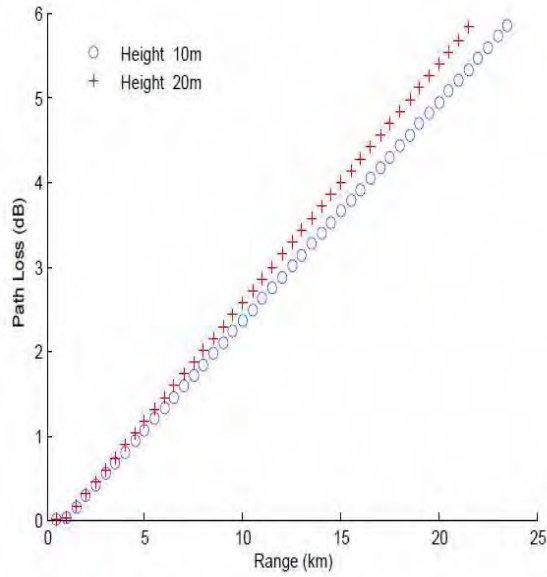


Figure 4.37 (a) Path Loss against Range at 19.5 GHz for MPE1 February 2004 Durban

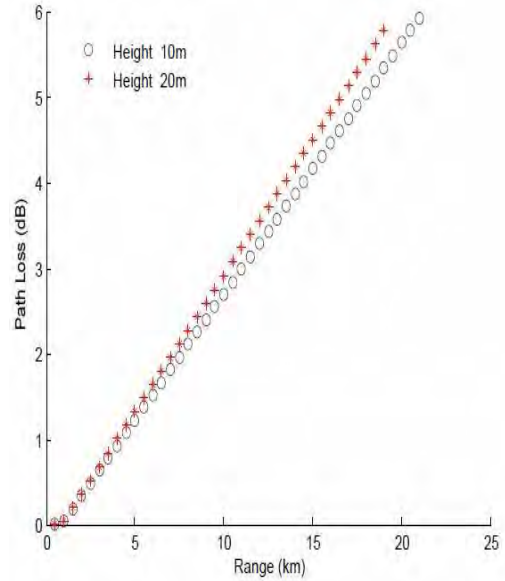


Figure 4.37(b) Path Loss against Range at 19.5 GHz for MPE1 February 1996 Botswana

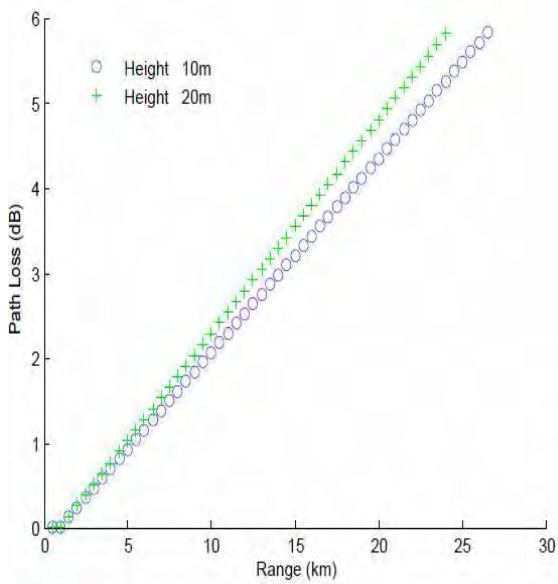


Figure 4.38(a) Path Loss against Range at 19.5 GHz for MPE1 August 2004 Durban

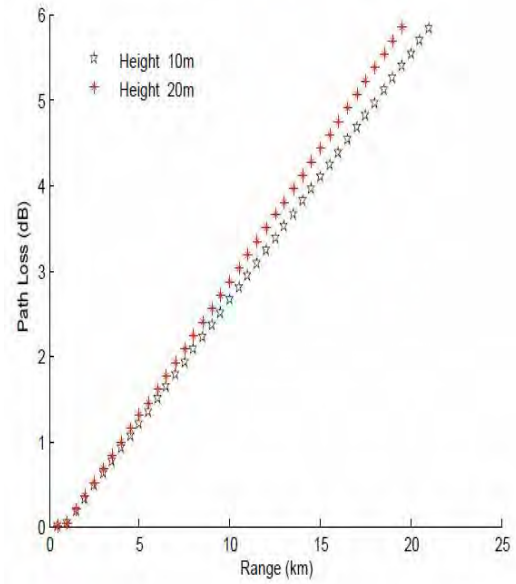


Figure 4.38(b) Path Loss against Range at 19.5 GHz for MPE1 August 1996 Botswana

In figures 4.37 (a) and (b), the path loss is plotted against the coverage range or distance for the summer months of February in both Durban and Botswana. On the other hand in figures 4.38 (a) and (b), path loss is plotted against range for the winter months of August in both Durban and Botswana. Several deductions can be made from these figures. It will be noticed that all the plot figures 4.35 – 4.38 show a progressive increase of path loss as the coverage range or distance increases, this is expected since theoretically more signal is lost as the propagation distance increases. The way each plot increases in path loss with distance is very unique to each location and season as can be seen from figures 4.35 – 4.38.

The remaining plots (Figure 4.37 – 4.38) corroborate most of our discussions in the preceding paragraphs. This is a plot of path loss versus range graphs and as could be seen from the plots, all the plots conspicuously show a gradual increase of the path loss with increasing range as expected. However, it should be noted that in all the plots, the two heights (10 m and 20 m a.g.l) selected in these plots coincide for some range distance before the difference becomes obvious after this range. The reason for this will be study further in future refinement of the model.

4.9 Second Modified Parabolic Equation (MPE2) (Takes into account the effect of diffraction fading)

The second modification of the parabolic equation called MPE2 which incorporates the k-factor or the diffraction fading effect will now be discussed. In the second modification we incorporate the clear-air parameter known as the k-factor into the parabolic equation. The k-factor has been discussed in chapter two and modeled in chapter three. We will therefore not repeat this discussion here. The k - factor determined in chapter three, equation (3.5) is placed in the refractive index portion of equation (4.32). Equation (4.32) then becomes:

$$\frac{\partial u_k}{\partial x} = ik_o \left(-1 + \sqrt{1 + X_k} \right) u \quad (4.34)$$

Where u_k is the reduce field component of the second modified parabolic equation (MPE2), X_k is $X_k = \left(1/ k_0^2 \right) \left(\partial^2 / \partial z^2 \right) + k$ and the remaining symbols have their usual meaning. The solution of the MPE2 is very similar to that of MPE1 detailed in previous section. The k-factor has a numeric value

for different seasons and for the two locations being studied. The remaining task of the solution is resolved by the M-File MATLAB software code developed to implement the solution.

The path loss plots against height and range generated after this second modification for Durban and Botswana, in the seasonal months of February (summer) and August (winter) are shown in figures 4.39 – 4.42. These results are then discussed below the plots as we did earlier.

The coverage diagram looks alike for all type of modifications of parabolic equation. It was therefore not included in the next set of plots. Similar trend to previous discussion was observed for the second modification, there is a little difference in the results though as discussed in the paragraphs that follow.

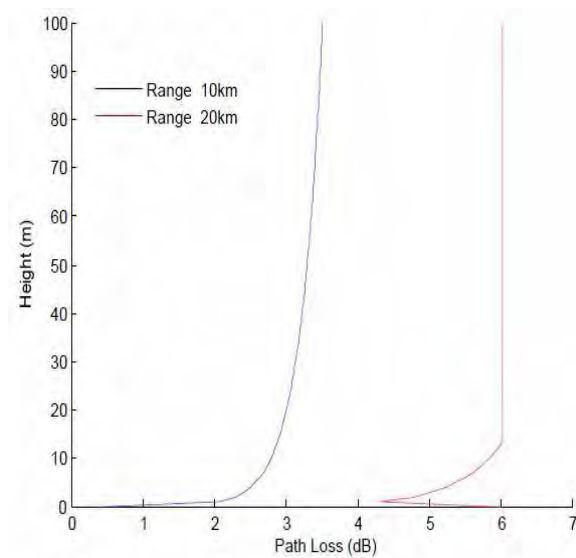


Figure 4.39(a) Path Loss against Height at 19.5 GHz for MPE2 February 2004 Durban

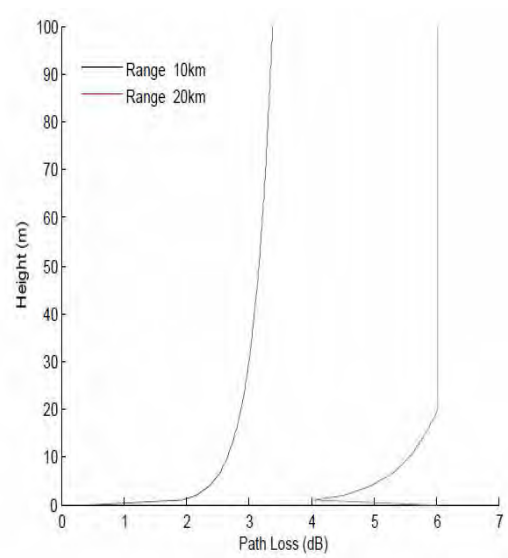


Figure 4.39(b) Path Loss against Height at 19.5 GHz for MPE2 February 1996 Botswana

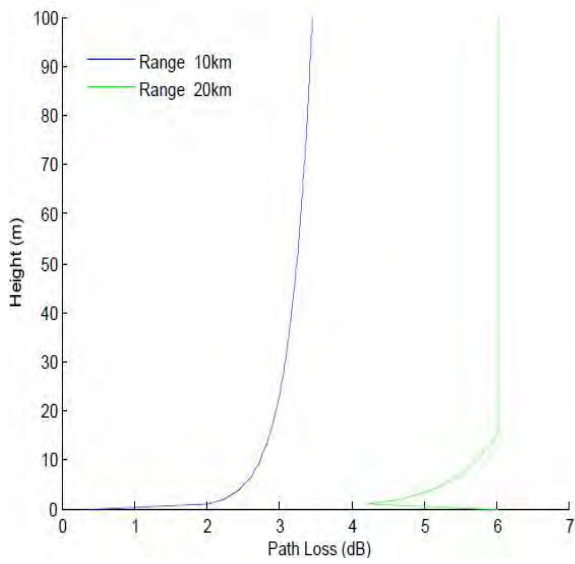


Figure 4.40 (a) Path Loss against Height at 19.5 GHz for MPE2 August 2004 Durban

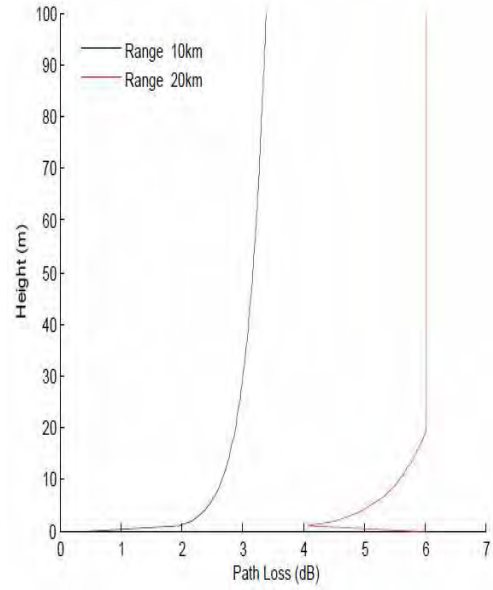


Figure 4.40(b) Path Loss against Height at 19.5 GHz for MPE2 August 1996 Botswana

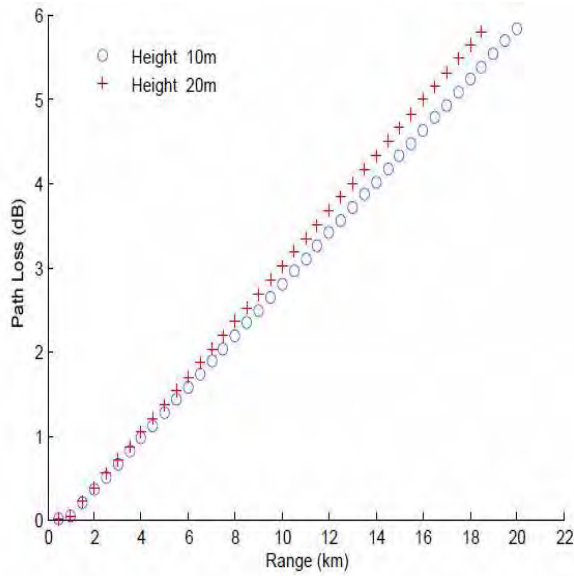


Figure 4.41(a) Path Loss against Range at 19.5 GHz for MPE2 February 2004 Durban

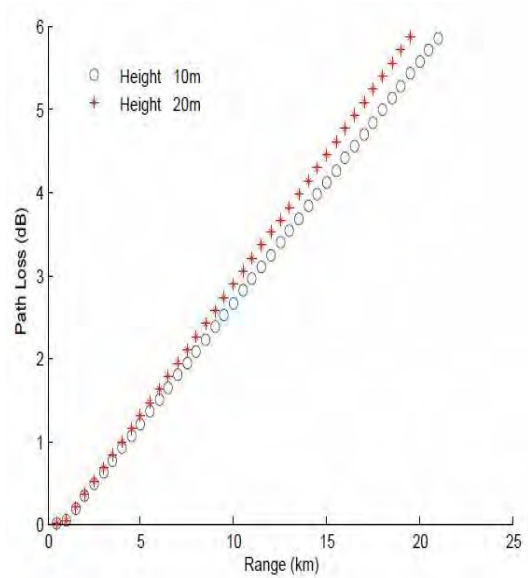


Figure 4.41(b) Path Loss against Range at 19.5 GHz for MPE2 February 1996 Botswana

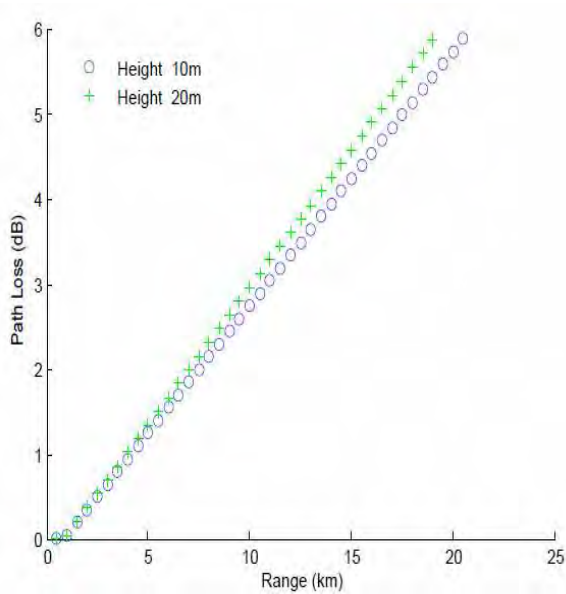


Figure 4.42(a) Path Loss against Range at 19.5 GHz for MPE2 August 2004 Durban

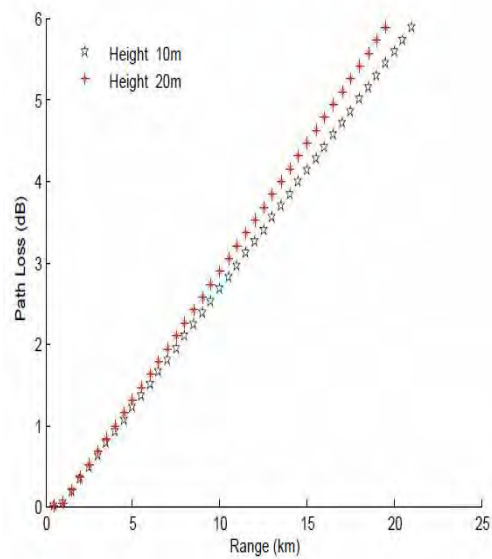


Figure 4.42(b) Path Loss against Range at 19.5 GHz for MPE2 August 1996 Botswana

The path loss versus height is plotted in figures 4.39 – 4.40 for the seasonal months of February (summer) and August (winter) in Durban and Botswana. On the other hand, figures 4.41 – 4.42 show the plots of path loss versus range for the seasonal months of February (summer) and August (winter) in both Durban and Botswana. At a height level of 10 m a.g.l. and coverage range of 10 km Durban recorded a path loss value of 2.8 dB while Botswana has a path loss value of 2.6 dB in the summer months of February (see Figure 4.39 (a) and (b)).

Moving to a higher height level of 20 m a.g.l. at the same coverage distance of 10 km, Durban recorded a path loss value of 3.05 dB while Botswana on the other hand has a path loss value of 2.9 dB for the summer months of February (see Figure 4.39 (a) and (b)). At a longer range of 20 km, and height level of 10 m a.g.l., the result is as follows: Durban recorded a path loss value of 5.8 dB in the summer month of February while Botswana recorded a path loss value of 5.6 dB (see Figure 4.41 (a) and (b)). On the other hand at the same coverage range of 20km and a higher height level of 20 m a.g.l. Durban recorded a path loss value of 6.7dB in the summer month of February (obtained by extrapolation of Figure 4.41(a)) while Botswana recorded a path loss value of 6 dB in the summer month of February (see Figure 4.41(b)).

The analysis for the winter months of August shows similar trend, for instance at a height level of 10 m a.g.l and a coverage range of 10 km in the winter months of August the result is as follows: Durban has a path loss value of 2.7 dB while Botswana has a path loss value of 2.6 dB (see Figure 4.40 (a) and (b)). Keeping the coverage range constant at 10 km and moving to a higher height level of 20 m a.g.l., Durban has a path loss value of 2.98 dB while Botswana at this new height level has a path loss value of 2.8 dB (see Figure 4.40 (a) and (b)).

In this same winter's month of August at a longer coverage range of 20 km and a height level of 10 m a.g.l. the result is as follows: Durban has a path loss value of 5.7 dB while Botswana has a path loss value of 5.5 dB (see Figure 4.42 (a) and (b)). If we move to a higher altitude level of 20 m a.g.l. at the same coverage range of 20 km we observe the following results: Durban has a path loss value of 6.2 dB (obtained by extrapolation of Figure 4.42 (a)), while Botswana has a path loss value of 5.9 dB for this same height level and coverage range (see Figure 4.42(b)).

The analysis of Figure 4.39 – 4.42 above shows generally that the path loss value at the different coverage range and height level is higher in Durban than it is in Botswana. This is very much in agreement with our expectation, since as explained earlier, we are, at this stage analyzing the effect of diffraction fading. Diffraction fading is evident by incorporating k-factor into SPE to form the second modified parabolic equation (MPE2). Since Durban generally has a more hilly terrain compared to Botswana which has a flatter terrain, we expect Durban to have a higher path loss value than Botswana for this type of modifications and this is what our results in Figure 4.39 – 4.42 show.

4.10 Chapter Summary

This chapter presents an extensive analysis of the clear-air signal level measurement across a line of sight link between Howard College Campus and Westville Campus of the University of KwaZulu-Natal. This analysis is very important in order to be able propose an appropriate clear-air radioclimatic model for Southern Africa. The measurement period spans eight months from February to December 2004. Measurements are taken across the LOS link at a frequency of 19.5 GHz. The analysis has been done in three phases. The first phase was done daily; the second phase was done monthly, and the last phase was done for all measurement periods.

Seven fade depth levels were analyzed in each of the phases. These fade depth levels are: fade depths, $A(\text{dB}) \geq 2 \text{ dB}$; $A(\text{dB}) \geq 5 \text{ dB}$; $A(\text{dB}) \geq 10 \text{ dB}$; $A(\text{dB}) \geq 15 \text{ dB}$; $A(\text{dB}) \geq 20 \text{ dB}$; $A(\text{dB}) \geq 30 \text{ dB}$; $A(\text{dB}) \geq 40 \text{ dB}$. The percentage of time that each of these fade depth levels is exceeded from the total measurement time – known as exceedance probability was determined at each phase of the analysis.

The analysis described above becomes the bedrock for determination of the proposed analytical model for clear-air radioclimatic study in Southern Africa. Having determined the exceedance probability at these different fade depths as discussed above, an analytical expression is proposed to model these exceedance probabilities as a function of fade depth. The proposed analytical model is a fourth order polynomial. The model can be used to predict the percentage of time that a particular fade depth is exceeded for different months and for the whole year in Southern Africa.

The second analytical model proposed in this study is the modified parabolic equation. This is an analytical model which captures the effect of the terrain characteristic of the study area. The standard parabolic equation (SPE) was modified to include the geoclimatic factor. This initial modification is called first modified parabolic equation (MPE1). The final modification includes the effective earth radius factor (k-factor). This final modification is called second modified parabolic equation (MPE2). Two different topographical terrains were chosen to test each of these modifications. The result obtained after the test shows that there is more signal loss due to multipath in Botswana, where the terrain is flat compared to the second location. MPE1 which incorporate geoclimatic factor was able to capture this effect. On the other hand, in Durban where the terrain is hilly and mountainous, more signal loss is experienced due to diffraction fading. The second modification (MPE2) was able to capture this effect.

CHAPTER FIVE

COMPARISON OF THE RESULTS OBTAINED USING DIFFERENT MODELS AND THE PROPOSED MODEL

5.0 INTRODUCTION

The various models proposed by different authors across the globe in chapter three need to be tested, verified and compared with our proposed model in chapter four for our region in Africa. In order to achieve this stated objective, we have, in chapter four done an extensive analysis of the signal level measurement across a line-of-sight (LOS) link in Durban, South Africa. These analyses precede our proposition of the analytical model for clear-air radioclimatic study in Southern Africa. The significant achievement of this exercise is that we are able to determine the exceedance probabilities across the LOS link for our region from a practical point of view. These results become very handy in testing and verification of the different models proposed by the various authors. This will enable us to determine which of these models is most comparable with our proposed model using the local data for this region. This will be the focus of this chapter as a whole.

5.1 Comparison of Morita and Kakita Models

The Morita and Kakita fit their data in Japan over a 4 GHz link with the following empirical relation:

$$P_R = \left(\frac{f}{4}\right)^{1.2} \cdot Q \cdot d^{3.5} \quad (P_R \leq 0.3) \quad (5.1)$$

Where P_R is the Rayleigh fading occurrence probability, f is the operating frequency of the microwave link in GHz, d is the path distance in km, and Q is a constant called the propagation terrain factor. The value of Q varies for different terrain types according to the following expression; $Q = 2.0 \times 10^{-9}$ (over the mountains), $Q = 5.1 \times 10^{-9}$ (over the plains), $Q = 3.7 \times 10^{-7} \sqrt{1/\bar{h}}$ (over the sea), \bar{h} = average path height in meters. The terrain type stated in bracket in the above expression is defined as follows: For over the mountains paths, most of the path is over mountainous terrain; for over the plains, most of the path is over plains; for over the sea region, the path is over the sea or the path is over the coastal region (within 10 km from the coast) (see Table 3.5).

In order to implement this model for our LOS link in Durban, South Africa, we must classify our link path to conform to one of these categories given by Morita and Kakita above. The description of our investigation study area in chapter two, section 2.3.1 shows that our propagation path is located in coastal areas (see Figure 2.1 and Figure 2.2). Hence we choose our Q value to be $Q = 3.7 \times 10^{-7} \sqrt{1/\bar{h}}$ (over the sea). Now that we know our Q value, our distance (6.73 km) and frequency (19.5GHz) can be obtained directly from Table 2.1. The last parameter is the average height which can be calculated using equation (3.22) as follows:

$$\bar{h} = \frac{h_1+h_2}{2}$$

Where $h_1 = 24 \text{ m} + 178 \text{ m} = 202 \text{ m}$, and $h_2 = 20 \text{ m} + 145 \text{ m} = 165 \text{ m}$ (see Table 2.1), the average height is therefore;

$$\bar{h} = \frac{h_1+h_2}{2} = \frac{202+165}{2} = \frac{367}{2} = 183.5 \text{ m}$$

Since all the relevant information is determined, we can now apply the Morita and Kakita Model for our LOS link as follows:

$$P_R = \left(\frac{f}{4}\right)^{1.2} \cdot Q \cdot d^{3.5} = \left(\frac{f}{4}\right)^{1.2} \times 3.7 \times 10^{-7} \times \sqrt{1/\bar{h}} \times d^{3.5}$$

$$P_R = \left(\frac{19.5}{4}\right)^{1.2} \times 3.7 \times 10^{-7} \times \sqrt{1/183.5} \times (6.73)^{3.5}$$

$$P_R = 6.6922097 \times 3.7 \times 10^{-7} \times 0.073821347 \times 790.7746248 = 0.0001445$$

Consequentially, this is the Rayleigh fading probability of occurrence for our line of sight link using Morita and Kakita Model. For verification purposes, we need to compare this with our results in chapter three and see any similarity or disparity. Unfortunately, Morita and Kakita did not specify in their model at which fade depth level they develop their model. This indicates that we need to compare this result with all the fade depths for all months. Comparing this result with the results presented in section 4.4 for all fade depths over all the months shows the following comparison. Although there is no perfect match with the results obtained in section 4.4, the value obtained here is comparable with some of the values obtained earlier at some fade depths for certain months. For instance, the value of exceedance probability obtain in April for the fade depths: $A \geq 5 \text{ dB}$, $A \geq 10 \text{ dB}$, $A \geq 15 \text{ dB}$, $A \geq 20 \text{ dB}$, $A \geq 30 \text{ dB}$, and $A \geq 40 \text{ dB}$ are all zeros (see Table 4.18). The value of

0.0001445 is close enough to zero; in other words both values (0 and 0.0001445) will guarantee 99.999 % link availability.

Similarly in chapter four for the month of July, we obtain zero exceedance probability for the fade depths: $A \geq 15$ dB, $A \geq 20$ dB, $A \geq 30$ dB, and $A \geq 40$ dB (see Table 4.18). For the same reason explained above, the value obtained here is comparable with those values for July at these fade depth levels. Finally for the month of August, the result obtained in chapter four shows zero exceedance probabilities for the fade depths: $A \geq 5$ dB, $A \geq 10$ dB, $A \geq 15$ dB, $A \geq 20$ dB, $A \geq 30$ dB, and $A \geq 40$ dB.

In all, we can conclusively say Morita and Kakita models fits Durban data in three out of the eight months analyzed in chapter four at different fade depth levels. These three months are April, July and August. The fade depth levels at which Morita and Kakita Model fits Durban data are: $A \geq 15$ dB, $A \geq 20$ dB, $A \geq 30$ dB, and $A \geq 40$ dB.

Though Morita and Kakita Model fits our data in some months at certain fade depths, one should also take cognisance of the fact that Morita and Kakita did not include any climatic parameter in their model. Probably if climatic parameters are included in Morita Kakita Model to cater for the climate change characteristic along the path, more data at more fade depths, would have been fitted. It is a known fact that climate changes affect propagation in no small way. Morita and Kakita in their model only included link path parameters.

5.2 Comparison of Vigants Models

Vigants explains the fading terminology by citing a practical example. To start with he supposed a transmitted signal with free space value of -30 dBm, and a single idealized fade decreases the received power temporarily to -80 dBm. Then the levels in dB relative to normal are denoted by $20\log L$. The time during which a signal is below a particular reference level is called the duration of that fade level. He stated that average duration of fades are independent of microwave frequency and are proportional to L . Vigants in his model defined the sum of durations for all fades of a particular depth as ‘time below level’. This term is said to be proportional to L^2 , since the number of fades is proportional to L , and its numerical values are given in [23]:

$$T = rT_0L^2, \quad L < 0.1 \quad (5.2)$$

Where T_0 is the time period over which the summation of fade durations is made (a month, for example); the units of T are identical to that of T_0 (seconds are normally used). The fade occurrence factor r for heavy fading months is:

$$r = c(f/4)D^310^{-5} \quad (5.3)$$

where;

- $c = 4$ over water and Gulf coast,
- $= 1$ average terrain and climate,
- $= \frac{1}{4}$ mountains and dry climate,
- $f =$ frequency in GHz,
- and
- $D =$ path length in miles.

The coefficient c in (5.3) incorporates the effect of both terrain and humidity but did not account for different terrains with similar climate. Paths of identical climate but different terrain can be accounted for by introducing terrain roughness parameter [25]. Terrain roughness is calculated from terrain heights above a reference level (sea level, for example) obtained at one – mile intervals, with the ends of the path excluded. The standard deviation of the resulting set of numbers is the terrain roughness, denoted by w . Applicable values of w range from 20 feet (“smooth”) to 140 feet (“rough”); values of 20 and 140 feet should be used when calculated values of w are less than 20 or larger than 140. In (5.3), c is modified for terrain roughness as follows:

$$\begin{aligned} c &= 2(w/50)^{-1.3}, \quad \text{coastal area,} \\ &= (w/50)^{-1.3}, \quad \text{average climate,} \\ &= 0.5 (w/50)^{-1.3}, \quad \text{dry climate,} \end{aligned} \quad (5.4)$$

where a roughness of 50 feet has been defined as "normal."

In order to test and verify this model, we need to first determine the terrain roughness for our LOS link path. When this is done, we can then start applying the different formulas using our link parameters. To calculate the terrain roughness from our path characteristic, we divide the path length into intervals of 1 km (see Figure 2.4 and Figure 2.5). Using the height information on the contour

map and DEM we determine the height profile a.g.l. for our propagation path as shown in Table 5.1 below:

Now that we have our height profile from the DEM contour maps, we can determine the standard deviation SD. However we should be mindful of the fact that the first and the last height profile value in Table 5.1 must be excluded from our calculation. Therefore values for $h(0)$ and $h(d)$ will not be included in the calculation of SD. The standard deviation is defined as the r.m.s. size of the deviations from the average [133].

Table 5.1 Height Profile Estimation for LOS Link Path

Distance From Transmitter (km)	Height Profile	
	$h(x)$	Value (m)
0	$h(0)$	178
1	$h(1)$	80
2	$h(2)$	150
3	$h(3)$	120
4	$h(4)$	110
5	$h(5)$	80
6	$h(6)$	80
6.73	$h(7) \rightarrow h(d)$	145

The SD is determined from the following expression:

$$SD = \sqrt{\frac{\sum (h(x) - \overline{h(x)})^2}{n}} \quad (5.5)$$

Where $h(x)$ is the xth height profile, $\overline{h(x)}$ is the average over all the height profiles excluding the first and the last height profiles, and n is the number of samples used for the calculation of SD. Using equation (5.5) above, the value of average height profile $\overline{h(x)}$ 103.33 m, while the standard deviation (SD) is 26.2466 m.

This SD is our terrain roughness in meters for our LOS path. In order to make it usable in Vigants model, we convert it to feet and it becomes 86.1 feet. This is our terrain roughness (w) value, as one can see it falls within the applicable range of 20 – 140 feet. Our path can be said to be fairly rough as evident from a terrain roughness value of 86.1 feet. The next step in applying Vigants model is to determine the propagation terrain parameter c using (5.4). Our terrain can be classified as coastal area; hence the first row of (5.4) is applicable.

$$c = 2 \left(\frac{w}{50} \right)^{-1.3} = 2 \times \left(\frac{86.1}{50} \right)^{-1.3} = 2 \times (1.722)^{-1.3} = 0.9867$$

Next we determine the propagation factor r using (5.3), but the formula uses distance in miles so we first convert our 6.73 km path length to statute miles. This gives us a value of 4.18 miles; then we can apply (5.3) as follows:

$$r = c(f/4)D^3 10^{-5} = 0.9867 \times (19.5/4) \times (4.18)^3 \times 10^{-5}$$

$$r = 0.9867 \times 4.875 \times 73.034632 \times 10^{-5} = 0.00351$$

The next stage is to now apply the Vigants model in (5.2), but before we can do this, we need to first determine the fade depth we will be working with and use this to determine the L values. Also we need to convert our measurement values from minutes to seconds for the month we will be working with. To determine the L values we used the relation A (dB) = $20 \log L$, the value L can therefore be determined as:

$$L = 10^{(A/20)} \tag{5.6}$$

Using equation (5.6), one can calculate the value of L for the seven fade depth levels analyzed in chapter three as follows:

For the fade depth $A = - 2$ dB

$$L = 10^{(-A/20)} = 10^{(-2/20)} = 10^{(-0.1)} = 0.7943$$

Similarly for the fade depth $A = - 5$ dB

$$L = 10^{(-A/20)} = 10^{(-5/20)} = 10^{(-0.25)} = 0.5623$$

Similarly for the fade depth $A = - 10$ dB

$$L = 10^{(-A/20)} = 10^{(-10/20)} = 10^{(-0.5)} = 0.3162$$

Similarly for the fade depth $A = - 15$ dB

$$L = 10^{(-A/20)} = 10^{(-15/20)} = 10^{(-0.75)} = 0.1778$$

Similarly for the fade depth $A = - 20$ dB

$$L = 10^{(A/20)} = 10^{(20/20)} = 10^{(1)} = 10$$

For the fade depth $A \geq 30$ dB

$$L = 10^{(-A/20)} = 10^{(-30/20)} = 10^{(-1.5)} = 0.03162$$

And for the fade depth A = - 40 dB

$$L = 10^{(-A/20)} = 10^{(-40/20)} = 10^{(-2)} = 0.01$$

These are corresponding L values for A(dB) varies from -2 to -40 analyzed in chapter four. From equation (3.25) and (3.26), $L < 0.1$ for A = 20 dB, 30 dB, and 40 dB as seen above. Hence the equation presented in Vigants model is only valid for these fade depths. In order to determine T_0 of equation (5.2), we refer to Table 4.17 of section 4.4. The total time for the whole measurement periods and for the different fade depth levels are as follows: for fade depth $A \geq 2$ dB, $T_0 = 10825$ mins = 649500 secs; for fade depth $A \geq 5$ dB, $T_0 = 3065$ mins = 183900 secs; for fade depth $A \geq 10$ dB, $T_0 = 3005$ mins = 180300 secs; for fade depth $A \geq 15$ dB, $T_0 = 2989$ mins = 179340 secs; for fade depth $A \geq 20$ dB, $T_0 = 2989$ mins = 179340 secs; for fade depth $A \geq 30$ dB, $T_0 = 2897$ mins = 173820 secs; and for fade depth $A \geq 40$ dB, $T_0 = 188$ mins = 11280 secs (see Table 4.17 in chapter four).

Now that we have all the variables in (5.2) in place we can now apply Vigants Model to our LOS link for different fade depths to the “time below level” as follow:

For Fade depth $A \geq 2$ dB we have;

$$T = rT_0L^2 = 0.00351 \times 649500 \times (0.7943)^2$$

$$T = 1,438.3 \text{ sec} = 23.97 \text{ mins}$$

If we convert this to the equivalent exceedance probability so that comparison can easily be made with our measurement result we have:

$$P(A \geq 2 \text{ dB}) = \frac{23.97}{194,243} \times \frac{100}{1} = \frac{2397}{194,243} = 0.012 \%$$

This is value is obviously too far from the value of 5.573 % obtained at this fade depth in chapter four (see Table 4.18). For Fade depth $A \geq 5$ dB we have;

$$T = rT_0L^2 = 0.00351 \times 183,900 \times (0.5623)^2$$

$$T = 204.09 \text{ sec} = 3.40 \text{ mins}$$

If we also convert this to the equivalent exceedance probability so that comparison can easily be made with our measurement result we have:

$$P(A \geq 5\text{dB}) = \frac{3.40}{194,243} \times \frac{100}{1} = \frac{340}{194243} = 0.00175 \%$$

Also this value is too distant from the value of 1.578 % obtained at this fade depth level in chapter four (see Table 4.18).

For Fade depth $A \geq 10$ dB we have;

$$T = rT_0L^2 = 0.00351 \times 180,300 \times (0.3162)^2$$

$$T = 63.274 \text{ secs} = 1.054 \text{ mins}$$

Converting this to the equivalent exceedance probability so as to make comparison possible with measurement result yields:

$$P(A \geq 10 \text{ dB}) = \frac{1.054}{194243} \times \frac{100}{1} = \frac{105.4}{194243} = 5.43 \times 10^{-4} \%$$

If we compare this value with the exceedance probability value of 1.547 % obtained in chapter four at this fade depth level (see Table 4.18), there is still a significant difference between these two results. The fade depth level compared next is fade depth $A \geq 15$ dB, for this fade depth level we determine the value T as follows:

$$T = rT_0L^2 = 0.00351 \times 179,340 \times (0.1778)^2$$

$$T = 19.8997 = 0.332 \text{ mins}$$

If we convert this to its equivalent exceedance probability for comparison purposes we have:

$$P(A \geq 15 \text{ dB}) = \frac{0.332}{194,243} \times \frac{100}{1} = \frac{33.2}{194243} = 1.709 \times 10^{-4} \%$$

This result is also too far from 1.539 % obtained at this fade depth level in chapter four (see Table 4.18). Next we check for the fade depth $A \geq 20$ dB we obtain the T value as follows:

$$T = rT_0L^2 = 0.00351 \times 179,340 \times (0.1)^2$$

$$T = 6.295 \text{ secs} = 0.1049 \text{ mins}$$

Converting the result to its equivalent exceedance probability value for verification purposes gives:

$$P(A \geq 20 \text{ dB}) = \frac{0.1049}{194,243} \times \frac{100}{1} = \frac{10.49}{194,243} = 5.4 \times 10^{-5} \%$$

This value is significantly less than the value of 1.539 % obtained at the same fade depth level in chapter four (see Table 4.18). The next fade depth level we compared is fade depth $A \geq 30$ dB, we obtain the T value as follows:

$$T = rT_0L^2 = 0.00351 \times 173,820 \times (0.03162)^2$$

$$T = 0.61 = 0.010 \text{ mins}$$

Converting the result to its equivalent exceedance probability value for verification purposes gives:

$$P(A \geq 30 \text{ dB}) = \frac{0.010}{194,243} \times \frac{100}{1} = \frac{1.0}{194,243} = 5.148 \times 10^{-6} \%$$

This value is significantly less than the value of 1.491 % obtained at the same fade depth level in chapter four (see Table 4.18). Finally we test for the fade depth $A \geq 40$ dB, we obtain the T value as follows:

$$T = rT_0L^2 = 0.00351 \times 11,280 \times (0.01)^2$$

$$T = 0.003959 \text{ secs} = 6.599 \times 10^{-5} \text{ mins}$$

If we convert this to its equivalent exceedance probability for verification purposes we have:

$$P(A \geq 40 \text{ dB}) = \frac{6.599 \times 10^{-5}}{194,243} \times \frac{100}{1} = \frac{6.599 \times 10^{-3}}{194,243} = 3.4 \times 10^{-8} \%$$

This value is still distant from the value of 0.0967 % obtained at the same fade depth level in chapter four (see Table 4.18).

The results displayed in the above analysis show that none of the result at the different fade depth has close proximity to the standard measurement results obtained in chapter four. Thus the Vigants model extremely underestimates the fade depths. The comparison shown above is done over all the months, we try the same calculation for each of the months for the applicable fade depth levels ($A = 20, 30, 40$ dB) for the models and plot the exceedance probabilities. The result of this exercise is shown in Figure 5.1 – Figure 5.4 below:

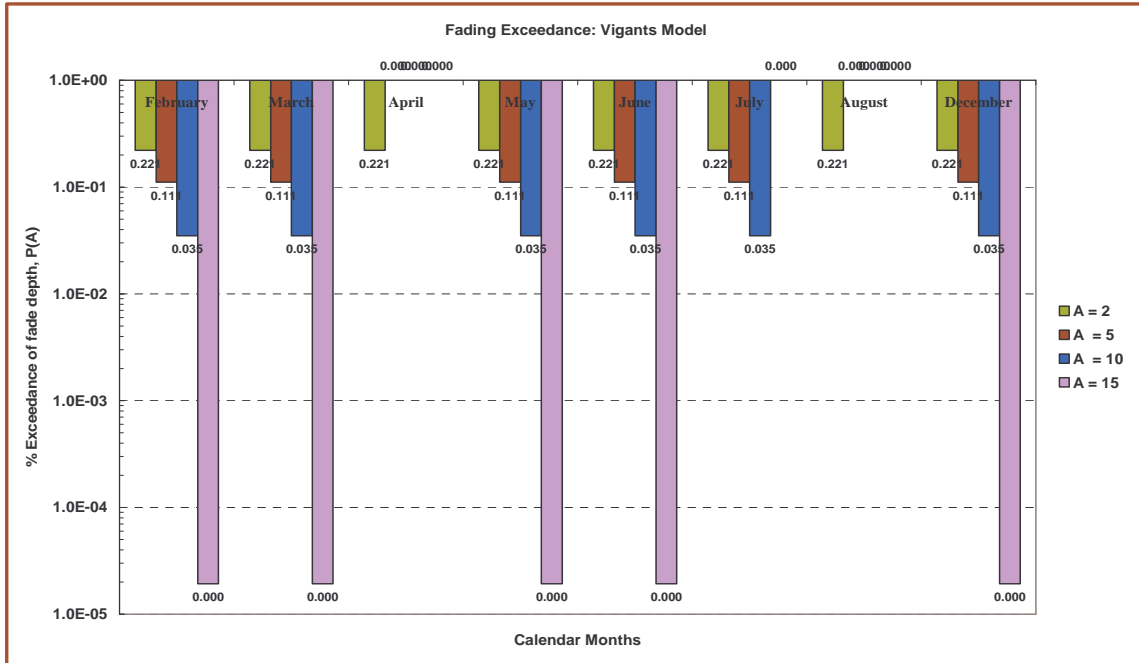


Figure 5.1 Fading Exceedance of Vigants Model: Fade depth; A = 2, A = 5, A = 10, and A = 15 dB

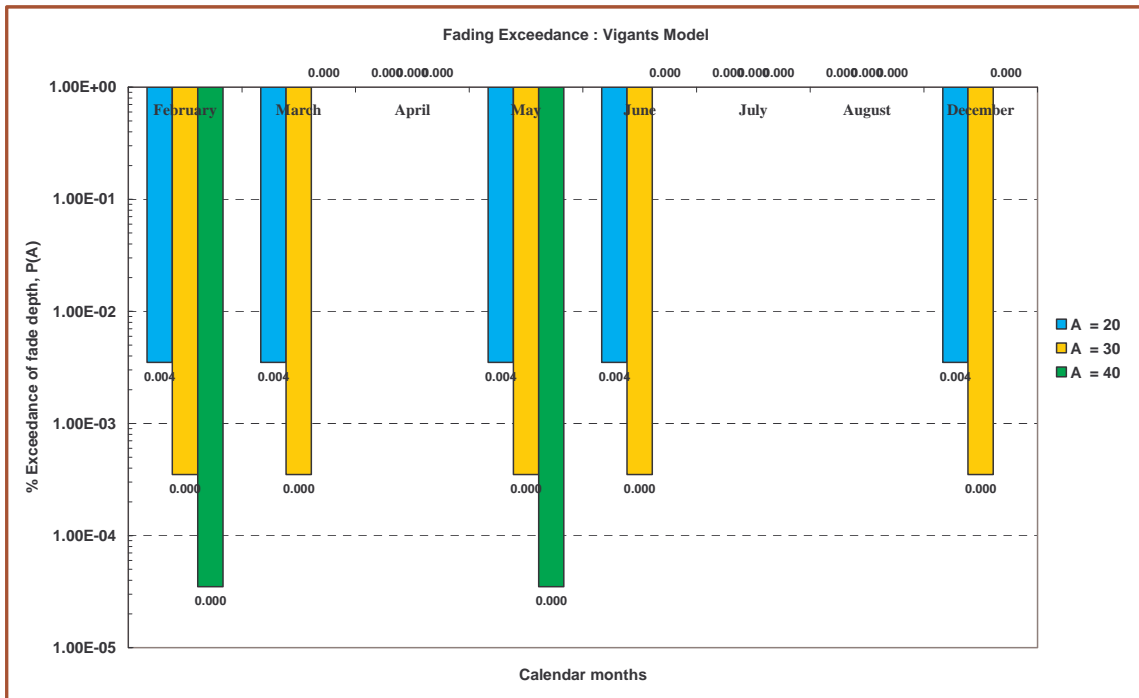


Figure 5.2 Fading Exceedance of Vigants Model: Fade depth; A = 20, A = 30, and A = 40 dB

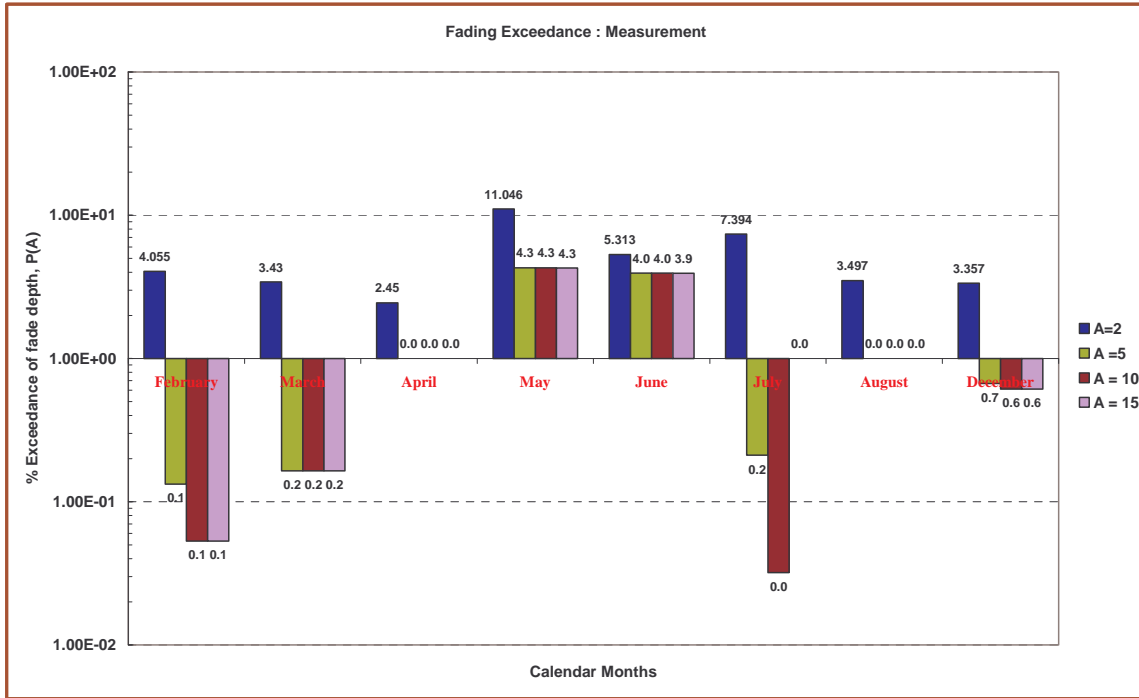


Figure 5.3 Fading Exceedance of Measurement: Fade depth; A = 2, A = 5, A = 10 and A = 15 dB

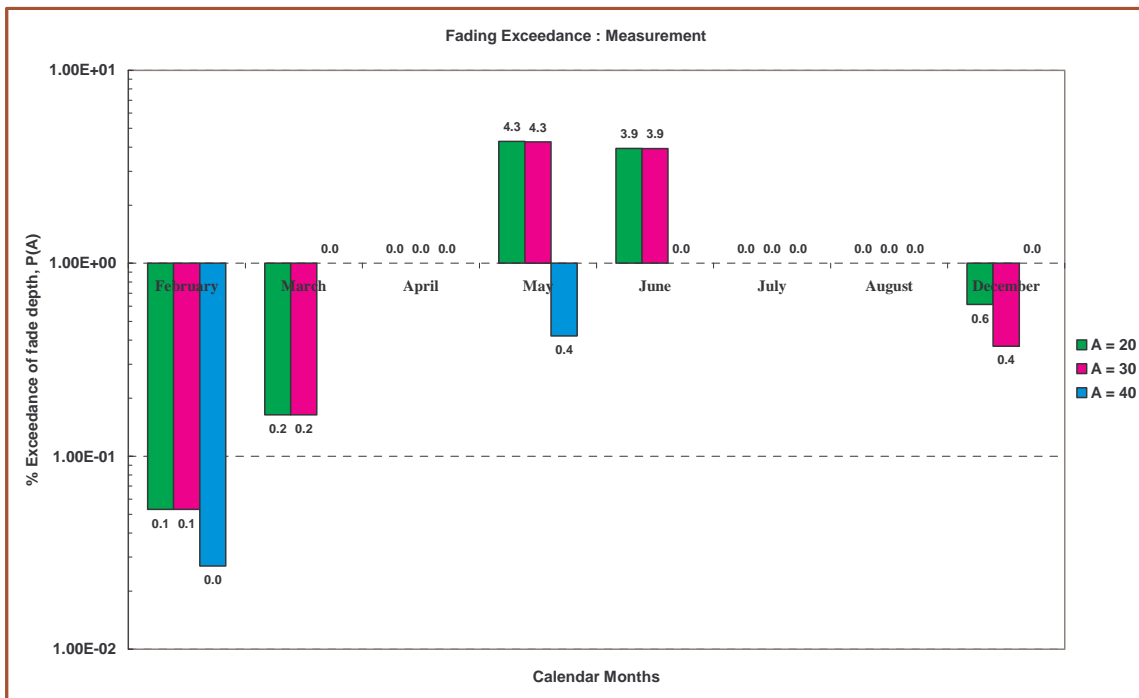


Figure 5.4 Fading Exceedance of Measurement: Fade depth; A = 20, A = 30, and A = 40 dB

The plots in Figure 5.1 – 5.4 above show a different situation compared to the whole measurement periods analyzed earlier. As we can see above, the results in almost all the months have exceededance probability value match with Vigants model in at least one fade depth level or more. For instance, in the month of March, there is a perfect match in exceedance values at a fade depth of 40 dB (see Figure 5.2 and Figure 5.4). The month of April is no different, in fact the month of April has matches in exceedance values at the following fade depths: A = 5, A = 10, A = 15, A = 20, A = 30 and A = 40 (see Figure 5.1 – Figure 5.4). For the month of May, there is no match in exceedance values with Vigants model at all the fade depths (see Figure 5.1 – Figure 5.4). The month of June however, has a match at a fade depth level of 40 dB (see Figure 5.2 and Figure 5.4). The month of July has exceedance probability value match with Vigants model at the following fade depths: A = 15 dB, A = 20 dB, A = 30 dB, and A = 40 dB (see Figure 5.1 – Figure 5.4). August has matches in exceedance value with Vigants model in six of the seven fade depth as (see Figure 5.1 – Figure 5.4). Finally the month of December has match with Vigants model at the fade depth A = 40 dB (see Figure 5.2 and Figure 5.4). This concludes our investigation that Vigants Model can be used to predict fade occurrence probabilities in Southern Africa at some fade depths in certain months.

5.3 Comparison of Crombies' Model

Crombie [34] in his model suggested that multipath fading probability (on terrestrial paths at frequencies above 11 GHz) can be estimated without detailed knowledge of climate or terrain [34]. Crombies [34] stated that such estimates require knowledge of path clearance and/or antenna beamwidths information. He stated fading probability predictability increases when antenna beamwidth is included in the analysis and inclusion of path clearance further increases the predictability. Crombie [34] in his model stated that the percentage of time for which multipath fading occurs in the worst month for a fade depth ≥ 20 dB can be expressed in the following forms [34]:

$$\begin{aligned} \text{Log } P(.01) &= -9.99 + 2.93 \log d + 1.86 \log f + 2.17 \log \theta \\ \text{or} & \\ P(.01) &= 10^{-10} \cdot d^{2.93} \cdot f^{1.86} \cdot \theta^{2.17} \end{aligned} \tag{5.7}$$

Where; $P(0.01)$ = percentage probability of fades of 20 dB or more

d = path length (km)

f = frequency (GHz)

$\theta = \sqrt{\theta_T \cdot \theta_R}$ is the antenna beamwidths for transmitter and receiver.

The model shown in (5.7) is called model 5 by Crombie [34]. In this model, the variables used are d, f, and θ . The second model similar to model 5 given by Crombie in [34] is stated as:

$$\begin{aligned} \text{Log } P(.01) &= -2.997 + 2.49 \log d + 0.84 \log f + 1.19 \log \theta - 2.44 \log h \\ \text{or} & \\ P(.01) &= 10^{-3} \cdot d^{2.49} \cdot f^{0.84} \cdot \theta^{1.19} \cdot h^{-2.44} \end{aligned} \tag{5.8}$$

Where h is the estimated height above the intervening terrain at the center of the path. The other symbols have the same meaning as in (5.7). Crombie called the model in (5.8) model 4 and the variables used in model 4 are d, f, θ and h.

5.3.1 Comparison of Crombies' Model 4

In order to compare Crombies' model 4, we first need to determine the necessary variables to implement this model from our LOS link. The variables applicable here are d, f, θ and h. We can obtain the path length from Table 2.1 to be d = 6.73 km, also the frequency f = 19.5 GHz, the antenna beamwidths can be determined as follow:

$$\theta = \sqrt{\theta_T \cdot \theta_R}$$

$$1 \text{ rad} = \left(\frac{180}{\pi} \right) \text{ degree} \approx 57.3^\circ$$

$$\text{From Table 2.1 } \theta_T = \theta_R = 1.9^\circ = 1 \text{ mR} = \left(\frac{180}{\pi} \right) \times 10^{-3} = 57.3 \times 10^{-3}$$

$$1.9^\circ = \frac{1.9}{57.3} \text{ rad} = \frac{1900}{57.3} \text{ mR} \approx 33.16 \text{ mR}$$

$$\theta = \sqrt{33.16 \times 33.16} = 33.16 \text{ mR}$$

h can be determined using the DEM and contour maps of Figure 2.1 and Figure 2.2., using this resources, h is determined to be h = 120 m a.g.l. We therefore apply Crombies' model 4 as follows:

$$P(.01) = 10^{-3} \cdot d^{2.49} \cdot f^{0.84} \cdot \theta^{1.19} \cdot h^{-2.44}$$

$$P(0.1) = 10^{-3} \times (6.73)^{2.49} \times (19.5)^{0.84} \times (33.16)^{1.19} \times (120)^{-2.44}$$

$$P(0.1) = 0.001 \times 115.28094 \times 12.1235 \times 64.495777 \times 0.000008488531$$

$$P(0.1) = 0.000761578$$

The value obtained above is infinitesimally small and very close to zero. Looking back at our result of chapter four, one will see that at the fade depth $A \geq 20$ dB, this result will match some months that record a zero value. As one will observe in Table 4.18 the months of April, July and August at fade depth of 30 dB, have exceedance probabilities that match Crombies' model 4. This indicates that one may use Crombies' Model 4 to predict the percentage of occurrence probabilities for the fade ≥ 20 dB in the months of April, July and August, in Durban South Africa.

5.3.2 Comparison of Crombies' Model 5

Next we compare Crombies' model 5 using the available resources from our LOS link in Durban, South Africa. The variables applicable for implementing this model are; path length d , frequency f , and antenna beamwidths θ . All these parameters have been determined in section 5.3.1, so we just apply it here as follows:

$$P(.01) = 10^{-10} \cdot d^{2.93} \cdot f^{1.86} \cdot \theta^{2.17}$$

$$P(.01) = 10^{-10} \times (6.73)^{2.93} \times (19.5)^{1.86} \times (33.16)^{2.17}$$

$$P(.01) = 0.0000000001 \times 266.7375379 \times 250.8790388 \times 1994.038377$$

$$P(.01) = 0.01334$$

The result obtained above using Crombies' model 5 did not match with the measurement result for most months in Table 4.18 except April, July and August.

5.4 Comparison of Olsen and Segal Models

Olsen and Segal model designed for application in North America and Canada can be categorized into two methods. The first method is for initial planning and Licensing purposes. The second method

requires path profile and is best suited for link design application. We will compare both methods in this section of the report.

5.4.1 Comparison of Olsen and Segal First Method

The detail of this method has been explained in section 3.5.16, it will therefore not be repeated here, but we will quickly review the method. The first step in applying this method is to determine the geoclimatic factor of the path in quest. Next is the determination of the magnitude of the path inclination using the transmitting and receiving antenna heights, h_e and h_r as follows:

$$|\varepsilon_p| = 1000 \text{Arctan} \left[\frac{|h_r - h_e|}{1000d} \right] \simeq |h_r - h_e| / d \quad (5.9)$$

Where d is the path length in km, and $|\varepsilon_p|$ is the path inclination in milli radians. Next calculate the percentage of time, $P(A)$, that fade depth A (dB) is exceeded in the average worst month from the power-law expression:

$$P = Kd^{3.6}f^{0.89} (1 + |\varepsilon_p|)^{-1.4} \cdot 10^{-A/10} \quad (5.10)$$

where K is the geoclimatic factor given by:

$$K = 10^{((G/10) - 5.7)} \quad (5.11)$$

and;

$$G = 10 \log K + 57 \quad (5.12)$$

The geoclimatic factor has earlier been determined for Durban in chapter two (see Figure 2.8). Using all the above information, we determine the exceedance probabilities for Durban at different fade depths using this first method. The results are then compared with the values obtained in chapter four for all measurement months. These findings are shown in Figure 5.5 below.

The Olsen-Segal method 1 over predicts the fading probability at $A = 20$ dB, and $A = 30$ dB (see Figure 5.4 and Figure 5.5), while it underpredicts the exceedance probability for $A = 40$ dB (see Figure 5.4 and Figure 5.5). It highly underpredicts the exceedance probability for fade depths of 20 dB, 30 dB and 40 dB for April, May, June, July, August and December.

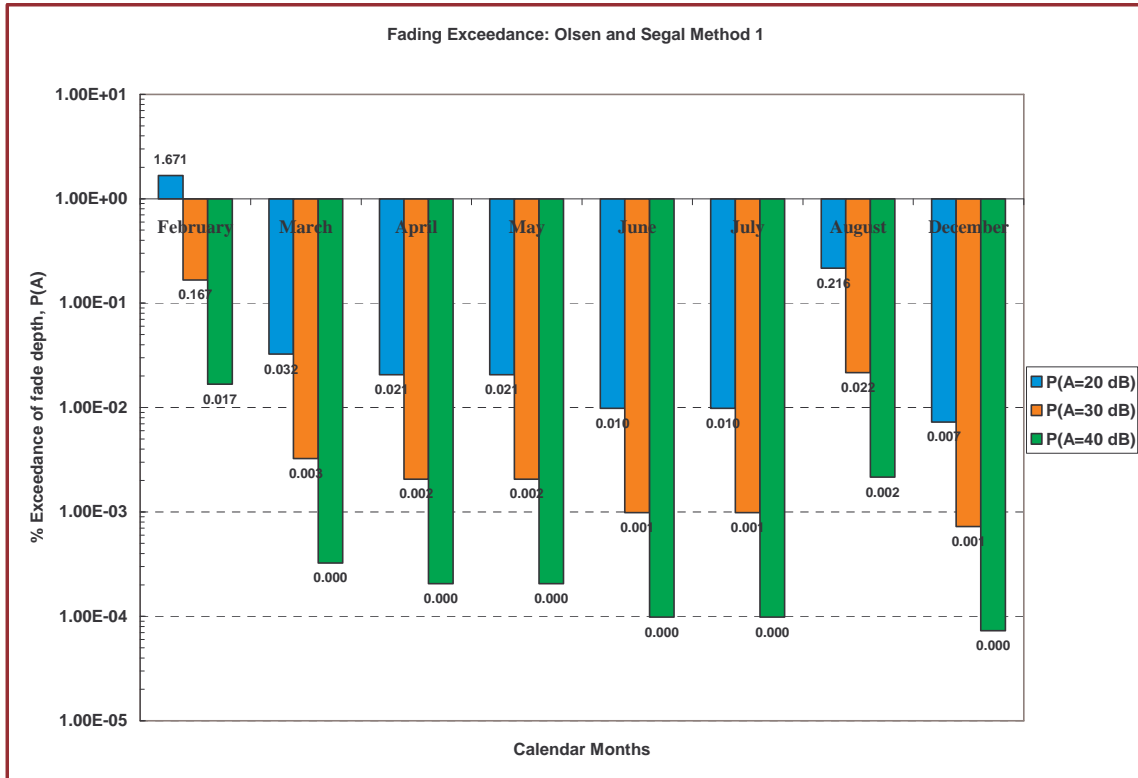


Figure 5. 5 Fading Exceedance of Olsen and Segal Method 1: Fade depth; A = 20, A = 30, and A = 40 dB

5.4.2 Comparison of Olsen and Segal Second Method

This method is best suited for link design applications and it has been detailed elsewhere (see section 3.5.17), we therefore will not repeat here but implement it. In addition to the path length, frequency and path inclination, this method requires the determination of an additional parameter known as the grazing angle ϕ . This method also starts with the determination of the geoclimatic factor K. The detailed procedure required to determine the grazing angle to implement this method is given in section 3.5.17. At the last stage of the method, one calculates the percentage of time, P, that the fade depth A (dB), is exceeded in the average worst month using the following relations:

$$P = Kd^{3.3}f^{0.93}(1+|\varepsilon_p|)^{-1.1}\phi^{-1.2}\cdot 10^{-A/10} \quad (5.13)$$

where K, d, f, and $|\varepsilon_p|$ have their usual meanings as given in section 5.4.1. We have extracted useful information from the DEM and contour map (see Figure 2.4 and Fig 2.5) to determine the grazing angle used in equation (5.13). Some of the coefficients used to achieve this as explained in equations (3.49) – (3.56) is shown in Table 5.2 below.

Table 5.2 Multipath Modeling Parameters for Olsen and Segal Method two

Distance From Transmitter (km)	Height Profile		Other Parameters	
	h(x)	Value (m)	Parameter	Value
0	h(0)	178	a ₀	-8.761
1	h(1)	80	a ₁	36.534
2	h(2)	150	h _r	165
3	h(3)	120	h _e	202
4	h(4)	110	h ₁	24
5	h(5)	80	h ₂	20
6	h(6)	80	n	8
6.73	h(7) → h(d)	145	ϕ	0.002162

The grazing angle for our LOS link has been determined to be 0.002162 mrad as seen in Table 5.2. It should be noted that the latest revision of ITU-R recommendation on the above subject has incorporated and embedded the grazing angle in (5.13). As a result of this latest revision, equation (5.13) now becomes (see [17]):

$$P = Kd^{3.2} \left(1 + |\varepsilon_p|\right)^{-0.97} \times 10^{0.0032f - 0.00085h_L - A/10} \quad (5.14)$$

where f is the frequency (GHz), h_L is the altitude of the lower antenna (i.e. the smaller of transmitter antenna altitude h_e and receiving antenna altitude h_r), and K is the geoclimatic factor. Equation (5.14) is now used to determine the exceedance probabilities at different fade depths across our LOS link. These exceedance probabilities are then compared with the measurement result of chapter four as shown in Figure 5.6 below.

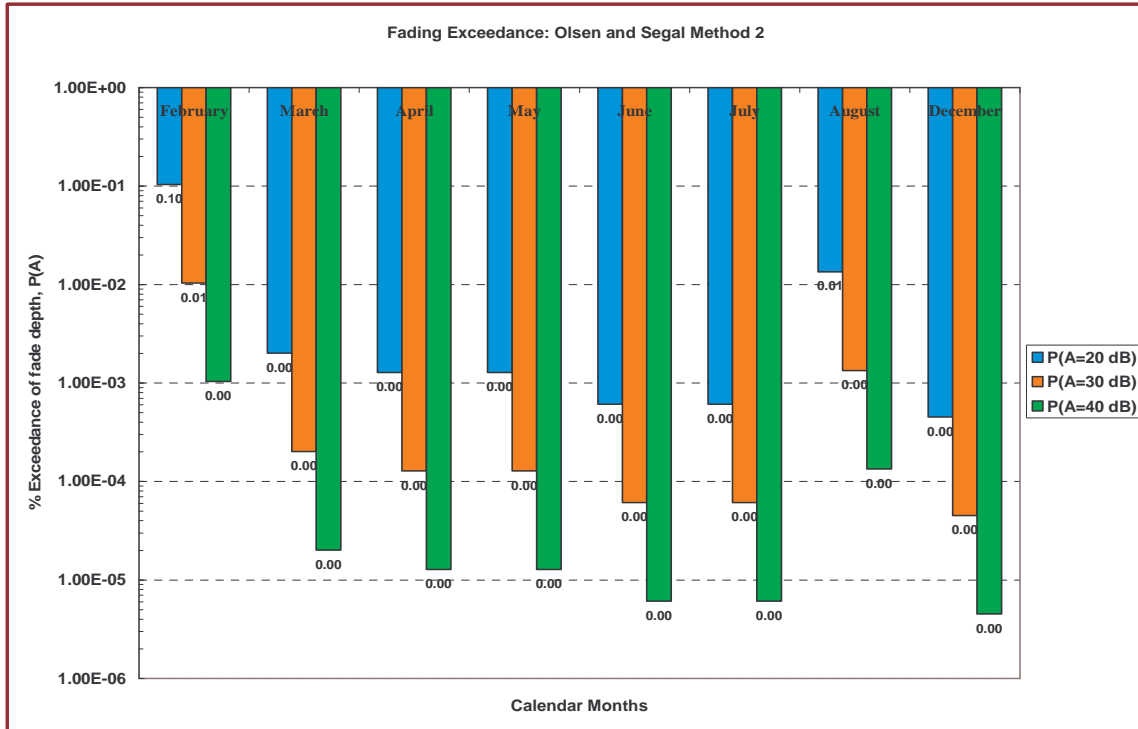


Figure 5.6 Fading Exceedance of Olsen and Segal Method 2: Fade depth; A = 20, A = 30, and A = 40 dB

Again, the conclusion arrived at before hold for the Olsen–Segal method 2, as it still underestimates the fading exceedance at each fading level. The two methods are compared in figures 5.7 and 5.8.

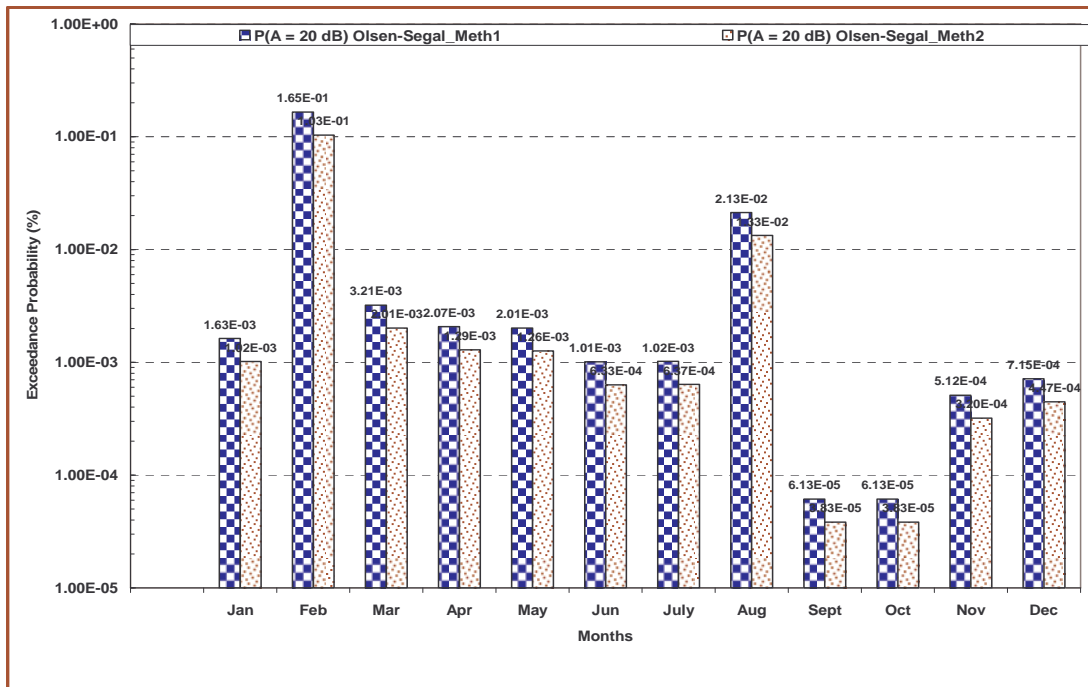


Figure 5.7 Comparison of Olsen-Segal Methods 1 and 2 at fade depth of 20 dB

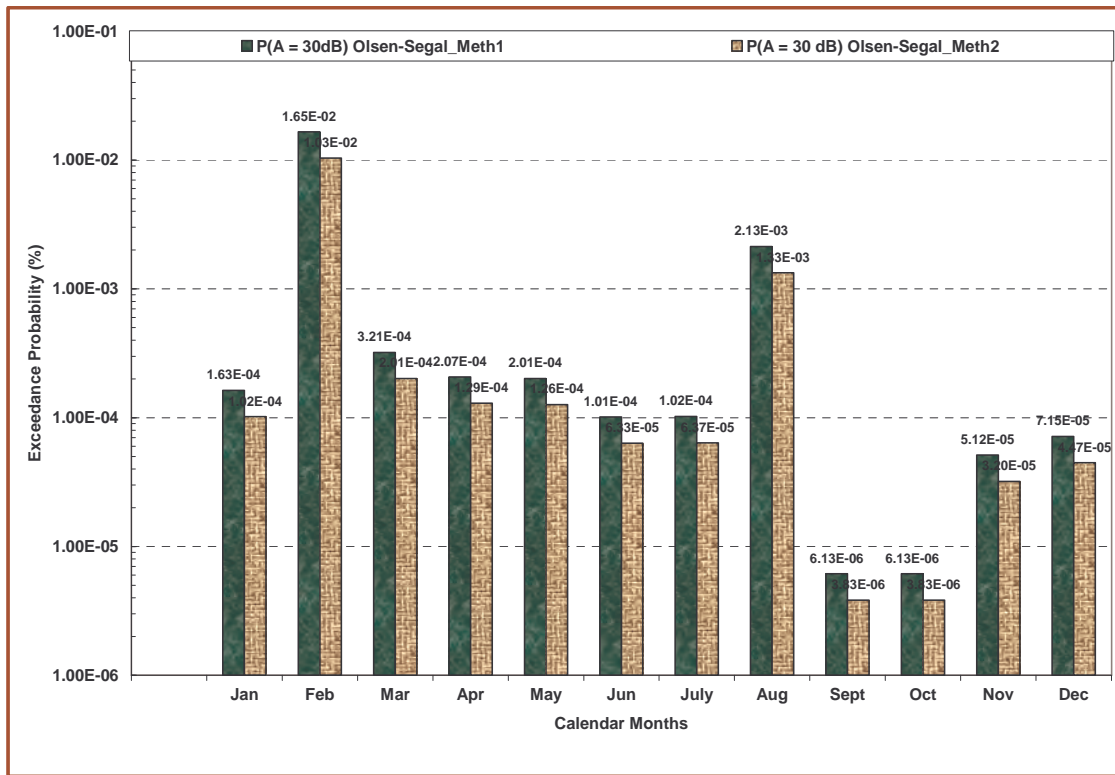


Figure 5.8 Comparison of Olsen-Segal Methods 1 and 2 at fade depth of 30 dB

5.5 Comparison of all Multipath Propagation Models with our Proposed Model

In previous sections, we have compared various models proposed by different authors using the local data obtain in Durban and we have analysed the result from this exercise. As one will note, some of the models fit local Durban data at some fade depth levels for certain months while others do not. In this section, we want to compare all these various models with our proposed analytical model developed in chapter four for the whole year.

The fourth order polynomial model proposed in chapter four (see Table 4.19) is now compared with the semi-empirical expressions due to ITU-R Recommendation P530-8 (as presented by Olsen et al), ITU_R Rec. P.530-12, the Morita model, and Vigants' model. For the current measurements, the average signal level over the year is at about -43 dBm, while the estimated noise level is at about -82 dBm. Morita's example on Figure1 of his paper shows the average received signal level at -30 dBm, and squelching or outage is achieved at -70 dBm.

A fade depth of approximately 40 dB thus gives complete outage, as the received signal is completely embedded in noise. Thus we use the given models to estimate the probability of link outage. In addition, note that the revised or improved Vigants' model incorporates a terrain roughness factor, w . This is defined as the square root of the average square of the deviations from the mean, given by [24]:

$$w = \sqrt{\frac{1}{13} \sum_{i=1}^{13} (x_i - M)^2} \quad (5.15)$$

In this case, x_i is the height above sea level of the i -th terrain point in the intervening path between transmitter and receiver, and M is the mean terrain height for the link. In this example, we have used 13 points for the link in Figure 2.3, resulting in a mean terrain height $M = 114.2$ m, and terrain roughness $w = 32.09$ m = 105.3 feet. The results are summarized in Table 5.3 below [125].

We should note also that Morita performed his tests in the 4-GHz band, and surmises that the formula be best applied in the frequency band between 2 to 15 GHz. Thus while the measured link outage probability of 0.037% is comparable to Morita's value of 0.060% over water and coastal areas, we should bear in mind the above caution. We also note that the ITU-R model of Recommendation P.530-8 gives an outage probability of 0.027% for this link, which is practically close to the measurement value obtained for our link (see Table 5.3). On the other hand, ITU-R Recommendation P.530-12 gives a marginally lower probability of 0.024%. All the Vigants's models (with and without the surface roughness factor) are seen to perform rather poorly in estimating the link outage. This may partly be due to the fact that they are not global, as compared to the ITU-R models.

Finally, we also note that the geoclimatic factor (K) used in the ITU-R models in Table 5.3 is a local one obtained by Dabideen et al [63]; and it is the worst-month value of 0.0318, which is the value for February. We note that the actual ITU-R value of K for the region is 9.12×10^{-4} , which could have resulted in very different results for the outage probability. Also note that the effective value of k exceeded 99.9% of the time in the worst month is 0.2 [36], and this also takes place in February. Thus, for KwaZulu-Natal, February is the worst month for the highest probability of multipath fading. Nevertheless, there will be need for more measurements to account for the 15 outage days.

Table 5.3 Outage Probability for the measurement compared with semi-empirical models [125]

Model	Outage Probability (%)
ITU-R P.530-8 (K = 0.0318)	0.027
ITU-R P.530-12 (k = 0.0318)	0.024
VIGANTS plain & average terrain	0.363
VIGANTS mountain & dry climate	0.091
VIGANTS over water	1.451
VIGANTS average climate (roughness factor w = 105.3 ft)	0.138
VIGANTS dry climate (roughness factor w = 105.3 ft)	0.069
VIGANTS coastal area (roughness factor w = 105.3 ft)	0.276
MORITA over mountains	0.011
MORITA over plains	0.027
MORITA over sea or coastal region (mean h = 114.2 m)	0.060
UKZN LOS LINK (measurements over the year)	0.037

5.6 Combined Parabolic Equation in Durban and Botswana for Different Seasons

In chapter four (see sections 4.8 – 4.9), we focus on individual analysis of the different modifications of parabolic equation. We are able to do this by plotting the path loss versus height and path loss versus range for the different seasonal months both in Durban and Botswana. We do this because these two locations have different features. In this section, we plot the different modifications of the parabolic equations together with the standard parabolic equation for the different seasonal months both in Durban and Botswana. The essence of doing this is for cross comparison between the values across the different modifications for the two seasons in both stations. The path loss versus height for the different modification of parabolic equation and for the two seasons is shown in Figure 5.9 – 5.10 whereas similar plots for path loss versus range is shown in Figure 5.11 – 5.12, the figures are then explained.

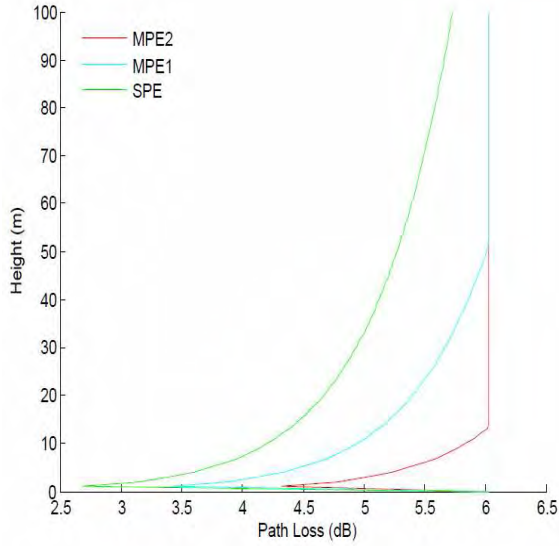


Figure5.9(a) Path Loss against Height for all PE at 19.5GHz, Range 20km February 2004 Durban

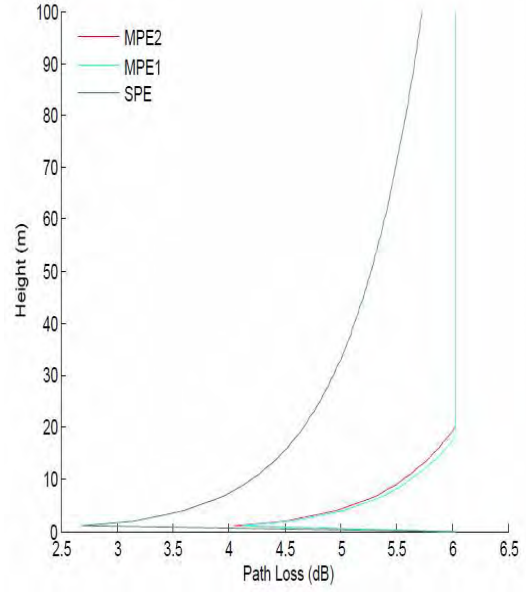


Figure5.9(b) Path Loss against Height for all PE at 19.5GHz, Range 20km February 1996 Botswana

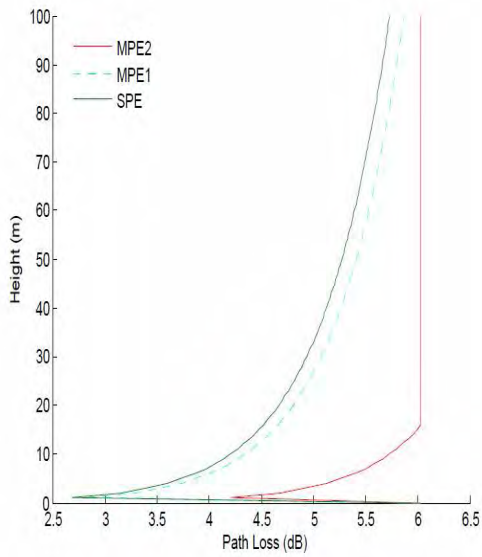


Figure5.10(a) Path Loss against Height for all PE at 19.5GHz, Range 20km August 2004 Durban

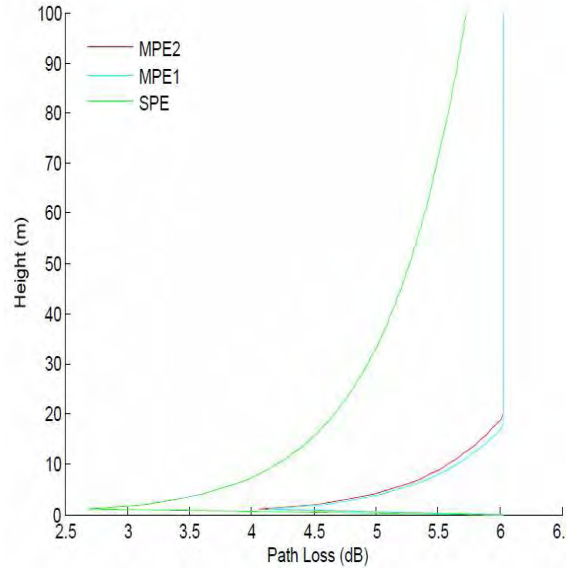


Figure5. 10 (b) Path Loss against Height for all PE at 19.5GHz, Range 20km August 1996 Botswana

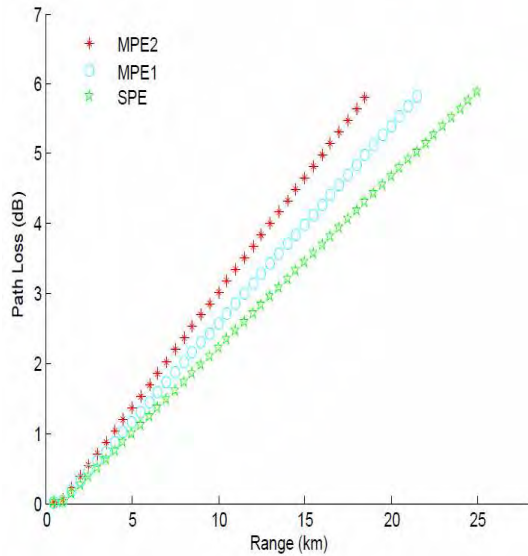


Figure 5.11(a) Path Loss against Range for all PE at 19.5GHz, Height 20m a.g.l. February 2004 Durban

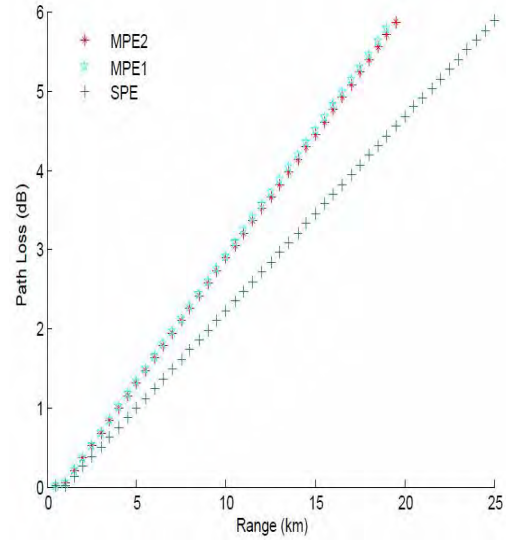


Figure 5.11(b) Path Loss against Range for all PE at 19.5GHz, Height 20m a.g.l. February 1996 Botswana

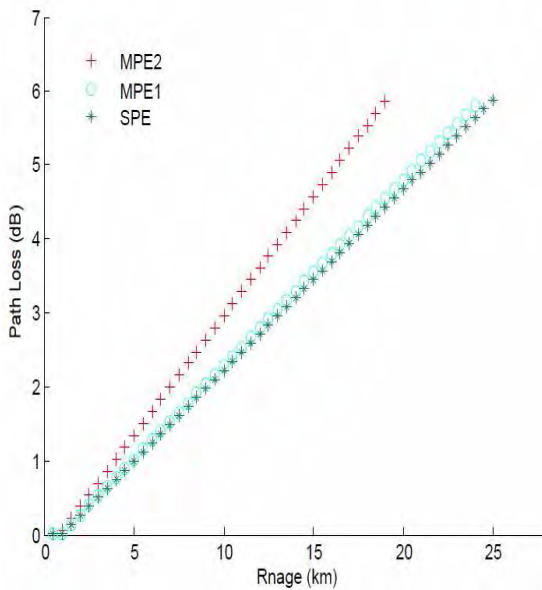


Figure 5.12(a) Path Loss against Range for all PE at 19.5GHz, Height 20 m a.g.l. August 2004 Durban

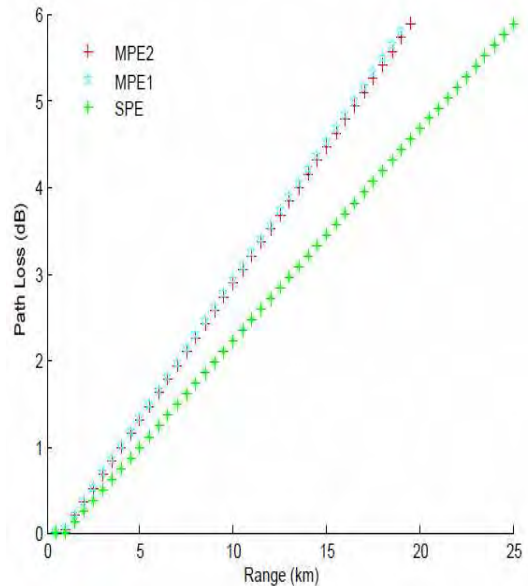


Figure 5.12(b) Path Loss against Range for all PE at 19.5GHz, Height 20 m a.g.l. August 1996 Botswana

Comparing the path loss versus height for the two locations (i.e. Durban and Botswana) and for the seasonal months of February (summer) and August (winter) reveals the following results: keeping the height level at 10 m a.g.l. the path loss value for the month of February in both Durban and Botswana

for the different modifications of parabolic equation could be extracted from Figures 5.9 above and displayed in Table 5.4.

Table 5.4 Path Loss value for different types of Parabolic Equation at height 10 m a.g.l., range 20 km for both Stations in February

Types of Parabolic Equation	Path Loss (dB)	
	Durban	Botswana
SPE	4.3	4.2
MPE1	5.05	5.6
MPE2	5.5	5.0

One can similarly draw another table of path loss values for the winter months of August in both stations from figure 5.10 as shown in Table 5.5 below.

Table 5.5 Path Loss value for different types of Parabolic Equation at height 10 m a.g.l., range 20 km for both Stations in August

Types of Parabolic Equation	Path Loss (dB)	
	Durban	Botswana
SPE	4.2	4.2
MPE1	4.35	5.72
MPE2	5.75	5.6

Tables 5.4 – 5.5 above show path loss comparison for the different types of parabolic equation in both Durban and Botswana for the summer month of February and the winter month of August. Looking at Table 5.4 one can make comparison between Durban and Botswana in February for the different parabolic equation. The path loss value for SPE is 4.3 dB in Durban while for Botswana at the same height path loss value is 4.2 dB there is a little difference between this values for SPE in both locations.

On the other hand for MPE1, the path loss value in Durban is 5.05 dB while in Botswana the path loss value for MPE1 is 5.6 dB. The significant difference between this path loss values is attributed to the flatter terrain nature of Botswana compared to Durban which is more hilly and undulating. Hence fading loss in Botswana is attributed more to multipath which is what MPE1 is capturing. The same trend of values is observed for the winter month in August (see MPE1 in Table 5.5).

For MPE2, Table 5.4 shows a path loss value of 5.5 dB in Durban compared to 5.0 dB in Botswana in February. For the winter month of August, Durban recorded in Table 5.5 a path loss value of 5.75 dB while in Botswana for the same month a path loss value of 5.6 dB is recorded. It should be noted that MPE2 now has a higher path loss value in Durban than in Botswana. This is expected since Durban has a hilly and more undulating terrain compared to Botswana. However, since MPE2 is designed to capture this effect, it follows that signal loss is due more to diffraction fading in Durban compared to Botswana.

Furthermore, for the month of February in Durban, the total signal loss is 14.85dB, out of this value, 28.95 % is attributed to free space loss (i.e. SPE), about 34 % is due to multipath (MPE1), and about 37% is due to diffraction fading (MPE2). Similar analysis was done for the same month in Botswana and the following results obtained: the total signal loss in Botswana is 14.8 dB, out of this value, about 28.37 % is due to free space loss (SPE), about 37.83 % is due to multipath (MPE1), and about 33.78 % is due to diffraction fading (MPE2).

Similar analysis can be done for the winter month of August in both locations as follows: in Durban, total signal loss is 14.3 dB and out of this value, about 29.37 % is due to free space loss (SPE), about 30.41 % is due to multipath (MPE1), and about 40.21 % is due to diffraction fading (MPE2). On the other hand in Botswana for the same month the following result is obtainable. The total signal loss is 15.52 dB, and out of this value, about 27.06 % is due to free space loss (SPE), about 36.85 % is due to multipath fading (MPE1), and about 36.08 % is due to diffraction fading (MPE2).

This comparative analysis corroborate the earlier finding in chapter four, in all multipath fading is a causative effect of signal loss in Botswana where the terrain is flatter while diffraction fading is a causative effect of signal loss in Durban where the terrain is dominated by hilly land and mountains.

Moving to a higher altitude of 20 m a.g.l. the analysis is observed to follow similar trend as discussed above for the two locations and at the two seasonal months. The path loss values extracted from figures 5.11 – 5.12 is shown in tables 5.6 and 5.7 for the two seasonal months in both Durban and Botswana.

Table 5.6 Path Loss value for different types of Parabolic Equation at height 20 m a.g.l., range 20 km for both Stations in February

Types of Parabolic Equation	Path Loss (dB)	
	Durban	Botswana
SPE	4.8	4.7
MPE1	5.5	6.4
MPE2	6.5	6.05

Table 5.7 Path Loss value for different types of Parabolic Equation at height 20 m a.g.l., range 20km for both Stations in August

Types of Parabolic Equation	Path Loss (dB)	
	Durban	Botswana
SPE	4.7	4.7
MPE1	5.0	6.25
MPE2	6.3	6.05

5.7 Chapter Summary

In this chapter, we have done a comparative analysis of some of the multipath propagation models presented by various authors, reviewed in chapter three. Based on our analysis and finding, one can convincingly say that no single model can accurately predict the line of sight propagation path in Southern Africa. The result of the analysis and subsequent comparison with practical measurement shows that while some of the models predict accurately well for some months, others do not. From the eight month measurement campaign in KwaZulu-Natal over a line-of-sight microwave link, we determine the analytical models for fade exceedance probability. The outage probability of 0.037% compares well with 0.060% from Morita's model for sea and coastal areas. It also compares reasonably well with outage values of 0.027% and 0.024% obtained from the model of ITU-R Recommendations P.530-8 and P.530-12, respectively [125].

However, it is observed that Vigants' model of the United States for coastal and over-water regions do not present a reasonable prediction for the link outage in South Africa, even with surface roughness incorporated. It should be noted that while the proposed model presents a good start, a longer measurement campaign in South Africa will ensure a refinement of the model. This will take

into account ducting and sea-breeze effects, which might possibly help explain the fifteen days of total outage during these measurements.

Finally a cross comparison was done among the different types of modified parabolic equation in this chapter. The results corroborate the earlier findings in chapter four. These findings show that signal loss is experience due to multipath fading in Botswana, while in South Africa; signal loss is due to diffraction fading. This result is due to the different topographical structures of these two Southern African countries. While Durban is of hilly rugged and mountainous terrain structure, Botswana on the other hand is of a flatter and gentler terrain.

CHAPTER SIX

SUMMARY, CONCLUSIONS AND RECOMMENDATION FOR FUTURE STUDIES

6.0 SUMMARY AND CONCLUSIONS

This work has investigated radioclimatological study in a clear-air environment as applicable to terrestrial line of sight link design problems. Radioclimatological phenomena were adequately reviewed both for the precipitation effect and clear-air effect. The research then focuses more on the clear-air effect of radioclimatological studies. Two Southern African countries chosen for case study in the report are Botswana and South Africa. To this end, radiosonde data gathered in Maun, Botswana and Durban, South Africa were used for model formulation and verification.

The data used in this thesis ranges from three years to ten years in these two stations. Three to ten years refractivity data gathered in Botswana and South Africa was used for the model formulation. On the other hand, eight months signal level measurement data recorded from the terrestrial line of sight (LOS) link set up between Howard College and Westville Campuses of the University of KwaZulu-Natal, Durban South Africa was used for model testing and verification. An extensive analysis of the clear-air signal level measurement across the LOS link was done. This analysis is very important in order to verify the different models presented by various researchers reviewed in chapter two. The measurement period spans eight months from February to December. Measurement is taken across the LOS link at a frequency of 19.5GHz. The analysis has been done in three phases. The first phase was done daily, the second phase monthly, and the last phase was done for all measurement periods.

Seven fade depth levels were analyzed in each of the phases. These fade depth levels are: fade depth A = 2 dB, fade depth A = 5 dB, fade depth A = 10 dB, fade depth A = 15 dB, fade depth A = 20 dB, fade depth A = 30 dB, and fade depth A = 40 dB. The percentage of time for each of these fade depth levels, occurs from the total measurement time known as exceedance probabilities was determined at each phase of the analysis. The average minimum threshold signal level was determined for each month before further analysis began. This was determined by plotting a probability density function (pdf) of all the signal level measurement for the concerned month. Then a curve fitting procedure was done on the pdf and the median of the curve with the minimum integral square error (ISE) becomes

the average threshold value for that month. Signal level measurement for all the days in each month is plotted to show the signal noise floor level. This signal noise floor level is used to determine the 99.99 % ($A_{0.01}$) availability of the link. The link is found to guarantee 99.99 % link availability for all the months except May which happens to be the worst month across the link. The value of $A_{0.01}$ determined across the link is also found to be comparable with the result obtained for a similar link in Durban, by a different author in [76].

The analysis described above becomes the bedrock for determination of the proposed analytical model for clear-air radioclimatic study in Southern Africa. Having determined the exceedance probability at these different fade depths as discussed above, an analytical expression is proposed to model these exceedance probabilities as a function of fade depth. The proposed analytical model is a fourth order polynomial. The model can be used to predict the percentage of time that a particular fade depth is exceeded for different months and for the whole year in Southern Africa.

The second analytical model proposed in this study is the modified parabolic equation. This is an analytical model which captures the effect of the terrain characteristic of the study area. The standard parabolic equation (SPE) was modified to include the geoclimatic factor. This initial modification is called first modified parabolic equation (MPE1). The final modification includes the effective earth radius factor (k-factor). This final modification is called second modified parabolic equation (MPE2). Two different topographical terrains were chosen to test each of these modifications. The result obtained after the test shows that there is more signal loss due to multipath in Botswana, where the terrain is flat compared to the second location. MPE1 which incorporate geoclimatic factor was able to capture this effect. On the other hand, in Durban where the terrain is hilly and mountaneous, more signal loss is experienced due to diffraction fading. The second modification (MPE2) was able to capture this effect.

These two proposed models are the most important findings of the thesis. While the first proposed analytical model was developed based on signal level measurement and compares favourably with other multipath model, the second proposed analytical model is able to marry the multipath fading effect with diffraction fading effect. This is very important in capturing the effect of the topographical characteristic of our LOS path. Various multipath propagation models proposed by different authors across the globe were tested and verified using the eight months signal level measurement data. Based on our analysis and findings, one can convincingly say that no single model can accurately predict the line of sight propagation path in Southern Africa. The result of the analysis and subsequent

comparison with practical measurement shows that while some of the models predict accurately well for some months, others do not.

From the eight month measurement campaign in KwaZulu-Natal over a line-of-sight microwave link, we determine the analytical models for fade exceedance probability. The outage probability of 0.037% compares well with 0.060% from Morita's model for sea and coastal areas. It also compares reasonably well with outage values of 0.027% and 0.024% obtained from the model of ITU-R Recommendations P.530-8 and P.530-12, respectively [125].

However, it is observed that Vigants' model of the United States for coastal and an over-water region does not present a reasonable prediction for the link outage in South Africa, even with surface roughness incorporated. It should be noted that while the proposed model presents a good start, a longer measurement campaign in South Africa will ensure a refinement of the model. This will take into account ducting and sea-breeze effects, which might possibly help explain the fifteen days of total outage during these measurements.

Finally a cross comparison was done among the different types of modified parabolic equation in the thesis. The results corroborate the earlier findings in chapter four. These findings show that signal loss is experience due to multipath fading in Botswana, while in South Africa; signal loss is due to diffraction fading. This result is due to the different topographical structures of these two Southern African countries. While Durban is of hilly rugged and mountainous terrain structure, Botswana on the other hand is of a flatter and gentler terrain.

The results of applying the modified parabolic equation to solve clear-air problems are as follows: for all the different types of modifications of PE, duct occurrence probabilities are obtainable within the range of 20 km of the propagation distance from the transmitting antenna. This duct occurrence is also noticeable within the first 10 m above ground level (a.g.l). This means that link designer should plan separately for this coverage area so as to mitigate the trapping of radio signal propagated in this duct vicinity.

In terms of seasonal distribution, the result is as follows: at a height level of 10 m a.g.l. signal loss is observed to be more for MPE2 in both Durban and Botswana for the winter month of August than February and lower for MPE1 and SPE for this same period. On the other hand at a higher height level of 20 m a.g.l. there is more signal loss for SPE, MPE1, and MPE2 in both Durban and Botswana

for the summer months of February than the winter months of August. More detail analysis of the result can be obtained in chapter four. The results presented in this thesis will be found very useful by radio system designers in these two countries.

6.1 Recommendation for Future Work

Though the topic has been dealt with in some detail in the thesis, there is room for improvement in future studies. The following recommendation is therefore proposed to improve the future work in this field:

- The study location should be expanded in future study, more regions should be covered in South Africa and Botswana other than Durban and Maun. This is because the more observation stations included in the research, the more diversified the topographical terrain structure and climatic or seasonal differences that will be observed. This will eventually increase the robustness and fidelity of the result.
- Radiosondes that report after every two seconds of ascent should be acquired for future studies. The one used in this study reports after every ten seconds of ascent, which translates into 50 m height intervals. Alternatively, tethersonde system which takes measurement at six different height level intervals can be used if radiosonde cannot be obtained because it is very expensive.
- Due to the financial constraints involved in obtaining a radiosonde or tethersonde since they are very expensive, ground data which can be gathered more easily should be used for future studies. The data should cover a much longer period and more locations.
- Correlation study and analysis of the geoclimatic factor should be done with signal level measurement. This will help in the refinement of the models proposed for Southern Africa in the thesis.
- Correlation study and analysis of the k-factor should be done with signal level measurement. This will help in model formulation for Southern Africa.

- Correlation study and analysis of temperature, pressure and humidity should be done with signal level measurement. This will help in the refinement of the models proposed for Southern Africa in the thesis.
- Correlation study and analysis of refractivity and refractivity gradient should be done with signal level measurement. This will help in the refinement of the models proposed for Southern Africa in the thesis.
- More LOS links should be set up in different locations across Southern Africa. This will help to determine the coefficients necessary to further refine the proposed models for Southern Africa.
- Future parabolic equation software should be modified to incorporate features that will give more detailed results of duct occurrence probabilities. This will help to address the outage problems experienced in the measurements used in the thesis.
- Future parabolic equation software should upload geographic information system (GIS) data directly, so that a better terrain profiling can be done and this will eventually improve the result.
- Data from Brazil should be collected in future, to further test and verify the models developed in this work.

REFERENCES

- [1] R.L. Olsen, “Radioclimatological Modeling of Propagation Effects in Clear-Air and Precipitation Conditions: Recent Advances and Future Directions,” in Proceedings of Radio Africa '99 Conference, Gaborone, Botswana, October 1999, pp 92-106.
- [2] Preprints of URSI Comm. F Open Symposium on “Regional Factors in Predicting Radiowave Attenuation due to Rain”, Rio de Janeiro, Brazil (CETUC/PUC, Rua Marques De Sao Vicente 225, 22453 Rio de Janeiro), 189 pp. 3 – 7 December 1990.
- [3] K.H. Craig, T. Tjelta and B. Segal, “Climatic parameters in clear-air propagation modelling”, in Preprints URSI Comm. F. Open Symposium on ‘Climatic Parameters in Radiowave Propagation Prediction’ (CLIMPARA '94), Moscow, Russia, 31 May – 3 June 1994.
- [4] COST Project 235, “Radiowave propagation effects on next-generation fixed-services terrestrial telecommunication systems”, Final Report, office for Official Publications of the European Community, Luxembourg, 1996.
- [5] E. Salonen, S. Karhu, S. Uppala, and R. Hyvonen, “Study of improved propagation predictions”, Final Report on Contract 9455/91/ NL/LC(SC) for European Space Agency/ESTEC, Noordwijk, The Netherlands, 1994.
- [6] M. van de Kamp, J. Tervonen, E. Salonen, and K. Kalliola, “Study of low elevation angle scintillation modelling”, Final Report on Contract 10827/94/ NL/NB(SC) for European Space Agency/ESTEC, Noordwijk, The Netherlands, Sep.1997.
- [7] F. Barbaliscia, M. Boumis, A. Martellucci, and J.P.V. Poiaraes Baptista, “Statistical modelling and world-wide mapping of propagation parameters in non-rainy atmosphere from climatic parameters”, in Proc. URSI Comm. F Workshop on ‘Climatic Parameters in Propagation Prediction’ (CLIMPARA '96), Oslo, Norway, pp. 44 – 45, 10 – 11 June 1996.

- [8] F. Barbaliscia, M. Boumis, and A. Martellucci, “ World-wide characterization of atmospheric vertical profiles”, in Proc. URSI Comm. F Open Symp. on ‘Climatic Parameters in Propagation Prediction’ (CLIMPARA ’98), Ottawa, Canada, pp. 27 – 30, 27 – 29 April 1998.
- [9] <http://www.estec.esa.nl/xewww/cost255/>
- [10] Preprints of URSI Commission F Open Symposium on ‘Wave Propagation and Remote Sensing’, Ravenscar, North Yorkshire, UK, 8 – 12 June 1992.
- [11] Proc. of URSI Comm. F Open Symp. on ‘Climatic Parameters in Propagation Prediction’ (CLIMPARA ’94), Moscow, Russia, 31 May – 3 June 1994.
- [12] Proc. of URSI Comm. F Open Symp. on ‘Climatic Parameters in Propagation Prediction’ (CLIMPARA ’96), Oslo, Norway (Telenor R&D, Main Library, P.O. Box 83, N-2007, Kjeller, Norway), 51 pp., 10 – 11 June 1996.
- [13] Proc. of URSI Comm. F Open Symp. on ‘Climatic Parameters in Propagation Prediction’ (CLIMPARA ’98), Ottawa, Canada (Communication Research Center, Industry Canada, P.O. Box 11490, Station H, Ottawa, Canada K2H 8S2), 243 pp., 27 – 29 April 1998.
- [14] M.P.M. Hall, B. Arbesser-Rastburg, M.T. Hewitt, R.L. Olsen, M.S. Pontes, D.V. Rogers, T. Tjelta, and C.D. Wilson, “Tropospheric work programme of ITU-R Working Party 3M,” in Proc. URSI Comm. F Open Symp. on ‘Climatic Parameters in Propagation Prediction’ (CLIMPARA ’98), Ottawa, Canada pp. 239 – 243, 27 – 29 April 1998.
- [15] B. Segal, “Surface-based meteorological parameters for use in global modelling of clear-air microwave fading characteristics,” in Proc. URSI Comm. F Workshop on ‘Climatic Parameters in Propagation Prediction’ (CLIMPARA ’96), Oslo, Norway, pp. 10 – 11, 10 – 11 June 1996.
- [16] S. Lystad and T. Tjelta, “ High resolution meteorological grid for clear-air propagation modelling in northern coastal regions,” in Symp. on ‘Propagation Assessment in Coastal

- Environment', Bremerhaven, Germany, 19 – 22 Sep. 1994, NATO/AGARD Conf. Proc. CP-567, North Atlantic Treaty Organization, Paris, France, pp. 41.1 – 12, 1995.
- [17] ITU Radiocommunication Assembly, "Propagation Data and Prediction Methods Required for the Design of Terrestrial Line of Sight Systems" ITU-R P. 530 – 11(1982-1986-1990-1992-1994-1995-1997-1999-2000-2001, 2005).
- [18] Recommendation ITU-R p. 618-8, "Propagation data and prediction techniques required for the design of earth-space telecommunication systems," vol. 2003, P Series, part 2, International Telecommunication Union, Geneva, Switzerland, 2003.
- [19] Recommendation ITU-R p. 452-11, "Prediction procedure for the evaluation of microwave interference between stations on the surface of the earth at frequencies above about 0.7 GHz," vol. 2003, P Series, Part 2, International Telecommunication Union, Geneva, Switzerland, 2003.
- [20] Recommendation ITU-R p. 620-5, "Propagation data required for the evaluation of coordination distances in the frequency range 0.85 –60 GHz," vol. 2003, P Series, Part 2, International Telecommunication Union, Geneva, Switzerland, 2003.
- [21] T. Tjelta, R.L. Olsen and L. Martin, "Systematic development of new multi-variable techniques for predicting the distribution of multipath fading on terrestrial microwave links," IEEE Transactions on Antenna and Propagation, vol. 38, pp. 1650 – 1665, Oct. 1990.
- [22] K. Morita, "Prediction of Rayleigh fading occurrence probability of line-of-sight microwave links," Rev. Elec.Comm.Lab.(Japan), vol. 18, pp.810-822, Nov.-Dec. 1970.
- [23] W.T. Barnett, "Multipath propagation at 4, 6, and 11 GHz," Bell Syst. Tech. J., vol. 51, pp. 321 – 361, Feb. 1972.
- [24] A. Vigants, "Space diversity engineering," Bell Syst.Tech. J., vol. 54, pp.103 –142, Jan. 1975.
- [25] K.W. Pearson, "Method for the prediction of the fading performance of a multisection microwave link," Proc. Inst. Elec. Eng., vol. 112, pp. 1291 – 1300, July 1965.

- [26] J.E. Doble, "Prediction of multipath delays and frequency selective fading on digital radio links in the UK," *Inst. Elec. Eng Dig.*, no. 62, 1979.
- [27] L.V. Nadeneko, "Calculation of signal stability in line-of-sight radio-relay systems," *NIIR Proc.*, vol. N5, 1980.
- [28] CCIR Report 338-6, "Propagation data and prediction methods required for line-of-sight radio-relay systems," Report of the CCIR, Annex to vol. V, XVIIth Plenary Assembly, International Telecommunication Union, Geneva, Switzerland, pp. 355-420, 1990.
- [29] K. Morita and K. Kakita, "Fading in microwave relays," *Rep. ECL, NTT, Japan*, vol. 6, pp. 352-370, Sept. 1958.
- [30] M.S. Wheeler, "Microwave relay fading statistics as a function of a terrain clearance factor," *IEEE Transaction on Antennas and Propagation*, vol. No. 2, AP-25, pp.269-273, Mar.1977.
- [31] A. Vigants, "Number and Duration of Fades at 6 and 4 GHz," *Bell System Technical Journal*, vol. 50, No. 3, pp. 815 – 841, March 1971.
- [32] A. Vigants, "Space-Diversity Performance as a Function of Antenna Separation," *IEEE Trans. Commun. Tech.*, COM-16, No. 6, pp. 831 – 836, December 1968.
- [33] A. Vigants, "The Number of Fades in Space-Diversity Reception," *Bell System Technical Journal*, vol. 49, No. 7, pp. 1513 – 1530, 1970.
- [34] D.C. Crombie, "Prediction of multipath fading on terrestrial microwave links at frequencies of 11 GHz and greater," in *NATO/AGARD Conf. Proc.*, CP-346, pp 10-1– 10-8 , North Atlantic Treaty Organization, Paris, France, 1984.
- [35] R.L. Olsen and Terje Tjelta, "Worldwide Techniques for Predicting the Multipath Fading Distribution on Terrestrial LOS Links: Background and Results of Tests" *IEEE Transactions on Antenna and Propagation*, Vol. 47, No.1 , pp. 157 – 170, January 1999.

- [36] T.J. Afullo and P.K. Odedina, "Effective Earth Radius Factor Characterization for Line of Sight Paths in Botswana," Proceedings of IEEE AFRICON 2004 Conference, ISBN 0-7803-8605-1, pp. 227 – 232, Gaborone, Botswana.
- [37] ITU Radiocommunication Study Group III: "The Radio Refractive Index: Its formula and Refractivity Data," ITU Radiocommunication Assembly Document No. ITU-R P.453 – 7, 11 July 2003.
- [38] D.C. Baker and A.J. Palmer, "A Model for the Fraction of time Availability of the Effective Earth Radius Factor for Communication Planning in South Africa – The Basic Model," SAIEE Transaction, Vol. 93, pp. 1 – 7, 2002.
- [39] D.C. Baker and A. J. Palmer, "A Proposed Empirical Model of the Effective Earth Radius Factor for Telecommunication Use in South Africa," SAIEE Transactions, Vol. 94, No.2 pp. 40 – 45, 2002.
- [40] T.J. Afullo, M.O. Adongo, T. Motsoela, "Seasonal Variation of Radio Refractivity in Botswana," Proceedings of URSI CLIMPARA '98 Conference, Communication Research Centre, Ottawa, Canada, pp. 195-198, April 1998.
- [41] T.J. Afullo, M.O. Adongo, T.Motsoela and D.F. Molotsi "Estimates of Refractivity Gradient and k-Factor Ranges for Botswana" Transactions of SAIEE, vol. 92, pp. 1 – 6, 2001.
- [42] P.K. Odedina and T.J. Afullo " Effective Earth Radius Factor (k-Factor) Determination and its Application in Southern Africa" Proceedings of the Second IASTED International Conference on Antennas, Radar and Wave Propagation, pp.222 – 227, July 19 – 21, 2005, Banff, Alberta, Canada.
- [43] D.H. Hamsher, "Communication System Engineering Handbook", McGraw Hill, Inc., 1967, pp 16 – 40.
- [44] T.J. Afullo and P.K. Odedina, "On the K-Factor Distribution and Diffraction Fading for Southern Africa," South Africa Institute of Electrical Engineers Research Journal Vol. 97 No. 2 pp. 172 – 181, June 2006.

- [45] M.O. Fashuyi, P. A. Owolawi, and T.J.O. Afullo, "Rainfall Rate Modelling for LOS Radio Systems in South Africa, Africa Research Journal of the South Africa Institute of Electrical Engineer, 2006, pp.74-81 ISSN No.1991-1696. Vol. 97, No. 1, pp.74 – 81., March 2006.
- [46] K. Naicker, "Rain attenuation modelling for line-of-sight terrestrial links," MSc. Dissertation, University of KwaZulu-Natal, Durban, 2006.
- [47] K. Naicker and S.H. Mnene, "Propagation measurement and multipath channel modelling for line-of-sight links at 19.5GHz," SAIEE Res. J., 97(2), 162 – 171 2006.
- [48] M. O. Fashuyi and T.J. Afullo, "Rain Attenuation Prediction and Modeling for Line of Sight Links on Terrestrial Paths in South Africa," American Geophysical Union: Radio Science Journal Vol. 42, RS5006, doi: 10.1029/2007/RS003618, 2007.
- [49] D. M. Pozar, Microwave Engineering, 2nd ed., chap. 12, John Wiley, New York. 1988.
- [50] <http://www.home.agilent.com/USeng/nav/-536900735.536879154/pd.html>
- [51] P.K. Odedina and T.J. Afullo, "Estimation of Secondary Radioclimatic Variables and Its Application to Terrestrial LOS Link Design in South Africa," Proceedings of the Southern Africa Telecommunication Networks and Applications Conference (SATNAC 2008), pp. 9 – 14, Wild Coast Sun, South Africa, 7 – 10, September, 2008.
- [52] P.A. Burrough, "Principles of geographical information systems for land resources assessment," Oxford University press. xiii, New York, pp. 193. 1986.
- [53] S.L. Lystad, T.G. Hayton. A.K. Marsh and T.Tjelta, "Interpolation of Clear-air Parameters Observed at Non-regular Observation Locations" in Proc. URSI Comm. F Open Symp. on 'Climatic Parameters in Propagation Prediction' (CLIMPARA '98), Ottawa, Canada, pp. 15 – 26, 27 – 29 April 1998.
- [54] P.K. Odedina and T.J. Afullo, "Multipath Propagation Modeling and Measurement in a Clear-Air Environment for LOS Link Design Application," Proceedings of the Southern

- Africa Telecommunications and Networks Application Conference (SATNAC 2009), Ezulwini, Royal Swazi Spa, Swaziland, August 31 – September 2 2009.
- [55] User Manual of Environmental System Research Institute, ESRI 2001, INC: ArcView Vol.8.1, pp. 114.
- [56] N.I. Fisher, T. Lewis, and B.J.J. Embleton “Statistical Analysis of Spherical Data,” Cambridge University Press, pp329, 1987.
- [57] P.K. Odedina and T.J. Afullo, “A Simplified Statistical Modeling of Radioclimatological Parameters for LOS Links in South Africa,” Proceedings of Progress In Electromagnetic Research Symposium (PIERS) ISBN: 978 – 1- 934142 – 08 – 0, pp. 1483 – 1486, Beijing, China March 23 – 27, 2009.
- [58] P.K. Odedina and T.J. Afullo, “Use of Spatial Interpolation Technique for the Determination of the Geoclimatic Factor and Fade Depth Calculation for Southern Africa,” Proceedings of IEEE AFRICON conference 2007 ISBN: 0 – 7803 – 8606 – X. IEEE Catalog number: 04CH37590C, September 26 – 28, 2007, Namibia.
- [59] B.W. Silverman: Density Estimation for Statistics and Data Analysis, Chapman & Hall, Chapter 2-4, 1990, ISBN 0-412-24620-1.
- [60] P.K. Odedina and T.J. Afullo, “Effective Earth Radius Factor Measurement and Modeling for Radio Link Design in Botswana,” SAIEE African Research Journal, vol. 99, no. 3, pp. 77 – 86, September 2008.
- [61] R. L. Freeman “Radio System Design for Telecommunications” 2nd Edition, John Wiley and Sons, Inc., New York, 1997.
- [62] B.R. Bean and E. J. Dutton, “Radio Meteorology” Dover Publications, New York, 1968.
- [63] A.S. Dabideen, M. Gopichund and T.J. Afullo, “Radio Refractivity Distribution and Duct and Fading Occurrence Measurements in KwaZulu-Natal,” The Transactions of South African

- Institute of Electrical Engineers (SAIEE) Research Journal, Vol. 96, No2, pp. 121 – 132, June 2005.
- [64] R . K . Crane, “ Propagation Handbook for Wireless Communication System Design”, Chap. 1., CRC Press, New York, 2003.
- [65] G.O. Ajayi, “ Physics of the Tropospheric Radiopropagation” Proc. of the 2nd Regional Workshop on Development of Radio Communication in Africa, 4 – 8 August, 1997, KCCT, Nairobi, Kenya, pp. 43 – 72.
- [66] F. Moupfouma, “Improvement of Rain Attenuation Prediction Method for Terrestrial Microwave Links,” IEEE Trans. Antennas & Propagation Vol. 32, No. 12, pp.1368-1372, 1984.
- [67] H. E. Green, “Propagation Impairment on Ka-band SATCOM Links in Tropical and Equatorial Regions,” IEEE Trans. Antennas & Propagation Vol. 46, No. 2, pp.31 – 44, 2004.
- [68] R. K. Crane, “Electromagnetic Wave Propagation Through Rain,” Chap. 1, John Wiley, New York. 1996.
- [69] Y. Huang and K. Boyle “Antennas from Theory to Practice”, 1st edition, John Wiley and Sons Ltd, West Sussex, United Kingdom, 2008.
- [70] P.K. Odedina, “Effective Earth Radius Factor (the k-Factor) Distribution for Southern Africa,” MSc. Dissertation, University of KwaZulu-Natal, Durban, South Africa 2005.
- [71] ITU Radiocommunication Study Group III: “Effects of Tropospheric Refraction on Radiowave Propagation,” ITU Radiocommunication Assembly, Document No. ITU-R p. 834 – 4 (1992-1994-1997-1999-2003).
- [72] T.S. Rappaport, “Wireless Communications” 2nd edition, Prentice Hall, 2002.

- [73] T.J. Afullo, T. Motsoela and D.F. Molotsi, "Refractivity Gradient and k factor in Botswana," Proceedings of the Third Regional Workshop on Development of Radio Communication in Africa, Gaborone, Botswana, 25 – 29, October 1999, pp. 107 – 110.
- [74] A. J. Palmer and D. C. Baker, "Predicting the Long – Term Average of the Effective Earth Radius Factor for South Africa Using Ground Based Observations," Proceedings of IEEE AFRICON 2004, September 2004, ISBN: 0 – 7803 – 8605 – 1, pp. 1003 – 1006.
- [75] T. J. Afullo and M. O. Adongo, "Refractivity Studies in Botswana – Initial Investigations," Proc. of the 2nd Regional Workshop on Development of Radio Communication in Africa, 4 – 8 August, 1997, KCCT, Nairobi, Kenya, pp. 79 – 82.
- [76] M. Gopichund, "Fading in Rural Radio Communication Links" An MSc. Dissertation, University of KwaZulu-Natal, Durban, South Africa 2004.
- [77] C. Salema, "Microwave Radio Links from Theory to Design," John Wiley and Sons, Inc., New Jersey, 2003, pp.89 – 91.
- [78] T.S. Rappaport, "Wireless Communications Principle and Practice," Prentice Hall PTR Upper Saddle River, N.J. 07458, 1996, pp91 – 97.
- [79] H. Makino and K. Morita, "Design of Space Diversity Receiving and Transmitting Systems for Line-of-Sight Microwave Links," IEEE Trans. COM., vol. 15, No. 4, p.603, 1967.
- [80] K. Morita, "Prediction of the Occurrence Probability of Rayleigh Fading in Line-of-Sight Microwave Links," E.C.L. Tech. Jour., NTT, Jap., vol. 18, No. 9, p. 2327, 1969.
- [81] H. Enomoto, "Fading Characteristics in Line-of-Sight Propagation of Microwave," The Journal of Electrical Communication Engineers of Japan, vol. 41, No. 1, p.42, 1958.
- [82] W.R. Barnett, "Microwave line-of-sight propagation with and without frequency diversity," Bell System Technical Journal, pp. 1827 – 1871, Oct. 1970.
- [83] J. Battesti and L. Baithias, "Etude des sections longues dans les faisceaux hertziens en

- visibilite,” *Annales des tele communications*, July – Aug. 1964.
- [84] Lendurt Electric Co., Inc., “Engineering considerations for microwave communication systems,” 1105 County Road, San Carlos, CA, pp. 16 and 51, June 1970.
- [85] CCIR, vol. II, part 1, Report 338-1, pp. 116, 119, and 125.
- [86] S. H. Lin, “Statistical Behavior of Deep Fade of Diversity Signals,” *IEEE Trans. Commun.*, COM-20, No.6, pp. 1100 – 1107, December 1972.
- [87] C.L. Ruthroff, “Multiple-Path Fading on Line-of-Sight Microwave Systems as a Function of Path Length and Frequency,” *Bell System Technical Journal*, vol. 50, pp. 2375 – 2398, 1971.
- [88] CCIR, “Propagation Data Required for Line-of-Sight Radio Relay Systems,” CCIR Report 338-4, XV Plenary Assembly, International Telecommunications Union, Geneva, 1982, vol. V, pp. 279-314.
- [89] R.L.O. Tattersall and N.E. Cartwright, “Multipath Propagation Data Collected from Tests on Line – of – Sight Radio Paths at 11, 20, and 37 GHz During the Period 1972 – 1975,” *Post Office Communication, Research Dept. Report No. 594*, 1977.
- [90] D. Turner, B.J. Easterbrook, and J.E. Golding, “Experimental Investigation into Radio Propagation at 11.0 – 11.5 Gc/s,” *Proc. IEE*, vol. 113, pp. 1477 – 1489, September 1966.
- [91] E.T. Stephansen and G.E. Mogensen, “Experimental Investigation of Some Effects of Multipath Propagation on a Line-of-Sight Path at 14 GHz,” *IEEE Transactions on Communications*, vol. COM 27, No. 3, March 1979, pp. 643 – 647.
- [92] O. Sasaki, and T. Akiyama, “Characteristics of Fadeout and Fade Speed in Microwave Radio Links,” *Review of the Electrical Communication Laboratories*, vol. 25, No. 3 – 4, pp. 315 – 323, March – April 1977.
- [93] S.H. Lin, “Impact of Microwave Depolarization During Multipath Fading on Digital Radio Performance,” *Bell System Technical Journal*, vol. 56, pp. 645-674, 1977.

- [94] R. S. Butler, "Cross-Polarization Discrimination at 11 GHz and 17 GHz," *Annales des Telecommunications*, vol. 36, No. 7 – 8, pp. 466 – 467, 1981.
- [95] R.L. Olsen and B. Segal "New techniques for predicting the multipath fading distribution on VHF/UHF/SH terrestrial line-of-sight links in Canada" *Can. J. Elec.& Comp. Eng.*, vol.17, No.1, pp 11 – 23, 1992.
- [96] [http:// www. Worlдатlas.com](http://www.Worlдатlas.com)
- [97] N.R. Draper and H. Smith, *Applied Regression Analysis*. New York: John Wiley and Sons, 1981.
- [98] K. H. Craig, and T.G. Hayton, "Climatic mapping of refractivity parameters from radiosonde data," in *NATO/AGARD Conf. Proc. CP-567*, North Atlantic Treaty Organization, Paris, France, pp. 43.1 – 12, 1995.
- [99] T. Tjelta, "Modelling line-of-sight worst month multipath occurrence as a function of basic link and geoclimatic variables," in *Proc. of URSI Commission F Workshop on Climatic Parameters in Radiowave Propagation*, Oslo, Norway, pp. 22 – 23, June 1996.
- [100] T.Tjelta, T.G. Hayton, B.Segal and E. Salonen: "Correlation of Observed Multipath Occurrence with Climatic Parameters derived from Radiosondes, Surface Stations and Numerical Atmosphere Models," in *Proceedings of URSI Commission F Open Symposium CLIMPARA'98* pp. 85-92, April 27-29 1998, Ottawa, Canada.
- [101] T.Tjelta and R.L. Olsen "Further development of methods for worldwide prediction of terrestrial radio link multipath fading distributions," in *Proc. of ECRR'98*, 1998.
- [102] A. J. Palmer and D.C. Baker, "Predicting the Monthly Cumulative Distribution of the Effective Earth Radius Factor for South Africa," *Proceedings of IEEE AFRICON 2004*, September 2004, ISBN: 0 – 7803 – 8605 – 1, pp. 1007 – 1010.
- [103] A.L. Martin and T. Vu-Dinh, "A Statistical Characterization of Point-to-Point Microwave

Links Using Biased Rayleigh Distributions,” IEEE Transactions on Antennas and Propagation, Vol. 45, No. 5, pp 806-821, May 1997.

- [104] A. Martin, “Key Radio Meteorological Parameters for Designing Line-of-Sight Links in a Multipath Fading Environment” Martin Communications Pty Ltd, 87 Peters Av, Mulgrave VIC 3170, Australia.
- [105] F.J. Ryan, “RPE: A parabolic equation radio assessment model”, in AGARD Operational Decision Aids for Exploiting or Mitigating Electromagnetic Propagation Effects, 1989.
- [106] K.H. Craig, “Propagation modeling in the troposphere: Parabolic equation method,” Electron. Lett., vol.24, pp.1136-1139, 1989.
- [107] H.W. Ko, H.S. Burkom, J.P. Skura, and D.A. Roberts, “An analysis of EMPE code performance in a selection of laterally inhomogeneous atmospheric-duct environments,” Johns Hopkins APL Tech. Dig., vol.9, no. 2, pp. 89-100, 1988.
- [108] R.H. Hardin and F.D. Tappert, “Application of the split-step Fourier method to the numerical solution of nonlinear and variable coefficient wave equations,” SIAM Rev., vol.15, p.423, 1973.
- [109] M. Leontovich and V. Fock, “Solution of the Problem of Propagation of Electromagnetic Waves Along the Earth’s Surface by the Method of Parabolic Equation, ” Journal of Physics, Vol. X, No.1, Academy of Science of the USSR, 1946.
- [110] S.A. Isaakidis and T.D. Xenos, “Parabolic Equation Solution of Tropospheric Wave Propagation Using FEM, ” Progress In Electromagnetic Research, PIER 49, 257-271, 2004.
- [111] G. D. Dockery, “Modeling Electromagnetic Wave Propagation in the Troposphere Using the Parabolic Equation,” IEEE Transactions on Antennas and Propagation, Vol. 36., pp. 1464-1470, No.10 Oct, 1988.
- [112] P. L. Slingsby, “Modelling Tropospheric Ducting Effects on VHF/UHF Propagation,” IEEE Transactions on Broadcasting, Vol. 37, No. 2, June 1991

- [113] G. D. Dockery and J.R. Kuttler, "An Improved Impedance-Boundary Algorithm for Fourier Split-Step Solutions of the Parabolic Wave Equation," IEEE Transactions on Antennas and Propagation, Vol. 44, No.12, December 1996.
- [114] Z. A. Hyaric, "Wide-angle nonlocal boundary conditions for the parabolic wave equation," IEEE Trans. Antennas and Propagation, 2001, vol. 49 no. 6, pp.916-922, June, 2001
- [115] T.B.A. Senior, "Impedance boundary conditions for imperfectly conducting surfaces," Appl. Sci. Res., Sec B. Vol. 8, 1960, pp. 418-436.
- [116] M.F. Levy, "Horizontal Parabolic Equation Solution of Radiowave Propagation Problems on Large Domains, " IEEE Transactions on Antennas and Propagation, Vol. 43, No.2, pp.137-144, February 1995.
- [117] D. J. Donohue and J.R. Kuttler, "Propagation Modeling Over Terrain Using the Parabolic Wave Equation, " IEEE Transactions on Antennas and Propagation, Vol. 48, No.2, February 2000.
- [118] A.E. Barrios, "Parabolic Equation Modeling in Horizontally Inhomogeneous Environments, " IEEE Transactions on Antennas and Propagation, Vol. 40, No.7, July 1992.
- [119] A. Kukushkin, Radio Wave Propagation in the Marine Boundary Layer, Wiley-VCH, ch. 2, 1998.
- [120] L.M. Brekhovskikh, Waves in Layered Media, 2nd Edition, Academic Press, New York, 1980.
- [121] J., Claerbout: Fundamentals of Geophysical Data Processing: With Applications to Petroleum Prospecting, McGraw Hill, New York, 1976.
- [122] P.P. Borsboom and Z. Hyaric, "RCS predictions using wide angles PE codes, "10th ICAP, 14-17 April 1997, Conference Publication No 436. Proceedings, pp.2.191 – 2.194.

- [123] M.F. Levy, and P.P. Borsboom, “Radar cross-section computations using the parabolic equation method,” 1996, *Electron. Lett.*, 1996, 32(13), 1234 – 1236.
- [124] M.D. Collins and R.B. Evans, “A two-way parabolic equation for acoustic back scattering in the ocean,” *J. Acoust. Soc Amer.*, vol. 91, p.1357, 1992.
- [125] P.K. Odedina and T.J. Afullo, “Clear-Air Signal Measurement Analysis for Microwave Line-Of-Sight Link in South Africa,” Presently under review for *SAIEE Research Journal* 2010.
- [126] D. Lee and S.T. McDaniel, “Ocean acoustics propagation by finite difference methods”, *Coastal Engng.* vol. 7, pp. 285 – 287, 1983.
- [127] G. D. Smith “Numerical solution of partial differential equations: finite difference Methods”, 3rd Edition (Clarendon Press, Oxford, 1985).
- [128] R. Garg, “Analytical and Computational Methods in Electromagnetics”, Artech House Inc., Chapter 7, pp. 233 – 268, 2008 ISBN-13: 978 – 1 – 59693 – 385 – 9.
- [129] R.A. Pappert, “Field Strength and Path Loss in a Multilayer Tropospheric Waveguide Environment”, Technical Note 1366, Naval Ocean Systems Center, 1984.
- [130] User’s Manual “Advanced Refractive Effects Prediction System” Document version 3.6 December 2006. Space and Naval Warfare Systems Center, San Diego Atmospheric Propagation Branch San Diego, CA.
- [131] International Telecommunication Union, Propagation in non-ionized media, (Reports of the CCIR, vol. 5, Geneva, 1990).
- [132] P.K. Odedina and T.J. Afullo “Alternative Formulation for Determination of Geoclimatic Factor, Using Local Radiosonde Data from Southern Africa” Proceedings of the Sixth IASTED International Conference on Antennas, Radar and Wave Propagation, pp31 – 36 ISBN : 978-0-88986-795-6 published by Acta Press, July 6 – 8, 2009, Banff, Alberta, Canada.

- [133] D. Freedman, R. Pisani and R. Purves: Statistics Published by W.W. Norton and Company pp. 62 – 63, United States 1978.
- [134] P.K. Odedina and T. J. Afullo “Clear-Air Analysis of Fade Exceedance Probability Statistic for Microwave Line-Of-Sight Link in South Africa,” Presently Under review at the Proceedings of the Seventh IASTED International Conference on Antennas, Radar and Wave Propagation, Massachusetts, USA Nov. 1 – 3 2010.

APPENDICES

Appendix A

Table A.1 Measured Occurrence Probability of Rayleigh Fading P_R for Propagation Test Paths (at 4GHz) [53]

Path	d(km)	\bar{h} (m)	$\Delta h/d$	Test Period	P_R	Path Condition
Tokyo – Enkai	37.4	115	0.0032	July – Aug (1959 – '60)	0.0007	Over plains
Enkai – Futago	52.5	640	0.0175	July – Aug (1959 – '60)	0.015	Over the sea
Futago – Yanbara	56.5	775	0.0110	July – Aug (1959 – '60)	0.018	Over the sea
Yanbara – Awagatake	42.3	490	0.0014	July – Aug (1959 – '60)	0	Over mountains
Awagatake – Tsukude	60.7	625	0.0035	July – Aug (1959 – '60)	0.007	Over mountains
Tsukude – Nogoya	46.7	420	0.0133	July – Aug (1959 – '60)	0.0028	Over plains
Nagoya – Onogi	56.7	250	0.0048	July – Aug (1959 – '60)	0.0028	Over plains
Onogi – Hiei	62.3	617	0.0076	July – Aug (1959 – '60)	0.015	Over plains
Tokyo – Tsukuba	71.6	445	0.0110	July – Aug (1959 – '60)	0.028	Over plains
Tsukuba – Utsunomiya	42.0	485	0.0164	July – Aug (1959 – '60)	0.0028	Over plains
Kacchi – Chikagawa	40.0	155	0.0075	July – Aug (1959 – '60)	0.0014	Over plains
Chikagawa – Shiokubi	66.5	285	0.0035	August 1959	0.0431	Over the sea
Shiokubi – Niyama	36.8	425	0.0014	July – Aug (1959 – '60)	0	Over plains
Niyama – Noboribetsu	74.5	545	0.0019	August (1959 – '60)	0.0472	Over the sea
Noboribetsu – Shikotsu	39.4	695	0.0056	July – Aug (1959 – '60)	0	Over mountains
Onoyama – Osaka	40.7	375	0.0167	July – Aug (1959 – '60)	0.0007	Over mountains
Yakushi – Oginajo	61.8	305	0.0008	July – Aug (1959 – '60)	0.046	Over the sea
Oginajo – Niigata	54.7	180	0.0055	July – Aug (1959 – '60)	0.028	Over the sea
Osaka – Rokko	26.2	455	0.0324	July – Aug (1959 – '60)	0	Over plains
Rokko – Hiromine	51.0	595	0.0125	July – Aug (1959 – '60)	0.0042	Over plains
Hiromine – Ishido	39.0	340	0.0046	July – Aug (1959 – '60)	0	Over mountains
Ishido – Tsuneyama	49.0	355	0.0031	July – Aug (1959 – '60)	0.0014	Over plains
Tsuneyama – Otani	56.0	350	0.0023	July – Aug (1959 – '60)	0.007	Over plains
Otani – Danbara	50.5	580	0.0065	July – Aug (1959 – '60)	0.0007	Over mountains
Danbara – Hiroshima	29.5	590	0.015	July – Aug (1959 – '60)	0	Over mountains
Hiroshima – Sofu	45.5	550	0.0051	July – Aug (1959 – '60)	0	Over plains
Sofu – Nishiki	53.3	500	0.0060	July – Aug (1959 – '60)	0.0028	Over plains
Nishiki – Katsuyama	56.6	320	0.0007	May – Jun (1959 – '60)	0.012	Over plains
Katsuyama – Sugadake	53.5	450	0.0054	July – Aug (1959 – '60)	0.0007	Over plains
Sugadake – Fukuoka	18.4	310	0.003	July – Aug (1959 – '60)	0	Over mountains
Fukuoka – Mino	42.1	390	0.0166	July – Aug (1959 – '60)	0	Over plains
Mino – Kumamoto	56.3	400	0.0128	July – Aug (1959 – '60)	0	Over mountains
Kumamoto – Yunozuru	80.5	340	0.0078	May – Jun (1959 – '60)	0.035	Over plains
Sendai – Sasatani	31.8	630	0.0029	Apr – Sept (1961 – '62)	0	Over mountains
Sasatani – Yamagata	12.0	575	0.0068	Apr – Sept (1961 – '62)	0	Over mountains
Michikawa – Akita	17.3	85	0.0075	Apr – Jun (1961 – '62)	0.0012	Over the sea
Sapporo – Nakagoya	32.2	170	0.0075	Apr – Sept (1961 – '62)	0	Over plains
Nakagoya – Tokiwayama	72.3	445	0.0046	Jun – Aug (1959 – '61)	0.017	Over plains
Tokiwayama – Asahikawa	11.2	375	0.0043	Jun – Aug (1959 – '61)	0	Over mountains
Asahikawa – Biei	17.2	210	0.0090	Jun – Aug (1959 – '61)	0	Over mountains
Biei – Ochiaidake	60.0	740	0.0015	Jun – Aug (1959 – '61)	0	Over mountains
Ochiaidake – Obihiro	52.5	625	0.0022	Jun – Aug (1959 – '61)	0	Over mountains
Obihiro – Kamiatsunai	44.5	180	0.0054	Jun – Aug (1959 – '61)	0	Over mountains
Kamiatsunai – Kushiro	53.9	120	0.0050	July – Sept (1959 – '60)	0.036	Over the sea

Table A.2 Measured Occurrence Probability of Rayleigh Fading P_R for Propagation Test Path [53]

Path	d(km)	\bar{h} (m)	$\Delta h/d$	Test Period	Freq. (GHz)	P_R	Path Condition
Tsukuba – Fujioka	90.8	485	0.0085	July – Aug 1951	4	0.12	Over plains
Fukuso – Tsuneyama	56.0	355	0.0017	May – June 1953)	4	0.0045	Over plains
Fukuso – Noro	59.5	612	0.007	May – June 1953)	4	0.024	Over plains
Togi – Tsuneyama	61.3	353	0.0015	May – June 1953)	4	0.013	Over plains
Togi – Odayama	57.3	560	0.0056	May – June 1953)	4	0.012	Over plains
Tsukuba – Futago	150.0	845	0.0033	Aug – Sept 1954	4	0.2	Over plains
Oginojo – Yakushi	61.8	305	0.0008	May – Jun 1959	4	0.04	Over the sea
Nakatsuhara – Horikoshi	70.6	525	0.0038	Apr – May 1960	4	0.041	Over the sea
Toyama – Asahi	44.0	135	0.0052	Apr – May 1960	4	0.022	Over the sea
Noboribetsu – Niyama	74.5	545	0.0019	Jun – July 1961	6	0.08	Over the sea
Oginojo – Yakushi	61.8	305	0.0008	July 1964	4	0.05	Over the sea
Takaoka – Kurehayama	15.7	50	0.0024	July – Aug 1962	11	0.001	Over the sea
Saido – Omiya	27.5	30	0.002	Sept. 1962	11	0.0008	Over plains
Omiya – Hanno	29.0	35	0.004	Sept. Oct 1962	11	0.0015	Over plains
Saido – Omiya	27.5	30	0.002	July – Sept. 1963	11	0.00036	Over plains
Omiya – Hanno	29.0	35	0.004	July – Sept. 1963	11	0.0035	Over plains
Nakashibetsu – Bettoga	50.8	58	0.0002	October 1964	4	0.02	Over the sea
Yokkaichi – Tsu	29.9	67	0.0001	August 1965	11	0.01	Over the sea
Kosuzume – Siroyama	35.6	77	0.0002	August 1965	2.2	0.01	Over the
Kosuzume – Siroyama	35.6	77	0.0002	August 1965	4.4	0.018	sea Over the sea
Kosuzume – Siroyama	35.6	77	0.0002	August 1965	6.7	0.04	Over the sea
Kosuzume – Siroyama	35.6	77	0.0002	August 1965	11	0.009	Over thesea
Tsuuken – Tokorozawa	11.6	20	0.0002	July – Sept. 1965	11	0	Over plains
Tsuuken – Tokorozawa	11.6	20	0.0002	July – Sept. 1965	15	0	Over plains
Musashino – Shogunzuka	10.8	20	0.0002	July – Sept. 1965	11	0	Over plains
Nakashibetsu – Bettoga	50.8	58	0.0002	Sept – Oct 1966	4	0.032	Over the sea
Nakashibetsu – Bettoga	50.8	58	0.0002	Sept – Oct 1967	4	0.04	Over the sea
Nakashibetsu – Bettoga	50.8	50	0.0006	Sept – Oct 1967	4	0.053	Over the sea
Nagoya – Ichinomiya	14	88	0.002	Jun – Sept 1967	11	0	Over plains

Appendix B

Table B.1 Characteristics of Propagation Paths Used by Crombie [62]

Path No.	Path	P(.01) % Probability of Fades \geq 20 dB	d Path Length (km)	f Nominal Frequency (GHz)	θ Nominal Beamwidths (mR) T/R	h Estimated Path Clearance (m)	Duration of Measurements (months)	Reference
1.	Crowfield – Mendlesham (UK)	0.04	7.5	10.95	58/58	30	37	[162]
2.	Crowfield – Mendlesham (UK)	0.035	7.5	19.65	32/32	30	50	[162]
3.	Crowfield – Mendlesham (UK)	0.011	7.5	36.3	17/17	30	43	[162]
4.	Somersham – Mendlesham (UK)	0.05	16.6	11.65	36/36	40	37	[162]
5.	Somersham – Mendlesham (UK)	0.10	16.6	20.3	16/16	40	37	[162]
6.	Somersham – Mendlesham (UK)	0.06	16.6	37.0	17/17	45	34	[162]
7.	Martlesham – Mendlesham (UK)	0.25	22.8	20.95	15/15	35	45	[162]
8.	Forder Battery – Caradon Hill (UK)	0.0008	26.4	10.92	8.7/8.7	160	41	[162]
9.	Dalton – Quernmore (UK)	0.005	31.7	10.84	8.7/8.7	130	33	[162]
10.	Tinshill – Stillingfleet (UK)	0.008	34.9	10.84	8.7/5.8(7.1)	63	34	[162]
11.	Stillingfleet – Cavewold (UK)	0.04	36.2	11.37	5.8/8.7(7.1)	80	34	[162]
12.	Copenhagen (Denmark)	0.5	44.7	14.25	21.8/21.8	32	12	[164]
13.	Pleasant Lake – West Unity (USA)	0.69	45.9	11	20.9/20.9	40	2.3	[166]
14.	Shiroyoma – Kosuzumel (Japan)	0.008	35.6	11	8.4/8.4	?	~1	[165]
15.	Shiroyoma – Kosuzumel (Japan)	0.033	35.6	18.0	9.4/9.4	?	~1	[165]
16.	Purdown – Pen Hill (UK)	0.01	27.8	10.92	13/13	?	31	[162]
17.	Sibleys – Kelvedon Hatch (UK)	0.10	31.0	11	6/6	30	12?	[163]
18.	Greenmore Hill – Dollis Hill (UK)	0.30	58.0	11	6/6	30	12?	[163]

Appendix C

Table C.1 (a) Data and characteristics of experimental links in Canada [80]

Link(Path coordinates)	Ant. Ht. (m)		d(km)	f(GHz)	$ \epsilon_p $	ϕ (mrad)	Measurement Period	Tail A(dB)	Tail P(%)	Obsev. G(dB) Eqn.2.19	Observ. G(dB) Eqn.2.31	Predict. G(dB) Figure2.11
	Above Ground Tx	Rx										
1. Corkery-Shirley Bay, Ont. ($45^{\circ} 16' 16''\text{N}$, $77^{\circ}3'44''\text{W}$ – $45^{\circ}20'52''\text{N}$, $76^{\circ}52'58''\text{W}$)	18	40	16.3	10.8	3.55	3.8	May – Sep 1979	25.8	0.001	9.8	7.3	5.0
2. Corkery-Shirley Bay, Ont.	18	40	16.3	11.08	3.55	3.8	May – Sep 1979	29.3	0.001	13.1	10.7	5.0
3. Corkery-Shirley Bay, Ont.	18	40	16.3	16.53	3.55	3.8	May – Sep 1979	18.0	0.001	0.3	-2.2	5.0
4. Corkery-Shirley Bay, Ont.	18	40	16.3	16.81	3.55	3.8	May – Sep 1979	19.9	0.001	2.2	-0.4	5.0
5. Kingsmere-Shirley Bay, Ont. . ($45^{\circ} 29' 17''\text{N}$, $75^{\circ}51'21''\text{W}$ – $45^{\circ}20'52''\text{N}$, $76^{\circ}52'58''\text{W}$)	18	40	15.7	11.35	15.5	22.2	May – Sep 1979	12.0	0.001	4.2	9.6	5.0
6. Kingsmere-Shirley Bay, Ont.	18	40	15.7	17.71	15.5	22.2	May – Sep 1979	15.3	0.001	5.8	11.1	5.0
7. Kemptville - Avonmore Bay, Ont. ($44^{\circ} 59' 57''\text{N}$, $73^{\circ}33'18''\text{W}$ – $45^{\circ}08'47''\text{N}$, $74^{\circ}56'48''\text{W}$)	63	78	50.5	3.65	0.326	2.1	11 Jun – 29 Jul 1985	16.2	0.311	4.1	1.8	5.0
8. Kemptville - Avonmore Bay, Ont.	63	65	50.5	3.65	0.079	1.9	11 Jun –	16.4	0.424	4.5	1.7	5.0

							29 Jul 1985						
9. Kemptville - Avonmore Bay, Ont.	63	78	50.5	8.05	0.326	2.1	9 Aug-12 Sep 1977	16.0	1.35	6.7	3.9	5.0	

Table C.1 (b) Data and characteristics of experimental links in Canada continued [80]

Link(Path coordinates)	Ant. Ht. (m)		d(km)	f(GHz)	$ \epsilon_p $	ϕ (mrad)	Measurement Period	Tail A(dB)	Tail P(%)	Obsev. G(dB) Eqn.2.19	Observ. G(dB) Eqn.2.31	Predict. G(dB) Figure2.11
	Above Ground Tx	Rx										
10. Kemptville -Avonmore Bay, Ont.	63	65	50.5	8.05	0.079	1.9	9 Aug-12 Sep 1977	16.0	1.35	6.7	3.9	5.0
11. Kemptville -Avonmore Bay, Ont	63	25	50.5	8.05	0.730	1.0	9 Aug-12 Sep 1977	22.0	0.14	5.1	-1.4	5.0
12. Firth – Tabor, B.C. ($54^{\circ} 48'45''$ N $122^{\circ}46'11''$ W – $53^{\circ}54'44''$ N, $122^{\circ}27'01''$ W)	6	6	102.3	7.5	1.98	3.9	Jul 1981-Oct1982 (Sep 1982)	15.0	0.197	-7.8	-7.0	-5.0
13. McEwan–Tabor, B.C. ($54^{\circ} 24'11''$ N, $122^{\circ}29'45''$ W – $53^{\circ}54'44''$ N, $122^{\circ}27'01''$ W)	11	9	54.7	3.8	2.5	18.7	Jul 1981-Oct1982 (Sep 1982)	15.0	0.0077	-8.6	-0.5	-5.0
14. Hixon–Tabor, B.C. ($53^{\circ} 28'43''$ N, $122^{\circ}38'00''$ W – $53^{\circ}54'44''$ N, $122^{\circ}27'01''$ W)	53	57	49.8	3.9	9.3	5.5	Jul 1981-Oct1982 (Sep 1982)	20.0	0.0011	-4.0	-3.7	-5.0
15. Cluculz – Frazer, B.C. ($53^{\circ} 54'54''$ N, $123^{\circ}27'25''$ W)	15	27	77.8	7.2	2.63	6.0	Apr 1980 – May 1981 (July 1980)	20.0	0.0119	-9.3	-6.4	-5.0

W – 54°01'51"N, 124°37'21"W)												
16. Cluculz – Frazer, B.C.	15	27	77.8	7.5	2.63	6.0	Apr 1980 – May 1981 (Sep 1980)	20.0	0.0085	-11.0	-8.1	-5.0
17. Creston – Salmon, B.C. (49° 05'35' N, 116°22' 45" W – 49°04'18"N, 117°04'56"W)	17	15	51.4	4.1	0.89	-	Feb-Oct 1982 (Feb 1982)	25.0	0.0006	-11.2	-	-4.5*
18. Rossland – Salmon, B.C. (49° 05'35' N, 117°47' 50" W – 49°04'18"N 117°04'56"W)	6	13	52.3	6.9	17.1	-	Feb-Oct 1982 (Oct 1982)	15.0	0.0022	-5.5	-	-5.0*

Table C.1 (c) Data and characteristics of experimental links in Canada continued [80]

Link(Path coordinates)	Ant. Ht. (m)		d(km)	f(GHz)	$ \epsilon_p $	ϕ (mrad)	Measurement Period	Tail A(dB)	Tail P(%)	Obsev. G(dB) Eqn.2.19	Observ. G(dB) Eqn.2.31	Predict. G(dB) Figure2.11
	Above Ground	Tx Rx										
19. Santa Rosa – Salmon, B.C. (49° 01'27' N, 118° 03' 31" W – 49°04'18"N, 117°04'56"W)	11	15	71.6	4.1	6.5	-	Feb-Oct 1982 (Oct 1982)	20.0	0.0105	-2.0	-	-5.0*
20. Blackwall – Hope, B.C. (49° 06'05' N, 120° 45' 25" W – 49°24'35"N 121°33'28"W)	18	11	67.6	3.8	8.2	-	Feb 1981- May 1982 (Dec 1981)	15.0	0.0038	-9.0	-	-2.0*
21. Hope – Chilliwack, B.C. (49° 24'35' N, 121° 33' 28" W – 49°06'52"N 121°54'07"W)	26	46	41.4	7.8	29.2	40.0	Feb 1981-Oct1982 (Jul 1982)	15.0	0.0012	-1.9	7.2	2.0
22. Uniondale – London, Ont. (43° 13'42' N, 81° 02' 18" W – 43°00'25"N, 81°16'28"W)	46	25	30.7	16.65	3.16	1.9	Jul 1981-Oct1982 (Sep 1982)	15.0	0.0077	-8.6	-0.5	-5.0
23. Otta Lake N.B.–Nictaux S.N.S. (45° 22'10' N,	69	81	80.4	9.5	0.684	5.7	31 Jul – 3 Sep 1981	27.5	0.315	6.1	9.1	11.0 (5.0)

65°46'23" W – 44°52'00"N, 65°02'10"W)												
24. Big Sicker – Vancouver, B.C. (48° 51'38' N, 123°45'20" W – 49°16'52"N 121°33'28"W)	15	72	66.1	4.2	9.6	6.7	Jul – Oct 1979 (Oct 1979)	20.0	0.0961	10.9	12.5	10.0 (4.0)
25. Vancouver – Big Sicker, B.C.	70	15	66.1	8.2	9.6	6.7	Jul – Oct 1980 (Jul 1980)	20.0	0.0352	4.0	5.5	10.0 (4.0)
26. Lowther Peak – Martyr Peak, N.W.T. (74° 31.8' N, 97°27.2' W – 74°41.2'N, 95°2.9'W)	7	7	72.0	0.468	0.125	3.0	2 Sep 1983- 22 Apr 1984, 4 Jun 1984 -7 Jan 1985 (Oct 1983)	22.8	0.1	7.2	2.4	11.9 (-7.1)
27. Schomberg Peak–Cockburn Peak,N.W.T. (75° 33.7' N, 105°35.1' W – 75°41.8'N, 100°15.1'W)	7	7	91.0	0.463	0.231	1.1	4 Jun 1984- 7 Jan 1985 (Jul 1984)	36.9	1.0	28.3	24.1	11.9 (-7.1)

Table C.1 (d) Data and characteristics of experimental links in Canada continued [80]

Link(Path coordinates)	Ant. Ht. (m)		d(km)	f(GHz)	$ \epsilon_p $	ϕ (mrad)	Measurement Period	Tail A(dB)	Tail P(%)	Obsev. G(dB) Eqn.2.19	Observ. G(dB) Eqn.2.31	Predict. G(dB) Figure2.11
	Above Ground	Tx Rx										
28. Cockburn Peak – Lowther Peak, N.W.T (75° 1.8' N, 100° 15.1' W – 74°31.8'N, 97°27.2'W)	7	7	98.8	0.453	0.253	0.7 ⁺	2 Sep 1983-10 Nov 1983, 4 Jun 1984 -7 Jan 1985 (Jul 1984)	41.5	0.1	21.8	14.7	11.9 (-7.1)
29. Cockburn Lake–Lowther Peak, N.W.T (75° 1.8' N, 100° 15.1' W – 74°31.8'N, 97°27.2'W)	7	5	96.5	0.458	1.05	0.0 ⁺	2 Sep 1983-20 Oct 1983, 3 Aug 1984 - 7 Jan 1985 (Sep 1983)	42.5	0.01	16.1	10.7	11.9 (-7.1)
30. Cape Warwick–Lacy, N.W.T (61° 36' N, 64° 38' W – 60°41'N, 64°35'W)	6	6	101.7	0.465	1.24	2.87	Dec 1986-Nov 1987 (Jun 1987)	23.0	1.0	16.4	16.4	12.1 (-6.9)
31. Cape Warwick–Cape Cracroft, N.W.T (61° 36' N, 64° 38' W – 62°44'N, 65°18'W)	6	6	131.9	0.453	0.48	2.11	Dec 1986-Nov 1987 (Jul 1987)	14.4	3.0	6.1	5.3	12.0 (-7.0)
32. Cape Cracroft–Vanderbilt, N.W.T (62° 44' N, 65° 18' W – 63°04'N, 67°39'W)	6	6	125.7	0.466	0.72	3.81	Dec 1986-Nov 1987 (Sep 1987)	12.6	2.0	4.1	6.2	3.9 (-7.1)
33. Cape Vanderbilt – Iqaluit , N.W.T (63° 04' N, 67° 39' W – 63°45'N, 68°32'W)	6	6	89.6	0.450	5.45	2.00	Dec 1986-Nov 1987 (Sep 1987)	10.5	0.1	2.4	-0.9	3.9 (-7.1)
<p>Notes : The predicted G values in parentheses are values from Figure 2.11 uncorrelated for over-water and Arctic paths. * The predicted G values for the mountainous paths indicated by an asterisk must be reduced by 2 dB for method 2, as discussed in section 2.3.6.2. ⁺ In the two paths noted $\phi = 1$ mrad assumed in observed G calculations for 4 – variable model, as discussed in the procedure for method 2.</p>												

Appendix D

Table D.1 Calculation of Total Signal Measurement Time in Hours and Minutes for February 2004

Date	Total Available Signal Level Measurement Time	
	Available measurement time (Hrs)	Available measurement time (Mins)
19 / 02 / 04	24	1413
20 / 02 / 04	24	1271
21 / 02 / 04	24	1439
22 / 02 / 04	24	1439
23 / 02 / 04	24	1439
24 / 02 / 04	24	1440
25 / 02 / 04	24	1439
28 / 02 / 04	24	1438
Total	192	11318

Table D.2 Calculation of Total Signal Measurement Time in Hours and Minutes for March 2004

Date	Total Available Signal Level Measurement Time	
	Available measurement time (Hrs)	Available measurement time (Mins)
06 / 03 / 04	24	1436
07 / 03 / 04	24	1440
08 / 03 / 04	24	1439
09 / 03 / 04	24	1439
10 / 03 / 04	24	1440
13 / 03 / 04	24	1440
14 / 03 / 04	24	1438
15 / 03 / 04	24	1439
16 / 03 / 04	24	1436
17 / 03 / 04	24	1435
18 / 03 / 04	24	1439
19 / 03 / 04	24	1435
20 / 03 / 04	24	1438
21 / 03 / 04	24	1438
22 / 03 / 04	24	1437
25 / 03 / 04	24	1438
26 / 03 / 04	24	1438
27 / 03 / 04	24	1436
28 / 03 / 04	24	1439
29 / 03 / 04	24	1437
30 / 03 / 04	24	1439
31 / 03 / 04	24	1437
Total	528	31633

Table D.3 Calculation of Total Signal Measurement Time in Hours and Minutes for April 2004

Date	Total Available Signal Level Measurement Time	
	Available measurement time (Hrs)	Available measurement time (Mins)
01 / 04 / 04	24	1439
02 / 04 / 04	24	1439
03 / 04 / 04	24	1437
04 / 04 / 04	24	1438
05 / 04 / 04	16	933
09 / 04 / 04	24	1440
10 / 04 / 04	24	1435
11 / 04 / 04	24	1440
12 / 04 / 04	24	1436
13 / 04 / 04	24	1439
14 / 04 / 04	24	1438
15 / 04 / 04	24	1438
16 / 04 / 04	24	1438
17 / 04 / 04	24	1437
18 / 04 / 04	24	1440
19 / 04 / 04	24	1436
20 / 04 / 04	24	1440
21 / 04 / 04	24	1436
22 / 04 / 04	24	1440
23 / 04 / 04	24	1436
24 / 04 / 04	24	1440
25 / 04 / 04	24	1440
28 / 04 / 04	24	1436
29 / 04 / 04	24	1440
30 / 04 / 04	24	1437
Total	592	35448

Table D.4(a) Calculation of Total Signal Measurement Time in Hours and Minutes for May 2004

Date	Total Available Signal Level Measurement Time	
	Available measurement time (Hrs)	Available measurement time (Mins)
01 / 04 / 04	24	1439
02 / 04 / 04	24	1439
03 / 04 / 04	24	1437
04 / 04 / 04	24	1438
05 / 04 / 04	16	933
09 / 04 / 04	24	1440
10 / 04 / 04	24	1435
11 / 04 / 04	24	1440
12 / 04 / 04	24	1436

Table D.4(b) Calculation of Total Signal Measurement Time in Hours and Minutes for May 2004

Date	Total Available Signal Level Measurement Time	
	Available measurement time (Hrs)	Available measurement time (Mins)
01 / 05 / 04	24	1438
02 / 05 / 04	24	1438
03 / 05 / 04	24	1438
04 / 05 / 04	24	1439
05 / 05 / 04	24	1436
06 / 05 / 04	24	1440
07 / 05 / 04	24	1437
08 / 05 / 04	24	1440
09 / 05 / 04	24	1435
10 / 05 / 04	24	1440
11 / 05 / 04	24	1439
12 / 05 / 04	24	1436
13 / 05 / 04	24	1440
14 / 05 / 04	24	1436
15 / 05 / 04	24	1439
16 / 05 / 04	24	1437
17 / 05 / 04	24	1439
18 / 05 / 04	24	1438
19 / 05 / 04	24	1437
20 / 05 / 04	16	941
21 / 05 / 04	24	1436
22 / 05 / 04	24	1439
23 / 05 / 04	24	1437
24 / 05 / 04	24	1439
25 / 05 / 04	24	1439
26 / 05 / 04	24	1437
27 / 05 / 04	24	1438
28 / 05 / 04	24	1439
29 / 05 / 04	24	1437
30 / 05 / 04	24	1440
31 / 05 / 04	24	1437
Total	736	44081

Table D.5 Calculation of Total Signal Measurement Time in Hours and Minutes for June 2004

Date	Total Available Signal Level Measurement Time	
	Available measurement time (Hrs)	Available measurement time (Mins)
01 / 06 / 04	8	520
03 / 06 / 04	24	1437
06 / 06 / 04	24	1438
08 / 06 / 04	24	1437
09 / 06 / 04	16	1439
10 / 06 / 04	24	1440
12 / 06 / 04	24	1438
13 / 06 / 04	24	1439
14 / 06 / 04	24	1439
15 / 06 / 04	24	1439
20 / 06 / 04	24	1439
21 / 06 / 04	24	1439
22 / 06 / 04	24	1440
24 / 06 / 04	24	1424
29 / 06 / 04	24	1432
30 / 06 / 04	24	1437
Total	368	22077

Table D.6 Calculation of Total Signal Measurement Time in Hours and Minutes for July 2004

Date	Total Available Signal Level Measurement Time	
	Available measurement time (Hrs)	Available measurement time (Mins)
01 / 07 / 04	24	1439
02 / 07 / 04	24	1439
03 / 07 / 04	24	1439
04 / 07 / 04	24	1439
06 / 07 / 04	24	1439
07 / 07 / 04	24	1439
08 / 07 / 04	7	455
21 / 07 / 04	13	780
22 / 07 / 04	24	1439
23 / 07 / 04	24	1436
30 / 07 / 04	24	1438
31 / 07 / 04	24	1439
Total	260	15621

Table D.7 Calculation of Total Signal Measurement Time in Hours and Minutes for August 2004

Date	Total Available Signal Level Measurement Time	
	Available measurement time (Hrs)	Available measurement time (Mins)
01 / 08 / 04	24	1439
02 / 08 / 04	24	1439
03 / 08 / 04	24	1439
05 / 08 / 04	24	1439
06 / 08 / 04	24	1439
07 / 08 / 04	24	1440
08 / 08 / 04	24	1439
09 / 08 / 04	24	1438
10 / 08 / 04	24	1440
12 / 08 / 04	24	1439
15 / 08 / 04	24	1439
16 / 08 / 04	24	1439
17 / 08 / 04	24	1439
18 / 08 / 04	24	1439
19 / 08 / 04	24	1439
21 / 08 / 04	16	1439
Total	368	22591

Table D.8(a) Calculation of Total Signal Measurement Time in Hours and Minutes for December 2004

Date	Total Available Signal Level Measurement Time	
	Available measurement time (Hrs)	Available measurement time (Mins)
02 / 12 / 04	24	1439
03 / 12 / 04	24	1432
04 / 12 / 04	24	1439
05 / 12 / 04	24	1439
09 / 12 / 04	24	1439
10 / 12 / 04	24	1439
11 / 12 / 04	24	1439
12 / 12 / 04	24	1439
13 / 12 / 04	24	1436
14 / 12 / 04	24	1417
15 / 12 / 04	24	1440
16 / 12 / 04	24	1438
17 / 12 / 04	24	1438
19 / 12 / 04	24	1440
20 / 12 / 04	24	1439
21 / 12 / 04	24	1438
22 / 12 / 04	24	1439

Table D.8(b) Calculation of Total Signal Measurement Time in Hours and Minutes for December 2004

Date	Total Available Signal Level Measurement Time	
	Available measurement time (Hrs)	Available measurement time (Mins)
25 / 12 / 04	24	1440
26 / 12 / 04	24	1440
28 / 12 / 04	24	1440
29 / 12 / 04	24	1439
30 / 12 / 04	24	1410
31 / 12 / 04	24	1440
Total	552	33039